T.C.
SELÇUK ÜNİVERSİTESİ
FEN BİLİMLERİ ENSTİTÜSÜ

TRANSIENT ANALYSIS OF SHORT CIRCUIT FAULTS WITH REFERENCE TO GRID-CONNECTED WIND/PV HYBRID SYSTEMS

Farhana Umer

Ph.D. Thesis

Electrical-Electronic Engineering

July 2017

KONYA

All rights reserved

Approval of Thesis

TRANSIENT ANALYSIS OF SHORT CIRCUIT FAULTS WITH REFERENCE TO GRID-CONNECTED WIND/PV HYBRID SYSTEMS

Submitted by FARHANA UMER in partial fulfillment of the requirements for the degree of **Doctor of Philosophy in Electrical-Electronics Engineering Department, Selçuk University** by:

Examining Committee Members:	**Signature**
Prof.Dr. Mehmet ÇUNKAŞ	
Assoc.Prof.Dr. Ahmet Afşin KULAKSIZ	
Assist.Prof.Dr. Nurettin ÇETİNKAYA	
Assist.Prof.Dr. Hüseyin Oktay ALTUN	
Assist.Prof.Dr. Mustafa YAĞCI	

I approve the results above.

Prof.Dr. Mustafa YILMAZ
FBE Müdürü

Date of Approval: 03.07.2017

TEZ BİLDİRİMİ

Bu tezdeki bütün bilgilerin etik davranış, ve akademik kurallar çerçevesinde elde edildiğini ve tez yazım kurallarına uygun olarak hazırlanan bu çalışmada bana ait olmayan her türlü ifade ve bilginin kaynağına eksiksiz atıf yapıldığını bildiririm.

DECLARATION

I hereby declare that all information in this document has been obtained and presented in accordance with academic rules and ethical conduct. I also declare that, as required by these rules and conduct, I have fully cited and referenced all material and results that are not original to this work.

Farhana UMER

Signature

Date: 03-07-2017

ABSTRACT

Ph.D. THESIS

TRANSIENT ANALYSIS OF SHORT CIRCUIT FAULTS WITH REFERENCE TO GRID-CONNECTED WIND/PV HYBRID SYSTEMS

Farhana UMER

THE GRADUATE SCHOOL OF NATURAL AND APPLIED SCIENCE OF SELÇUK UNIVERSITY

THE DEGREE OF DOCTOR OF PHILOSPHY IN ELECTRIC-ELECTRONIC ENGINEERING

Thesis Advisor: Assist.Prof.Dr. Nurettin ÇETİNKAYA

2017, 154 Pages

Examining Committee Members

Prof.Dr. Mehmet ÇUNKAŞ

Assoc.Prof.Dr. Ahmet Afşin KULAKSIZ

Assist.Prof.Dr. Nurettin ÇETİNKAYA

Assist.Prof.Dr. Hüseyin Oktay ALTUN

Assist.Prof.Dr. Mustafa YAĞCI

Contribution of short circuit current into the transmission network under various fault condition is a significant feature of Wind/PV hybrid power system. It's a challenging job to protection engineers due to the topology variations among Wind/PV and conventional generating units. This paper presents simulation results for various types of faults and contribution of Wind/PV generators got through transient analysis.

The objective of this research is to examine the transient behavior of a Wind/PV hybrid system due to short circuit faults and resulting waveforms explained the behavior, such as peak values and rate of decay, of the Wind/PV generators. Firstly, a conventional power system is studied, such that the transmission system is fed at one-end by a synchronous generator. Secondly, the power system studied is a hybrid power system in which the conventional power system is integrated with a 100 MW Wind/PV system. Short circuit fault takes place at different locations along a 400 kV transmission line. In this study several scenarios have been considered regarding the types of faults, fault location, fault resistance, Peterson coil and the line lengths. In the studies, ATP/ EMTP program is used for modelling the Wind/PV hybrid power system; As a result, transient overvoltage and overcurrent waveforms are computed and plotted.

Keywords— Transient Analysis; Wind/PV System; Short Circuit Fault; Peterson Coil; Fault Resistance; Overcurrent; Overvoltage and ATP/EMTP

This work is dedicated to my family

ACKNOWLEDGEMENTS

First of all, I would like to express my gratitude to God for granting me with wisdom and the opportunity of an education.

My sincere appreciation and gratitude goes to my advisor Dr. Nurettin ÇETİNKAYA for his advice, assistance, encouragement and valuable guidance in the preparation of this work.

I am grateful to acknowledge and thank all of those who assisted me in my doctorate program at Selçuk University. Special thanks are given to my other doctorate committee members Dr. Mehmet ÇUNKAŞ, Dr. Ahmet Afşin KULAKSIZ, Dr. Hüseyin Oktay ALTUN and Dr. Mustafa YAĞCI.

I would like to thank my special friend Engr. Noor KHAN for his support and encouragement throughout this work.

I would like to thank my family members and closest friends, who have been a constant source of inspiration and support throughout my life and academic career.

Acknowledgement is extended to my youngest sister Maryam UMER for her support and cares throughout this work.

TABLE OF CONTENTS

DECLARATION ..... **iii**
ABSTRACT ..... **iv**
ACKNOWLEDGEMENTS ..... **vi**
TABLE OF CONTENTS ..... **vii**
LIST OF FIGURES ..... **x**
LIST OF TABLES ..... **xv**
LIST OF SYMBOLS/ABBREVIATIONS ..... **xvii**
1. INTRODUCTION **1**
1.1 Hybrid Power System 1
1.1.1 Transient analysis 1
1.2 Research Objective 2
1.3 Research Methodology 2
2. LITERATURE REVIEW **4**
2.1 Overview 4
3. DISTRIBUTED ENERGY RESOURCES **8**
3.1 Introduction 8
3.2 Photovoltaic System as a Resource of Electric Energy 8
3.3 Worldwide Growth of Photovoltaics 8
3.3.1 Estimation for 2015 9
3.4 Photovoltaic Cell 9
3.4.1 Voltage-current characteristics and maximum power of PV system 10
3.5 Series and Parallel Circuits of PV Cells 11
3.5.1 Series connection of solar cells 12
3.5.2 Parallel connection of PV cells 12
3.5.3 From cells to arrays 13
3.6 Classification of PV Systems 14
3.7 Wind System as a Resource of Electric Energy 14
3.8 Wind Energy System 15
3.8.1 Power extracted from wind 15
3.8.2 Conversion system for wind energy 16
4. COMPUTATIONAL TECHNIQUES OF TRANSIENT ANALYSIS **19**
4.1 Introduction 19
4.1.1 Modified Fourier transform 19

4.1.2 Travelling wave technique 20
4.1.3 Phase-domain techniques (PDT) 21
4.1.4 Graphical techniques 22
4.1.5 Root-matching method (RMM) 22
4.1.6 State variable method 23
5. C OMPUTATION OF SHORT CIRCUT FAULT 25
5.1 Introduction 25
5.2 Consequences of Faults 25
5.3 Fault Statistics for Different Items of Equipment in a Power System 26
5.4 Fault Types 27
5.4.1 Series faults 27
5.4.2 Shunt faults 28
6. COMPONENTS MODELLING OF WIND/PV HYBRID SYSTEM IN ATP/EMTP 35
6.1 Introduction 35
6.2 Synchronous Generator 35
6.3 Transmission Line 38
6.4 Transformer 41
6.4.1 Single phase transformer 41
6.4.2 Three phase transformer 43
6.5 Induction Generator 48
6.6 Proposed Mathematical Formulations for the Power System Studied 50
7. SIMULATION RESULTS FOR THE PROPOSED WIND/PV HYBRID SYSTEMS ATP/EMTP SOFTWARE 53
7.1 Introduction 53
7.2 Studied Conventional Power System 56
7.2.1 Effect of line length on fault current 56
7.2.2 Effect of fault resistance 63
7.2.3 Effect of types of fault 67
7.3 PV Hybrid Power Systems 72
7.3.1 Effect of 3-phase SCF at different location on PV hybrid power system 74
7.3.2 Effect of 3-phase SCF on current at PV side i.e. location G 76
7.3.3 Effect of fault resistance on PV hybrid system 77
7.3.4 Effect of PV system and line length on fault current on PV hybrid system .. 82
7.4 Wind Hybrid Power System 86

7.4.1 Effect of 3-phase SCF at different location on wind hybrid power system ... 87
7.4.2 Effect of 3-phase SCF on current at wind generator side (bus P) 90
7.4.3 Effect of fault resistance on wind hybrid system 93
7.4.3.1 Effect of fault resistance due to 3-phase SCF 101
7.4.4 Effect of wind farm and line length on fault current on wind hybrid system 104
7.5 Hybrid Power System Connected with Wind/PV Hybrid System 107
7.5.1 Effect of 3-phase SCF at different location on Wind/PV hybrid power system 107
7.5.2 Effect of 3-phase SCF current at Wind/PV generator side (bus P and bus G) 109
7.5.3 Effect of fault resistance on Wind/PV hybrid system 115
7.5.3.1Effect of fault resistance with 3-phase SCF 123
7.5.4 Effect of line length on Wind/PV hybrid system 126
7.5.5 Comparison between conventional and Wind/PV hybrid power system due to various faults 133
7.5.6 Effect of Peterson coil with SCF 136
7.5.7 Comparison between Wind/PV GCS with solidly grounding and with Peterson coil under various faults 140
8. CONCLUSION AND FUTURE WORK 143
8.1 Conclusion..... 143
8.2 Future Work 144
REFERENCES..... 145
APPENDIX..... 149
CURRICULUM VITAE..... 153

LIST OF FIGURES

Figure 3.1 Energy received on the earth's surface 8
Figure 3.2 worldwide growths of photovoltaics 9
Figure 3.3 Projected global growth MW 9
Figure 3.4 A typical single-crystal silicon PV cell 10
Figure 3.5 The equivalent electrical circuit for a solar cell 10
Figure 3.6 A typical I -V curve for a solar cell 11
Figure 3.7 Maximum power curves for a solar cell 11
Figure 3.8 Series Connection 12
Figure 3.9 By pass diodes connected across series PV cells 12
Figure 3.10 Parallel connections 13
Figure 3.11 Forward diodes connected across parallel PV cells 13
Figure 3.12 Cells to array 13
Figure 3.13 Classification of PV systems 14
Figure 3.14 Global net renewable energy generation by fuel type from 2012-2040 15
Figure 3.15 Block diagram of wind system 17
Figure 3.16 Constant speed, variable speed and constant & variable speed WECS 18
Figure 4.1 Propagation of electromagnetic wave due to fault 20
Figure 4.2 Simple RLC circuit 23
Figure 5.1 General representation of a LG fault 28
Figure 5.2 Sequence network diagram of LG fault 29
Figure 5.3 Sequence network diagram of a LL fault 30
Figure 5.4 Sequence network diagram of LL fault 30
Figure 5.5 General representation of a DLG fault 32
Figure 5.6 Sequence network diagram of a DLG fault 32
Figure 5.7 General representation of SCF 33
Figure 5.8 Sequence network diagram of a SCF 33
Figure 6.1 Equivalent circuit of synchronous generator 35
Figure 6.2 Line segment 38
Figure 6.3 Two port representation of a transmission line 40
Figure 6.4 Single phase two winding transformer equivalent circuit 41
Figure 6.5 Three-phase Hybrid Transformer 44

Figure 6.6 Delta connection of primary side winding 45

Figure 6.7 Star-connection of the secondary windings..... 46

Figure 6.8 Block diagram of transformer 1 47

Figure 6.9 Equivalence circuit of Wind/PV hybrid system 51

Figure 7.1 Conventional power system (without PV & Wind) studied..... 53

Figure 7.2 Configuration of conventional power system with SLG fault occurs at receiving end..... 56

Figure 7.3 to 7.9 Fault current at location Z and X: when line length is 20 km, 100 km, 180 km, 200 km, 220 km, 240 km & 260 km.....57-60

Figure 7.10 to 7.16 Voltage of un-faulted phases at location Z when line length is 20 km, 100 km, 180 km, 200 km, 220 km, 240 km & 260 km 61-63

Figure 7.17 Configuration of conventional power system for fault resistance..... 63

Figure 7.18 to 7.24 Fault Current at fault location X and Z when fault resistance is 1Ω, 5Ω, 10Ω, 20Ω, 30Ω, 50Ω and 100Ω 64-67

Figure 7.25 Configuration of conventional power system for 3-phase SCF 68

Figure 7.26 Faulted phase current at location Z and X when SLG fault occurs on phase A..... 69

Figure 7.27 Current of faulted phases A and B at fault location X and Z when DLG fault occurs on phases A and B 69-70

Figure 7.28 Three phase currents at fault location X and Z when 3-phase SCF occur .. 70

Figure 7.29 Voltages of un-faulted phases at location Z and X when SLG fault occurs on phase A 71-71

Figure 7.30 Three phase voltage at location Z and X when DLG fault occur on phases A and B 71-72

Figure 7.31 Three phase voltage at fault location X and Z when 3-phase SCF occurs.. 72

Figure 7.32 P-V and V-I characteristic curves of PV 73

Figure 7.33 Hybrid power system (with PV only) at no-load 74

Figure 7.34 Configuration of PV hybrid system when 3-phase SCF occurs at location A 75

Figure 7.35 to 7.37 Fault current at fault location, when 3-phase SCF occurs at location A, B and C 75-76

Figure 7.38 to 7.40 Effect of 3-phase SCF at location G on PV terminal at ac terminal when fault occurs at location A, B and C 77

Figure 7.41 Configuration of studied PV hybrid power system: when fault resistance varies from 1Ω to 100Ω with SLG fault occurs on phase A at location A..... 78

Figure 7.42 to 7.48 Fault Current at fault location A and C when fault resistance is 1Ω, 5Ω, 10Ω, 20Ω, 30Ω, 50Ω and 100Ω on PV hybrid system 79-82

Figure 7.49 Configuration of studied PV hybrid system: when line length varies from 100 km to 260 km and Effect of line length on fault current..... .83

Figure 7.50 to 7.55 Fault Current at location C and A on PV hybrid system: when line length is 100 km, 180 km, 200 km, 220 km, 240 km and 260 km 83-86

Figure 7.56 Wind hybrid power system at no-load 87

Figure 7.57 Configuration of wind hybrid systems when SCF occurs at bus X..... 88

Figure 7.58 to 7.60 Fault current at fault location, when 3-phase SCF occur at location X, Y and Z on wind hybrid system 88-89

Figure 7.61 to 7.63 Effect of 3-phase SCF at bus P on wind generator terminal 34.5 kV side when fault occurs at bus X, Y and Z 90

Figure 7.64 to 7.66 Voltages at bus at K: when fault occurs at bus X, Y and Z on wind hybrid system 91-92

Figure 7.67 to 7.69 Voltages at bus P: when SCF occurs at bus X, Y and Z on wind hybrid system 92-93

Figure 7.70 Configuration of studied Wind hybrid power system: when fault resistance varies from 1Ω to 100Ω with SLG fault occurs on phase A at bus X 94

Figure 7.71 to 7.77 Fault Current at fault location X and Z when fault resistance is 1Ω, 5Ω, 10Ω, 20Ω, 30Ω, 50Ω and 100Ω on wind hybrid system 94-98

Figure 7.78 to 7.81 3-phase voltages at fault location X and Z: With fault resistance 1 Ω, 10 Ω, 50 Ω and 100 Ω on wind hybrid system 99-100

Figure 7.82 Configuration of studied Wind hybrid power system: when fault resistance varies from 1Ω to 100Ω with 3-phase SCF occurs at bus X..... 101

Figure 7.83 to 7.89 3-phase voltages at fault location X: when SCF occurs at fault location X with fault resistance 1 Ω1 Ω, 5 Ω, 10 Ω, 20 Ω, 30 Ω, 50 Ω and 100 Ω on wind hybrid system 102-103

Figure 7.90 to 7.94 Fault Current at fault location X on wind hybrid system: when line length is 100 km, 200 km, 220 km, 240 km and 260 km 105-106

Figure 7.95 to 7.98 Voltages of un-faulted phases at location Z on wind hybrid system: when line length is 200 km, 220 km, 240 km and 260 km.....106-107

Figure 7.99 Configuration of Wind/PV hybrid system: when 3-phase SCF occur at bus X..... 108

Figure 7.100 to 7.102 Fault current at fault location, when 3-phase SCF occurs at location X, Y and Z on Wind/PV hybrid system 108-109

Figure 7.103 to 7.105 Effect of 3-phase SCF at bus P on wind generator terminal 34.5 kV side when fault occurs at bus X, Y and Z 110

Figure 7.106 to 7.108 Effect of 3-phase SCF at bus P on wind generator terminal 34.5 kV side when fault occurs at bus X, Y and Z 111

Figure 7.109 to 7.111 Voltages at bus at K: when SCF occurs at bus X, Y and Z on Wind/PV hybrid power system 112-113

Figure 7.112 to 7.114 Voltages at bus P: when SCF occurs at bas bar X,Y and Z on Wind/PV hybrid power system 113-114

Figure 7.115 to 7.117 Voltages at bus G: when SCF occurs at bas bar X, Y and Z on Wind/PV hybrid system 114-115

Figure 7.118 Configuration of studied PV/Wind hybrid power system: when fault resistance varies from 1Ω to 100Ω with SLG fault occurs on phase A at bus X..... 116

Figure 7.119 to 7.125 Fault Current at fault location X and Z when fault resistance is 1Ω, 5Ω , 10Ω , 30Ω , 50Ω and 100Ω on Wind/PV hybrid system 116-120

Figure 7.126 to 7.129 3-phase voltages at fault location X and Z with fault resistance 1 Ω, 10 Ω, 50 Ω and 50 Ω on Wind/PV hybrid power system 121-122

Figure 7.130 Configuration of studied Wind/PV hybrid power system: with SCF occurs at bus X 123

Figure 7.131 to 7.137 SC current at location X: when SCF occurs at fault location X with fault resistance1 Ω, 5Ω, 10 Ω, 30 Ω, 50Ω and 100Ω on Wind/PV hybrid system 124-125

Figure 7.138 Configuration of studied Wind/PV hybrid system: when line length varies from 20 km to 260 km 126

Figure 7.139 to 7.144 Fault Current at fault location X on Wind/PV hybrid system: when line length is 20 km, 100 km, 200 km, 220 km, 240 km and 260 km..... 127-128

Figure 7.145 to 7.150 Fault Current at location Z on Wind/PV hybrid system: when line length is 20 km, 100 km, 200 km, 220 km, 240 km and 260 km 129-130

Figure 7.151to 7.156 Voltages of un-faulted phases at location X and Z on Wind/PV hybrid system: when line length is 20 km, 100 km, 200 km, 220 km, 240 km and 260 km 130-133

Figure 7.157 Three phase currents at fault location X when 3-phase SCF occur on conventional system alone and on Wind/PV hybrid system 134

Figure 7.158 Faulted phase current at fault location X with SLG fault on conventional system alone and on Wind/PV hybrid system 135

Figure 7.159 Current of faulted phases A and B at fault location X when DLG fault occurs on conventional system and on Wind/PV hybrid system 135

Figure 7.160 Configuration of studied Wind/PV GCS when Peterson coil varies from 1H to 65H with SCF occurs at bus X..... 137

Figure 7.161to 7.165 SC current at fault location X: when SCF occurs at fault location X with fault inductances 1H, 10H, 30H, 58.6 and 65H on Wind/PV GCS 137-138

Figure 7.166to 7.170 SC voltage at fault location X: when SCF occurs at fault location X with fault inductances 1H, 10H, 30H, 58.6H and 65H on Wind/PV GCS 139-140

Figure 7.171 SCF currents without Peterson coil at fault location X when SCF occur on Wind/PV GCS..... 141

Figure 7.172 SCF currents with Peterson coil of 58.6at fault location X when SCF occur on Wind/PV GCS..... 141

Figure 7.173 Faulted phase current without Peterson coil at fault location X with SLG fault on Wind/PV GCS. 141

Figure 7.174 Faulted phase current with Peterson coil of 58.6H at fault location X with SLG fault on Wind/PV GCS..... 142

Figure 7.175 Current of faulted phases A and B without Peterson coil at fault location X when DLG fault occurs on Wind/PV GCS 142

Figure 7.176 Current of faulted phases A and B with Peterson coil of 58.6H at fault location X when DLG fault occurs on Wind/PV GC. 142

LIST OF TABLES

Table 5.1 Probability of fault occurrence 26

Table 5.2 Fault statistics for different equipment in a power system 26

Table 5.3 Statistics of faults on overhead TLs at various voltage levels 27

Table 5.4 Statistics of faults on overhead TLs at various voltage levels 27

Table 7.1 Data of Conventional Generator 54

Table 7.2 Data of Hybrid Transformers T_1 54

Table 7.3 Data of Transmission Lines TL 54

Table 7.4 Serial impedance and shunt admittance of Transmission line 1. 55

Table 7.5 Maximum magnitudes of faulted phase current against line length at sending end Z and faulted location X 57

Table 7.6 Effect of Line Length on line Voltage at location Z 61

Table 7.7 Effect of Fault Resistance & maximum magnitudes of fault current 64

Table 7.8 Maximum magnitudes of fault current at location X and Z for different types of fault on conventional power system 68

Table 7.9 Maximum magnitudes of voltages of faulted and un-faulted phases at locations X and Z for different types of fault on conventional power system 71

Table 7.10 Data for PV generator 73

Table 7.11 Data of Hybrid Transformers T_2 73

Table 7.12 Magnitude of 3-Phase SCF currents at different locations on PV hybrid system 75

Table 7.13 Effect of 3-Phase SCF at location G 76

Table 7.14 Effect of fault resistance on fault current at location C and fault location A on PV hybrid power system 78

Table 7.15 Maximum magnitude of faulted phase current against line length at location C and fault location A and effects of PV on it 83

Table 7.16 Data for wind Generator 87

Table 7.17 Data of Hybrid Transformers T_3 87

Table 7.18 Maximum magnitude of 3-Phase SCF currents when fault occurs at different location on wind hybrid power system 88

Table 7.19 Effect of 3-phase SCF at bus P on wind hybrid power system 90

Table 7.20 Effect of 3-phase SCF at bus K on conventional generator side and maximum magnitude of Voltages at bus K 91

Table 7.21 Effect of 3-Phase SCF on Voltages at bus P 92

Table 7.22 Effect of fault resistance on fault current at bus Z and X on wind hybrid power system 94

Table 7.23 Maximum magnitude of voltage of un-faulted phases at bus Z and fault location X: when SLG fault occurs with fault resistance varies from 1 Ω to 100 Ω 98

Table 7.24 Maximum magnitudes of faulted phase currents at fault location X on wind hybrid system due to SLG fault and 3-phase SCF for different fault resistances..... 102

Table 7.25 Maximum magnitude of faulted phase current against line length at location Z and fault location X and effects of wind on it 104

Table 7.26 Maximum Magnitude of 3-Phase SCF currents at different locations on Wind/PV hybrid power system 108

Table 7.27 Effect of 3-phase SCF at bus P on wind generator side hybrid power system 109

Table 7.28 Effect of 3-phase SCF at bus G on PV generator side hybrid power system 111

Table 7.29 Effect of 3-phase SCF on at bus K on conventional generator side and maximum magnitude of Voltages at bus K 112

Table 7.30 Effect of 3-Phase SCF on Voltages at bus P at wind generator and maximum magnitude of Voltages at bus K..... 113

Table 7.31 Effect of fault resistance on fault current at location Z and fault location X on Wind/PV hybrid power system and its comparison with conventional system alone 116

Table 7.32 Maximum magnitude of voltage of un-faulted phases at bus Z and fault location X: with fault resistance varies from 1 Ω to 100 Ω 120

Table 7.33 Maximum magnitudes of faulted phase currents at fault location X on Wind/PV hybrid system due to SLG fault and SCF for different fault resistances 124

Table 7.34 Maximum magnitude of faulted phase current against line length at location fault location X on Wind/PV hybrid power system..... 127

Table 7.35 Maximum magnitude of faulted phase current against line length at location Z and effects of Wind/PV system on it 128

Table 7.36 Maximum magnitude of faulted phase current at fault location X on Wind/PV GCS..... 134

Table 7.37 Minimization of fault currents at fault location X on Wind/PV GCS due to SCF for different values of Peterson coil..... 137

Table 7.38 Comparison between solidly grounding and Peterson coil grounding of 58.6H inductance on Wind/PV GCS under various fault condition 141

LIST OF SYMBOLS/ABBREVIATIONS

SYMBOLS	EXPLANATION
ATP	Alternative Transients Program
AC	Alternating Current
Ra	Armature winding resistance
ρ_{air}	Air density
A	Area swept by the rotor blades
β	Blade pitch angle
CMRESSS	Combined Multiple Renewable Energy Sources System Simulator
Z_0	Characteristic impedance of the line
DFIG	Double Fed Induction Generator
DLG	Double Line-to-Ground Fault
Q	Differential operator
Rd	D-damper winding resistance
v_o	Downstream wind velocity
EPIA	European Photovoltaic Industry Association
EMTP	Electromagnetic Transient Program
FF	Fill Factor
λ	Flux linkage
I_F	Fault current
R_f	Field winding resistance
λ_f (t)	Flux linkage linking field winding
λ_d (t)	Flux linkage linking D-damper winding
λ_q (t)	Flux linkage linking the Q-damper winding
Z_f	Fault impedance

F	Fault location
GCPS	Grid connected photovoltaic system
GUI	Graphic User Interface
Z_g	Ground impedance
GCS	Grid Connected Systems
HV	High Voltage
XFMR	Hybrid Transformer
IGS	Integrated Generation System
IG	Induction Generator
LG	Line-to-Ground
l	Length of the line
MPPT	Maximum Power Point Tracker
P_{max}	Maximum power
K_m	Mass flow rate
NISM	Numerical Integrator Substitution Method
PCC	Point of Common Coupling
P and O	Perturb and Observe
PDT	Phase-Domain Techniques
PV	Photovoltaic
γ	Propagation constant
R_q	Q-damper winding resistance
Re	Real part of the integration
R_r	Radius of turbine blade
RMM	Root Matching Method
Rr	Radius of turbine blade
C_P	Rotor power coefficient

SEIG	Self-Excited Induction Generator
SPE	Solar Power Europe
SG	Synchronous Generator
SCIG	Squirrel Cage Induction Generator
SCF	Short Circuit Fault
V_S	Sending end voltage
I_S	Sending end current
TL	Transmission Line
P_T	Theoretical power
TSR	Two-Sided Recursions
τ	Travel time of the traveling wave
Cg	Turn to earth capacitor
n_r	Turbine rotating speed in rpm
ULM	Universal Line Model
WR	Wound Rotor
WECS	Wind Energy Conversion System
v	Wind speed

1. INTRODUCTION

1.1 Hybrid Power System

The global reduction fossil-fuel has necessitated an urgent search for alternative energy resources. The wind, PV and hydro sources of energy are inexhaustible, pollution-free, and freely available. The hybrid systems have been considered as attractive and preferred alternative resources (Borowy, 1996; Patel, 2000).

Hybrid power system used number of generation sources i.e. PV, wind, hydro and/or with other conventional systems. PV and wind powers are the most significant part of the globally produced generation (Bhandari and etc., 2015).

1.1.1 Transient Analysis

Transient analysis of faults in hybrid systems is one of the most challenging and vital task. Transients occur in power system due to various reasons resulting because of power system configuration changes i.e. switch opening switch closing, faults, lightning strikes or load variations.

The time of transients is short and equipment faces high transient current and high transient voltage during a transient period. It causes severe damage i.e. thermal stress, fire risk that possibly damages the power system apparatus (Velasco, 2014; Sluis, 2001).

Two types of stress can be caused by transient phenomena in power system

- Over-currents
- Over-voltages

In order to provide adequate protection against both types of stresses, it's important to calculate their main features, location and estimate the most unfavourable operating conditions. Accurate analysis of transients is hard due to the size of the system, complexity of the interaction between power devices. Now the study of transients is done with the help of computer (Velasco, 2014).

Power system engineer must understand transients and quantify transients so that, system components are designed to withstand or control transients to avoid damage from high transient voltages and high transient currents. Transients include higher frequencies up to kHz and MHz

When the network changes from one steady state into another transient occurs. It can be due to lightning hits the earth or when it strikes a substation directly. Most of the transient are due to switching action i.e. load disconnect switches. Fuses and circuit breakers interrupt high currents and clear small currents during fault (Sluis, 2001).

Fault contributes the system to an abnormal condition. Transients occur in the system due to various types of faults i.e. SLG LL, DLG and SCFs. SCFs result in a switching action, which often results in transient over-voltages (Velasco, 2014; Sluis, 2001).

1.2. Research Objective

This research examines the behaviour of hybrid power system against transients during symmetrical and asymmetrical faults. The objectives of this research are given below:

- Analyse the transients due to symmetrical and asymmetrical faults on a hybrid power system.
- Examine the variation of fault currents and voltages under the influence of various factors such as types of faults and fault locations in the hybrid power system studied.
- Investigate the transient voltages and currents resulting from various types of faults under the effect of non-linear protective devices.

1.3. Research Methodology

- Literature study and collection of data for hybrid power system.
- Selection of a hybrid power system (Integration of conventional power system, PV and Wind).

- Modelling of PV, Wind and conventional power systems.
- Analyse the symmetrical and asymmetrical faults in the hybrid power system considered.

A theoretical background & Literature review is given in Chapter 2. Numerical & theoretical discussion related to distributed generation resources is done in Chapter 3. A theoretical background of different methods of transient analysis for short circuit fault is given in Chapter 4. Types of fault, Mathematical calculation of different types of fault & representation of short circuit faults are given in Chapter 5. In Chapter 6, a representation of transmission system component, generator, hybrid transformer (XFMR) and transmission line models are all presented. A general analysis of the transient short circuit fault is presented in Chapter 7. The analysis presented in Chapter 6 and 7 allow determining the transient short circuit currents and voltages of different system configuration. Chapter 8 summarizes the conclusions of this thesis & few suggestions for future study.

2. Literature Review

2.1 Overview

Several researchers have been studied transient analysis of hybrid power systems due to faults, switching transient etc. Some of such studies are mentioned below.

It has been shown in (Ünver, 1995), that severity of fault and its transient component in transmission systems depends on several factors, such as the magnitude of voltage when fault occur, type of fault and fault location. These factors have important influence on magnitude and shape of voltage and current waveforms.

Demetrios in (Tziouvaras, 2008), use the two-port theory based on symmetrical component transformation for the analysis of simultaneous faults in power systems. Similarly, LEVA applied time-dependent symmetrical components in (Leva, 2009) to study the dynamic analysis of asymmetrical faults in power system. This approach explored Lyon state model of faulted line to examine the transient over-voltages and current due to short circuit.

Wilson and Schmidt in (Wilson, 1974), analysed the behaviour of transmission line for open & short circuit. The voltage and current can be symbolized by both space and partial differential equations, and the solution of such equation become tedious especially when it involves a complex network. But the numerical methods after usage of computers has made the whole process easy and several methods have been developed. Dommel combined the trapezoidal integration for lumped parameters and method of characteristics for transmission lines to solve power system transients (Dommel, 1969). In (Phukan and etc., 2013), a Waveform matching technique is used based on Bare Bones Particle Swarm Optimization techniques of diagnosed short circuit fault.

Valarmathi worked on PV/Wind hybrid system and MATLAB and Model-sim was used for simulation. In this work a VLSI based fuzzy logic controller is used into the hybrid system for supply of continuous power to the grid. Static and dynamic behaviour of the system is analysed. Different type of faults such as LG, LL, DLG and symmetrical faults are studied on 25 kV side of wind generator and also results are

analysed. The results show that hybrid system provided continuous power to the grid under faulty wind farm by means of VLSI based fuzzy logic controller (Valarmathi and etc., 2012).

Jafar Zangina Sulaiman worked on transient behaviour of a hybrid power system (wind and conventional power system) due to SC fault and investigates the effect of type of fault and fault location. EMTP/ATP is used to simulate short circuit faults resulting in transient over voltages and currents. The system components are connected in cascades with a power line of 132 kV. The first power system studied is a conventional power system, in which the TL is fed at one end by a SG. The short circuit occurs at the receiving end of the line. Several scenarios have been considered in the studies. These include the effect of line length, source impedance and fault type. The second power system studied is a Wind hybrid system. In this system, conventional system integrated with a wind power system. The system under study is a balanced system, but the models of various components such as load, wind turbine control system etc. have effects on the transient behaviour of the system during fault. It's proved from the results that severity of fault transients in the power system studied varies on line length, source impedance and fault location. The analysis carried out in this work is fundamental designing and operating stages of a hybrid system (Sulaiman, 2014).

Lin Ye (2012) in his paper ATP/EMTP is used for simulations. A dynamic model of wind/PV/hydropower system created in EMTP/ATP software. These sources are directly connected to grid through power electronic devices and have direct impression on grid frequency and voltage. Case study has done to examine the dynamic behaviour of DGs during faulty and steady states and short circuit faults on LV 400 V (Lin Ye and etc., 2012).

Seul-Ki Kim worked on modelling and simulation of a GCPS to examine the behaviour grid interface and performance of the design. Grid connected photovoltaic system was presented for transient analysis. It included detailed model of the PV and its controllers. PSCAD/EMTDC was used for modelling. This simulation analyse the dynamic performance and control of a PV system and its interaction behaviour with the power system i.e. harmonics, anti-islanding performance, and response to grid faults i.e.

SCF and LG fault. The faults occurred at 380 V and 100 m long lines away from PCC at 0.1sec (Kim and etc., 2009).

Seul-Ki Kim in his paper worked on modelling of PV and Wind generator on PSCAD/EMTDC software. Author worked on control of a wind/PV hybrid system for interconnection operation & it consists of variable speed wind/PV generators, converter and grid interface inverter. It is used to compute the maximum energy available from varying condition of wind speed and solar irradiance and MPPT is applied for PV. The simulation results demonstrate dynamic behaviour and control performance of the wind/PV system (Kim and etc., 2006).

F. Bonanno in his paper deals with the implementation in a continuous simulation language of the dynamic model of an IGS named CMRESSS. It is useful tool to determine the IGS electric transient behaviour during the planning stage. GUI is easy handling for events scheduling and input data, it simulated transient under normal faulty condition. Transient behaviour of IGSs is analysed during dump load insertions and sudden load variations, which have various features, to calculate the electrical quantities either in normal or in faulty condition. This analysis assists to limit or reduce electrical and mechanical stresses. Results verified the consistency of the simulation package and the advantages are achieved in design by comparative analysis of various power plants (Bonanno and etc., 1999).

Jin Yang in his paper studied transient behaviour of SCF and LG fault analyses of VSC based dc systems. The analysis of the most severe SCF provides a critical time limit for switchgear operation. Fault location method is used for LG faults with analysis due to different fault distances and resistances. Single iteration method has been suggested and modifies the accuracy of the distance and estimated resistance. The proposed method is a prerequisite for determining the fault location to meet the relay protection & coordination (Yang and etc., 2012).

E. M. Natsheh in his paper has developed a model of WT/PV hybrid system. It uses MATLAB for modelling of PV/WT, IG, converters and controller. P and O algorithm is used for implementation of MPPT. The dynamic behaviour of the model is analysed under various operating conditions, irradiance, temperature and wind speed data collected from a 28.8 kW PV system connected to grid, situated in Manchester.

The proposed model and its control scheme give a right tool for the performance optimization of WT/PV hybrid system (Natsheh and etc., 2011).

Sweeka Meshram in his paper worked on complete modelling of PV-grid connected system at 132 kV. In this paper, 10 kW PV systems and 7.5 kW hydro are considered as RESs integrated with grid. To insure the uninterrupted power flow due to the irregular nature of PV and hydro sources, grid is integrated with system. SEIG and converters are used by hydro generation system. To set the generated voltage to the rated voltage of grid, AC/DC/AC converter is used. The control of PV/hydro system is supported by constant current controller. Results show that the proposed system has ability to place into service and can supply power to users (Meshram and etc., 2013).

Y. Kang in his research worked on a new method for transient analysis of power system. This method has combined benefits of state variable method and Dommel's nodal analysis method but it efficiently prevents their drawbacks. This method is capable for the problems of transient analysis of power system with and without power converters. It might apply the nodal analysis method for improvement such as EMTP (Kang and Lavers, 1996).

In this work author presents contribution of SC current for various type of Wind generator. The resulted waveforms are analysed for understanding the behaviours i.e. rate of decay and maximum value of WT. The consequences of the control algorithms of converters on SCF are also examined (Muljadi and etc., 2010).

3. DISTRIBUTED ENERGY RESOURCES

3.1 Introduction

The demand of the improved and environment friendly energy system has grown worldwide. Wind and solar energy systems are most widely used energy systems (E.ZB, 2010). Distributed generation (DG) are more cost effective, inexhaustible and high reliability than conventional systems. Although DG comprises a small fraction of the total capacity, DG technologies are considered to be a solution to achieve a better energy system (Ackermann and etc., 2001). Hybrid systems are considered as an efficient way to decrease fuel demand and emissions as compare to conventional systems (Shahirinia and etc., 2005).

3.2 Photovoltaic System as a Resource of Electric Energy

The sun is the main source of all the alternative energies on the earth's surface. It's shown in Figure 3.1 that the solar radiation is lower when it comes to the surface because of atmospheric medium among the sun and surface (Ghosh and Prelas, 2011).

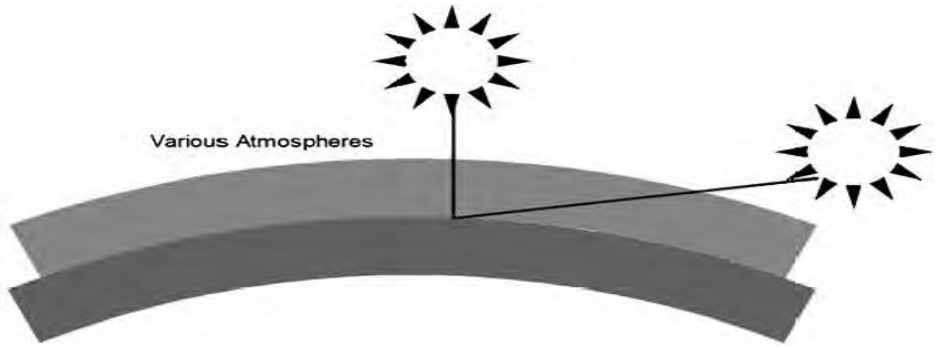

Figure 3.1 Energy received on earth's surface (Ghosh, 2011)

3.3 Worldwide Growths of Photovoltaics

Today photovoltaic has become a globally critical issue and at the end of 2014 its demand has arrived up to 178 GW. The growing demand of PV market from 2006 to 2014 is shown in Figure 3.2 (Wikipedia, 2015; IEA, 2014).

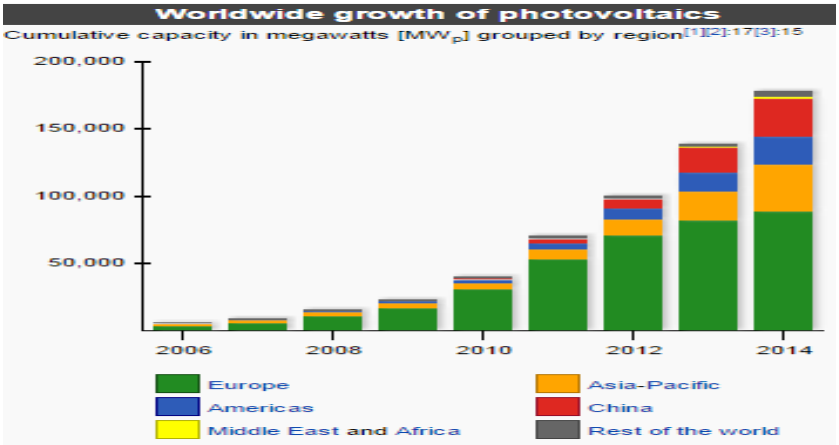

Figure 3.2 worldwide growths of photovoltaics (Wikipedia, 2015)

3.3.1 Estimation for 2015

In June 2015, SPE, the former EPIA issued its current report for power projection from 2015–2019 as shown in Figure 3.3 ("International Energy Agency Photovoltaic Power Systems Program", 2015; "Global Market Outlook for Solar Power 2015-2019", 2015).

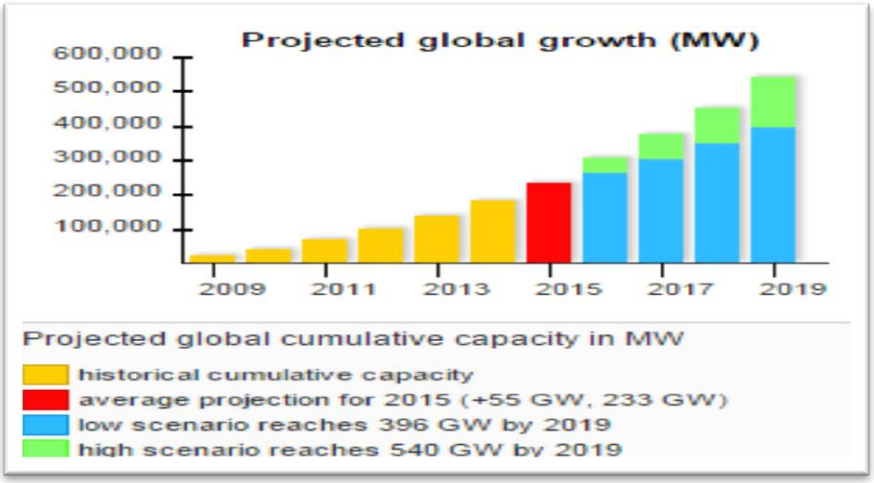

Figure 3.3 Projected global growth MW (SPE, 2015)

3.4 Photovoltaic Cell

A typical single crystal silicon PV cell consists of several layers:

- A conducting grid on the top surface

- An antireflective coating
- Treated surface layer
- A thin layer of silicon n-type which is a collector
- A silicon based layer p-type doped oppositely to the collector
- Back contact electrode.

Single-crystal silicon PV cell is given in Figure 3.4

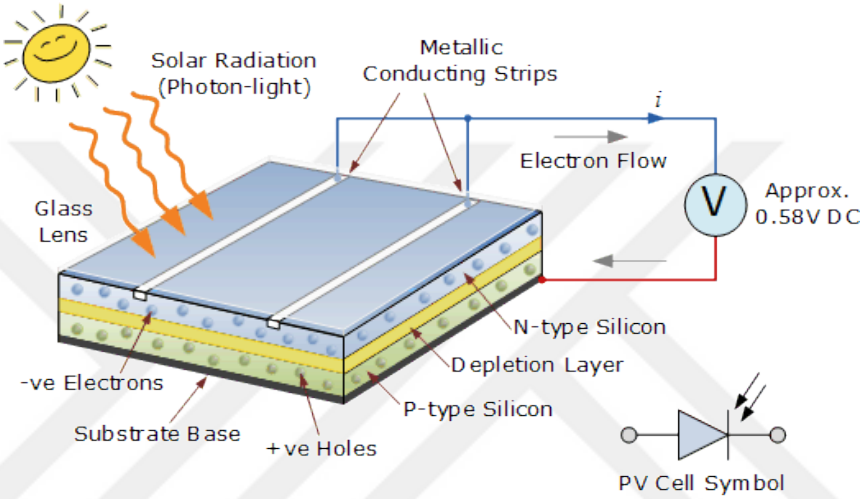

Figure 3.4 A typical single crystal silicon PV cell (Mahela, 2013)

3.4.1 Voltage-current characteristics and maximum power of PV system

To calculate the current & voltage from solar cells, we can consider an equivalent circuit given in Figure 3.5. Output current (I) from a solar cell is given by Equation 3.1 (Mahela and Ola, 2013).

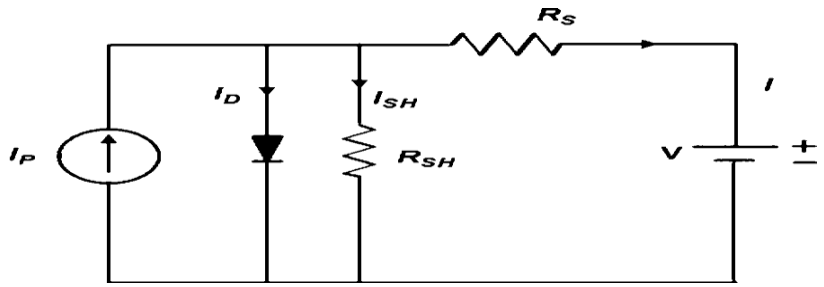

Figure 3.5 The equivalent electrical circuit for a solar cell (Mahela and Ola, 2013)

$$I = I_P - I_0 \left[e^{\frac{q(V+I R_S)}{nKT}} - 1 \right] - \frac{V + I R_S}{R_{SH}} \tag{3.1}$$

V- I curve represented by Equation 3.1 is given in Figure 3.6.

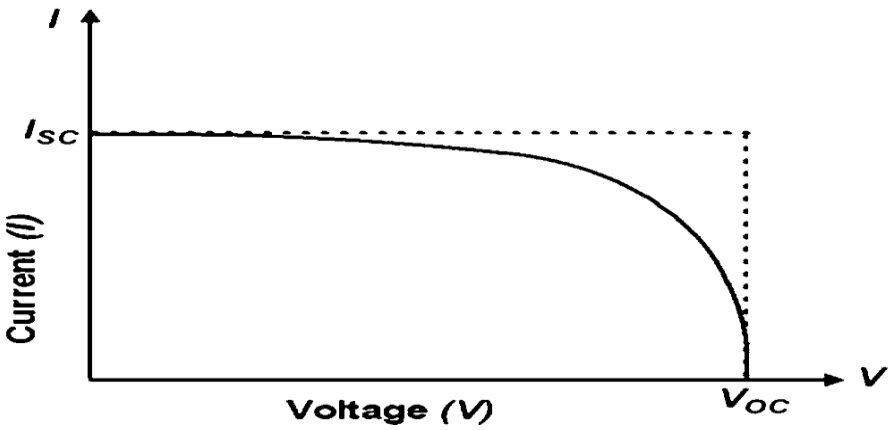

Figure 3.6 A typical I -V curve for a solar cell (Mahela and Ola, 2013)

Maximum power will appear between I_{SC} and V_{OC} as given in Figure 3.7. Fill factor is defined as the ratio of P_{max} to P_T and FF is considered to be a measure of the quality of a solar cell.

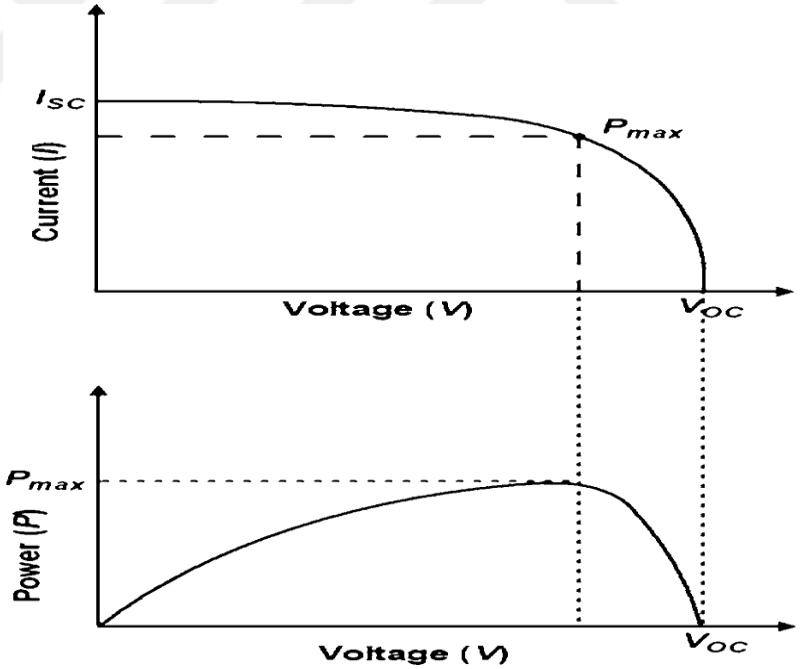

Figure 3.7 Maximum power curve for a solar cell (Mahela and Ola, 2013)

3.5 Series and Parallel Circuits of PV Cells

PV modules are the system's building blocks and they can be connected either in series or shunt to get a required voltage.

3.5.1 Series connection of solar cells

Usually PV cells are not operated separately because of their low voltage. Cells are mostly connected in series in PV modules as given in Figure 3.8. Bypass diodes are usually connected across strings of cells as shown in Figure 3.9.

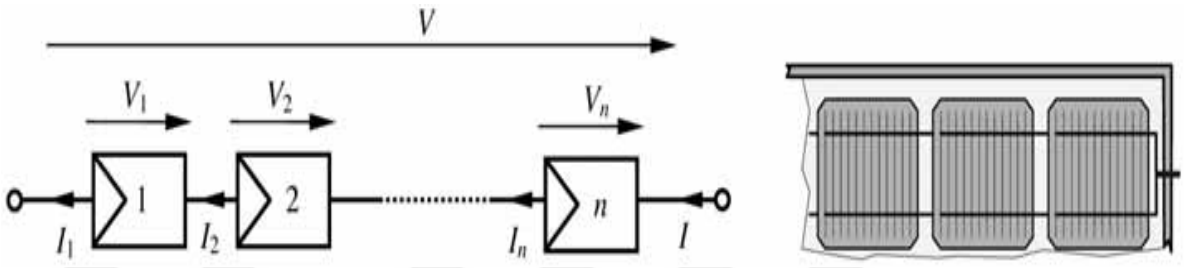

Figure 3.8 Series Connection (Quaschning, 2005)

The current Ii through all cells is same & the cell voltages V_i are added to obtain the overall module voltage V:

$$I = I_1 = I_2 = \ldots\ldots\ldots\ldots I_n \quad (3.2)$$

$$V = \sum_{i=1}^{n} V_i \quad (3.3)$$

$$V = n\,V_i \quad (3.4)$$

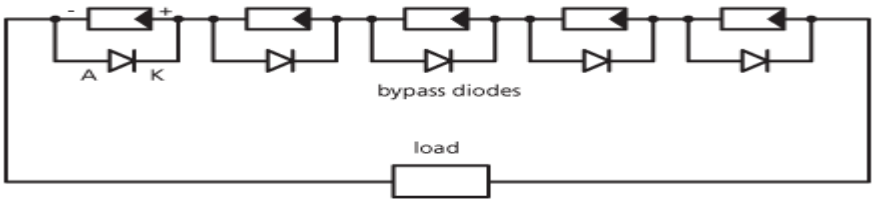

Figure 3.9 By pass diodes connected across series PV cells (Quaschning, 2005)

3.5.2 Parallel connection of PV cells

PV cells can also be connected in parallel. Parallel connections are rarely used because increase in current results in higher losses in transmission. Parallel connection is shown in Figure 3.10. Parallel bypass diodes are used for cell protection as shown in Figure 3.11 (Quaschning, 2005).

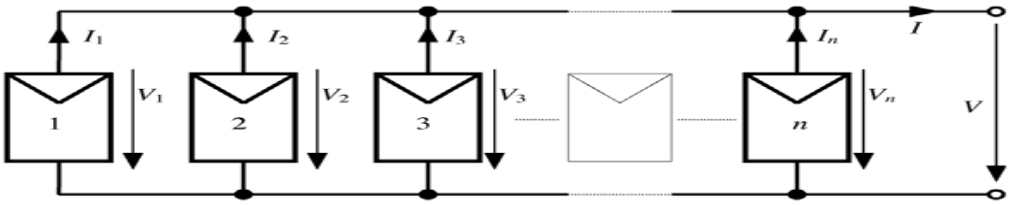

Figure 3.10 Parallel connections (Quaschning, 2005)

$$V = V_1 = V_2 = \ldots\ldots\ldots V_n \tag{3.5}$$

$$I = \sum_{i=1}^{n} I_i \tag{3.6}$$

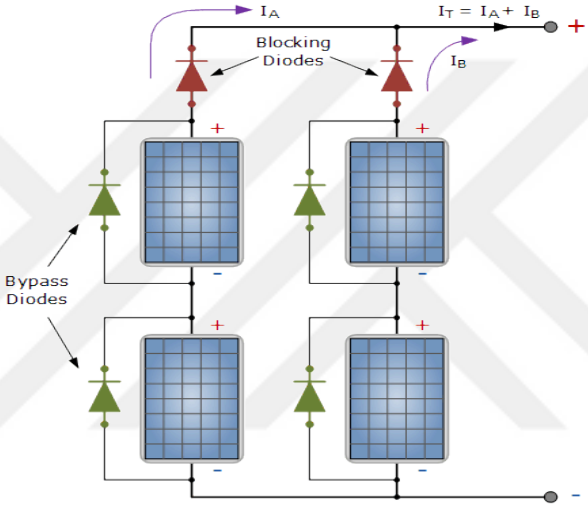

Figure 3.11 Forward diodes connected across parallel PV cells (Quaschning, 2005)

3.5.3 Cells to Arrays

A single PV cell is the basic unit of a PV system. Number of individual cells are connected together to form larger unit called modules. Modules are then connected to form arrays as given in Figure 3.12 (Patel, 2000).

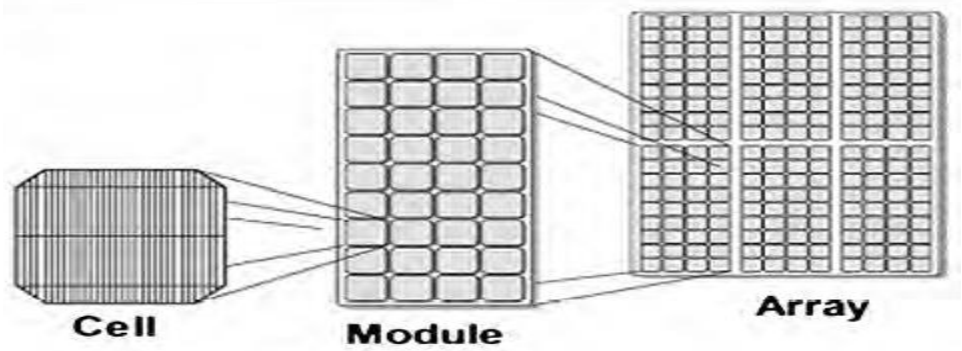

Figure 3.12 Cells to array (Patel, 2000)

3.6 Classifications of PV Systems

PV systems are classified according to the diagram in Figure 3.13. Stand-alone and grid connected systems are the two main classifications; however the hybrid systems are of significant value (Ventre et al, 2004).

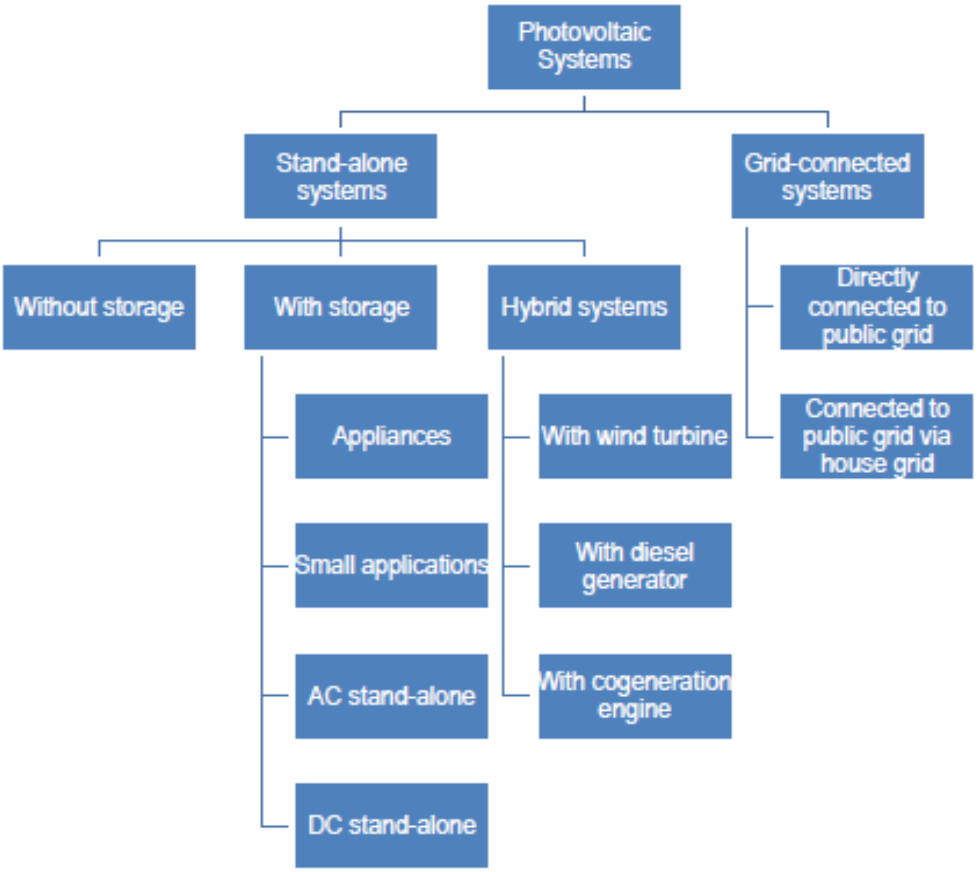

Figure 3.13 Classification of PV systems (Ventre et al, 2004)

3.7 Wind System as a Resource of Electric Energy

Wind energy is one of the fastest growing technologies. Wind energy is a crucial part for clean energy substitute. The development of wind technology provided advances in drive system, control systems. Wind farm is a group of wind turbines in the same location (Patel, 2000). It's a common practice to represent the entire WPP as a single turbine generator (Muljadi and Ellis, 2010).

Total generation increases by 2.9%/year from renewable resources and will grow 29% in 2040. Figure 3.14 shows that hydro and wind energy each account for 33% and solar energy for 15% during projection period (EIA, 2016).

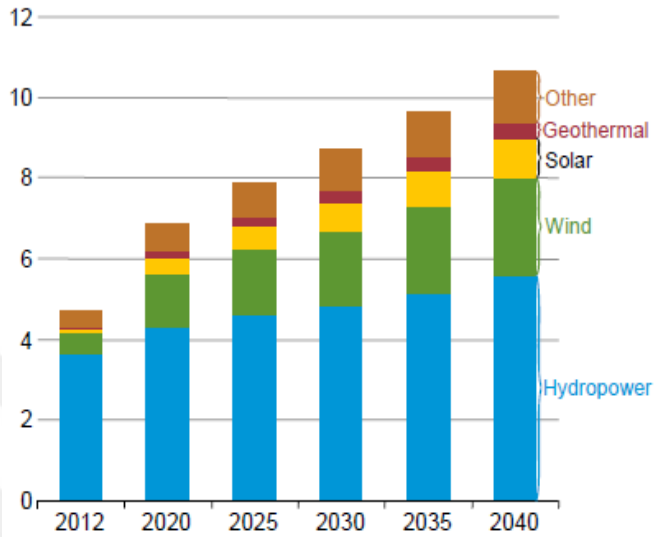

Figure 3.14 Global net renewable energy generation by fuel type from 2012-2040 (EIA, 2016)

3.8 Wind Energy System

Wind energy systems convert kinetic energy of wind into electrical energy. The kinetic energy of air of mass m moving at speed v can be expressed as in Equation 3.7.

$$E_k = \frac{1}{2}\, m\, v^2 \tag{3.7}$$

$$m = \rho\, A\, v\, t \tag{3.8}$$

Wind power is given by Equation 3.9

$$P = \frac{1}{2}\, \rho\, A\, v^3 \tag{3.9}$$

3.8.1 Power extracted from wind

Power extracted by the rotor blades from wind is the difference between the up and down stream wind powers

$$P = \frac{1}{2}\, K_m\, (v^2 - v_0^2) \tag{3.10}$$

Where v_0& v are the up & down stream wind velocity respectively. K_m is the flow rate of mass.

Mechanical power obtained by the rotor is given by:

$$P = \frac{1}{2}\left[\rho\, A\, \frac{v + v_0}{2}\right](v^2 - v_0^2) \tag{3.11}$$

Let $C_p = \frac{1}{2}\left[1 + \frac{v_0}{v}\right]\left[1 - \left(1 - \frac{v_0}{v}\right)^2\right]$ and rearrange the terms in Equation 3.11, we have:

$$P = \frac{1}{2}\,\rho\, A\, v^3\, C_P \tag{3.12}$$

Equation 3.13 is used to calculate the extractable mechanical power.

$$P_w = \frac{1}{2} C_P \left(\frac{R_r\, n_r}{v}, \beta\right) \rho_{air} \pi R_r^2 v^3 \tag{3.13}$$

ρ_{air}: Air Density; R_r : Radius of turbine blade; v: Wind speed respectively

C_p: Rotor Power Coefficient; n_r : Turbine rotating speed in rpm;

β: Blade Pitch angle

3.8.2 Conversion system for wind energy

The block diagram of a wind energy conversion system is shown in Figure 3.15 (Masters, 2004). The main parts of a wind turbine are the tower, the yaw, the rotor and nacelle, which accommodate the gear box and the generator. Wind turbine is categorized in terms of rotor configuration, and the speed at which a wind turbine begins to generate electricity is referred as cut-in speed while cut-out speed at which the turbine must fold to protect itself from being overwhelmed (Gilbert, 2004).

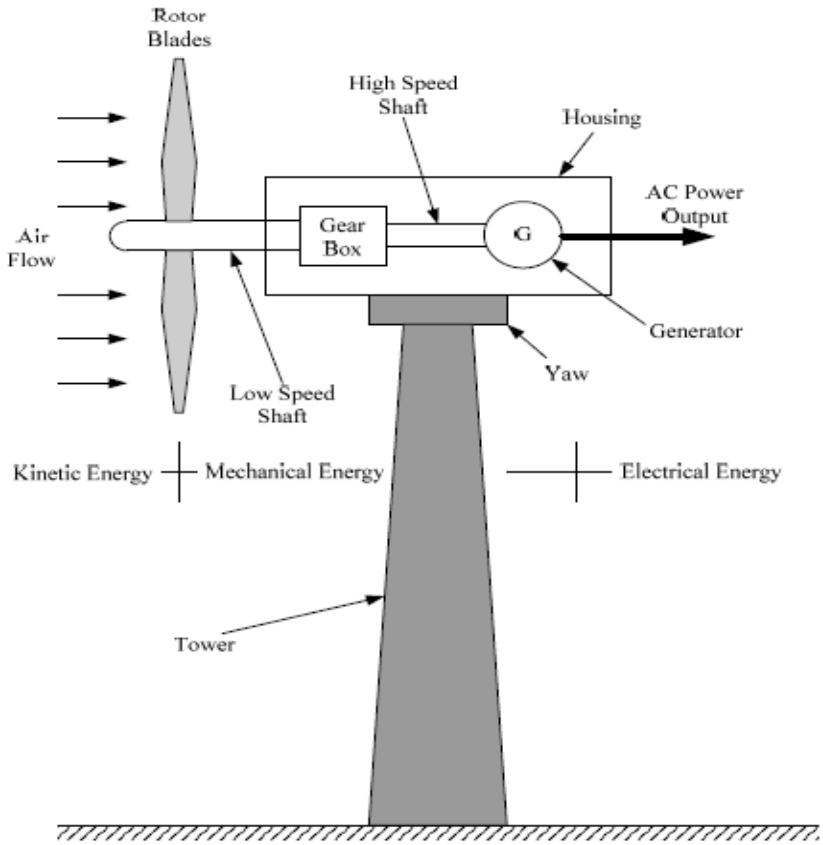

Figure 3.15 Block diagram of wind system (Gilbert, 2004)

There are two types of wind energy conversion systems: constant and variable speed systems as shown in Figure 3.16. In Figure 3.16 (a), SCIG is connected to a grid directly, since generator is directly coupled, the wind turbine rotates at a constant speed. Generation systems, shown in Figure 3.16 (b) and (c), are variable speed systems. In Figure 3.16 (b), the generator is a DFIG (WR). The rotor is fed by a back to back voltage source converter and the stator is directly connected to grid. Figure 3.16 (c) is completely decoupled from load or grid through a power electronic interfacing circuit. The generator can either be a SG or an IG (Slootweg, 2003). In this thesis, WECS, similar to that shown in Figure 3.16 (a), is used.

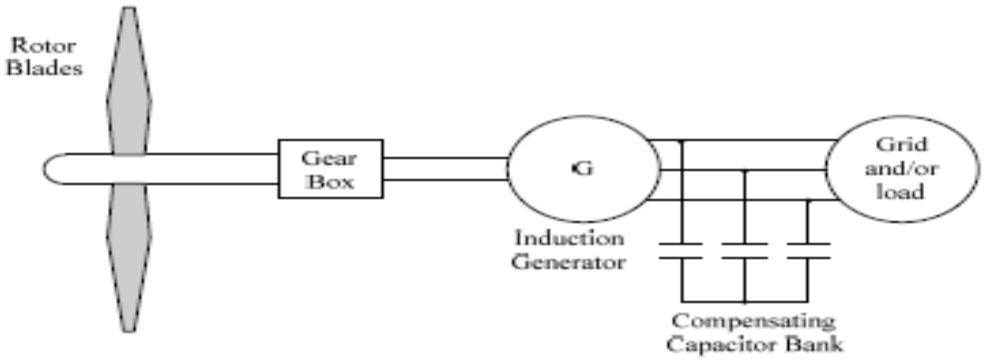

Figure 3.16(a) Constant speed WEC (Gilbert, 2004)

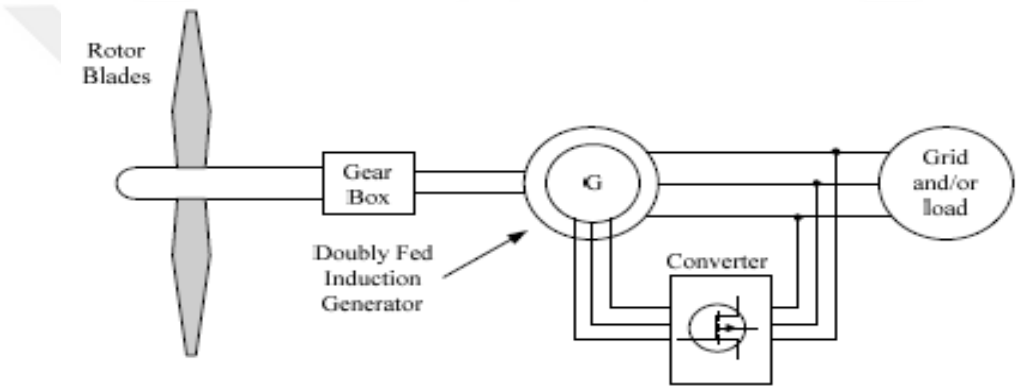

Figure 3.16(b) Variable speed WECS (Gilbert, 2004)

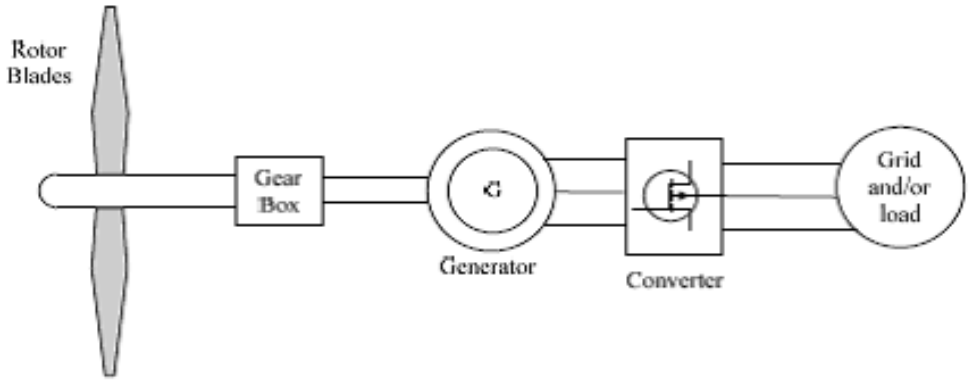

Figure 3.16(c) Constant and variable speed WECS (Gilbert, 2004)

4. COMPUTITIONAL TECHNIQUES OF TRANSIENT ANALYSIS

4.1 Introduction

For understanding the performance of power systems, explanation of failures of components, calculating ratings of equipment & analysis of electromagnetic transients are key methodology. In general study of transients is a develop field that plays significant role for designing of power systems. Various numerical methods, GUI and simulation tools are available for study of transients (Velasco, 2015). There are various analytical methods used for transient analysis of power system such as

- Modified Fourier Transform
- Travelling Wave Technique
- Phase Domain Technique
- Graphical Technique
- Root Matching Technique
- State Variable Technique

4.1.1 Modified Fourier Transform

The solution of this technique involves both time and frequency domain, and the complexity posed by the element of frequency dependence within the system parameter is resolved by using modified Fourier integral transform (Kim, 2009). The principal Fourier transform is determined by the following equations:

$$f(t) = \frac{1}{2\pi} \int_{-\infty}^{\infty} F(\omega)\, e^{j\omega t}\, d\omega \tag{4.1}$$

$$f(\omega) = \frac{1}{2\pi} \int_{-\infty}^{\infty} F(t)\, e^{j\omega t}\, dt \tag{4.2}$$

The modified Fourier transform is attained by shifting the integration path of Equation 4.1 in the jω plane below the real axis by a constant factor α, since all poles of the integral lies above or on the real frequency axis for real and stable system. Thus, all the executable poles within the axis may induce imbalance in finding the inverse

transform. The value of integral would be unaffected if the direction of integration is lowered, since there is no pole in the lower half plane.

Let ω' be the new angular frequency due to the lowered path of integration and be given by

$$\omega' = \omega + j\alpha$$

Then, the inverse modified transform can be expressed by

$$f(t) = \frac{1}{2\pi} \int_{-\infty - j\alpha}^{\infty - j\alpha} F(\omega' - j\alpha)\ e^{[j(\omega' - j\alpha)]}\, d\omega' \tag{4.3}$$

$$f(t) = \frac{e^{(\alpha t)}}{2\pi} \int_{-\infty - j\alpha}^{\infty - j\alpha} F(\omega' - j\alpha)\ e^{[j\omega' t]}\, d\omega' \tag{4.4}$$

In Equation 4.4 real part of the integral is even and the imaginary part is odd, so that the integration of the odd part within the limits of $-\infty - j\alpha$ to $\infty - j\alpha$ become zero. But then, making use of the consistency of the real part, that is, integration of the real part within the limit of $-\infty - j\alpha$ to 0 equal to that within the limit of0 $to\ \infty - j\alpha$, Equation 4.4 may be simplified to

$$f(t) = \frac{e^{(\alpha t)}}{\pi} R_e \int_{0}^{\infty - j\alpha} F(\omega' - j\alpha)\ e^{[j\omega' t]}\, d\omega' \tag{4.5}$$

4.1.2 Travelling Wave Technique

Traveling wave phenomenon for HV lines establishes one of the smallest system transients and it occurs for m-sec to µs (Krzysztof and etc., 2011). A fast and substantial vary in voltage within the HV line as shown in Figure 4.1, an electromagnetic wave which transmits in reverse directions from that point.

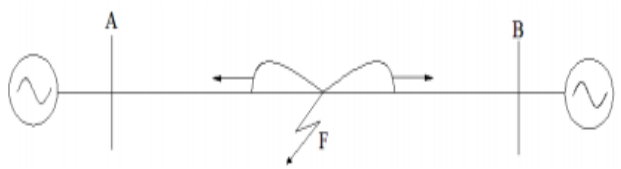

Figure 4.1 Transmission of electromagnetic wave due to fault (Krzysztof and etc., 2011)

Electromagnetic wave can be separated into a voltage wave. A significant characteristic of such wave is moving the particular values of current and voltage with

finite speed along lines. Wave propagation in high voltage TL is given Equations 4.6 and 4.7, for lossless line (R=0, G=0) are:

$$\frac{\partial v(x,t)}{\partial x} = -L\,\frac{\partial i\,(x,t)}{\partial t} \tag{4.6}$$

$$\frac{\partial i(x,t)}{\partial x} = -C\,\frac{\partial v\,(x,t)}{\partial t} \tag{4.7}$$

Where, $L = {}^{\text{Inductance}}/_{\text{unit length of line}}$, $C = {}^{\text{Capacitance}}/_{\text{unit length of line}}$

Equations given above have voltage wave and current wave that describe electrical and propagation of magnetic field respectively. Lattice diagram of the propagation field assigned using Bewley method (Bewley, 1951) accepted that if the travelling wave of the above expression can travel without distortion or attenuation on strips line, then both the reflection and refraction coefficient can be found from the understanding of line surge impedances.

4.1.3 Phase-Domain Technique (PDT)

The complexity of transformation matrices dependent on frequency could be avoided by doing transient measurement of the transmission system with phase quantities. Initially the PDTs based on numerical convolution in time domain (Mahmutcehajic and etc., 1993). Though, in simulating using these techniques is consuming long time, as it required a lot of time steps.

An effective tactic is based on the usage of TSR (Martinez and etc., 2010). Let us consider a brief approaches given below, the basic frequency domain input output is showed as given below:

$$y(s) = H(s)\,u(s) \tag{4.8}$$

$$y(s) = D'\,(s)\,N\,(s)\,u(s) \tag{4.9}$$

Where, $y(s)$ is O/P, $u(s)$is I/P & $H(s)$ is response of a transfer function

$D(s)$ is the polynomial matrix for rational approximation of $H(s)$

$N(s)$is also a polynomial matrix for approximation of $H(s)$

4.1.4 Graphical Techniques

Graphical methods are beneficial teaching tools in understanding the incident of transient phenomena but they cannot come to the more exact analytical method. Bewley Lattice became awkward method for large systems (Dommel, 1971). Graphical method was used to create computer programs for large systems. An influential graphical technique that provided additional details into travelling wave theory is described in (Alrett and Shelley, 1996). Actually, non-linear elements and complex system setup are adopted in this technique. Transformers are represented by shunt and series elements, large surge impedance with lumped inductance and capacitance are all considered for precise transient study.

There are several mode of propagation as there are many conductors within the system; as such attenuation is attainable by introducing series resistance. The transient analysis with graphical method is effective, but when compared with analytical technique, there is a little discrepancy which might be as a result of complex equipment approximation.

4.1.5 Root-Matching Method (RMM)

The integration techniques based on Taylor's series having tendency to numerical oscillations while simulation respond. The implementation of this technique needs the use of RMM. The aim RMM is to transfer zeros and poles from the *s* to *z* plane. It explains how RMM can apply in simulation of electromagnetic transient and it’s performance is compared with conventional NISM.

The application of NISM and trapezoidal rule, to a series RL branch gives the following equation for branch:

$$i_k = e^{(-\Delta tR/L)}\, i_{k-1} + \left(1 - e^{(-\Delta tR/L)}\right) v_k \tag{4.10}$$

The RMM gives a rigorous technique. The root matching technique precisely transfers the poles and zeros of a transfer function from s to z plane. Exponential form of difference equation is regarded as the basis of implementing this method. Consider Equation 4.11 representing transfer function relating current and voltage in a network.

$$H(s) = \frac{(s - s_{z1})(s - s_{z2}).....(s - s_{zM})}{(s - s_{P1})\,(s - s_{P2}).....(s - s_{PN})} \tag{4.11}$$

Transformation to discrete domain is done by substituting the s, s_z and s_P with $z = e^{s_z t}$ & $z = e^{s_P t}$

$$H(s) = \frac{D(z - e^{s_{z1} t})(s - e^{s_{z2} t}).....(s - e^{s_{zM} t})}{(s - e^{s_{P1} t})\,(s - e^{s_{P2} t}).....(s - e^{s_{PN} t})} \tag{4.12}$$

Equation (4.12) is called a matched Z transform. Where, the subscript z, p represent zero and pole respectively. The D is a constant that stand for comparison of a specified excitation steady state response. The matching technique can be attained by using a first order differential pole to develop a difference equation for transient study (Watson and Arrillaga, 2003).

4.1.6 State Variable Method

State variable analysis method uses an indefinite numerical integration of the system variables in conjunction with the differential equation to achieve the derivatives of the states.

The significance of this technique are its straightforwardness and absence of command, a significant attribute in the presence of power electronic devices to guarantee that the steps are made to coincide with the switching instants. In addition, non-linearity is easier to represent in state variable analysis (Chua and Lin, 1975). The main drawbacks are difficulty to model distributed parameters, greater solution time and extra code complexity.

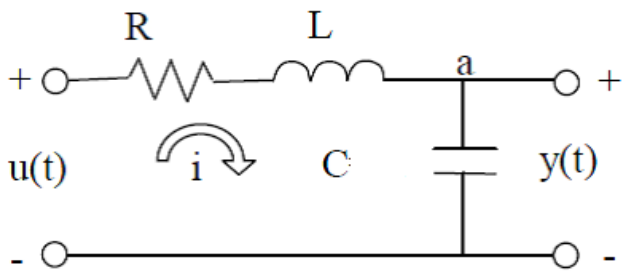

Figure 4.2 Simple RLC circuit (Chua and Lin, 1975)

Consider a simplified mathematical model of the hybrid network below in which the input vector is related with the variable output vector.

$i_c = C\,\frac{dv_c}{dt}$ & $v_L = L\,\frac{di_L}{dt}$

$x_1 = v_c\,(t)$

$x_2 = i_L\,(t)$

KCL at node a: $\frac{dx_1}{dt} = \frac{1}{C}\,x_2$ (4.13)

KVL $\frac{dx_2}{dt} = -\frac{1}{L}\,x_1 - \frac{R}{L}\,x_2 + \frac{1}{L}\,u$ (4.14)

Equation 4.13 and 4.14 can be more compactly written in matrix form:

$$\begin{bmatrix} \dot{x_1} \\ \dot{x_2} \end{bmatrix} = \begin{bmatrix} 0 & 1/C \\ -1/L & -R/L \end{bmatrix} \begin{bmatrix} x_1 \\ x_2 \end{bmatrix} + \begin{bmatrix} 0 \\ 1/L \end{bmatrix} u \quad (4.15)$$

Equation 4.15 is called the State. State and output equations in general are written in the following form:

$$\dot{x} = Ax + Bu \quad (4.16)$$

$$y = Cx + Du \quad (4.17)$$

5. COMPUTATION OF SHORT CIRCUIT FAULT

5.1 Introduction

In a power system consisting of generators, switchgear, transformers and transmission lines sooner or later in such a large network some failure will occur somewhere in the system. Fault means abnormal condition which reduces the basic insulation strength between:

- Phases or
- Phase and earth conductors or any earthed screens surrounding the conductors.

Until it produces some effect on the system such reduction of the insulation is not considered as a fault, i.e. until it results either in an excess of current or reduction of the impedance between phases and earth. Main causes of failures:

- Breakdown at normal voltage on account of:
- ✓ Deterioration of insulation
- ✓ Damage due to unpredictable causes such as the perching of birds, accidental short circuiting by snakes, kite strings, tree branches, etc.
- Breakdown at abnormal voltages on account of:
- ✓ Switching surges
- ✓ Surges caused by lightning

Few faults are also occurred by switching mistakes (Sriyananda et al, 1986).

5.2 Consequences of Faults

Fire is a serious result of major un-cleared faults, may destroy the equipment of its origin, but also may disperse widely in the system causing complete failure. Short circuit fault may have any of the following after effects:

- Decrease of the line voltage to the main parts of system, leading to the breakdown of the electrical supply to the consumer and may produce wastage in production,

- An electrical arc – often accompanying a short circuit may damage the other apparatus in the system,
- Damage of equipment because of overheating and mechanical forces,
- Disturbances to the stability of the electrical system and this may even lead to a complete blackout of a given power system,
- Considerable reduction of voltages of healthy feeders, which can cause abnormal currents drawn by motors or the motors will be stopped (causing loss of industrial production) and then will have to be restarted (Tleis, 2007).

5.3 Fault Statistics for Different Items of Equipment in a Power System

Power systems have been in operation for over a hundred years now. Accumulated experience shows that all faults are not equally likely. The probability of fault occurrence is given in Table 5.1

Table 5.1 Probability of fault occurrence

Fault Type	Probability of Occurrence %
L-G	85
L-L	8
L-L-G	5
L-L-L	2

It is very important in fault analysis, how faults are distributed in different sections of a power system. However, fault distribution is shown in Table 5.2.

Table 5.2 Fault statistics for different equipment in a power system

Equipment	Fault Statistics %
Overhead lines	50
Cables	10
Switchgear	15
Transformers	12
CTs/PTs	2
Control Equipment	3
Miscellaneous	8

The probability of the failure is more on overhead lines. This is so due to their:

- Larger length

- Exposure to the atmosphere

Most of the faults occur on overhead TLs. There are fault probabilities which show that more than 75% of faults occur on TLs. This exposes high significance of fault analysis for TLs. Statistics of faults occurrence on overhead lines are given in Table 5.3 and 5.4 (Izykowski, 2008).

Table 5.3 Statistics of faults on overhead TLs at various voltage levels

AREA (RESOURCE)	**VOLTGE: 300 kV ≤ V ≤ 500 kV**
Poland	1–3
CIGRE	0.4-4.68
IEEE	0.83
NORDEL (Denmark, Finland, Norway, Sweden)	0.3
Former Soviet Union	1

Table 5.4 Statistics of faults on overhead TLs at various voltage levels

FAULT TYPE	**VOLTAGE: 300 kV ≤V ≤500 kV**
Phase-to-earth	2.2
DLG	0.16
Faults involving more than one circuit	0.06
Faults between systems of different voltages	0.004

5.4 Fault Types

There are two types of faults usually related with a power networks, these are symmetrical and unsymmetrical faults. The balance three phase faults rarely occur on system unlike the case of unbalanced faults. Fault can further be categorized as series and shunt faults (Gonen, 2015). The study in this thesis is mainly emphasis on transient analysis of Wind/PV hybrid systems under shunt types of fault condition.

5.4.1 Series faults

Series faults represent open line and occur when series impedance of the lines is unbalanced are introduced. Series fault occurs when one or two broken lines holds by

system, or impedance inserted in one or two lines. Series faults occurs, when CBs controls lines and do not open all phases (Gonen, 2015). Series faults causes decrease in current of the faulted phases and increase of frequency and voltage.

5.4.2 Shunt faults

The most common type of fault is shunt faults. It includes power conductors or LG or SC between lines. One of the most significant features of shunt fault is the rise of the current and drop in voltage. Classification of shunt faults can be divided into following categories.

a) Line-to-ground (LG) fault
b) Line-to-line (LL)fault
c) Double line-to-ground (DLG) fault
d) Three phase short circuit fault (SCF)

First three of these faults are known as asymmetrical faults (Wadhwa, 2006; Saadat, 1999).

a. Line-to-ground fault

The LG fault occurs when it makes contact with the neutral wire or one line drop to earth. The general representation of LG fault is given in Figure 5.1 where F is the fault location with impedanceZ_f. Figure 5.2 shows the sequences network, usually it is presumed that fault takes place on phase A and it's for simplicity in the fault analysis calculations (Saadat, 1999).

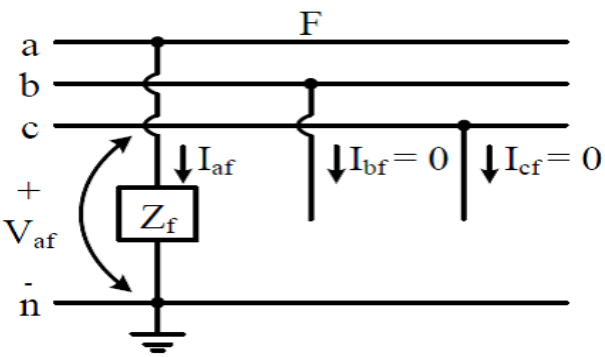

Figure 5.1 General representation of a LG fault (Saadat, 1999)

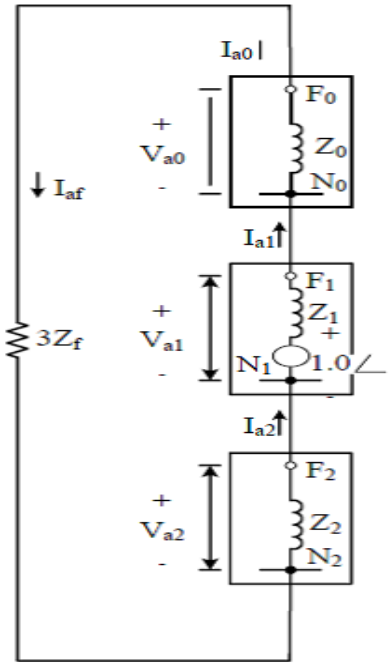

Figure 5.2 Sequence network diagram of LG fault (Saadat, 1999)

Since only phase A, is connected to ground at the fault, phases B and C are open circuited i.e.$I_b = 0$, $I_c = 0$ and the fault current isI_a. The voltage at fault point F is $V_a = Z_f\, I_a$

At fault location symmetrical components of fault current in phase A, can be written as

$$\begin{bmatrix} I_{a0} \\ I_{a1} \\ I_{a2} \end{bmatrix} = \frac{1}{3} \begin{bmatrix} 1 & 1 & 1 \\ 1 & \alpha & \alpha^2 \\ 1 & \alpha^2 & \alpha \end{bmatrix} \begin{bmatrix} I_a \\ I_b \\ I_c \end{bmatrix} \tag{5.1}$$

$$\begin{bmatrix} I_{a0} \\ I_{a1} \\ I_{a2} \end{bmatrix} = \frac{1}{3} \begin{bmatrix} 1 & 1 & 1 \\ 1 & \alpha & \alpha^2 \\ 1 & \alpha^2 & \alpha \end{bmatrix} \begin{bmatrix} I_a \\ 0 \\ 0 \end{bmatrix} = \frac{I_a}{3} \begin{bmatrix} 0 \\ 0 \\ 0 \end{bmatrix} \tag{5.2}$$

$$I_{a0} = I_{a1} = I_{a2} = \frac{1}{3}\, I_a \tag{5.3}$$

For a balance system

$E_{a0} = E_{a2} = 0$ and $E_{a1} = V_f$

The phase voltages V_a, V_b and V_c at the fault location F can be found from the following relations:

$$\begin{bmatrix} V_a \\ V_b \\ V_c \end{bmatrix} = \begin{bmatrix} 1 & 1 & 1 \\ 1 & \alpha & \alpha^2 \\ 1 & \alpha^2 & \alpha \end{bmatrix} \begin{bmatrix} V_{a0} \\ V_{a1} \\ V_{a2} \end{bmatrix} \tag{5.4}$$

Fault current flow through phase a is given in equation 5.5

$$I_f = I_a = \frac{3V_f}{Z_{a0} + Z_{a1} + Z_{a2} + 3Z_f} \quad (5.5)$$

$$I_b = I_c = 0$$

b. Line-to-line fault

LL fault may take place when two lines are short circuited. The general representation of a LL fault is given in Figure 5.3 and Figure 5.4 represents sequences network diagram (Saadat, 1999).

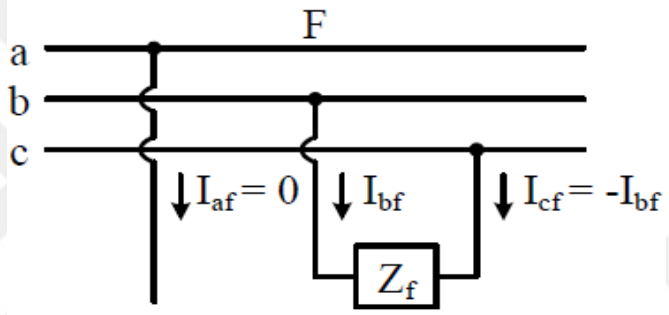

Figure 5.3 Sequence network diagram of a LL fault (Saadat, 1999)

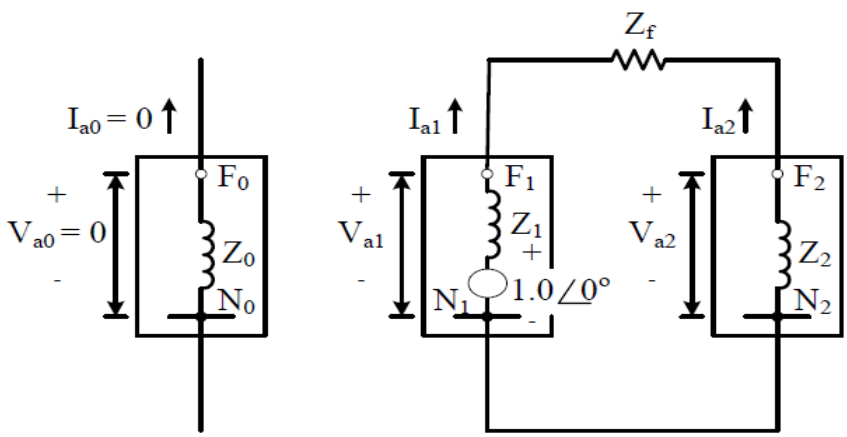

Figure 5.4 Sequence network diagram of LL fault (H.Saadat, 1999)

The boundary conditions are

$$I_a = 0 \quad (5.6)$$

$$I_b = -I_c \quad (5.7)$$

$$V_b - V_c = Z_f I_b \quad (5.8)$$

$$\text{Fault Current } I_f = I_b \tag{5.9}$$

The sequence currents can also be found by matrix method as follows:

$$I_{012} = A^{-1} I_{abc}$$

$$\begin{bmatrix} I_{a0} \\ I_{a1} \\ I_{a2} \end{bmatrix} = \frac{1}{3} \begin{bmatrix} 1 & 1 & 1 \\ 1 & \alpha & \alpha^2 \\ 1 & \alpha^2 & \alpha \end{bmatrix} \begin{bmatrix} I_a \\ I_b \\ I_c \end{bmatrix} \tag{5.10}$$

$$\begin{bmatrix} I_{a0} \\ I_{a1} \\ I_{a2} \end{bmatrix} = \frac{1}{3} \begin{bmatrix} 1 & 1 & 1 \\ 1 & \alpha & \alpha^2 \\ 1 & \alpha^2 & \alpha \end{bmatrix} \begin{bmatrix} 0 \\ I_b \\ -I_b \end{bmatrix} \tag{5.11}$$

$$I_{a0} = 0 \quad \text{and} \quad I_{a1} = -I_{a2}$$

The sequence components of voltages at the fault location are found by the given relation

$$V_{012} = E - Z_{012} I_{012}$$

$$\begin{bmatrix} V_{a0} \\ V_{a1} \\ V_{a2} \end{bmatrix} = \begin{bmatrix} 0 \\ V_f \\ 0 \end{bmatrix} - \begin{bmatrix} Z_{a0} & 0 & 0 \\ 0 & Z_{a1} & 0 \\ 0 & 0 & Z_{a2} \end{bmatrix} \begin{bmatrix} I_{a0} \\ I_{a1} \\ I_{a2} \end{bmatrix} \tag{5.12}$$

$$I_{a1} = \frac{V_f}{Z_{a1} + Z_{a2} + Z_f} \tag{5.13}$$

The fault current is given by

$$I_f = I_b = -I_c$$

$$I_f = I_b = \frac{-j\sqrt{3}\, V_f}{Z_{a1} + Z_{a2} + Z_f} \tag{5.14}$$

Equation 5.14 shows that for a LL fault the zero sequence component of current I_{a0} is zero.

c. Double line-to-ground (DLG) fault

A DLG fault is a serious fault that results an important asymmetry in a 3-phase symmetrical system and it may spread into a three-phase fault when not clear in appropriate time (Zhu, 2004).

The representation of a DLG fault is shown in Figure 5.5 where Z_f and Z_g are the fault impedances and ground impedance. Figure 5.6 shows the sequences network diagram (Saadat, 1999).

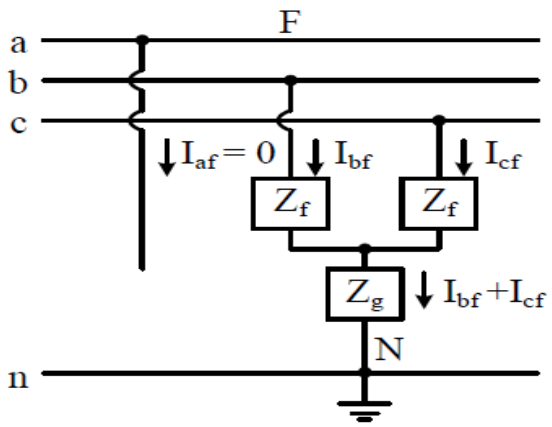

Figure 5.5 General representation of a DLG fault (Saadat, 1999)

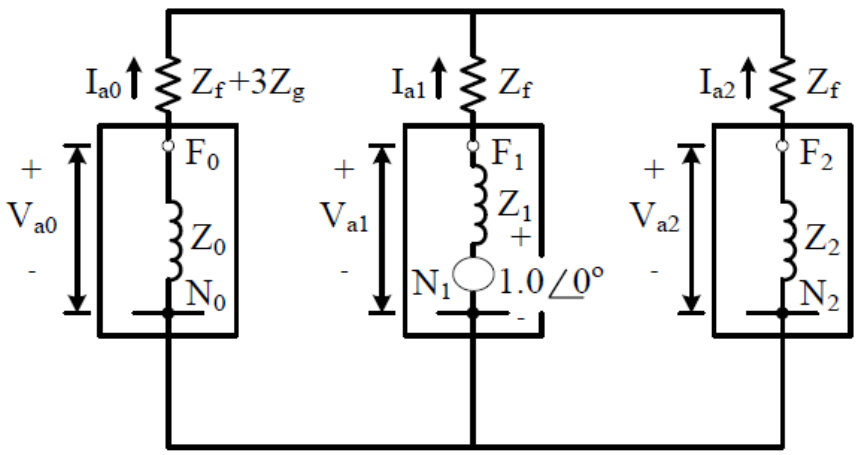

Figure 5.6 Sequence network diagram of a DLG fault (Saadat, 1999)

Positive sequence of currents is

$$I_{a1} = \frac{V_f}{Z_{a1} + Z_f + \left[\frac{(Z_{a2} + Z_f)\,(Z_{a0} + Z_f + 3Z_g)}{Z_{a2} + Z_{a0} + 2Z_f + 3Z_g}\right]} \tag{5.15}$$

The negative sequence current is

$$I_{a2} = -\,I_{a1}\left(\frac{Z_{a0} + Z_f + 3Z_g}{Z_{a2} + Z_{a0} + 2Z_f + 3Z_g}\right) \tag{5.16}$$

The zero sequence current is found from

$$I_{a0} = -\,(I_{a1} + I_{a2})$$

$$I_{a0} = -\left[\frac{(Z_{a2} + Z_f)}{(Z_{a2} + Z_f) + (Z_{a0} + Z_f + 3Z_g)}\right] I_{a1} \tag{5.17}$$

$$\begin{bmatrix} V_{a0} \\ V_{a1} \\ V_{a2} \end{bmatrix} = \begin{bmatrix} 0 \\ V_f \\ 0 \end{bmatrix} - \begin{bmatrix} Z_{a0} & 0 & 0 \\ 0 & Z_{a1} & 0 \\ 0 & 0 & Z_{a2} \end{bmatrix} \begin{bmatrix} I_{a0} \\ I_{a1} \\ I_{a2} \end{bmatrix} \tag{5.18}$$

Phase voltages can be expressed as

$$V_a = V_{a0} + V_{a1} + V_{a2} = 3\,V_{a1} \tag{5.19}$$

$$V_b = V_c = 0 \tag{5.20}$$

d. Three phase fault

Three phase fault occur least frequently and known as symmetrical fault. It is the most severe fault (Markovic, 2009). Representation of a balanced three-phase fault is shown in Figure 5.7 with impedances Z_f and Z_g. Figure 5.8 shows the sequences networks diagram of SCF.

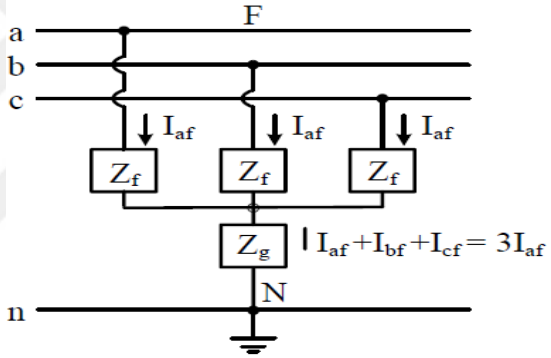

Figure 5.7 General representation of SCF (Markovic, 2009)

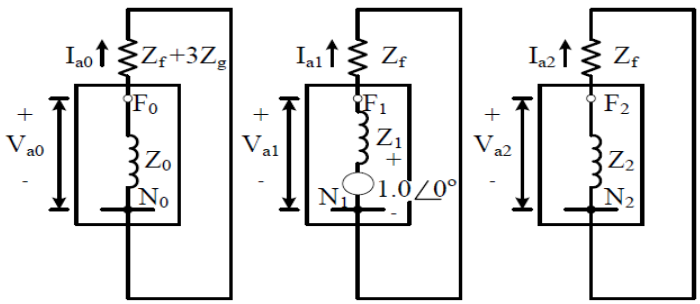

Figure 5.8 Sequence network diagram of a SCF (Markovic, 2009)

Currents for each of the sequences is given as

$$I_{a0} = 0$$

$$I_{a2} = 0$$

$$I_{a1} = \frac{V_f}{Z_{a1} + Z_f} \tag{5.21}$$

If the fault impedance Z_f is zero,

$$I_{a1} = \frac{V_f}{Z_{a1}} \tag{5.22}$$

If equation is substituted into equation

$$\begin{bmatrix} I_a \\ I_b \\ I_c \end{bmatrix} = \begin{bmatrix} 1 & 1 & 1 \\ 1 & \alpha^2 & \alpha \\ 1 & \alpha & \alpha^2 \end{bmatrix} \begin{bmatrix} 0 \\ I_{a1} \\ 0 \end{bmatrix} \tag{5.23}$$

Solving Equation 5.23

$$I_a = I_{a1} = \frac{V_f}{Z_{a1} + Z_f}$$

$$I_b = \alpha^2 I_{a1} = \frac{\alpha^2 V_f}{Z_{a1} + Z_f} \tag{5.24}$$

$$I_c = \alpha I_{a1} = \frac{\alpha V_f}{Z_{a1} + Z_f} \tag{5.25}$$

$$V_{a0} = 0$$

$$V_{a1} = Z_f I_{a1} \tag{5.26}$$

$$V_{a2} = 0$$

If Equation 5.26 is substituted into Equation 5.23

$$\begin{bmatrix} V_a \\ V_b \\ V_c \end{bmatrix} = \begin{bmatrix} 1 & 1 & 1 \\ 1 & \alpha^2 & \alpha \\ 1 & \alpha & \alpha^2 \end{bmatrix} \begin{bmatrix} 0 \\ V_{a1} \\ 0 \end{bmatrix} \tag{5.27}$$

Therefore,

$$V_a = V_{a1} = Z_f I_{a1} \tag{5.28}$$

$$V_b = \alpha^2 V_{a1} = Z_f I_{a1} < 240^0 \tag{5.29}$$

$$V_b = \alpha V_{a1} = Z_f I_{a1} < 120^0 \tag{5.30}$$

If Z_f equals to zero,

$$I_a = \frac{1 < 0^0}{Z_{a1}} \tag{5.31}$$

$$I_b = \frac{1 < 240^0}{Z_{a1}} \tag{5.32}$$

$$I_c = \frac{1 < 120^0}{Z_{a1}} \tag{5.33}$$

The phase voltages becomes,

$$V_a = 0 , V_b = 0 \ \& \ V_c = 0 \tag{5.34}$$

6. COMPONENTS MODELING OF WIND/PV HYBRID SYSTEM IN ATP/EMTP SOFTWARE

6.1 Introduction

The selected transient simulator for this thesis is ATP/EMTP. The ATP/EMTP contains extensive modelling capabilities for transmission lines, cables, transformer, synchronous and asynchronous machines loads, breakers, converters and electromagnetic coupling. Modelling the transmission components of a power system, hybrid transformer, synchronous generator and wind generator is one of the important steps in electromagnetic transient studies. The components are modelled regarding their well-known equivalent circuit models (Alternative Transient Program Rule Book, 1987).

6.2 Synchronous Generator

Three phase synchronous generator (SG) is most widely used for converting mechanical energy into electrical energy. It comprises of a set of armature coils and a field winding that carries current to generate rotational magnetic field between the rotor and stator. The equivalent circuit of the generator consists of four independent circuits given in Figure 6.1 (Alternative Transient Program Rule Book, 1987).

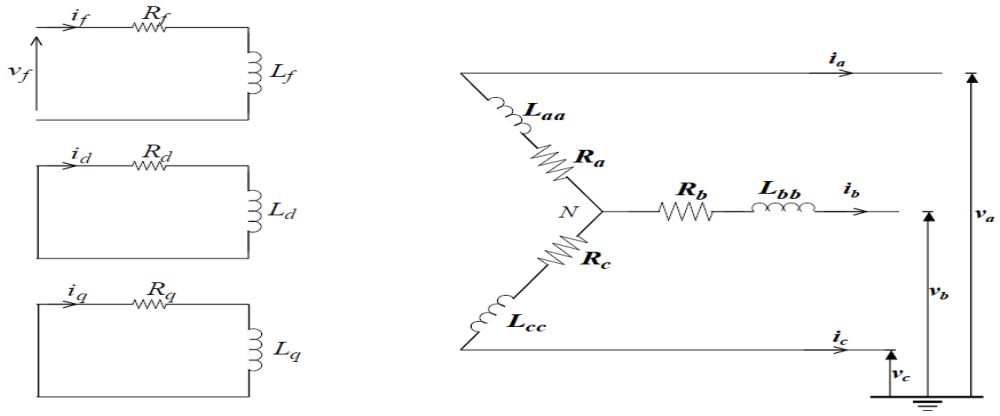

Figure 6.1 Equivalent circuit of synchronous generator (Alternative Transient Program Rule Book, 1987)

Flux, current, and voltage relation of the magnetic coupled windings are given below:

$$[v(t)] = [R]\,[i\,(t)] + \frac{d[\lambda\,(t)]}{dt} \tag{6.1}$$

$$\begin{bmatrix} v_a\,(t) \\ v_b\,(t) \\ v_c\,(t) \\ v_f\,(t) \\ 0 \\ 0 \end{bmatrix} = \begin{bmatrix} R_a & 0 & 0 & 0 & 0 & 0 \\ 0 & R_a & 0 & 0 & 0 & 0 \\ 0 & 0 & R_a & 0 & 0 & 0 \\ 0 & 0 & 0 & R_f & 0 & 0 \\ 0 & 0 & 0 & 0 & R_d & 0 \\ 0 & 0 & 0 & 0 & 0 & R_q \end{bmatrix} \begin{bmatrix} i_a\,(t) \\ i_b\,(t) \\ i_c\,(t) \\ i_f\,(t) \\ i_d\,(t) \\ i_q\,(t) \end{bmatrix} + \frac{d}{dt} \begin{bmatrix} \lambda_a\,(t) \\ \lambda_b\,(t) \\ \lambda_c\,(t) \\ \lambda_f\,(t) \\ \lambda_d\,(t) \\ \lambda_q\,(t) \end{bmatrix} \tag{6.2}$$

Where,

$v_a\,(t) =$ Voltage of phase A

$v_b\,(t) =$ Voltage of phase B

$v_c\,(t) =$ Voltage of phase C

$v_f\,(t) =$ Field winding terminal voltages

$R_a =$ Armature winding resistance

$R_f =$ Field winding resistance

$R_d = D -$ damper winding resistance

$R_q = Q -$ damper winding resistance

$i_a\,(t) =$ Current through phase A winding

$i_b\,(t) =$ Current through phase B winding

$i_c\,(t) =$ Current through phase C winding

$i_f\,(t) =$ Current through field winding

$i_d\,(t) =$ Current through $D -$ damper winding

$i_q\,(t) =$ Current through $Q -$ damper winding

$\lambda_a\,(t) =$ Flux linkage linking phase A

$\lambda_b\,(t) =$ Flux linkage linking phase B

$\lambda_c\,(t) =$ Flux linkage linking phase C

$\lambda_f\,(t) =$ Flux linkage linking field winding

$\lambda_d\,(t) =$ Flux linkage linking $D -$ damper winding

$\lambda_q\,(t) =$ Flux linkage linking $Q -$ damper winding

The flux linkage in Equation (6.1) is expressed as follows:

$$[\lambda\,(t)] = [L\,(t)]\,[i\,(t)] \tag{6.3}$$

And

$$[L\ (t)] = \begin{bmatrix} L_s & L_{sr} \\ L_{rs} & L_r \end{bmatrix} \tag{6.4}$$

Where,

L_s & L_r = Inductance sub − metrices of the stator and rotor windings respectively

L_{sr} & L_{rs} = Mutual Inductance sub − metrices of the stator

− rotor wnding and rotor − stator winding respectively

And

$$[L_s] = \begin{bmatrix} L_{aa}\ (t) & L_{ab}\ (t) & L_{ac}\ (t) \\ L_{ba}\ (t) & L_{bb}\ (t) & L_{bc}\ (t) \\ L_{ca}\ (t) & L_{cb}\ (t) & L_{cc}\ (t) \end{bmatrix}$$

$$[L_r] = \begin{bmatrix} L_{ff}\ (t) & L_{fq}\ (t) & L_{fd}\ (t) \\ L_{qf}\ (t) & L_{dd}\ (t) & L_{dq}\ (t) \\ L_{qf}\ (t) & L_{qd}\ (t) & L_{qq}\ (t) \end{bmatrix}$$

$$[L_{sr}] = \begin{bmatrix} L_{af}\ (t) & L_{aq}\ (t) & L_{aq}\ (t) \\ L_{bf}\ (t) & L_{bq}\ (t) & L_{bq}\ (t) \\ L_{cf}\ (t) & L_{cq}\ (t) & L_{cq}\ (t) \end{bmatrix}$$

$$[L_{rs}] = \begin{bmatrix} L_{fa}\ (t) & L_{fb}\ (t) & L_{fc}\ (t) \\ L_{da}\ (t) & L_{db}\ (t) & L_{dc}\ (t) \\ L_{qa}\ (t) & L_{qb}\ (t) & L_{qc}\ (t) \end{bmatrix}$$

Where,

$L_{aa}\ (t), L_{bb}\ (t)$ and $L_{cc}\ (t)$: Magnitude of the self inductance of phase A, B and C respectively

$L_{ff}\ (t)$: Magnitude of the self inductance of the field winding

$L_{dd}\ (t)$: Magnitude of the self inductance of the D − damper winding

$L_{qq}\ (t)$: Magnitude of the self inductance of the Q − damper winding

$L_{ab}\ (t), L_{ac}\ (t)$ and $L_{bc}\ (t)$: Magnitude of the mutual inductance of the phases

$L_{fa}(t), L_{fb}(t)$ & $L_{fc}(t)$: Magnitude of the mutual inductance between the phases and field winding

$L_{da}\ (t), L_{db}\ (t)$ and $L_{dc}\ (t)$: Magnitude of the mutual inductance between the phases and D − winding winding

$L_{qa}\ (t), L_{qb}\ (t)$ and $L_{qc}\ (t)$: Magnitude of the mutual inductance between the phases and Q − winding winding

6.3 Transmission Line

The ATP contains extensive modelling capabilities for transmission lines. It is considered as a passive and bilateral device means behaviour of TL remains the same no matter the direction of the current.

Below are the different choices for TL models in ATP/EMTP (Alternative Transient Program Rule Book, 1987):

1. Bergeron line model is a distributed parameter model including the traveling wave phenomena.
2. PI-model: It's an equivalent model with lumped parameters and is suitable for short lines.
3. Noda-model: It's a frequency dependent model. This algorithm models the frequency dependent transmission lines and cables directly in the phase domain.
4. Semlyen-model: It's one of the first frequency-dependent line models. It may give unstable or inaccurate results at high frequencies.
5. JMarti: It's a frequency dependent model with constant transformation matrix and is suitable for simulating traveling wave phenomena in long TLs.

In this study, J Marti frequency-dependent model of transmission system has been adopted as it shows a good correlation with actual line responses (Sulaiman, 2014; Marti, 1982). It has following features:

1. Accurate for wide frequency range; 2. Computationally relatively efficient calculation; 3. Limitation for calculation time step; 4. May be inaccurate for very low frequency range

The steady state model of the long line can be achieved by considering a small portion of the long segment of the line as shown in Figure 6.2

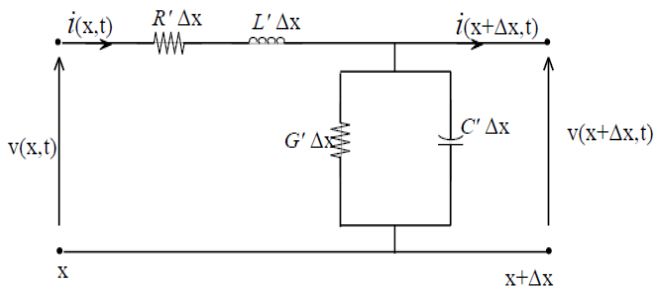

Figure 6.2 Line segment (Sulaiman, 2014)

Where,

$i\,(x,t), i(x + \Delta x, t)$: Sending and recieving end currents respectively of the line segment as a function of time

$v(x,t), v(x + \Delta x, t)$: Sending and recieving end voltages respectively of the line segment as a function of time

$R'\,\Delta x, L'\,\Delta x$: Series line resistance and inductance per unit length of the line respectively

$G'\,\Delta x, C'\,\Delta x$: Conductance and capacitance per unit length of the line respectively

According to the Kirchoff's law current-voltage equations for a single line which is parallel to ground can be given as (Dau, 2008).

$$v(x,t) = R'\,\Delta x.\,i(x,t) + L'\,\Delta x\,\frac{\partial i(x,t)}{\partial t} + v(x + \Delta x, t) \tag{6.5}$$

$$i(x,t) = G'\,\Delta x.\,v(x,t) + C'\,\Delta x\,\frac{\partial v(x+\Delta x,t)}{\partial t} + i(x + \Delta x, t) \tag{6.6}$$

After dividing both sides of Equations 6.5 and 6.6 by ∂x and at ∂x approaching 0 it is possible to write the equation system:

$$-\frac{\partial v\,(x,t)}{\partial x} = R'\,i(x,t) + L'\,\frac{\partial i\,(x,t)}{\partial t} \tag{6.7}$$

$$-\frac{\partial i\,(x,t)}{\partial x} = G'\,v(x,t) + C'\,\frac{\partial i\,(x,t)}{\partial t} \tag{6.8}$$

For the case of three phase system, the distributed parameters of a line are given in matrix forms.

For simplicity let $v = v(x,t)$, $i = i(x,t)$in Equation 6.7 and 6.8, above. Taking the derivative of Equation 3.3 and substituting $\frac{\partial i}{\partial x}$ yields:

$$\frac{\partial v^2}{\partial x^2} = R'\,G'\,v + (R'\,C' + G'\,L')\,\frac{\partial v}{\partial t} + L'\,C'\,\frac{\partial v^2}{\partial t^2} \tag{6.9}$$

$$\frac{\partial i^2}{\partial x^2} = R'\,G'\,i + (R'\,C' + G'\,L')\,\frac{\partial i}{\partial t} + L'\,C'\,\frac{\partial i^2}{\partial t^2} \tag{6.10}$$

Equations 6.9 and 6.10 are second order hyperbolic partial differential equations.

For lossless distributed LC line $[R'] = 0$ and $[G'] = 0$ .The solution of the above equation is characterized by the surge impedance matrix Z_0 is given as:

$$Z_0 = [L']^{1/2}\,.\,[C']^{-1/2}$$

And the wave propagation speed u is given as;

$$[u] = [L']^{-1/2}\,.\,[C']^{-1/2}$$

Where, $[L']$ and $[C']$ are inductance and capacitance matrices per unit length of the line.

$$v\,(x,t) = \frac{1}{2}\,[v_1\,(t + {}^{x}/_{u}) + v_1\,(t - {}^{x}/_{u})] - \frac{1}{2}\,Z_0 \int_{t-\,{}^{x}/_{u}}^{t+\,{}^{x}/_{u}} di_1(t) \tag{6.11}$$

For $x = l$

$$v_2(t) = \frac{1}{2}\,[v_1\,(t + \tau) + v_1\,(t - \tau)] - \frac{1}{2}\,Z_0\,[i_1\,(t + \tau) - i_1\,(t - \tau)] \tag{6.12}$$

$$i_2(t) = \frac{1}{2}\,[i_1\,(t + \tau) + i_1\,(t - \tau)] - \frac{1}{2\,Z_0}\,[v_1\,(t + \tau) - v_1\,(t - \tau)] \tag{6.13}$$

Where,

$\tau = \dfrac{l}{u}$; Travel time of the travelling wave

v_2 and i_2: Recieving end voltage & current respectively

v_1 and i_1: Sending end voltage & current respectively

To establish a simplified input-output relation of a transmission line, consider the two port block diagram of three phase line in the form of two port network depicted in Figure 6.3.

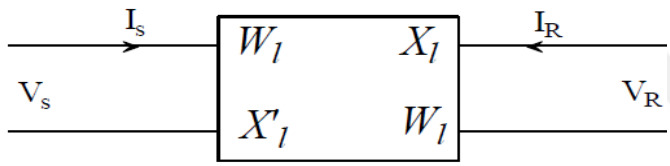

Figure 6.3 Two port representation of a transmission line Sulaiman, 2014)

Where,

V_S and I_S: Sending end voltage and current respectively

V_R and I_R: Recieving end voltage and current respectively

W_l and X_l: Submatrices of distributed line parameters

$$\begin{bmatrix} V_S \\ I_S \end{bmatrix} = \begin{bmatrix} \cosh(\psi) & Z_0\ \sinh(\Psi) \\ \frac{1}{Z_0}\ \sin(\Psi) & \cosh(\Psi) \end{bmatrix} \begin{bmatrix} V_R \\ I_R \end{bmatrix} \tag{6.14}$$

Where,

$\psi = \gamma\, l$

$\gamma = [Z]^{1/2} . [Y]^{1/2}$

$Z_0 = [L']^{1/2} . [C']^{-1/2}$

γ : Propagation constant

Z_0: Characteristics impedance

l: Line length

Receiving end voltages and currents can be found from Equation 6.14 as:

$$\begin{bmatrix} V_R \\ I_R \end{bmatrix} = \begin{bmatrix} W_l & X_l \\ X_l' & W_l \end{bmatrix}^{-1} \begin{bmatrix} V_S \\ I_S \end{bmatrix} \tag{6.15}$$

$$\begin{bmatrix} W_l & X_l \\ X_l' & W_l \end{bmatrix}^{-1} = \begin{bmatrix} \cosh(\psi) & Z_0 \sinh(\Psi) \\ \frac{1}{Z_0} \sin(\Psi) & \cosh(\Psi) \end{bmatrix}^{-1} \tag{6.16}$$

6.4 Transformer

The transformer is vitally necessary equipment in power systems. Different approaches are given in the literature (Martinez and Mork, 2005). Hybrid Transformer model is recently developed in ATP Draw and is known XFMR. Low frequency and high frequency transformer models are one of the major types of the model used in transient study. The studies of a system with fast-front waves consider high frequency models as it accounts for the skin effect, the capacitances between the winding and ground, also between coils of a winding (Mork and etc., 2004; Mork and etc., 2007).

6.4.1 Single phase transformer

The transformer shown in Figure 6.4 is an equivalent circuit of 1-phase two-winding transformer. This approach can be extended for multi-winding transformer model. The analysis of the transformer is based on its circuit model. After obtaining the equivalent circuit of this transformer, the circuit is discretized for time domain analysis.

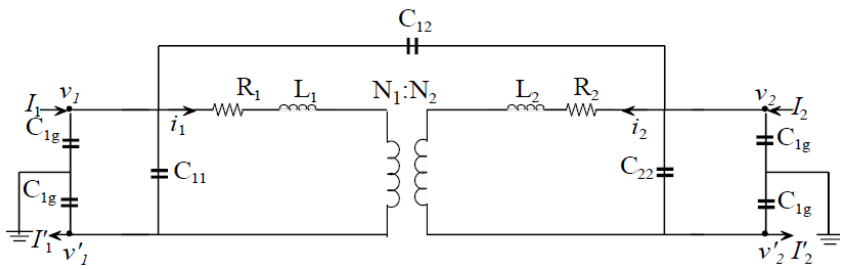

Figure 6.4 Single phase two winding transformer equivalent circuit (Chimklai and Marti, 1995)

L_1 , L_2

: Series inductance of the winding for primary and secondary sides respectively

R_1 , R_2

: Series resistance of the winding for primary and secondary sides respectively

C_{11} , C_{22}

: Tutn to turn winding capacitance for primary and secondary sides respectively

C_{1g} , C_{2g}

: Winding to groung capacitance for primary and secondary sides respectively

C_{12} : Capacitance between high and low voltage sides

v_1 , v_2 : Low and High voltage respectively

As mentioned in Ercelebi, 1992) the winding currents are given by Equations 6.17 and 6.18.

$$I_1 = i_1 + C_{1g}\frac{dv_1}{dt} + C_{11}\frac{d(v_1 - v_1')}{dt} + C_{12}\frac{d(v_1 - v_2)}{dt}$$

$$I_1' = i_1 - C_{g1}\frac{dv_1'}{dt} + C_{11}\frac{d(v_1 - v_1')}{dt} - C_{21}\frac{d(v_1' - v_2')}{dt} \tag{6.17}$$

$$I_2 = i_2 + C_{2g}\frac{dv_2}{dt} + C_{22}\frac{d(v_2 - v_2')}{dt} + C_{12}\frac{d(v_2 - v_1)}{dt}$$

$$I_2' = i_2 - C_{g2}\frac{dv_2'}{dt} + C_{22}\frac{d(v_2 - v_2')}{dt} - C_{21}\frac{d(v_2' - v_1')}{dt} \tag{6.18}$$

Equation 6.17 and 6.18 is also written as,

$$\begin{bmatrix} I_1 \\ I_1' \\ I_2 \\ I_2' \end{bmatrix} = \begin{bmatrix} 1 & 1 \\ 1 & 0 \\ 0 & 1 \\ 0 & 1 \end{bmatrix} \begin{bmatrix} i_1 \\ i_2 \end{bmatrix} + \frac{d}{dt}\begin{bmatrix} (C_{2g} + C_{22} + C_{21}) & -C_{11} & -C_{12} & 0 \\ C_{11} & -(C_{2g} + C_{22} + C_{21}) & 0 & C_{21} \\ -C_{21} & 0 & (C_{2g} + C_{22} + C_{21}) & -C_{22} \\ 0 & C_{21} & C_{22} & -(C_{2g} + C_{22} + C_{21}) \end{bmatrix} \begin{bmatrix} v_1 \\ v_1' \\ v_2 \\ v_2' \end{bmatrix} \tag{6.19}$$

The Terminal phase voltages are

$$v_1 - v_1' = L_1\frac{di_1}{dt} + L_m\frac{di_2}{dt} \tag{6.20}$$

$$v_2 - v_2' = L_2\frac{di_2}{dt} + L_m\frac{di_1}{dt} \tag{6.21}$$

In matrix form,

$$\begin{bmatrix} v_1 - v_1' \\ v_2 - v_2' \end{bmatrix} = Q \begin{bmatrix} L_1 & L_m \\ L_m & L_2 \end{bmatrix} \begin{bmatrix} i_1 \\ i_2 \end{bmatrix} \tag{6.22}$$

$$\begin{bmatrix} i_1 \\ i_2 \end{bmatrix} = \frac{1}{Q} \begin{bmatrix} L_1 & L_m \\ L_m & L_2 \end{bmatrix}^{-1} \begin{bmatrix} v_1 - v_1' \\ v_2 - v_2' \end{bmatrix} \tag{6.23}$$

Where,

L_1 , L_2 : Self inductance of the primary and secondary windings respectively

L_m : Mutual inductance

Q: It's a differential operator $\left(\frac{d}{dt}\right)$

For simplicity, assuming both windings are solidly earthed $v_1' = v_2' = 0$ substituting Equation 6.23 in 6.19 yields;

$$\begin{bmatrix} I_1' \\ I_2' \end{bmatrix} = \begin{bmatrix} I_1 \\ I_2 \end{bmatrix} =$$

$$\frac{1}{Q} \begin{bmatrix} L_1 & L_m \\ L_m & L_2 \end{bmatrix}^{-1} \begin{bmatrix} v_1 \\ v_2 \end{bmatrix} + Q \begin{bmatrix} (C_{1g} + C_{11} + C_{12}) & -C_{12} \\ -C_{12} & (C_{2g} + C_{22} + C_{12}) \end{bmatrix} \begin{bmatrix} v_1 \\ v_2 \end{bmatrix} \tag{6.24}$$

6.4.2 Three phase transformer

The transformer windings are assumed to be symmetrical that implies the identical winding equivalent parameters. In the low frequency range up to 2000 Hz, the transformer capacitances (LL and LG) as well as the skin effect can be neglected (Martinez and etc., 2010).

Just like for the single phase transformer the three-phase unit can be considered as a multi-terminal element or as the circuit corresponding to the transformer design with distinguished primary and secondary side. The transformer winding connections are normalized according to respective standards. Generally, different winding connection groups are applied to different power networks. The magnetic core design in the three phase transformer determines the transformer properties (Mork and etc., 2004). The parameters indicated in Figure 3.4 are described below:

ABC, abc : Three phase high and low voltage sides respectively

R_H, R_P : Phase resistance for high and low voltage sides respectively

L_s, L_m : Self and mutual inductances of the winding respectively

C_{tt} : Capacitance from outer winding of one phase to the outer winding of the other phase

C_{ww} : Capacitance between two windings

C_{wg} : Capacitance from winding to ground for both high and low voltage sides

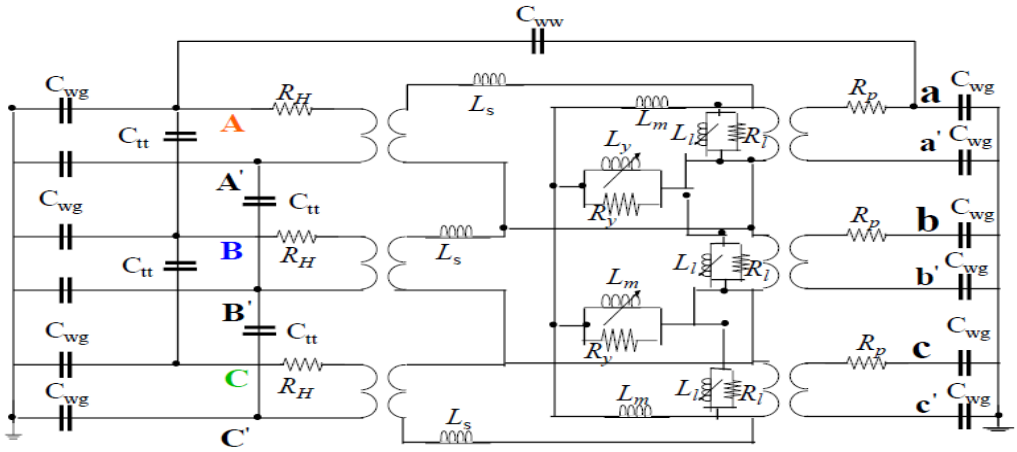

Figure 6.5 Three-phase Hybrid Transformer (Høidalen, 2007)

The voltages across windings of the three phase transformer in matrix form are given in Equation (6.25)

$$\begin{bmatrix} v_1 \\ v_2 \\ v_3 \\ v_4 \\ v_5 \\ v_6 \end{bmatrix} = \frac{d}{dt} \begin{bmatrix} L_{11} & M_{12} & M_{13} & M_{14} & M_{15} & M_{16} \\ M_{21} & L_{22} & M_{23} & M_{24} & M_{25} & M_{26} \\ M_{31} & M_{32} & L_{33} & M_{34} & M_{35} & M_{36} \\ M_{41} & M_{42} & M_{43} & L_{44} & M_{45} & M_{46} \\ M_{51} & M_{52} & M_{53} & M_{54} & L_{55} & M_{56} \\ M_{61} & M_{62} & M_{63} & M_{64} & M_{65} & L_{66} \end{bmatrix} \begin{bmatrix} i_1 \\ i_2 \\ i_3 \\ i_4 \\ i_5 \\ i_6 \end{bmatrix} \tag{6.25}$$

Where,

$M_{ij} = M_{ji}$: *Mutual inductanc*

The subscript 1, 2, 3 denote primary side and 4, 5, 6 denote secondary side phase quantities. The winding currents for the three phase transformer in matrix form are given in Equation 6.26

$$\begin{bmatrix} I_1 \\ I_2 \\ I_3 \\ I_4 \\ I_5 \\ I_6 \end{bmatrix} = \begin{bmatrix} i_1 \\ i_2 \\ i_3 \\ i_4 \\ i_5 \\ i_6 \end{bmatrix}$$

$$+Q \begin{bmatrix} (C_{11}+C_{1g}+C_{14}) & 0 & 0 & -C_{14} & 0 & 0 \\ 0 & (C_{22}+C_{2g}+C_{25}) & 0 & 0 & -C_{25} & 0 \\ 0 & 0 & (C_{33}+C_{3g}+C_{36}) & 0 & 0 & -C_{63} \\ -C_{41} & 0 & 0 & (C_{44}+C_{4g}+C_{41}) & 0 & 0 \\ 0 & -C_{52} & 0 & 0 & (C_{55}+C_{5g}+C_{52}) & 0 \\ 0 & 0 & -C_{63} & 0 & 0 & (C_{66}+C_{6g}+C_{63}) \end{bmatrix}$$

$$\begin{bmatrix} v_1 \\ v_2 \\ v_3 \\ v_4 \\ v_5 \\ v_6 \end{bmatrix} - Q \begin{bmatrix} C_{11} & 0 & 0 & 0 & 0 & 0 \\ 0 & C_{22} & 0 & 0 & 0 & 0 \\ 0 & 0 & C_{33} & 0 & 0 & 0 \\ 0 & 0 & 0 & C_{44} & 0 & 0 \\ 0 & 0 & 0 & 0 & C_{55} & 0 \\ 0 & 0 & 0 & 0 & 0 & C_{66} \end{bmatrix} \begin{bmatrix} v'_1 \\ v'_2 \\ v'_3 \\ v'_4 \\ v'_5 \\ v'_6 \end{bmatrix} \tag{6.26}$$

Where,

Q is a differential operator $Q = \frac{d}{dt}$

The connection type of the primary and secondary windings determines the capacitive coupling between different phases. For the case of delta connection, Equation 6.27 is used to express the phase voltages across the delta connected windings.

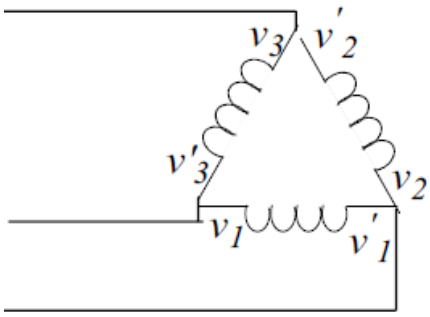

Figure 6.6 Delta connection of primary side winding (Sulaiman, 2014)

In the case of delta connection;

$v_1 = v'_3$, $v_2 = v'_1$ and $v_3 = v'_2$

Then, phase voltage across the delta connection in matrix form is given as;

$$\begin{bmatrix} v_1 - v_1' \\ v_2 - v_2' \\ v_3 - v_3' \end{bmatrix} = \begin{bmatrix} 1 & -1 & 0 \\ 0 & 1 & -1 \\ -1 & 0 & 1 \end{bmatrix} \begin{bmatrix} v_1 \\ v_2 \\ v_3 \end{bmatrix} \tag{6.27}$$

For the case of star connection, Equation 6.28 is used to express the phase voltages across the star connected windings.

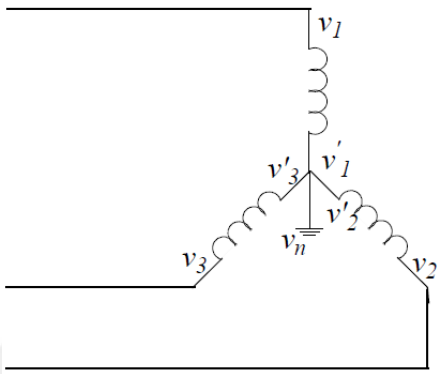

Figure 6.7 Star-connection of the secondary windings (Sulaiman, 2014)

In the case of solidly grounded neutral point, the voltages are given as

$$\mathrm{v}_1' = \mathrm{v}_2' = \mathrm{v}_3' = \mathrm{v}_\mathrm{n} = 0$$

Therefore, phase voltages across the star connection in matrix form are given as;

$$\begin{bmatrix} \mathrm{v}_1 - \mathrm{v}_1' \\ \mathrm{v}_2 - \mathrm{v}_2' \\ \mathrm{v}_3 - \mathrm{v}_3' \end{bmatrix} = \begin{bmatrix} 1 & 0 & 0 \\ 0 & 1 & 0 \\ 0 & 0 & 1 \end{bmatrix} \begin{bmatrix} \mathrm{v}_1 \\ \mathrm{v}_2 \\ \mathrm{v}_3 \end{bmatrix} \tag{6.28}$$

In a simplify form, Equation 6.27 and 6.28 can be represented by

$$[\bar{\mathrm{v}} - \bar{\mathrm{v}}'] = [\mathrm{K}]\,[\bar{\mathrm{V}}]$$

Where, $[\mathrm{K}]$ is the matrix that specifies the type of connections described by Equations 6.27 and 6.28. In general, current-voltage relation of three phase transformer in matrix form with capacitive coupling between different phases is shown in Equation 6.29. It should be noted that the values of $\mathrm{v}_1', \mathrm{v}_2', \mathrm{v}_3', \mathrm{v}_4', \mathrm{v}_5'$ and v_6' depend on the type of connection as mentioned earlier.

$$\begin{bmatrix} I_1 \\ I_2 \\ I_3 \\ I_4 \\ I_5 \\ I_6 \end{bmatrix} = \frac{1}{Q} \begin{bmatrix} L_{11} & M_{12} & M_{13} & M_{14} & M_{15} & M_{16} \\ M_{21} & L_{22} & M_{23} & M_{24} & M_{25} & M_{26} \\ M_{31} & M_{32} & L_{33} & M_{34} & M_{35} & M_{36} \\ M_{41} & M_{42} & M_{43} & L_{44} & M_{45} & M_{46} \\ M_{51} & M_{52} & M_{53} & M_{54} & L_{55} & M_{56} \\ M_{61} & M_{62} & M_{63} & M_{64} & M_{65} & L_{66} \end{bmatrix}^{-1} [K] \begin{bmatrix} V_1 \\ V_2 \\ V_3 \\ V_4 \\ V_5 \\ V_6 \end{bmatrix}$$

$$+Q\begin{bmatrix}(C_{11}+C_{1g}+C_{14}) & 0 & 0 & -C_{14} & 0 & 0\\ 0 & (C_{22}+C_{2g}+C_{25}) & 0 & 0 & -C_{25} & 0\\ 0 & 0 & (C_{33}+C_{3g}+C_{36}) \cdots & 0 & 0 & -C_{63}\\ -C_{41} & 0 & 0 & (C_{44}+C_{4g}+C_{41}) & 0 & 0\\ 0 & -C_{52} & 0 & 0 & (C_{55}+C_{5g}+C_{52}) & 0\\ 0 & 0 & -C_{63} & 0 & 0 & (C_{66}+C_{6g}+C_{63})\end{bmatrix}$$

$$\begin{bmatrix}v_1\\v_2\\v_3\\v_4\\v_5\\v_6\end{bmatrix}-Q\begin{bmatrix}C_{11} & 0 & 0 & 0 & 0 & 0\\ 0 & C_{22} & 0 & 0 & 0 & 0\\ 0 & 0 & C_{33} & 0 & 0 & 0\\ 0 & 0 & 0 \cdots & C_{44} & 0 & 0\\ 0 & 0 & 0 & 0 & C_{55} & 0\\ 0 & 0 & 0 & 0 & 0 & C_{66}\end{bmatrix}\begin{bmatrix}v_1'\\v_2'\\v_3'\\v_4'\\v_5'\\v_6'\end{bmatrix} \tag{6.29}$$

To establish simplified input-output relation of transformer; consider two-port nodal equation of the equivalent model of transformer 1 shown in Figure 6.8 is given in Equation 6.30

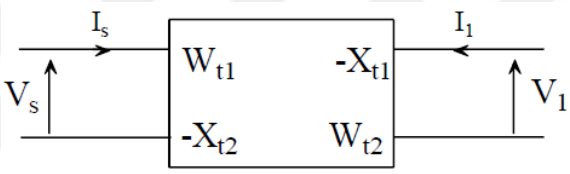

Figure 6.8 Block diagram of transformer 1 (Sulaiman, 2014)

Where, W_{t1}, X_{t1}, W_{t2} and X_{t2} are the sub-matrices of the equivalent transformer admittance matrix, and is defined as follows;

$$W_{t1}=\begin{bmatrix}(\bar{L}_{11}+C_{11}+C_{1g}+C_{14}) & \bar{M}_{12} & \bar{M}_{13}\\ \bar{M}_{21} & (\bar{L}_{22}+C_{22}+C_{2g}+C_{25}) & \bar{M}_{23}\\ \bar{M}_{31} & \bar{M}_{32} & (\bar{L}_{33}+C_{33}+C_{3g}+C_{36})\end{bmatrix}$$

$$X_{t1}=\begin{bmatrix}(C_{14}+\bar{M}_{14}) & \bar{M}_{15} & \bar{M}_{16}\\ \bar{M}_{24} & (C_{25}+\bar{M}_{25}) & \bar{M}_{25}\\ \bar{M}_{34} & \bar{M}_{35} & (C_{36}+\bar{M}_{36})\end{bmatrix}$$

$$W_{t2}=\begin{bmatrix}(\bar{L}_{44}+C_{44}+C_{4g}+C_{41}) & \bar{M}_{45} & \bar{M}_{46}\\ \bar{M}_{54} & (\bar{L}_{55}+C_{55}+C_{5g}+C_{52}) & \bar{M}_{56}\\ \bar{M}_{64} & \bar{M}_{65} & (\bar{L}_{66}+C_{66}+C_{6g}+C_{63})\end{bmatrix}$$

$$X_{t2}=\begin{bmatrix}(C_{41}+\bar{M}_{41}) & \bar{M}_{42} & \bar{M}_{43}\\ \bar{M}_{51} & (C_{52}+\bar{M}_{52}) & \bar{M}_{53}\\ \bar{M}_{61} & \bar{M}_{65} & (C_{63}+\bar{M}_{63})\end{bmatrix}$$

The following relation is obtained;

$$\begin{bmatrix}I_S\\I_1\end{bmatrix}=\begin{bmatrix}W_{t1} & -X_{t1}\\ -X_{t2} & W_{t2}\end{bmatrix}\begin{bmatrix}V_S\\V_1\end{bmatrix} \tag{6.30}$$

If the receiving end is OC,$I_1 = 0$ then, the Equation 6.30 becomes

$$\begin{bmatrix} I_S \\ 0 \end{bmatrix} = \begin{bmatrix} W_{t1} & -X_{t1} \\ -X_{t2} & W_{t2} \end{bmatrix} \begin{bmatrix} v_S \\ v_1 \end{bmatrix} \tag{6.31}$$

This implies

$$I_S = W_{t1}\, v_S - X_{t1}\, v_1$$

$$0 = -X_{t2}\, v_S + W_{t2}\, v_1 \implies v_1 = (W_{t2})^{-1}\, X_{t2}\, v_S$$

Therefore,

$$I_S = [W_{t1} - X_{t1}\, (W_{t2})^{-1}\, X_{t2}]\, v_S \tag{6.32}$$

6.5 Induction Generator

The voltage- current relation for the stator side is given as follows;

$$\begin{aligned} v_A &= r_A\, i_A + \frac{d}{dt}\,(L_{AA}i_A + L_{AB}i_B + L_{AC}i_C + L_{Aa}i_a + L_{Ab}i_b + L_{Ac}i_c) \\ v_B &= r_B\, i_B + \frac{d}{dt}\,(L_{BA}i_A + L_{BB}i_B + L_{BC}i_C + L_{Ba}i_a + L_{Bb}i_b + L_{Bc}i_c) \\ v_C &= r_C\, i_C + \frac{d}{dt}\,(L_{CA}i_A + L_{CB}i_B + L_{CC}i_C + L_{Ca}i_a + L_{Cb}i_b + L_{Cc}i_c) \end{aligned} \tag{6.33}$$

Where,

L_{AA}, L_{BB}, L_{CC}: Self impedances for phase windings A, Band C respectively

L_{AB}: Mutual inductance between phase winding A and B

L_{AC}: Mutual inductance between phase winding A and C

L_{BC}: Mutual inductance between phase winding B and C

L_{Aa}: Mutual inductance between stator phase winding A and rotor phase winding a

L_{Ab}: Mutual inductance between stator phase winding A and rotor phase winding b

L_{Ac}: Mutual inductance between stator phase winding A and rotor phase winding c

L_{Ba}: Mutual inductance between stator phase winding B and rotor phase winding a

L_{Bb}: Mutual inductance between stator phase winding B and rotor phase winding b

L_{Bc}: Mutual inductance between stator phase winding B and rotor phase winding c

L_{Ca}: Mutual inductance between stator phase winding C and rotor phase winding a

L_{Cb}: Mutual inductance between stator phase winding C and rotor phase winding b

L_{Cc}: Mutual inductance between stator phase winding C and rotor phase winding c

i_a, i_b, i_c: Rotor phase currents

Similarly, the voltage current relation for the rotor side is as follows;

$$v_a = r_a\, i_A + \frac{d}{dt}\,(L_{aA}i_A + L_{aB}i_B + L_{aC}i_C + L_{aa}i_a + L_{ab}i_b + L_{ac}i_c)$$

$$v_b = r_b\, i_B + \frac{d}{dt}\,(L_{bA}i_A + L_{bB}i_B + L_{bC}i_C + L_{ba}i_a + L_{bb}i_b + L_{bc}i_c) \qquad (6.34)$$

$$v_c = r_c\, i_C + \frac{d}{dt}\,(L_{cA}i_A + L_{cB}i_B + L_{cC}i_C + L_{ca}i_a + L_{cb}i_b + L_{cc}i_c)$$

For the case of symmetrical condition,

$r_A = r_B = r_C = r_s$ and $r_a = r_b = r_c = r_r$

Where, r_s, r_r is the stator and rotor phase winding resistances respectively

Since the flux path for phase A, B and C windings, A, B and C, are identical, then;

$L_{ss} = L_{AA} = L_{BB} = L_{CC}$ and $L_{sm} = L_{AB} = L_{BC} = L_{AC}$

$L_{rr} = L_{aa} = L_{bb} = L_{cc}$ and $L_{rm} = L_{ab} = L_{bc} = L_{ac}$

L_{ss}, L_{rr}: Self inductances of stator and rotor phase windings respectively

L_{sm}, L_{rm}: Mutual inductances between any stator and rotor phase windings respectively

Similarly,

$L_{Aa} = L_{Bb} = L_{Cc} = L_{srm}\ \cos(\sigma)$

$L_{Ab} = L_{Bc} = L_{Ca} = L_{srm}\ \cos\left(\sigma + {}^{2\pi}/_{3}\right)$

$L_{Ac} = L_{Ba} = L_{Cb} = L_{srm}\ \cos\left(\sigma + {}^{4\pi}/_{3}\right)$

Where,

L_{srm} is the maximum mutual inductance between the stator

$-$ rotor phase windings

σ is the angle between the axis of stator and rotor windings

The overall voltage current matrix relation is given in Equation 6.35

$$\begin{bmatrix} v_A \\ v_B \\ v_C \\ v_a \\ v_b \\ v_c \end{bmatrix} = \begin{bmatrix} r_s & 0 & 0 & 0 & 0 & 0 \\ 0 & r_s & 0 & 0 & 0 & 0 \\ 0 & 0 & r_s & 0 & 0 & 0 \\ 0 & 0 & 0 & r_r & 0 & 0 \\ 0 & 0 & 0 & 0 & r_r & 0 \\ 0 & 0 & 0 & 0 & 0 & r_r \end{bmatrix} \begin{bmatrix} i_A \\ i_B \\ i_C \\ i_a \\ i_b \\ i_c \end{bmatrix} +$$

$$\frac{d}{dt}\begin{bmatrix} L_{ss} & L_{sm} & L_{sm} & L_{srm}\cos(\sigma) & L_{srm}\cos(\sigma+{}^{4\pi}/_{3}) & L_{srm}\cos(\sigma+{}^{4\pi}/_{3}) \\ L_{sm} & L_{ss} & L_{sm} & L_{srm}\cos(\sigma+{}^{4\pi}/_{3}) & L_{srm}\cos(\sigma) & L_{srm}\cos(\sigma+{}^{4\pi}/_{3}) \\ L_{sm} & L_{sm} & L_{ss} & \dots L_{srm}\cos(\sigma+{}^{4\pi}/_{3}) & L_{srm}\cos(\sigma+{}^{4\pi}/_{3}) & L_{srm}\cos(\sigma) \\ L_{srm}\cos(\sigma) & L_{srm}\cos(\sigma+{}^{4\pi}/_{3}) & L_{srm}\cos(\sigma+{}^{4\pi}/_{3}) & L_{rr} & L_{rm} & L_{rm} \\ L_{srm}\cos(\sigma+{}^{4\pi}/_{3}) & L_{srm}\cos(\sigma) & L_{srm}\cos(\sigma+{}^{4\pi}/_{3}) & L_{rm} & L_{rr} & L_{rm} \\ L_{srm}\cos(\sigma+{}^{4\pi}/_{3}) & L_{srm}\cos(\sigma+{}^{4\pi}/_{3}) & L_{srm}\cos(\sigma) & L_{rm} & L_{rm} & L_{rr} \end{bmatrix}$$

(6.35)

6.6 Proposed Mathematical Formulations for the Studied Wind/PV Hybrid Power System

The block diagram of studied system is shown in Figure 6.9. A large equivalent synchronous generator (1110 MVA) supplies power to the infinite bus over a 200 km and 400 kV transmission line. This line length is typical of a long line carrying bulk power in Ontario power system. In this study 100-MW PV and Wind farm are connected at the midpoint of the transmission line (Varma and etc., 2015).

When the frequency dependence of the line parameters and the distributed nature of the losses are taken into account, it becomes very difficult, if not impossible in a practical way, to write the solution of the line equations directly in time domain. This solution, however, can easily be obtained in frequency domain, and is given by JMarti state variable well-known relations (JMarti, 1982).

$$V_K(\omega) = \cosh[\gamma(\omega)\, l]\, V_m\,(\omega) - Z_C(\omega)\sinh[\gamma(\omega) l]\, I_m(\omega) \tag{6.36}$$

And,

$$I_K(\omega) = \frac{1}{Z_C(\omega)}\sinh[\gamma(\omega) l]\, V_m(\omega) - \cosh[\gamma(\omega) l]\;\, I_m(\omega) \tag{6.37}$$

Where

$$Z_C(\omega) = \sqrt{Z'(\omega) * Y'(\omega)} \;\; = \text{Characteristic Impedance}$$

$$\gamma(\omega) = \sqrt{\frac{Z'(\omega)}{Y'(\omega)}} = \text{Propagation Constant}$$

$$Z'(\omega) = R'(\omega) + j\omega L'(\omega)$$

$$Y'(\omega) = G'(\omega) + j\omega C'(\omega)$$

$$R' = \text{Series Resistance}, L' = \text{Series Inductance}$$

$$G' = \text{Shunt Conductance}, C' = \text{Shunt Capacitance}$$

Primed quantities are in per unit length. Block diagram of Wind/PV hybrid system is given in Figure 6.9

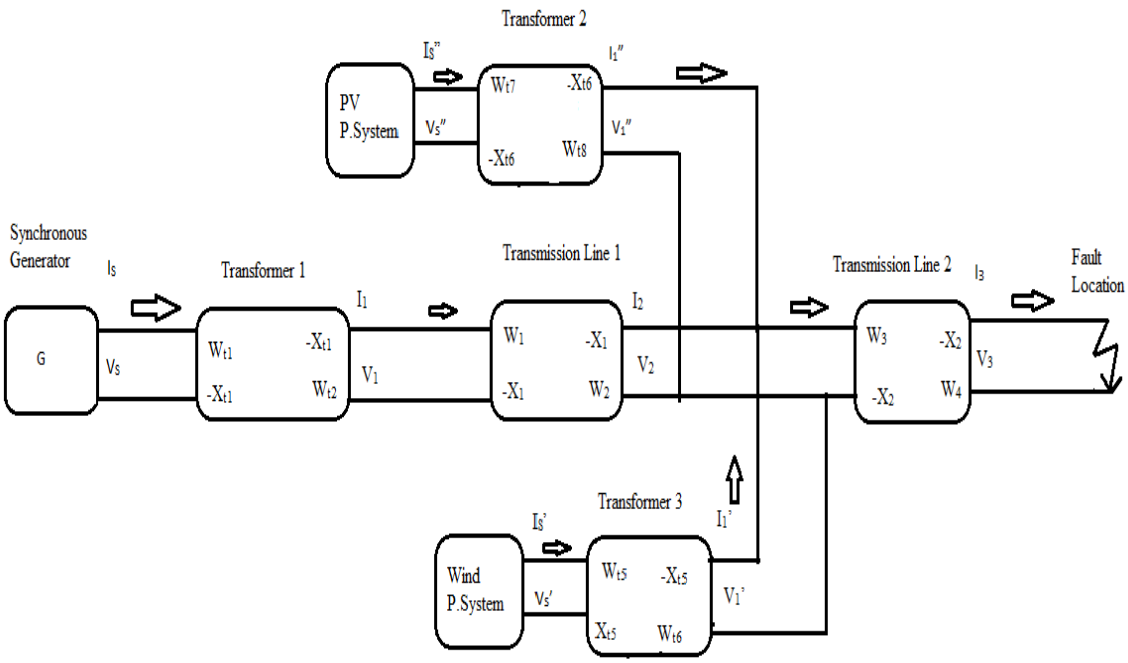

Figure 6.9 Equivalence circuit of Wind/PV hybrid system

V_S: Source Voltage = input voltage to the transformer 1

I_S: input current to the transformer 1

V_1: Transformer output Voltage = Sending end voltage lof the ine 1

V_3: Line 2 receiving end Voltage = Pre − fault voltage at the line end

I_S' = Transformer 2 input primary current

V_S' = Source voltage of Wind generator = Input voltage to the Transformer 2

V_1' = Transformer 2 output voltage

I_1' = Transformer 2 output current

I_S'' = Transformer 3 input primary current

V_S'' = Source voltage of PV generator = Input voltage to the Transformer 3

Using the two-port matrix equations, all injected currents are assumed to be positive. Two-port network presented in [Ercelebi, 1992; Jaffar, 2014] utilized equation 6.35 to denote the mathematical equivalent of the system.

$$\begin{bmatrix} i_{g1} \\ -i_F \\ i_{g2} \\ i_{g3} \end{bmatrix} = \begin{bmatrix} (W_2 + Y_S) & -X_2 & 0 & 0 \\ B & 0 & A & C \\ 0 & -X_{t5} & (W_{t6} + Y_S') & 0 \\ 0 & 0 & -X_{t6} & (W_{t8} + Y_S^{''}) \end{bmatrix} \begin{bmatrix} v_S \\ v_2 \\ v_S' \\ v_S^{''} \end{bmatrix} \tag{6.38}$$

Where

i_{g1}, i_{g2}, i_{g3}: Conventional generator current, Wind generator current and PV generator current

i_F : Fault current

$v_S, v_S', v_S^{''}$: Sending end voltages for Conventional generator, Wind generator and PV generator

W_2: Submatrices self impedance matrix of the conventional generator and transformer 1

Y_S: Admittance matrix of the conventional generator

W_{t6}: Submatrices self impedance matrix of the wind generator and transformer 2

Y_S': Admittance matrix of the wind generator

W_{t8}: Submatrices self impedance matrix of the PVgenerator and transformer 3

$Y_S^{''}$: Admittance matrix of the PV generator

X_2: Submatrices mutual impedance matrix of conventional generator and transformer 1

X_{t5}: Submatrices mutual impedance matrix of wind generator and transformer 2

X_{t6}: Submatrices mutual impedance matrix of PVgenerator and transformer 3

submatrices W_t, X_t are given in in section 6.4.2

$$A = \left[W_{t8}X_{t6}^{-1}\left(W_{t8} + Y_S^{''}\right) - X_2\right].v_S$$

$$B = \left[W_{t6}X_{t5}^{-1}(W_{t6} + Y_S') - X_2\right].v_S$$

$$C = \left[W_2X_2^{-1}(W_2 + Y_S) - X_2\right].v_S$$

$$i_F = A\,v_S' + B\,v_S + Cv_S^{''} \tag{6.39}$$

7. SIMULATION RESULTS FOR WIND/PV HYBRID SYSTEM IN ATP/EMTP SOFTWARE

7.1 Introduction

The main objective of this thesis is to examine the transient behaviour of a hybrid system (with PV and Wind generator together) due to various types of fault i.e. SCF, SLG and DLG. The system components are connected in cascades with transmission line of 400 kV. The length of transmission line is 200 km long.

The first power system studied is a conventional power system (without PV and Wind Generator), in which the transmission system is fed at one-end by a synchronous generator as shown in Figure 7.1. Different types of fault i.e. SCF, LG fault and DLG fault take place at the end of 400 kV transmission line. In this study several scenarios have been considered. These scenarios include the effect of types of fault, effect of SCF at different location on power system, effect of line length and the effect of fault resistance. The second power system studied is a PV hybrid system. The third power system studied is a Wind hybrid system and the forth studied system is a hybrid power system in which conventional power system is connected with Wind/PV power system together.

The system under study is a balanced system, but the models of various components such as load, PV inverter, wind turbine control system, capacitance of transmission and hybrid transformers etc. have effects on the transient behaviour of the system during fault. Data of the conventional generator, transformers and transmission lines are given in Table 7.1 to 7.3, respectively. Serial impedance and shunt admittance of TL is given in Table 7.4.

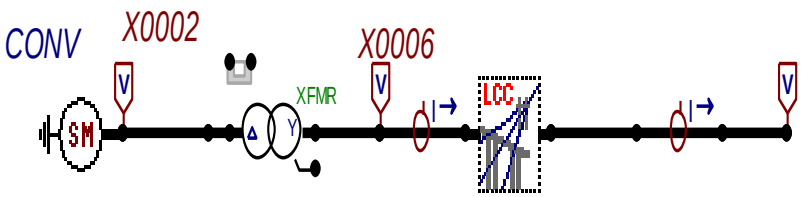

Figure 7.1 Conventional power system (without PV & Wind) studied

Table 7.1 Data of Conventional Generator

Conventional Generator	
L-L Voltage(kV)	34.5
Power (MVA)	100
Test Frequency	60 Hz
Poles	2
$R_A\ (pu)$	0.0036
$X_L\ (pu)$	0.13
$X_d\ (pu)$	1.933
$X_q\ (pu)$	1.743
$X'_d\ (pu)$	0.467
$X'_q\ (pu)$	1.144
$X''_d\ (pu)$	0.312
$X''_q\ (pu)$	0.312
$T'_{d0}\ (pu)$	6.66
$T'_{q0}\ (pu)$	0.44
$T''_{d0}\ (pu)$	0.032
$T''_{q0}\ (pu)$	0.057

Table 7.2 Data of Hybrid Transformers T_1

Hybrid Transformer T1	
L-L Voltage(kV)	22/400 (Δ-Y)
Power (MVA)	1110
Test Frequency	60 Hz
Type of Core	3 leg stacked
Number of Windings	2
$C_{P\text{-}G}$	13.7881 nF
$C_{S\text{-}G}$	4.6316 nF
C_m	1.9849 nF
Where, P-G : Capacitance between the primary winding and the ground S-G : Capacitance between the secondary winding and the ground P-G : Mutual capacitance between the primary and secondary winding	

Table 7.3 Data of Transmission Lines TL

Transmission Line TL 1		
	Phase Conductors	Ground Wire
Length (km)	100	
DC Resistance for 3-phases (Ω / km)	0.156489	0.1469
Resistivity of the soil (Ω-m)	20	
Conductor Radius (cm)	0.976	0.976
Horizental Distance of Tower (m)	Phase A= 3.35 Phase B = 4.65	0

	Phase C = 3.73	
Vertical Tower Height (m)	Phase A= 24.61 Phase B = 20.65 Phase C = 17	26.31
Model of Transmission Line	JMarti	

Table 7.4 Serial impedance and shunt admittance of Transmission line 1

Calculated steady state benchmark data for line/cable model
Frequency [Hz]: 60.
Positive sequence serial impedance

Ohm/km	Z_A	Z_B	Z_C
Line1	0.0913+j0.2345	0.1118+j0.2371	0.039+j0.2853

Zero sequence serial impedance

Ohm/km	Z_A	Z_B	Z_C
Line1	0.1932+j0.7706	0.2104+j0.8493	0.2051+j0.8571

Positive sequence average mutual and self-impedance

Ohm/km	Line1	Line2	Line3
Line1	0.0807+j0.2523		

Zero sequence average mutual and self-impedance

Ohm/km	Line1	Line2	Line3
Line1	0.2029+j0.8257		

Positive sequence shunt admittance

uF/km	Y_A	Y_B	Y_C
Line1	-0.002+j0.0171	-2.E-4+j0.0188	0.0016+j0.0171

Zero sequence shunt admittance

uF/km	Y_A	Y_B	Y_C
Line1	-1.E-5+j0.0084	3.3E-6+j0.0072	1.9E-5+j0.0082

Positive sequence average mutual and self-admittance

uF/km	Line1	Line2	Line3
Line1	-6.E-5+j0.0177		

Zero sequence average mutual and self-admittance

uF/km	Line1	Line2	Line3
Line1	3.2E-6+j0.0079		

7.2 Studied Conventional Power System

7.2.1 Effect of line length on fault current

The conventional power system studied is shown in Figure 7.2. LG fault takes place on phase A at the end of line when the voltage is at the maximum value i.e. 18.14 msec. The faulted phase currents at location Z and fault location X, during fault are computed for various line lengths from 20 km to 260 km and plotted to obtain faulted phase current waveforms as given in Figures 7.3 to 7.9 respectively. The Maximum values of the faulted phase current at location Z and fault location X, harmonics frequency and travel time for different line lengths are shown in Table 7.5. Fault current at location Z increases from 0.381 kA at 20 km line length to 2.541 kA at 260 km line length. Fault current at fault location X, increases from 1.159 kA at a line length of 20 km to 2.205 kA at a line length of 260 km. Fault occurs at 18.14 msec at fault point but at sending end it takes some travel time.

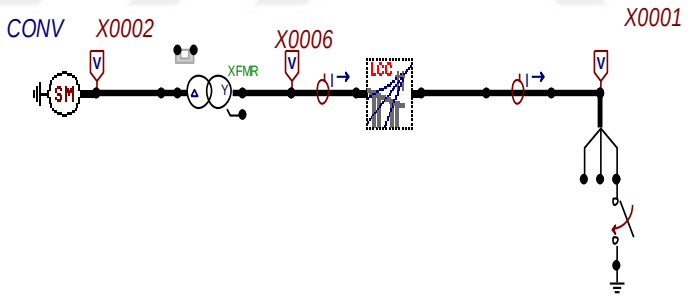

Figure 7.2 Configuration of conventional power system with LG fault occurs at receiving end

The simulation result shows that the maximum magnitude of the currents at location Z and fault location X increases as the line length increases due to capacitance of transmission line, also ripples along the line attenuate as the line length increases. It is also observed that as line length increases travel time of sending end fault current is increasing and harmonics frequency is decreasing. Red colour represents phase A.

Table 7.5 Maximum magnitudes of faulted phase current against line length at location Z and fault location X

Line Length (km)	Time of fault occur and time of 1st peak of fault at location Z (sec)	Maximum fault current at location Z (A)	Maximum fault current at fault location X (A)	Harmonics Frequency at Fault location X at Peak Point (kHz)	$Travel\ Time = l/v$ (m/Sec)
20	0.01699-0.02223	381.1	1159	3.183	0.067
100	0.01725-0.02114	1014	1483	1.852	0.333
180	0.01745-0.0223	1951	1760	1.268	0.6
200	0.01756-0.02276	2146	1754	0.847	0.666
220	0.01761-0.02324	2307	1814	0.2114	0.733
240	0.01765-0.02371	2439	2005	0.193	0.8
260	0.01776-0.02414	2541	2205	0.173	0.867

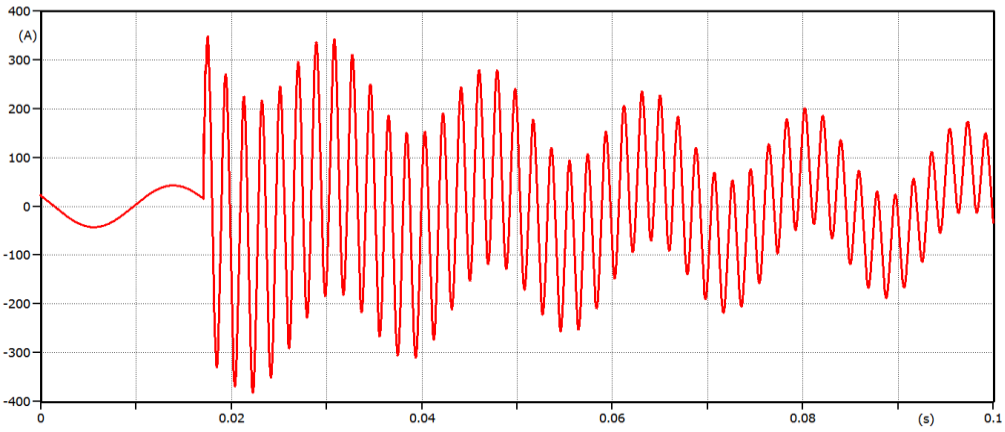

Figure 7.3(a) Fault current at location Z: when line length is 20 km

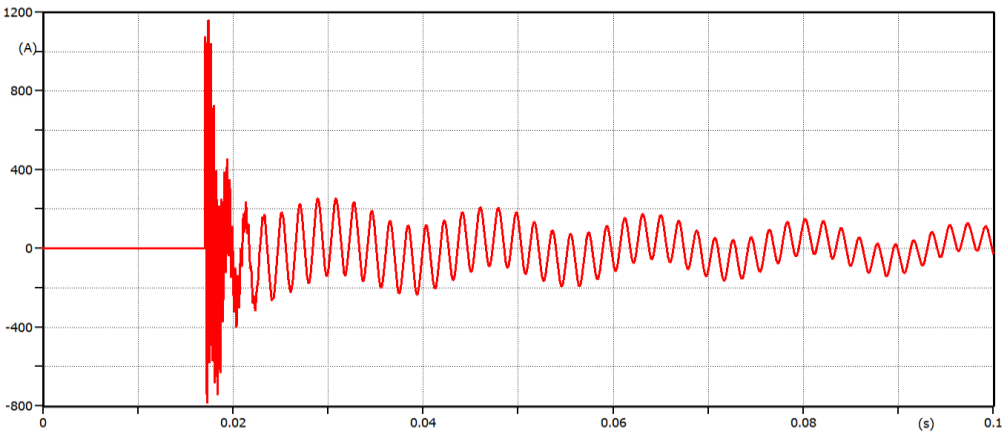

Figure 7.3(b) Fault current at fault location X: when line length is 20 km

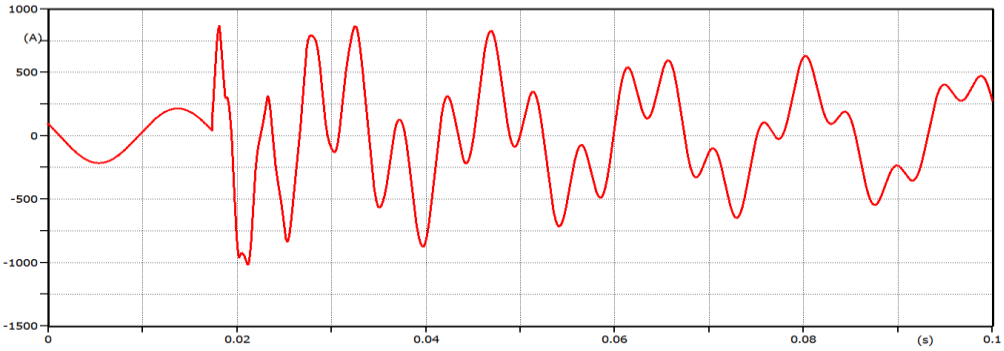

Figure 7.4(a) Fault current at location Z: when line length is 100km

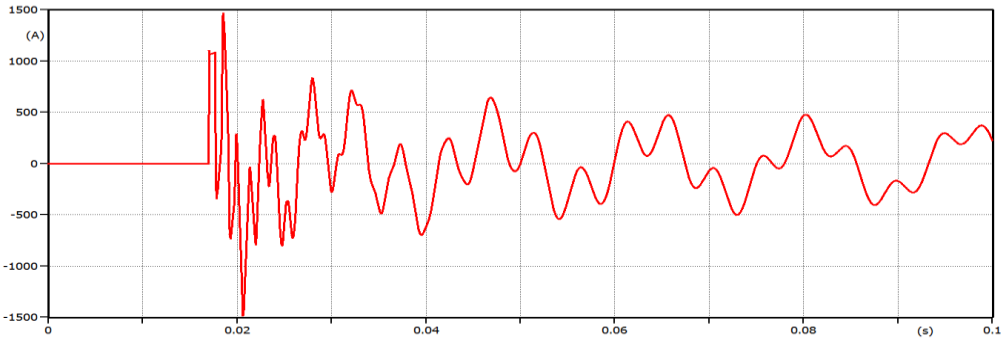

Figure 7.4(b) Fault current at fault location X: when line length is 100km

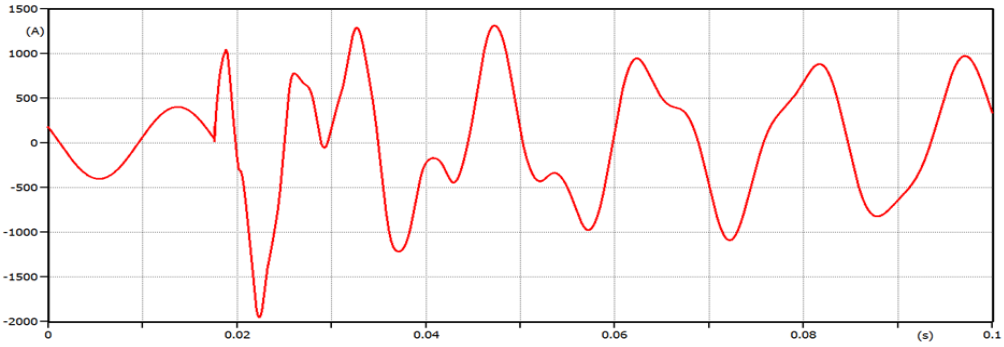

Figure 7.5(a) Fault current at location Z: when line length is 180 km

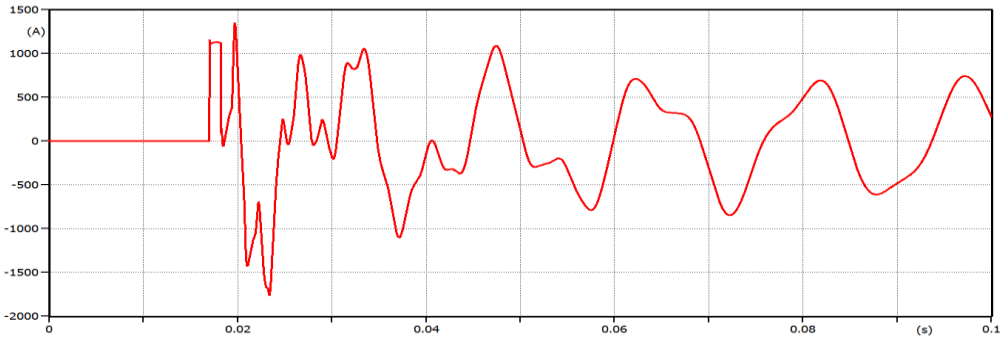

Figure 7.5(b) Fault current at fault location X: when line length is 180 km

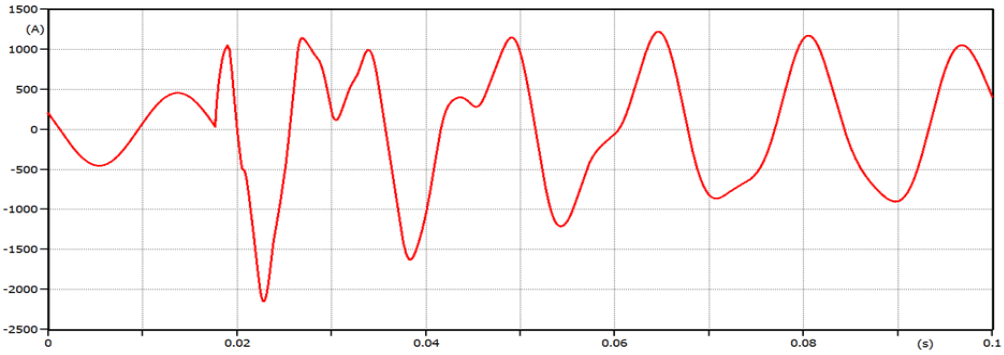

Figure 7.6(a) Fault current at location Z: when line length is 200 km

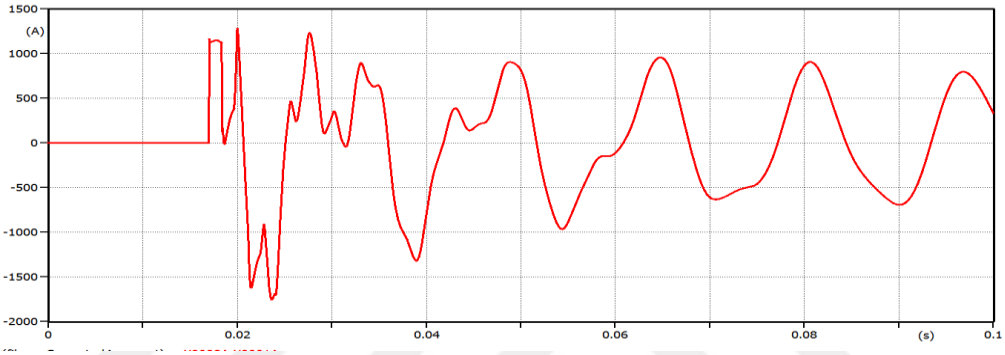

Figure 7.6(b) Fault current at fault location X: when line length is 200 km

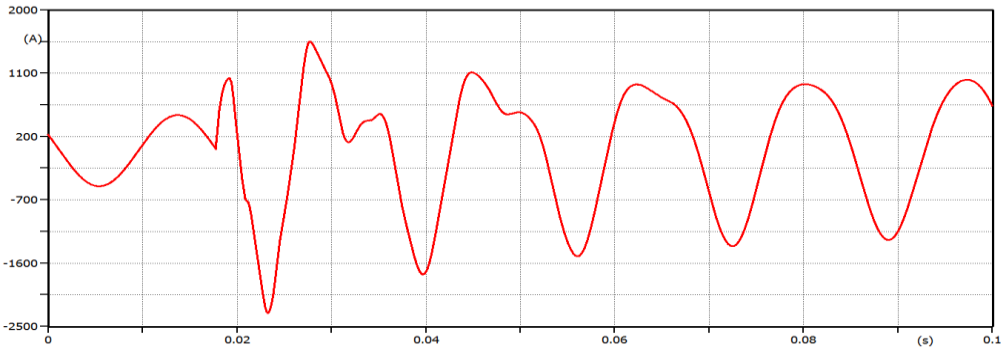

Figure 7.7(a) Fault current at location Z: when line length is 220 km

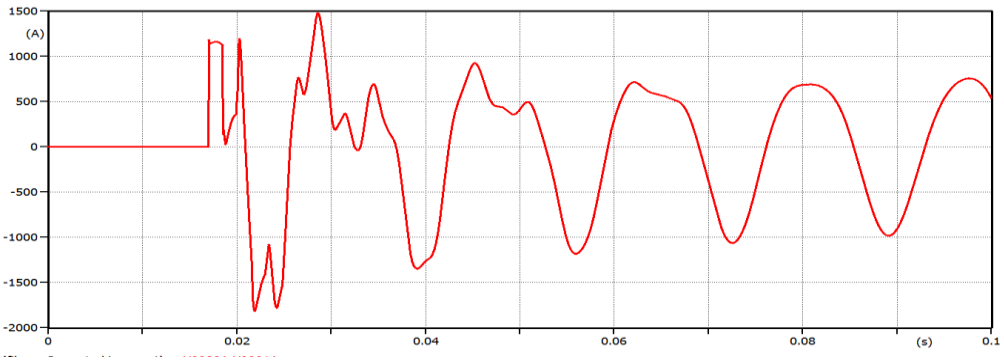

Figure 7.7(b) Fault current at fault location X: when line length is 220 km

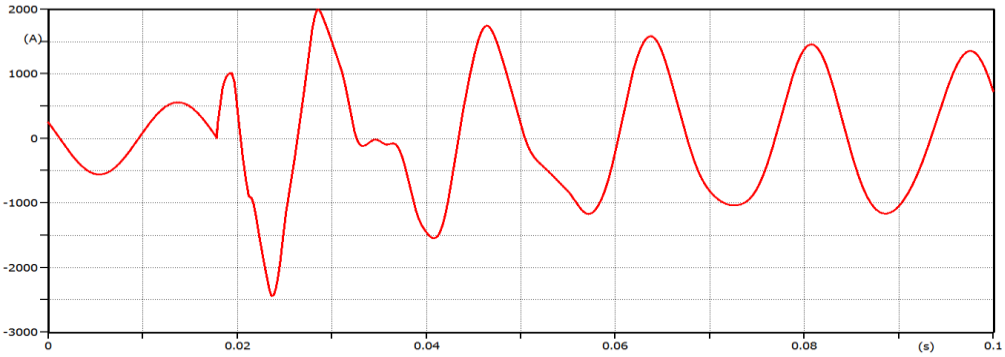

Figure 7.8(a) Fault current at location Z: when line length is 240 km

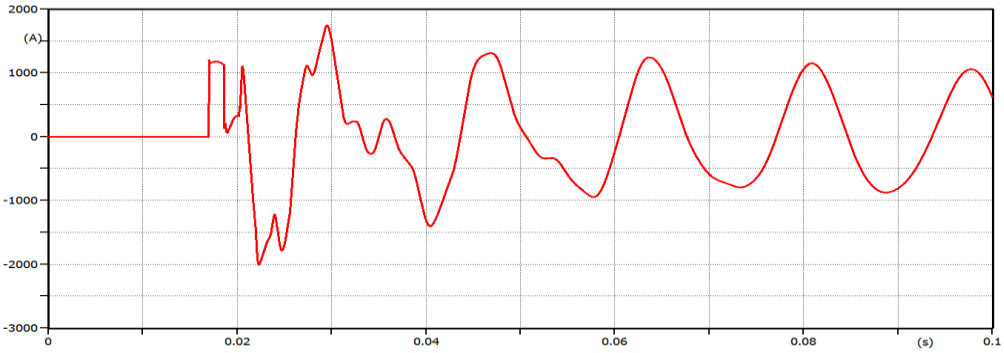

Figure 7.8(b) Fault current at fault location X: when line length is 240 km

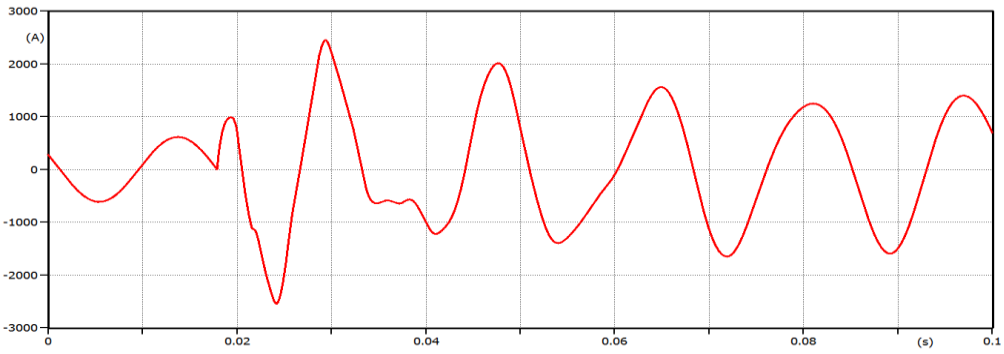

Figure 7.9(a) Fault current at location Z: when line length is 260 km

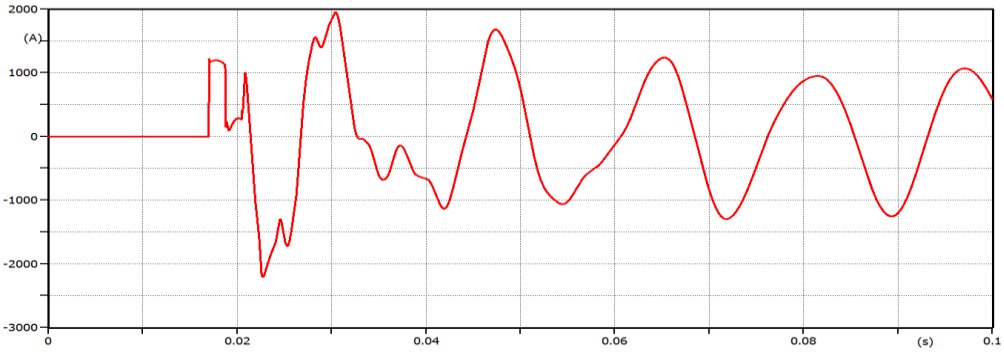

Figure 7.9(b) Fault current at fault location X: when line length is 260 km

The un-faulted phase voltages waveforms at location Z are shown in Figures 7.10 to 7.16 from 20 km to 260 km, respectively. It is observed from the results given in Table 7.6 that as the line length increase the un-faulted phase voltages increases and the distortion decreases. Line voltages of un-faulted phases also become unbalanced and voltage of faulted phase goes to zero. Here red colour represents phase A, green colour phase B and blue colour phase C in all waveforms.

Table 7.6 Effect of Line Length on line Voltage at location Z

Distance between sending end and fault point (km)	**Maximum sending end voltage of un-faulted phases(kV)**	
	Phase B	Phase C
20	781.2	755.1
100	810.4	909
180	950.9	987.4
200	1026	978.2
220	1054	955.8
240	1062	1015
260	1053	1127

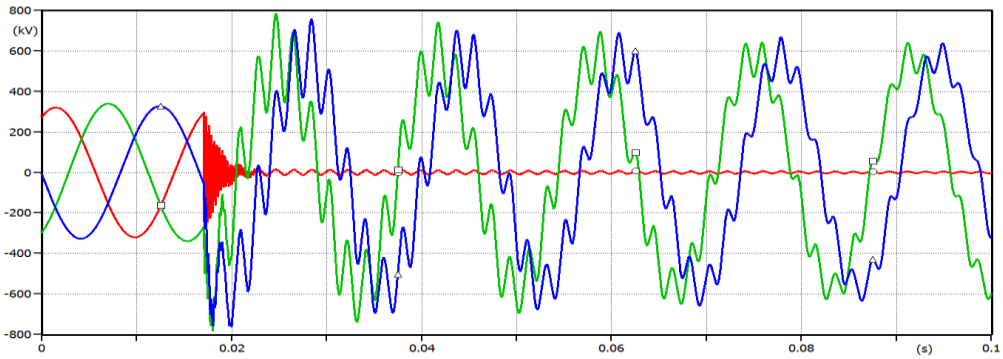

Figure 7.10 Voltage at location Z when line length is 20 km

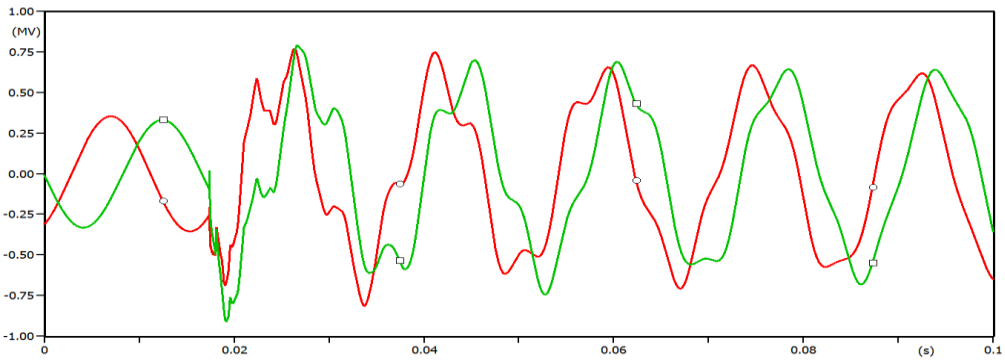

Figure 7.11 Voltage at location Z when line length is 100 km

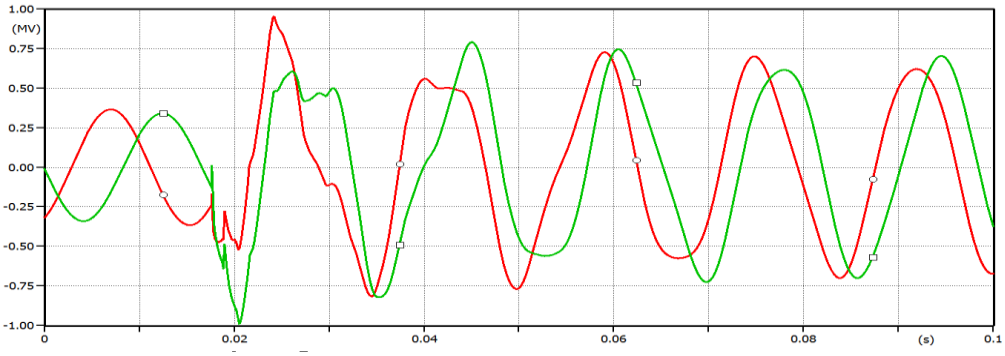

Figure 7.12 Voltage at location Z when line length is 180 km

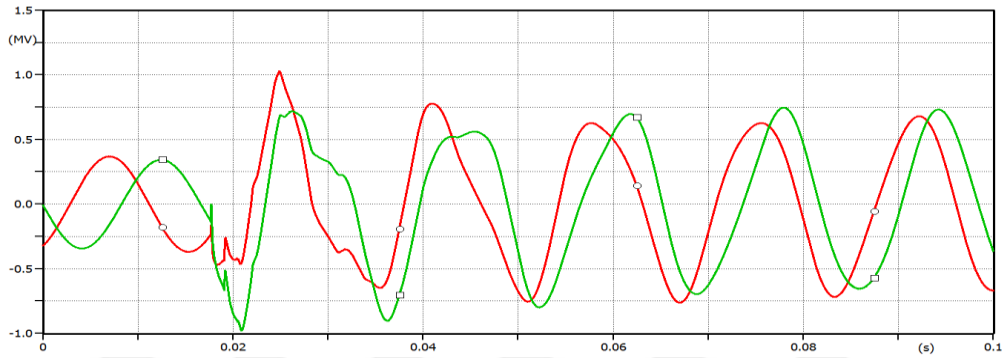

Figure 7.13 Voltage at location Z when line length is 200 km

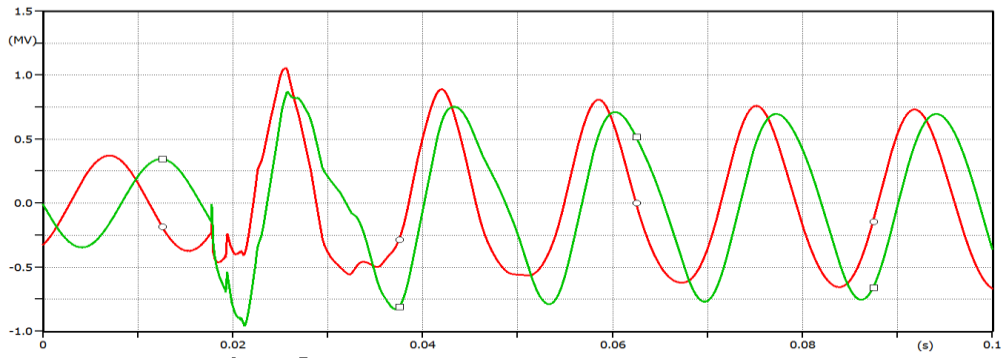

Figure 7.14 Voltage at location Z when line length is 220 km

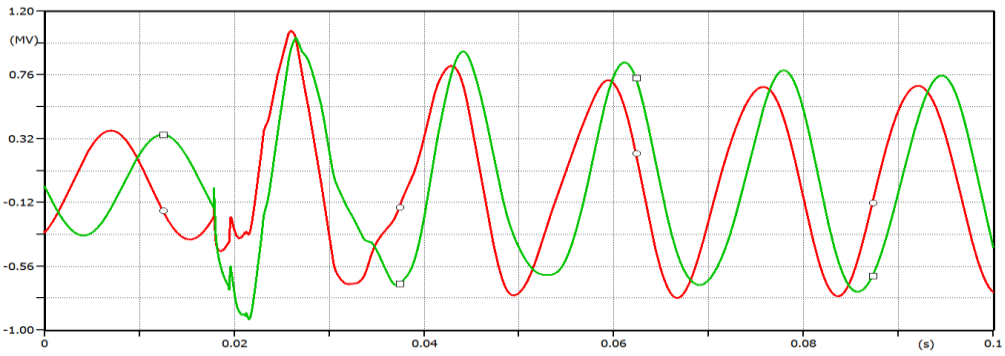

Figure 7.15 Voltage at location C when line length is 240 km

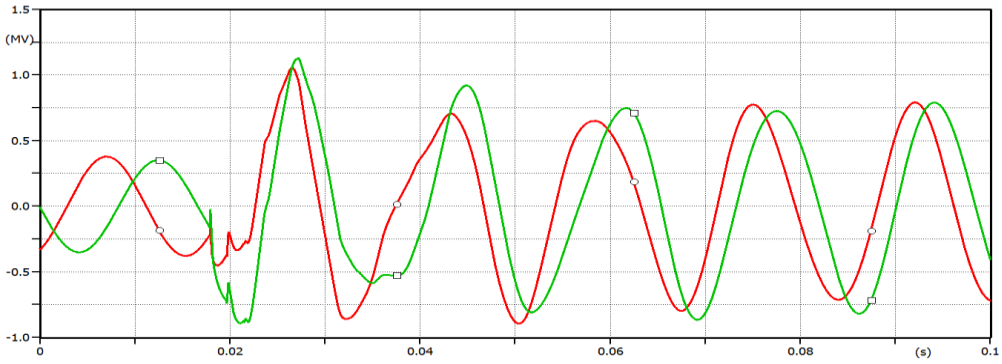

Figure 7.16 Voltage at location Z when line length is 260 km

7.2.2 Effect of fault resistance

LG fault is considered to take place at the end of the TL i.e. location X as shown in Figure 7.17. The length of transmission line between location Z (secondary side of transformer at 400 kV) and location X is 200 km. For various values of fault resistance, maximum magnitude of fault currents at the location Z and at the fault location X is given on Table 7.7. The waveforms of the fault current at location Z and fault location X are given in Figures from 7.18 to 7.24 respectively.

The maximum magnitude of fault currents at the both location X and Z decreases as the fault resistance increases. Fault current at location Z decreases from 2.136 kA at 1Ω fault resistance to 1.499 kA at 100 Ω fault resistances and fault current at fault location X decreases from 1.742 kA at 1Ω fault resistance to 1.159 kA at 100 Ω fault resistances. Transients in the fault current waveform are higher at lower value of the fault resistance as compared to that of higher value.

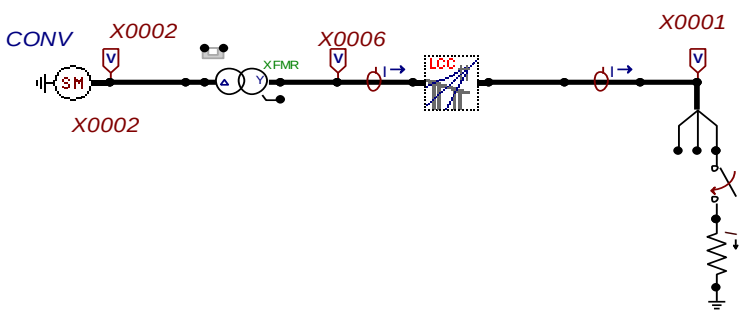

Figure 7.17 Configuration of conventional power system for fault resistance

Table 7.7 Effect of Fault Resistance & maximum magnitudes of fault current

Fault Resistance (Ω)	Time of Fault Current at Location Z (Sec)	Fault Current at Location Z (A)	Time of Fault Current at Fault Location X (Sec)	Fault Current at Fault Location X (A)
1	0.02276	2136	0.02365	1742
5	0.02282	2098	0.02364	1699
10	0.02284	2051	0.02361	1649
20	0.0228	1966	0.02361	1561
30	0.02284	1889	0.02359	1486
50	0.02292	1753	0.02358	1365
100	0.02292	1499	0.0235	1159

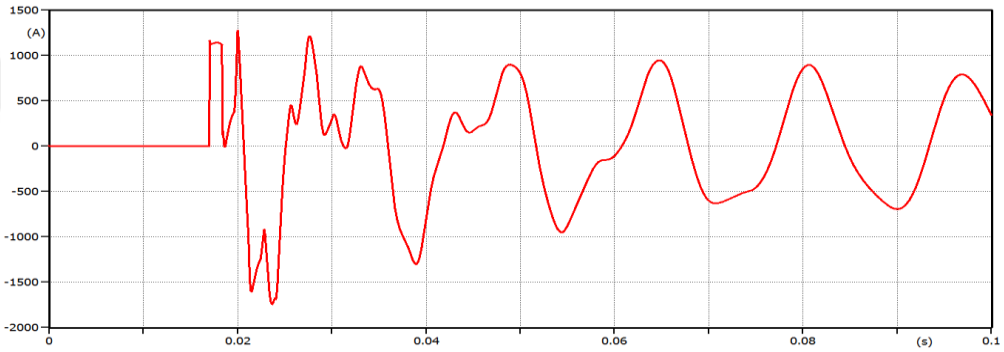

Figure 7.18(a) Fault Current at fault location X when fault resistance is 1Ω

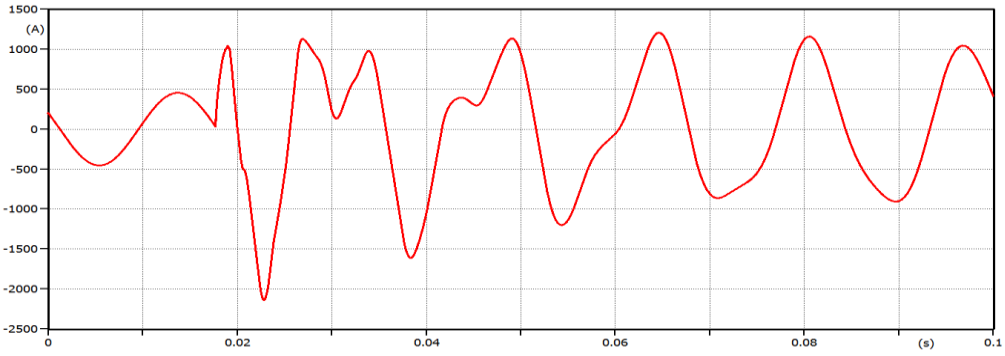

Figure 7.18(b) Fault Current at location Z when fault resistance is 1Ω

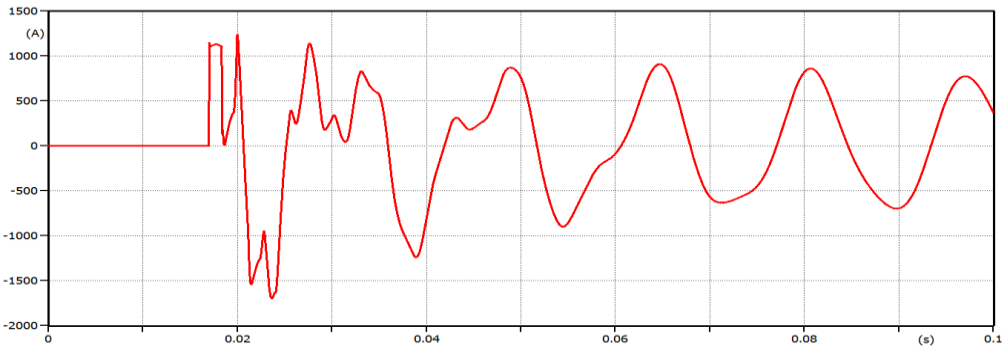

Figure 7.19(a) Fault Current at fault location X when fault resistance is 5Ω

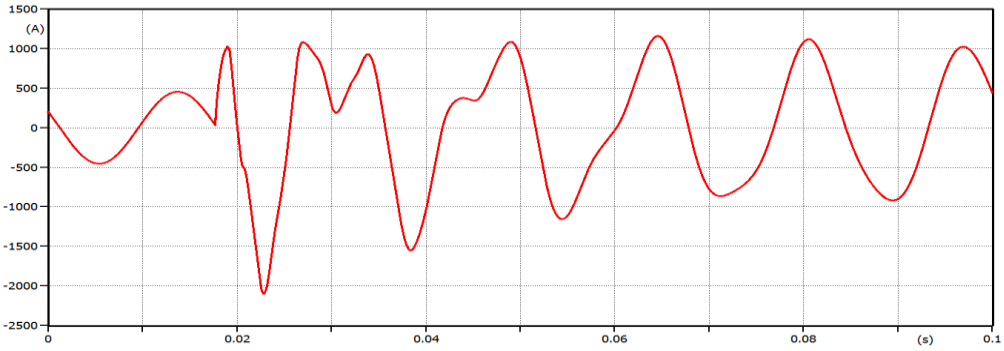

Figure 7.19(b) Fault Current at location Z when fault resistance is 5Ω

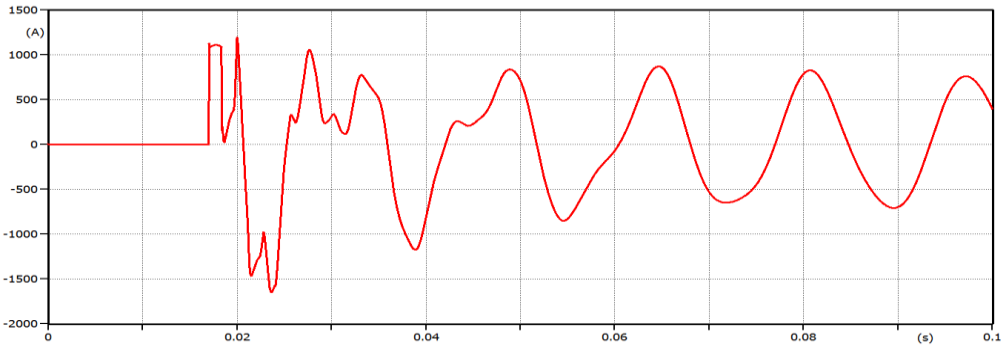

Figure 7.20(a) Fault Current at fault location A when fault resistance is 10Ω

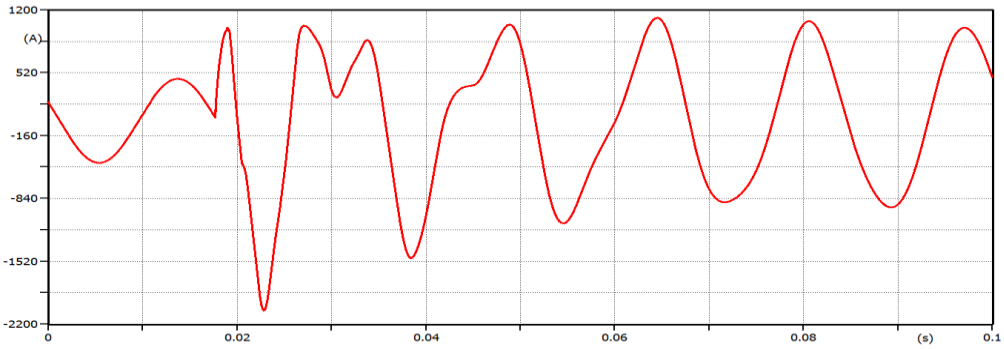

Figure 7.20(b) Fault Current at Location Z when fault resistance is 10Ω

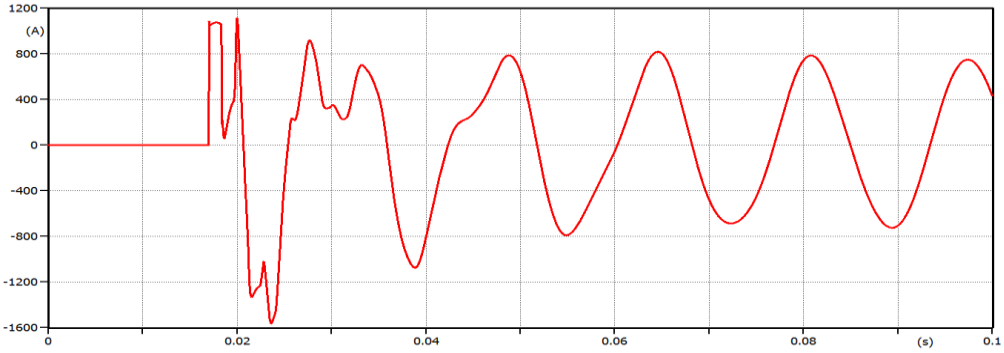

Figure 7.21(a) Fault Current at fault location A when fault resistance is 20Ω

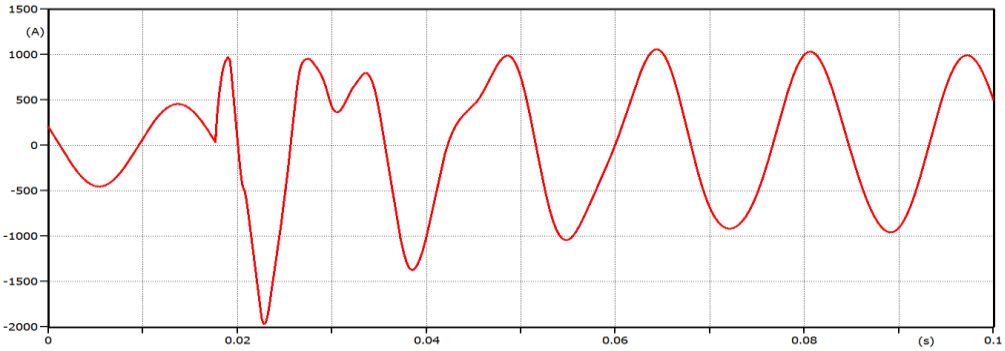

Figure 7.21(b) Fault Current at location Z when fault resistance is 20Ω

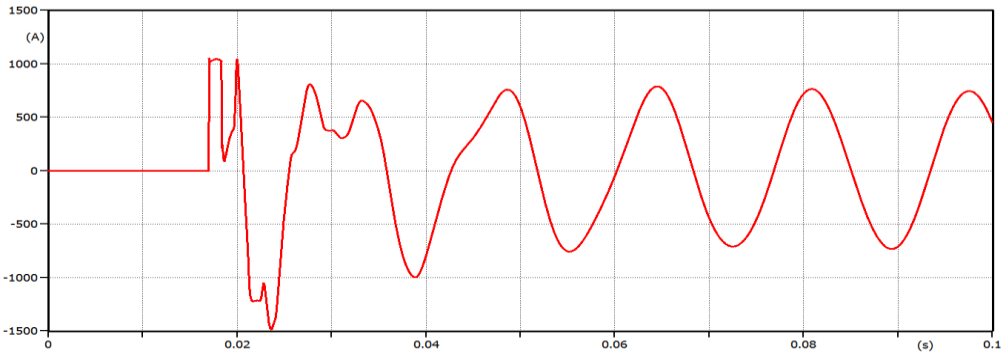

Figure 7.22(a) Fault Current at fault location X when fault resistance is 30Ω

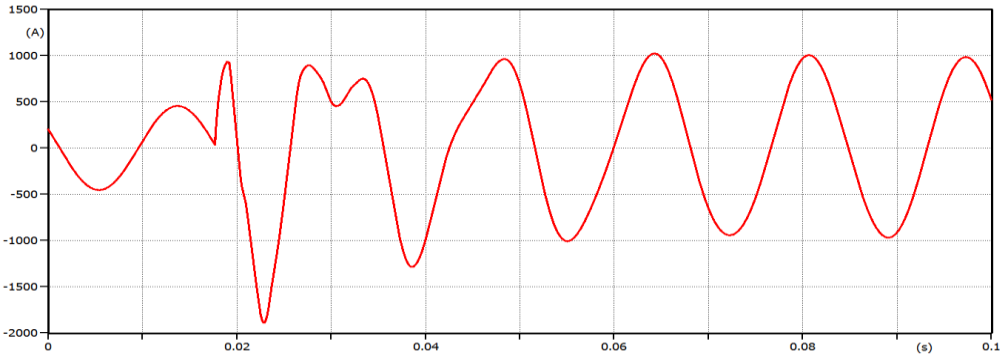

Figure 7.22(b) Fault Current at location Z when fault resistance is 30Ω

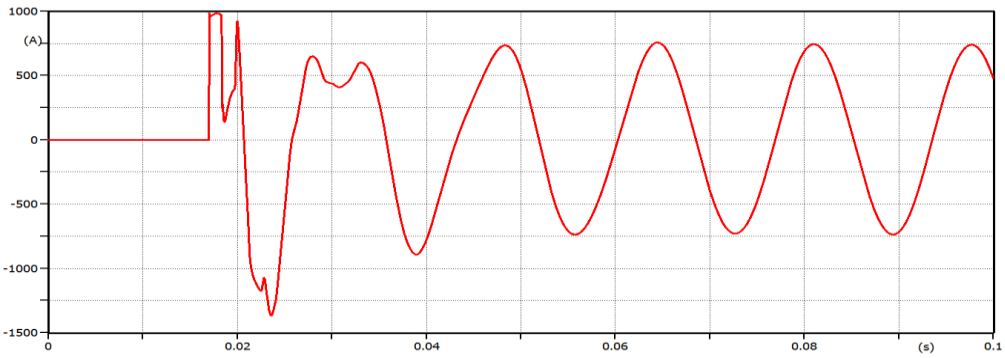

Figure 7.23(a) Fault Current at fault location X when fault resistance is 50Ω

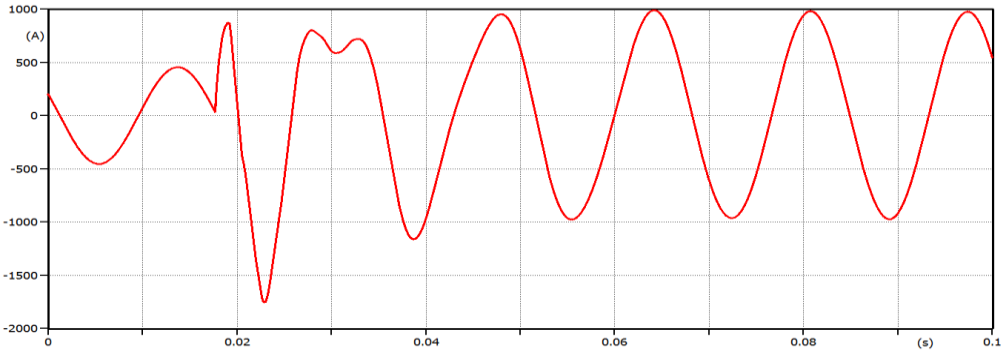

Figure 7.23(b) Fault Current at location Z when fault resistance is 50Ω

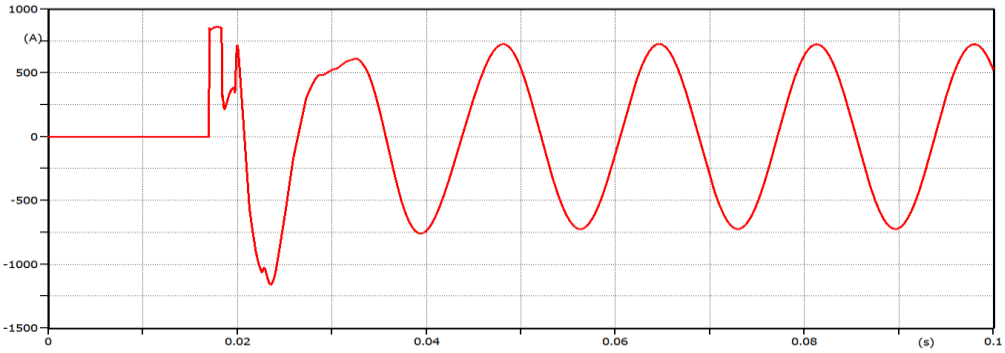

Figure 7.24(a) Fault Current at fault location X when fault resistance is 100Ω

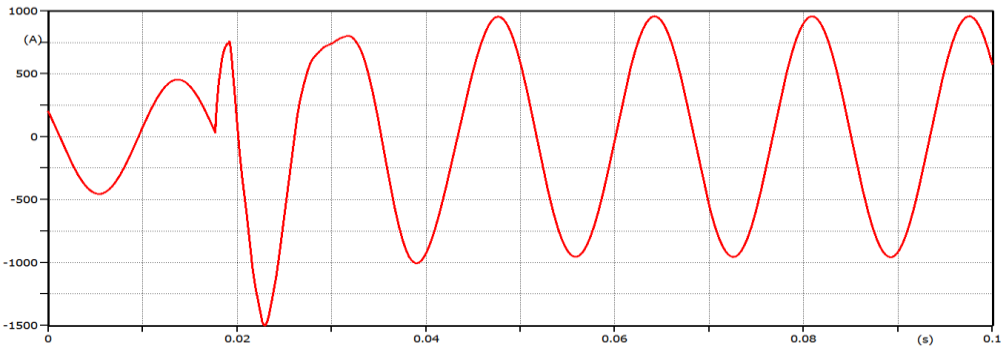

Figure 7.24(b) Fault Current at location Z when fault resistance is 100Ω

7.2.3 Effect of types of fault

On this conventional power system different types of faults are considered such as SLG fault, DLG and 3-phase SCF. The SLG fault occurs on phase A at receiving end of transmission line i.e. 400 kV. In case of DLG fault, fault occurs at the receiving end of the line on phases A and B. The maximum magnitude of faulted and un-faulted currents at location Z and fault location X is given in Table 7.8. Similarly, in the case of three-phase SCF simulation and currents computed were also taken at the fault location

X and location Z respectively as given in Table 7.8. The system configuration is shown in Figure 7.25.

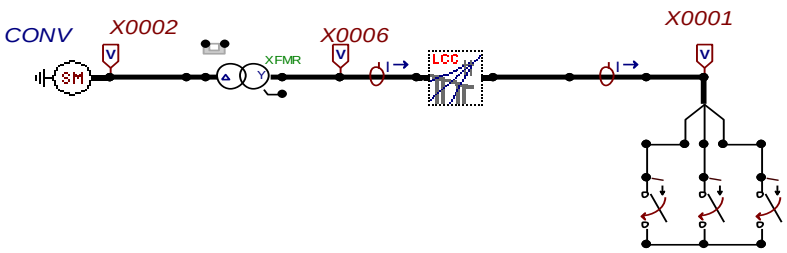

Figure 7.25 Configuration of conventional power system for 3-phase SCF

For different types of fault, waveforms of faulted and un-faulted phase currents at the both locations X and Z are given in Figures 7.26 to 7.28 respectively.

It has been observed that maximum wave distortion occurs on the voltage waveform as compared to the current waveform. The dynamic behaviour of 3-phese fault is most severe fault than other type of faults. Hence, highest magnitude of fault current occurs at 3-phese fault. Here red colour represents phase A, green colour phase B and blue colour phase C in all waveforms.

Table 7.8 Maximum magnitudes of fault current at location X and Z for different types of fault on conventional power system

Type of Fault	**Location X**		**Fault Location Z**	
	Maximum Magnitude of Current of Un-Faulted Phases (A)	Maximum Magnitude of Current of Faulted Phases (A)	Maximum Magnitude of Current of Un-Faulted Phases (mA)	Maximum Magnitude of Current of Faulted Phases(A)
LG Fault (Phase A)	1025-1130	2147	-	1754
DLG Fault (Phase A and B)	784.3	4279-4003	-	5030-4692
Three Phase SCF	-	3716-5570-5220	-	4870-5764-5529

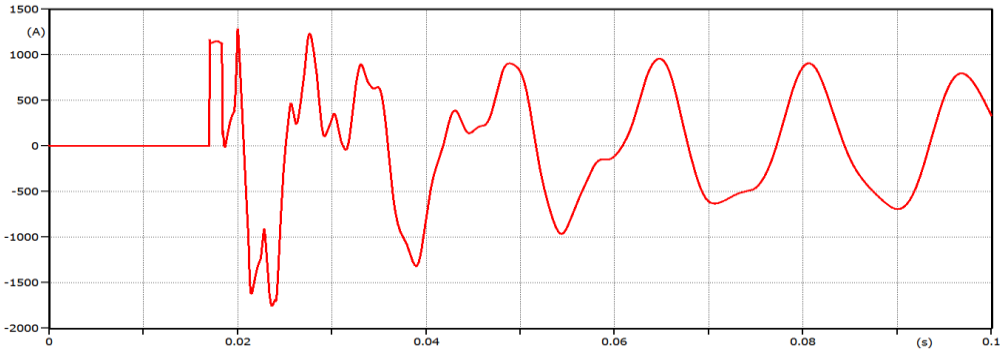

Figure 7.26(a) Faulted phase current at fault location X with SLG fault

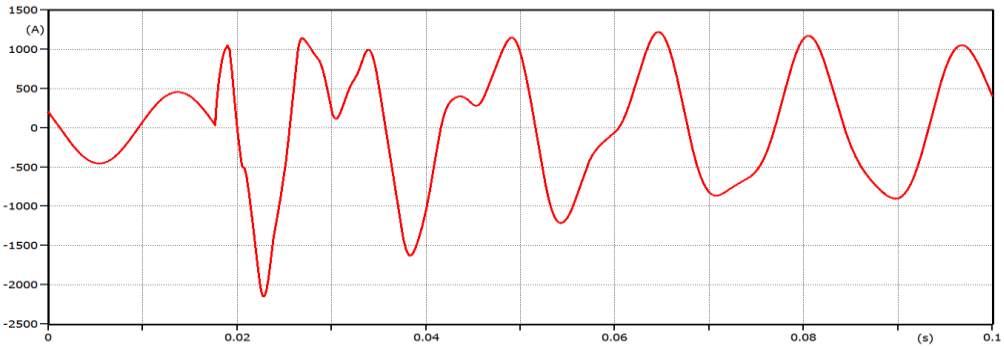

Figure 7.26(b) Faulted phase current at location Z with SLG

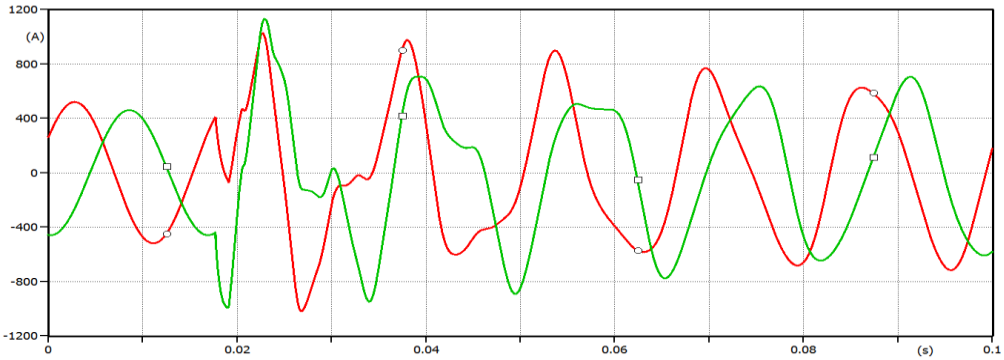

Figure 7.26(c) Current of un-Faulted phase at location Z when SLG fault occurs on phase A

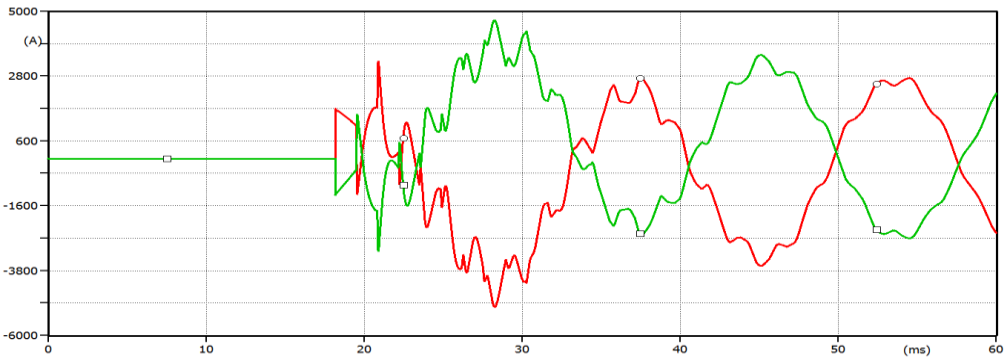

Figure 7.27(a) Currents of faulted phases A and B at location Z with DLG fault

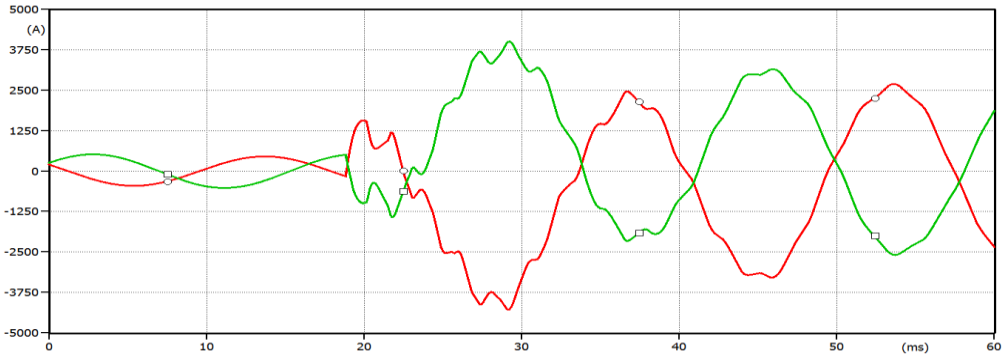

Figure7.27 (b) Currents of faulted phases A and B at location Z with DLG fault

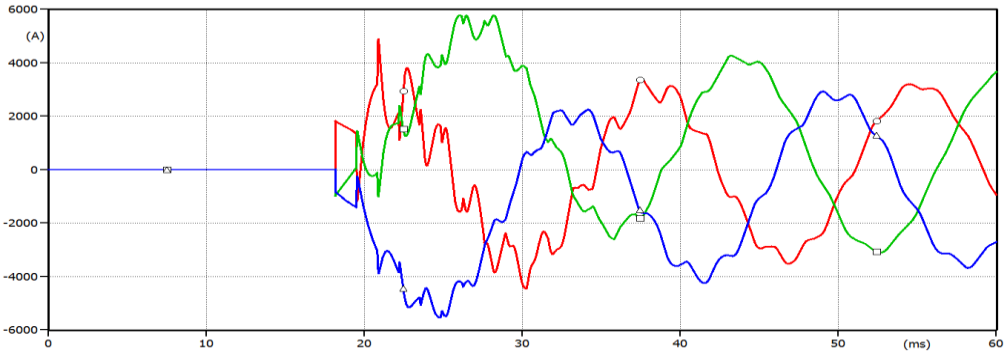

Figure 7.28(a) Three phase currents at fault location X when 3-phase SCF occur

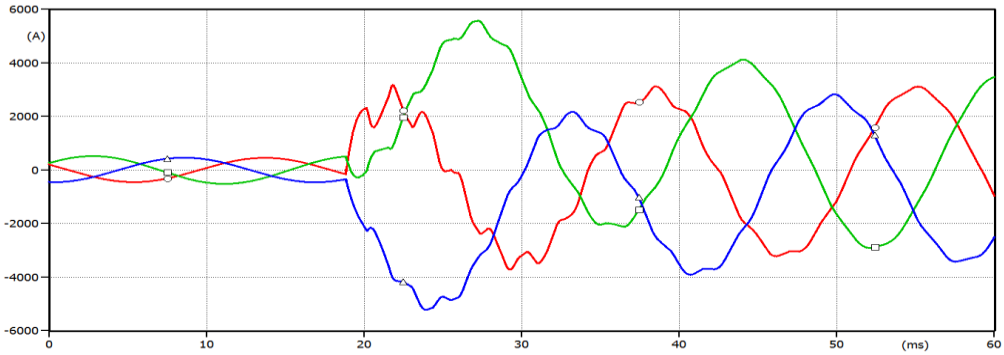

Figure 7.28(b) 3-phase currents at location Z when 3-phase SCF occurs

The maximum magnitude of faulted and un-faulted voltages at location Z and location X are given on Table 7.9. For different types of fault, waveforms of faulted and un-faulted phase voltages at both locations X and Z are given in Figures 7.29 to 7.31 respectively.

It has been observed that maximum wave distortion occurs in voltage waveform as compared to current waveform. Effect of SLG fault is most severe for voltages both at location X and Z as compare to other faults i.e. DLG fault and 3-phese SCF.

Table 7.9 Maximum magnitudes of voltages of faulted and un-faulted phases at locations X and Z for different types of fault on conventional power system

Type of Fault	**Location Z**		**Location X**	
	Maximum Magnitude of Voltages of Un-faulted Phases (kV)	Maximum Magnitude of Voltage of Faulted Phases (kV)	Maximum Magnitude of Voltage of Un-Faulted Phases (kV)	Maximum Magnitude of Voltage of Faulted Phases (kV)
LG Fault (Phase A)	1025-978.2	-	966.7-914.5	-
DLG Fault (Phase A and B)	617.1	-	682.9	-
Three Phase SCF	-	668.6-350.5-446.5	-	Drops to zero

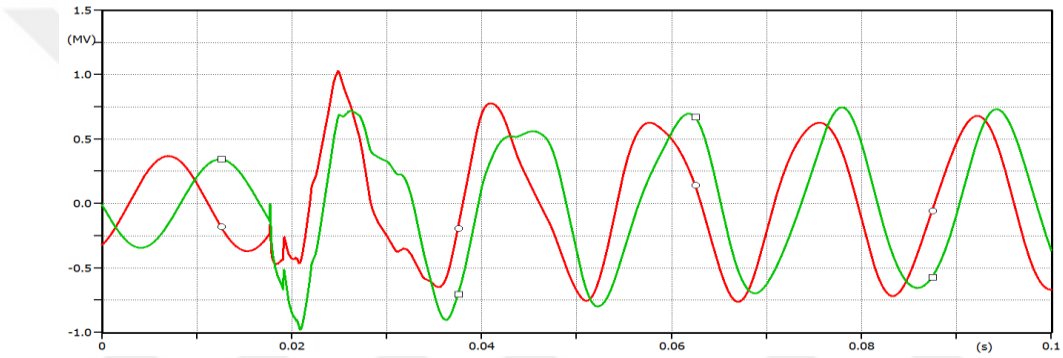

Figure 7.29(a) Voltages of un-faulted phases at location Z when SLG fault occurs on phase A

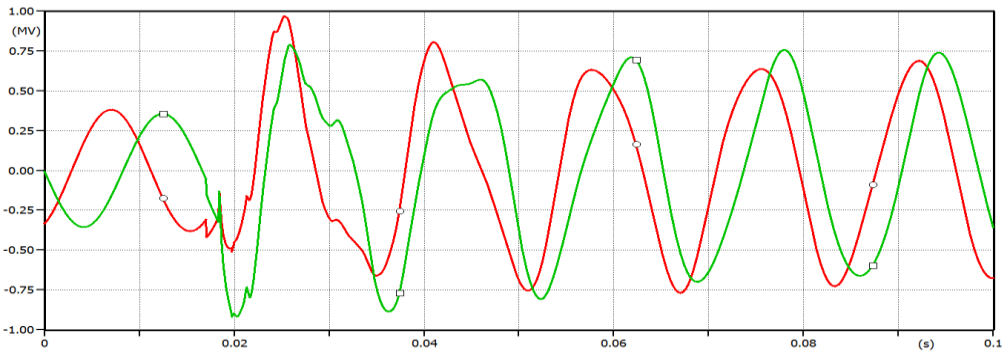

Figure 7.29(b) Voltages of un-faulted phases at fault location X when SLG fault occurs on phase A

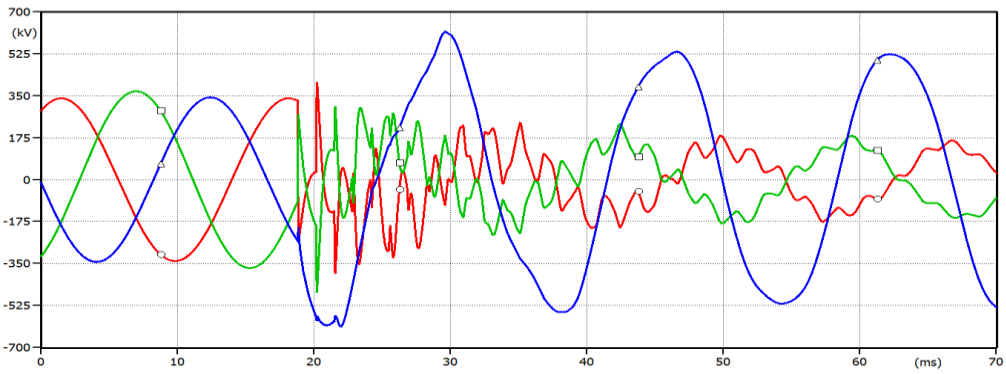

Figure 7.30(a) Three phase voltage at location Z when DLG fault occur on phases A and B

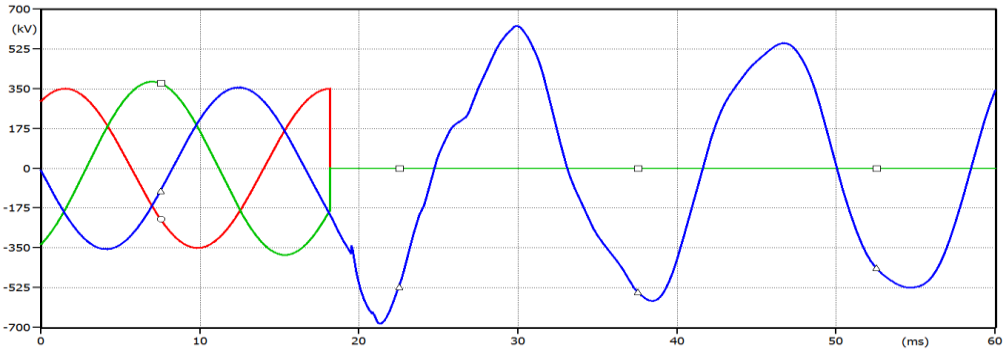

Figure 7.30(b) Voltage of un-faulted phase at X when DLG fault occur on phases A and B

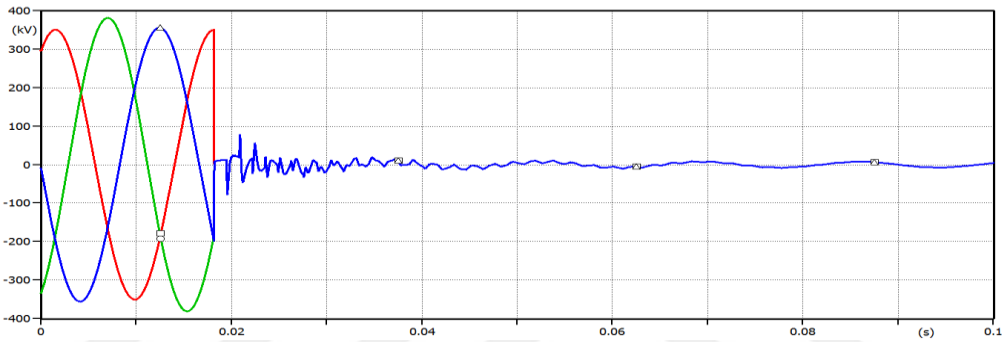

Figure 7.31(a) Three phase voltage at fault location X when 3-phase SCF occurs

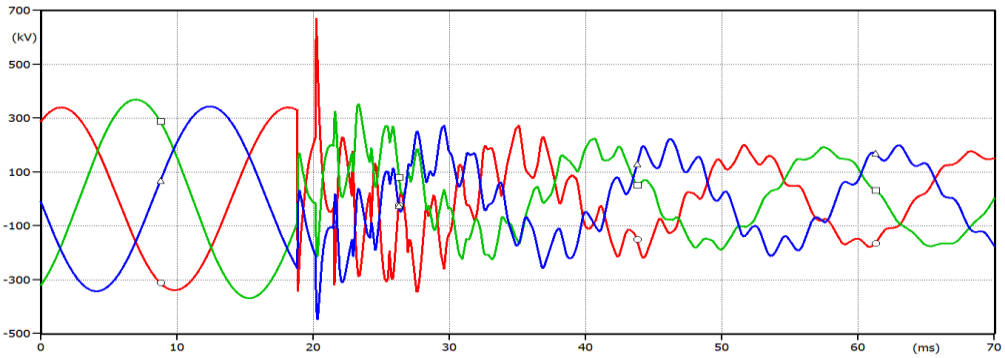

Figure 7.31(b) Three phase voltage at location Z when 3-phase SCF occurs

7.3 PV Hybrid Power Systems

The integrated photovoltaic (PV) power generator and the transformer T_2 specifications are given in Tables 7.10 and 7.11 respectively. P-V and V-I characteristic curves are shown in figure 7.32. It shows that at 900 W/m^2 irradiance and 30 ℃ ambient temperatures, open circuit voltage (V_{OC}) of PV is 36.24 V, short circuit current (I_{SC}) of PV is 8.09 and power at maximum power point (MPP) is 220.9 W.

Table 7.10 Data for photovoltaic (PV) generator

PHOTOVOLTAIC (PV) POWER SYSTEM	
Manufacturer	Moser Baer Solar
Model	MBPV-CAAP BB
Type	Poly-crystalline
V_{OC} (Volt)	36.24
I_{SC} (Amp)	8.09
V_{MP} (Volt)	29.61
I_{MP} (Amp)	7.46
Power (Watt)	220.9
Irradiance G (W/m^2)	900
Ambient Temperature (℃)	30
Fill Factor (%)	75.34
Efficiency (%)	12.8
NSER	47
NPAR	10000
Where, NSER is number of individual PV modules in each string NPAR is the number of strings in the entire array	

Table 7.11 Data of Hybrid Transformers T_2

Hybrid Transformer T_2	
L-L Voltage(kV)	0.44/400 (Δ-Y)
Power (MVA)	100
Test Frequency	60 Hz
Type of Core	3 leg stacked
Number of Windings	2
C_{P-G}	19.82 nF
C_{S-G}	4.532 nF
C_m	1.942 nF

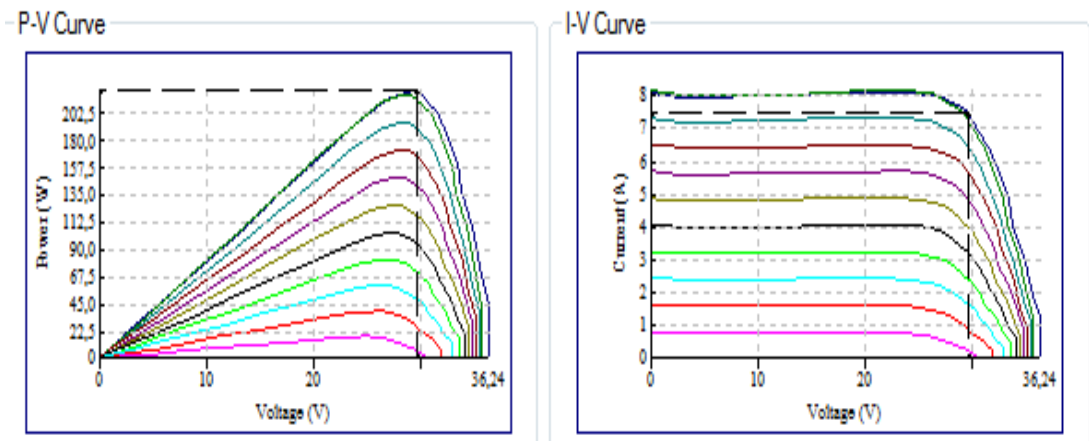

Figure 7.32 P-V & V-I characteristic curves of PV

Integrated PV generator connected with conventional power system. 100 MW PV generator is connected at mid-point of 100 km TL. In this case PV module runs at irradiance of 900 W/m^2 and a temperature of 30 ℃ as shown in Figure 7.33.

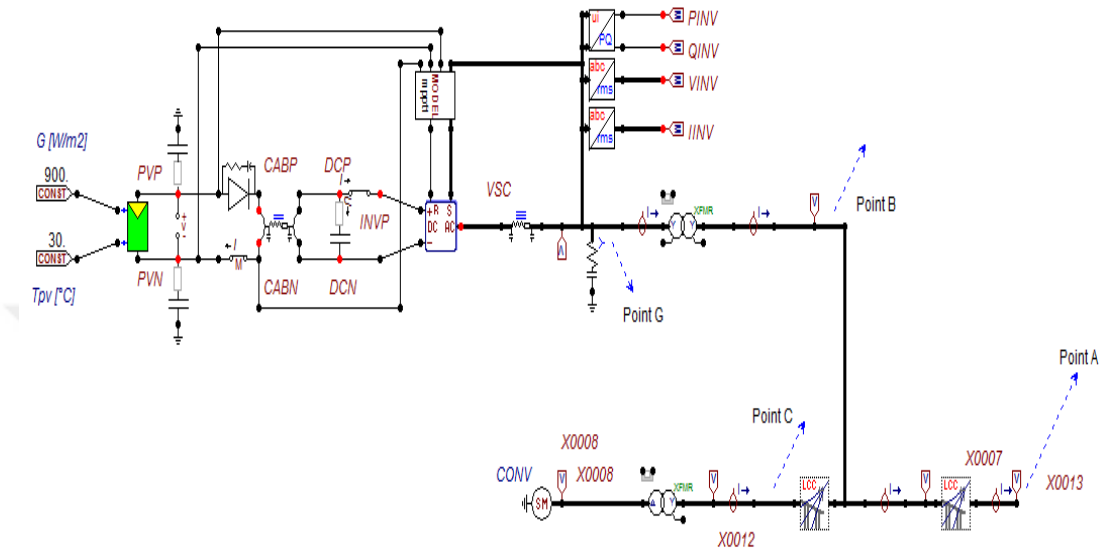

Figure 7.33 Hybrid power system (with PV only) at no-load

7.3.1 Effect of 3-phase SCF at different location on PV hybrid system

Here, we analysis the effect of 3-phase SCF at different location on PV hybrid system, It means 3-phase SCF occurs firstly at location A, B and then C respectively. System configuration is shown in Figure 7.34. Waveforms for 3-phase SCF at different locations on PV hybrid system are shown in Figures 7.35 to 7.37 respectively.

It is observed from the results that as fault come closer to source point (location C) from end point (location A), magnitude of 3-phase SCF currents increases, so 3-phase SCF is most severe near to source i.e. location C and it's least severe at end point near to load i.e. location A. Wave attenuation is higher when fault occurs at location C and its least at location B. Magnitude of 3-phase SCF currents increases from 5.318 kA to 10.230 kA as shown in Table 7.12. Here red colour represents phase A, green colour phase B and blue colour phase C in all waveforms.

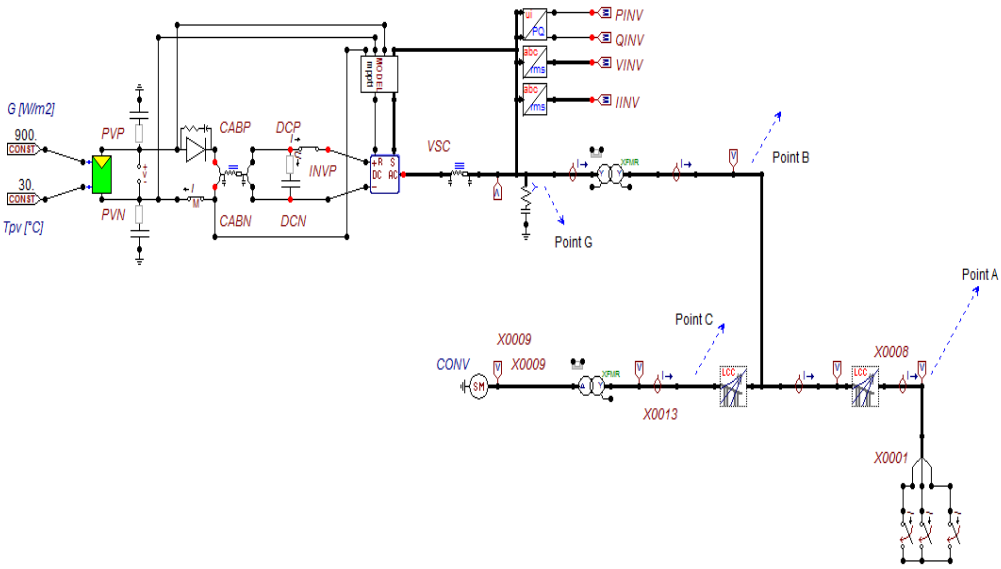

Figure 7.34 Configuration of PV hybrid system when 3-phase SCF occurs at location A

Table 7.12 Maximum magnitude of 3-Phase SCF currents at different locations on PV hybrid system

Fault Location	Maximum Magnitude of 3-Phase SCF Currents at Fault Point (A)		
	Phase A	Phase B	Phase C
3-phase SCF occur at Point A	5318	5107	5175
3-phase SCF occur at Point B	6592	6894	6903
3-phase SCF occur at Point C	8622	8320	10230

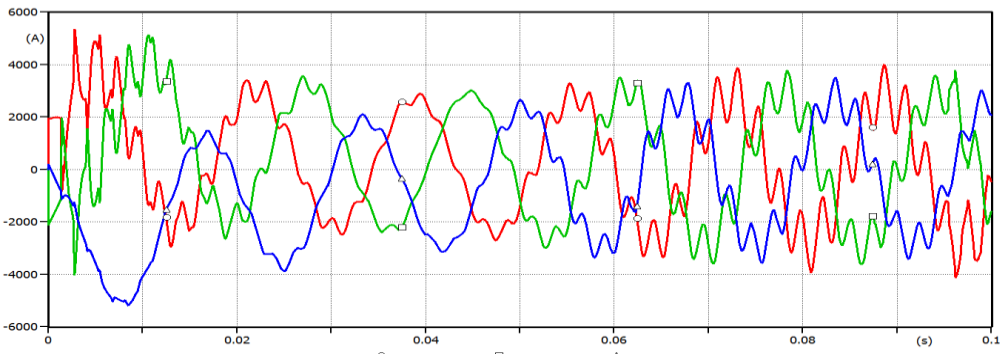

Figure 7.35 Fault current at fault location, when 3-phase SCF occurs at location A

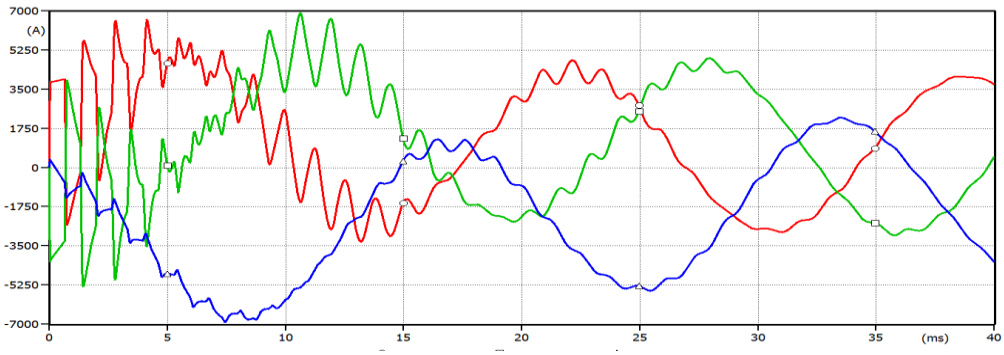

Figure 7.36 Fault current at fault location, when 3-phase SCF occurs at location B

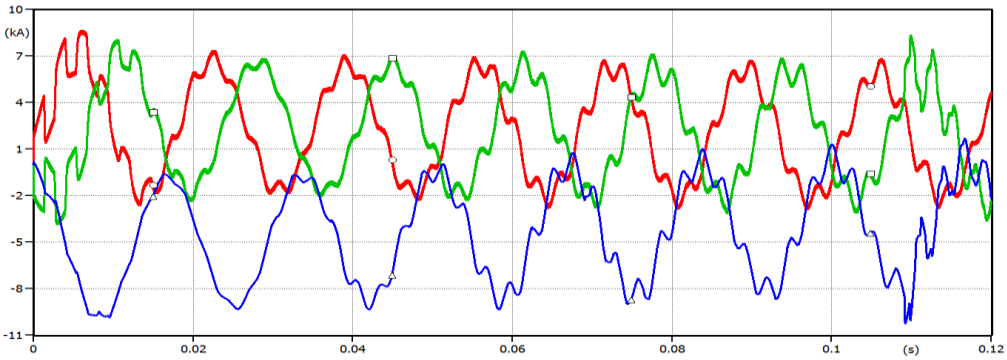

Figure 7.37 Fault current at fault location, when 3-phase SCF occurs at location C

7.3.2 Effect of 3-phase SCF on current at PV side i.e. Bus G

3-phase SCF occurs at different location on PV hybrid power system, it also causes an effect on currents flowing through PV module i.e. point G. As 3-phase SCF come closer to generation system its effects on PV module increases as shown in Figures from 7.38 to 7.40 respectively. It is observed from results that current flowing through PV increases as it come closer to generation point i.e. point C as shown on Table 7.13. Wave attenuation is higher at location G when short circuit fault occurs at location A and least at location B as shown in Figures 7.38 to 7.40 respectively. Table 7.13 shows the effect of 3-phase SCF at location G and maximum magnitude of currents flow through PV i.e. from 1312 kA to 2248 kA, when 3-phase SCF occur at different locations A to location C . Here red colour represents phase A, green colour phase B and blue colour phase C in all waveforms.

Table 7.13 Effect of 3-Phase SCF at location G

Fault Location	**Maximum Magnitude of 3-Phase SCF Currents at Point G (kA)**		
	Phase A	Phase B	Phase C
3-phase SC F occur at Point A	1312	1080	940.8
3-phase SCF occur at Point B	699.9	698	723.1
3-phase SCF occur at Point C	1028	1919	2248

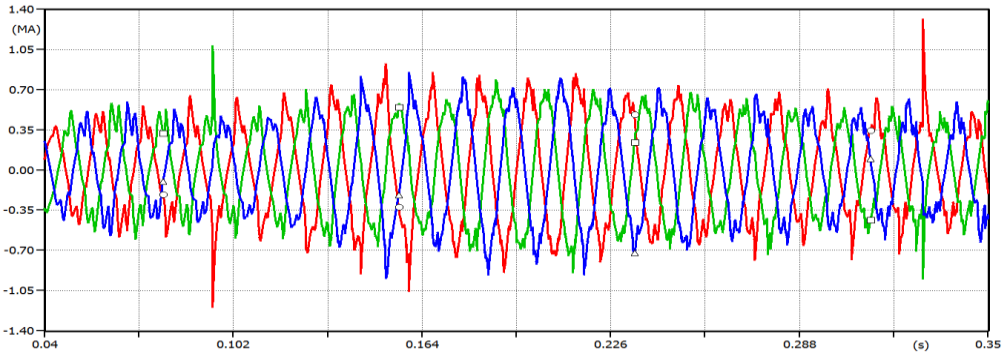

Figure 7.38 Effect of 3-phase SCF at location G on PV terminal current at ac terminal when fault occurs at location A

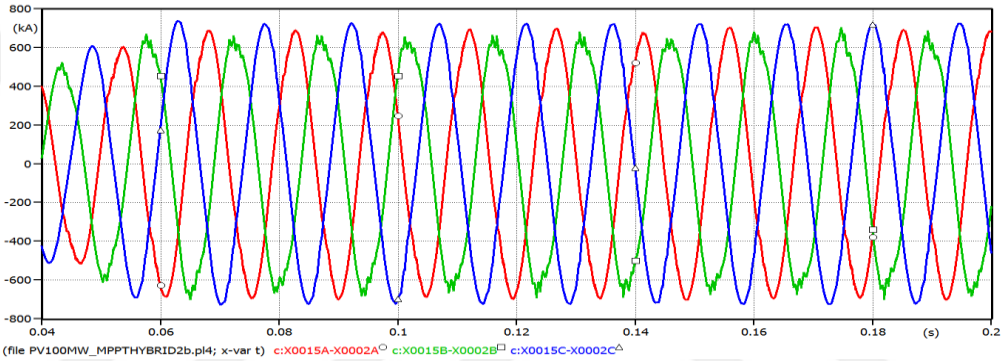

Figure 7.39 Effect of 3-phase SCF at location G on PV terminal current at ac terminal when fault occurs at location B

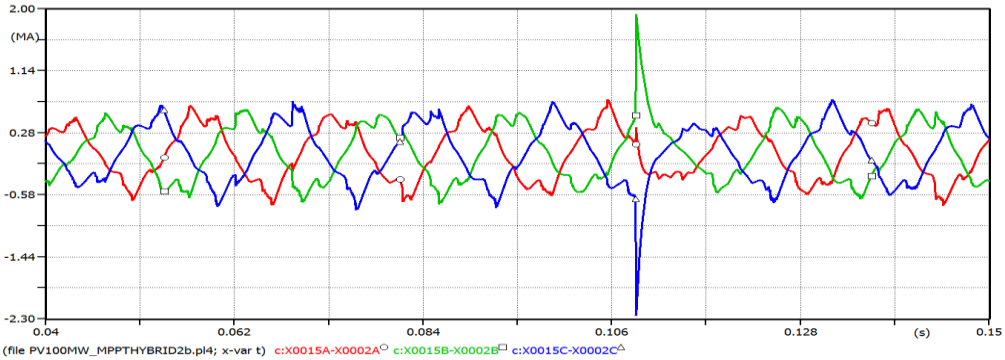

Figure 7.40 Effect of 3-phase SCF at location G on PV terminal current at ac terminal when fault occurs at location C

7.3.3 Effect of fault resistance on PV hybrid system

A LG fault is considered to take place on phase A at the point A on the line as shown in Figure 7.41. SLG fault occurs when voltage of phase A is at peak value i.e. at 18.14 msec. The length of transmission line between point A and C (at 400 kV) is 200 km. The waveforms of the fault current at location C and A are given in Figures 7.42 to

7.48. For various values of fault resistance, maximum magnitude of fault currents at location C and at the fault location A is given on Table 7.14.

The maximum magnitude of fault currents at the location C and at fault location A decreases as the fault resistance increase. Fault current at location C on hybrid system (with PV) is decreases from 2.203 kA at 1Ω fault resistance to 1.627 kA at 100 Ω fault resistances. Fault current at fault location A is decreases from 2.093 kA at 1Ω fault resistance to 1.276 kA at 100 Ω fault resistances. Comparison between conventional and hybrid system given on Table 7.14, it is observed that fault currents on conventional system is less as compare to hybrid system. It means PV has considerable effects on conventional system, when effect of fault resistance is studied. Transients in the fault current waveform are higher at lower value of the fault resistance as compared to that of higher value.

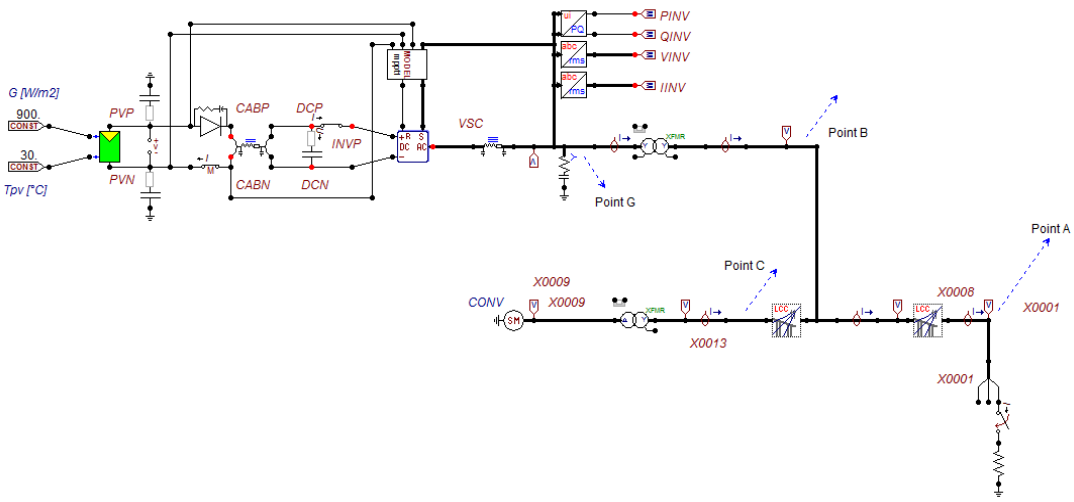

Figure 7.41 Configuration of studied PV hybrid power system: when fault resistance varies from 1Ω to 100Ω with LG fault occurs on phase A at location A

Table 7.14 Effect of fault resistance on fault current at location C and fault location A, on PV hybrid power system

Fault Resistance (Ω)	**Maximum Magnitude of Fault Current at Point C (A)**		**Maximum Magnitude of Fault Current at Fault Location A (A)**	
	Conventional Power System Alone	PV Hybrid System	Conventional Power System Alone	PV Hybrid System
1	2136	2203	1742	2093
5	2098	2166	1699	2004
10	2051	2124	1649	1905
20	1966	2045	1561	1742
30	1889	1974	1486	1618
50	1753	1853	1365	1448
100	1499	1627	1159	1276

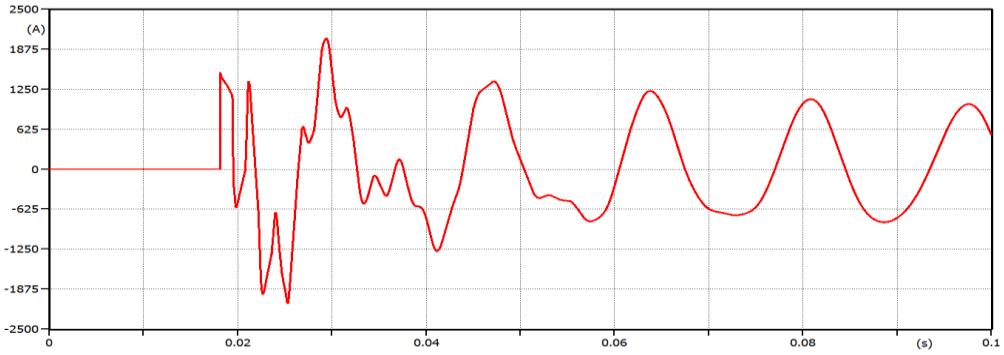

Figure 7.42(a) Fault Current at fault location A when fault resistance is 1Ω on PV hybrid system

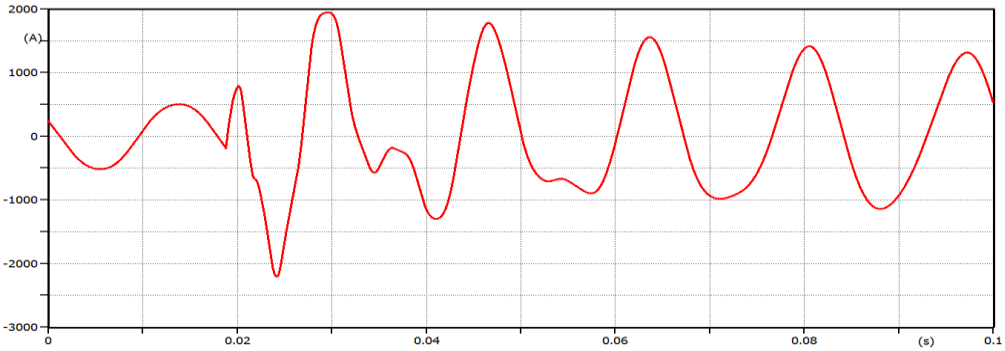

Figure 7.42(b) Fault Current at location C when fault resistance 1Ω on PV hybrid system

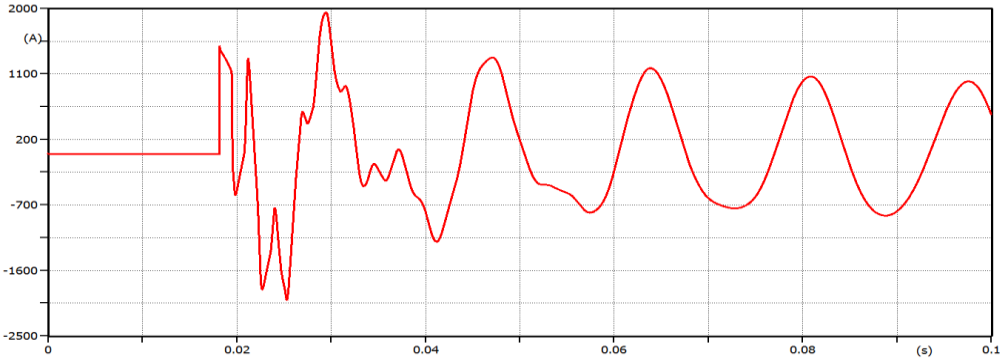

Figure 7.43(a) Fault Current at fault location A when fault resistance is 5Ω on PV hybrid system

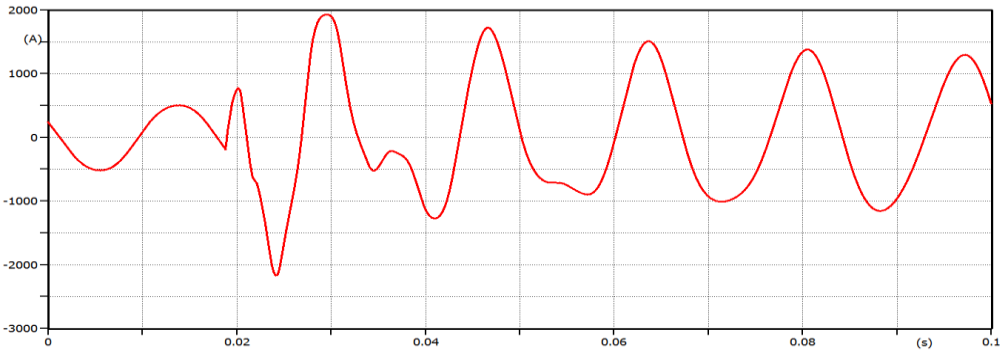

Figure 7.43(b) Fault Current at location C when fault resistance is 5Ω on PV hybrid system

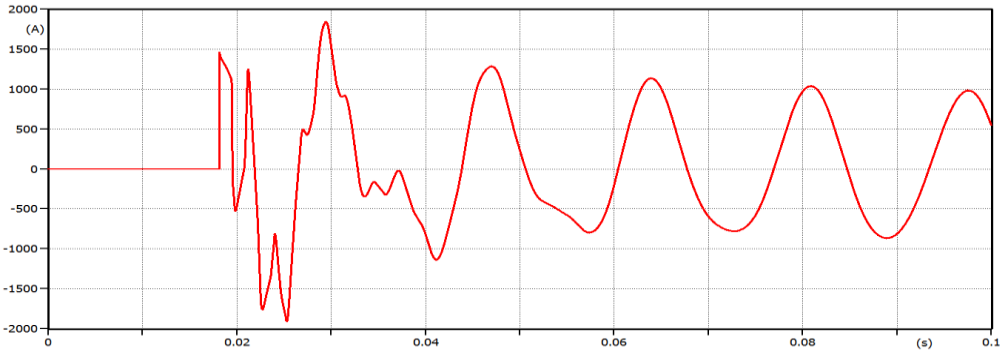

Figure 7.44(a) Fault Current at fault location A when fault resistance is 10Ω on PV hybrid system

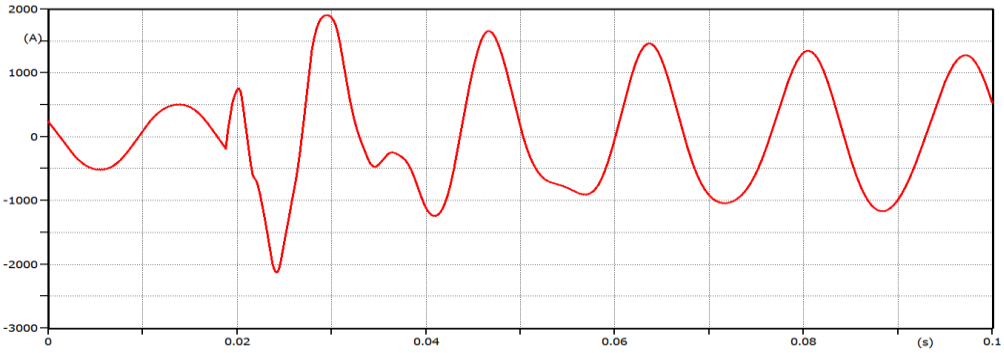

Figure 7.44(b) Fault Current at location C when fault resistance is 10Ω on PV hybrid system

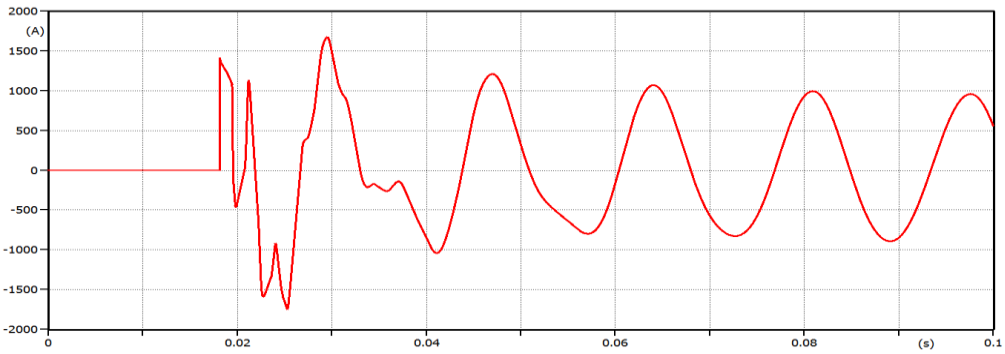

Figure 7.45(a) Fault Current at fault location A when fault resistance is 20Ω on PV hybrid system

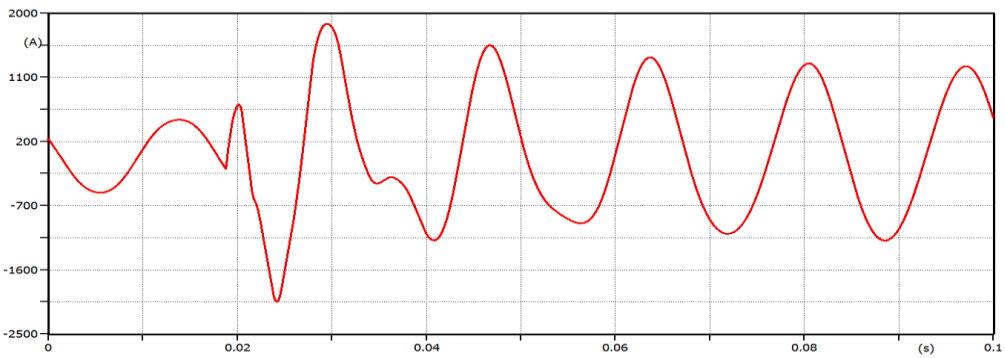

Figure 7.45(b) Fault Current at location C when fault resistance is 20Ω on PV hybrid system

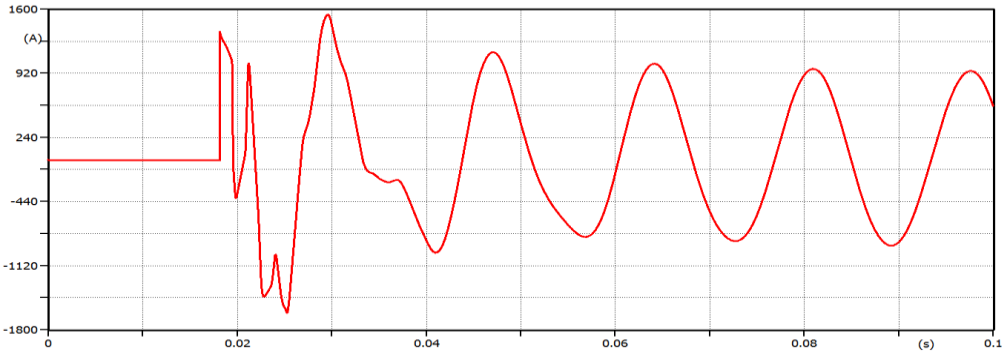

Figure 7.46(a) Fault Current at fault location A when fault resistance is 30Ω on PV hybrid system

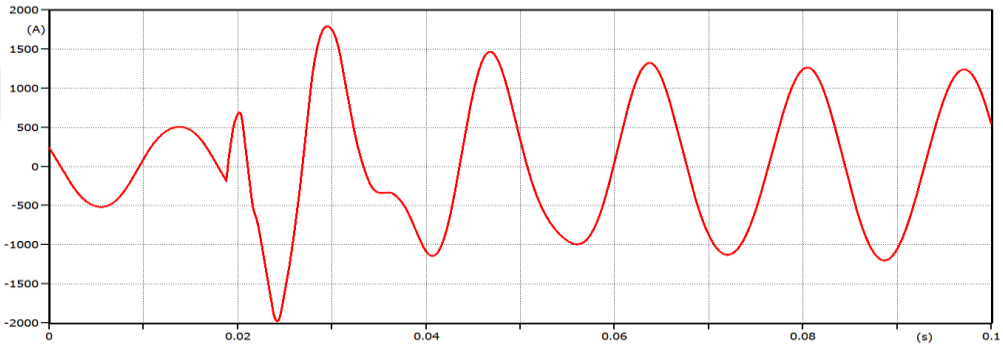

Figure 7.46(b) Fault Current at location C when fault resistance is 30Ω on PV hybrid system

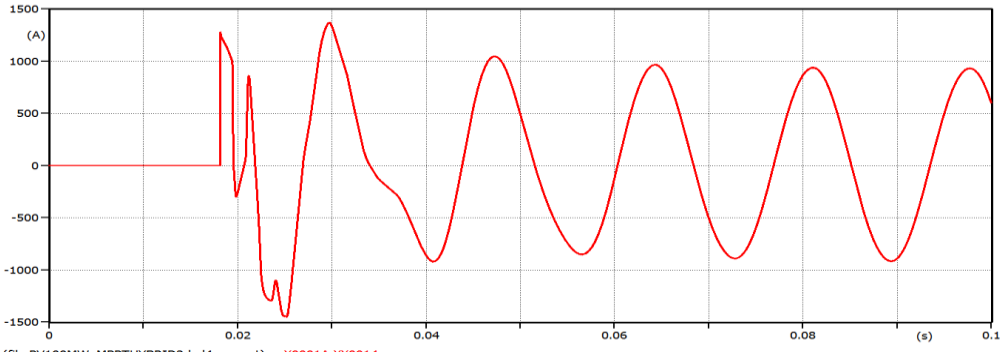

Figure 7.47(a) Fault Current at fault location A when fault resistance is 50Ω on PV hybrid system

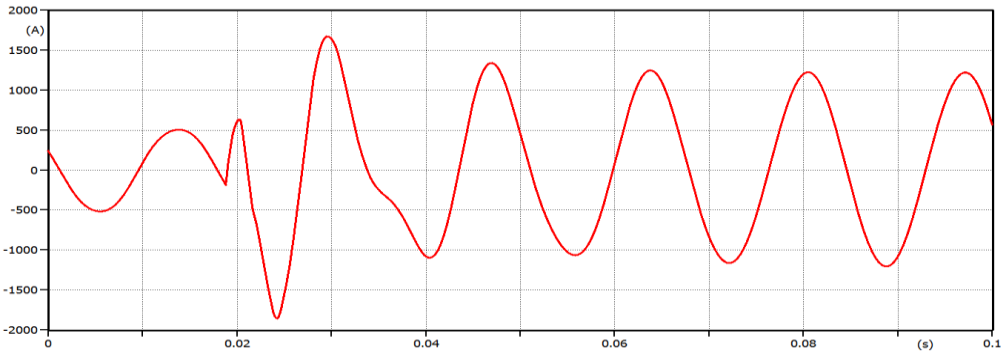

Figure 7.47(b) Fault Current at location C when fault resistance is 50Ω on PV hybrid system

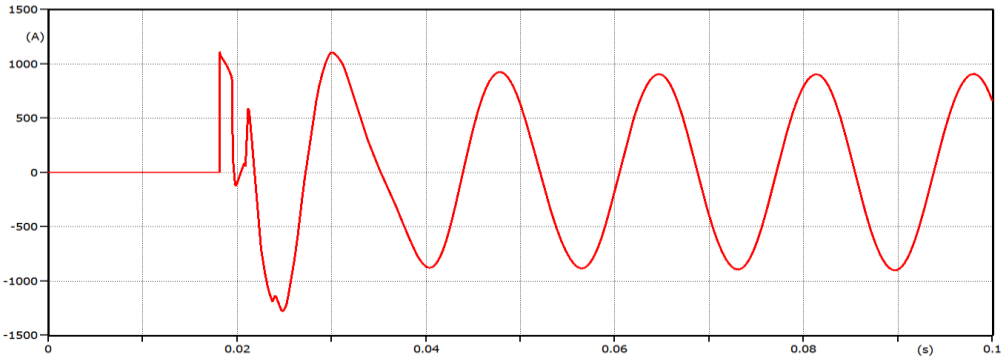

Figure 7.48(a) Fault Current at fault location A when fault resistance is 100Ω on PV hybrid system

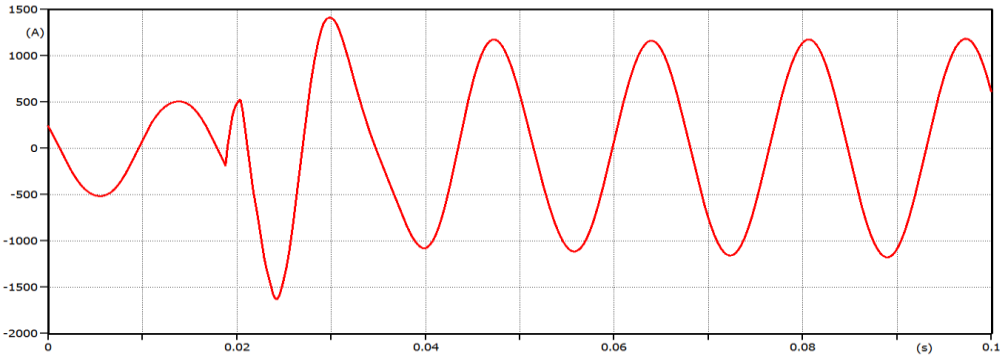

Figure 7.48(b) Fault Current at location C when fault resistance is 100Ω on PV hybrid system

7.3.4 Effect of PV system and line length on fault current on PV hybrid system

The configuration of studied PV hybrid system is as shown in Figure 7.49. SLG fault takes place on phase A at the end of line. Fault occurs on phase A, when the phase voltage is at the peak value i.e. 18.12 msec at fault point but at sending end it takes some travel time. The faulted phase currents at location C and fault location A, during fault are computed for various line lengths from 100 km to 260 km and plotted to obtain faulted phase current waveforms both at location A and location C are shown in Figures 7.50 to 7.55 on hybrid power system (with PV). The Maximum values of the faulted phase current at sending end i.e. location C and at fault location A for different line lengths are shown on Table 7.15.

The simulation result shows that the maximum magnitude of the currents at location C and fault point increases as the line length increases due to capacitance of transmission line, also ripples along the line attenuate as the line length increases. Fault current at location C increases 1.349 kA to 3.188 kA and fault current at fault location A increases from 1.689 kA to 2.631 kA as shown on Table 7.15 so, effect of PV on fault

currents both at location C and fault location A is much more as compare to conventional system alone. It is also observed that as line length increases travel time of fault current at location C is increasing and harmonics frequency is decreasing.

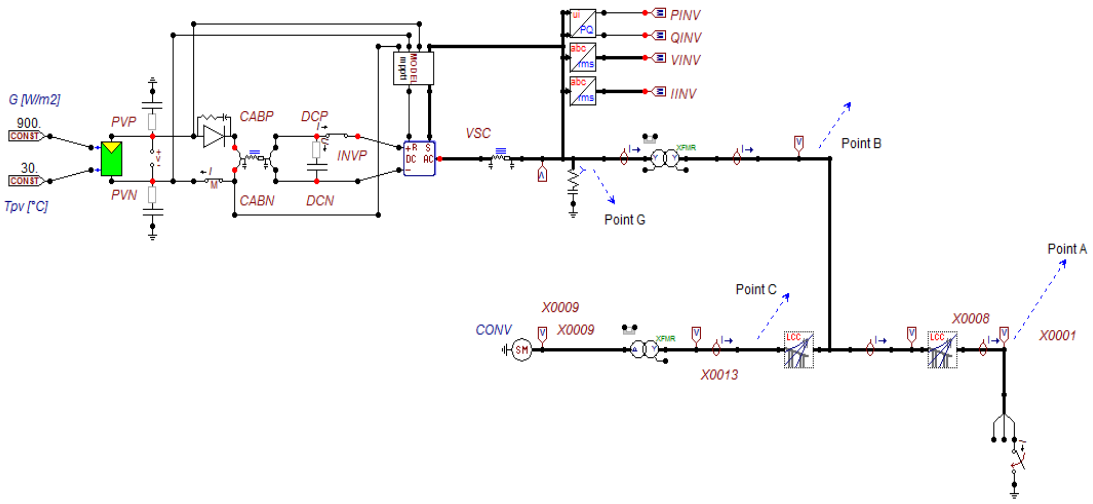

Figure 7.49 Configuration of studied PV hybrid system: when line length varies from 100 km to 260 Km and Effect of line length on fault current

Table 7.15 Maximum magnitude of faulted phase current against line length at location C and fault location A and effects of PV on it

Line Length (km)	**Fault Current at Location C (A)**		**Fault Current at Fault Location A (A)**	
	Conventional system Alone	PV Hybrid system	Conventional System Alone	PV Hybrid System
100	1014	1349	1483	1689
200	2146	2212	1754	2117
220	2307	2381	1814	2319
240	2439	2807	2005	2537
260	2541	3188	2205	2631

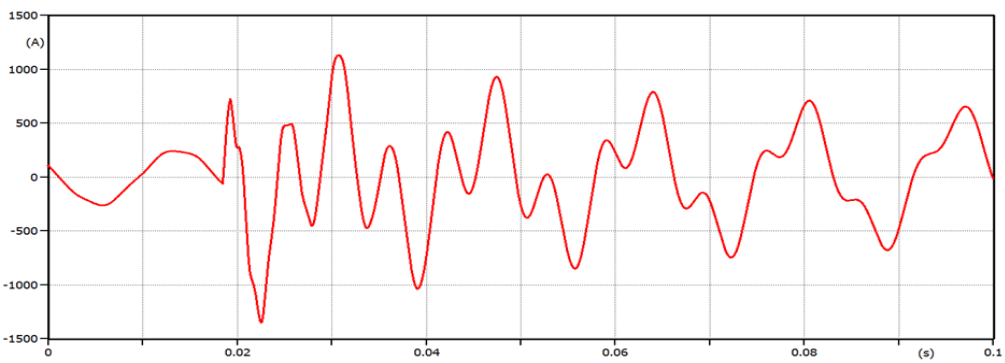

Figure 7.50(a) Fault Current at location C on PV hybrid system: when line length is 100 km

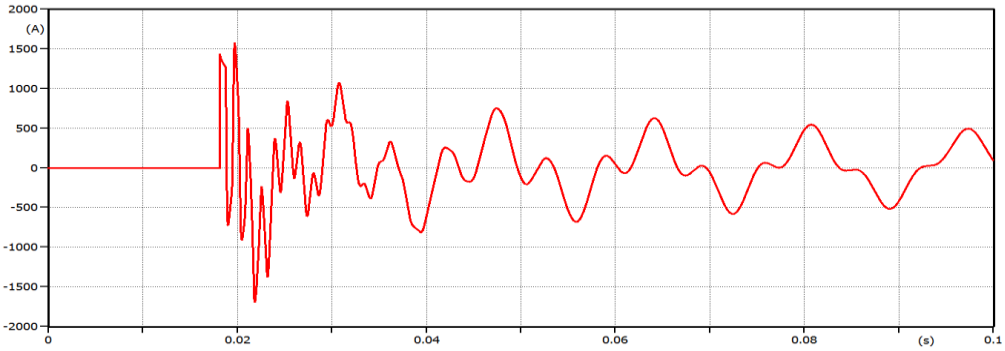

Figure 7.50(b) Fault Current at fault location An on PV hybrid system: when line length is 100 km

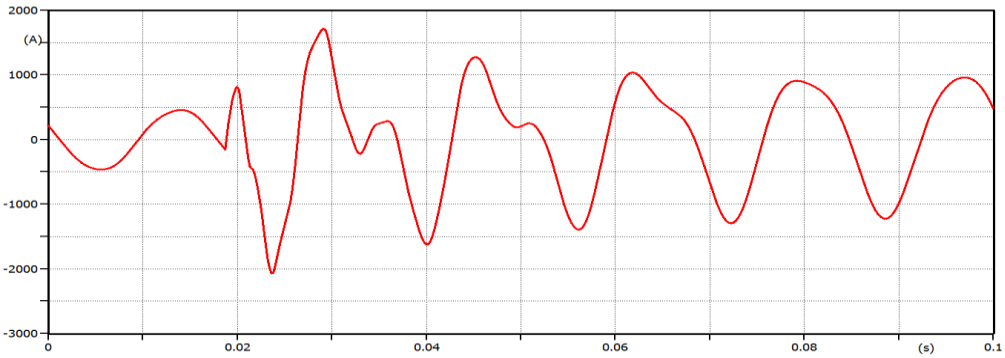

Figure 7.51(a) Fault Current at location C on PV hybrid system: when line length is 180 km

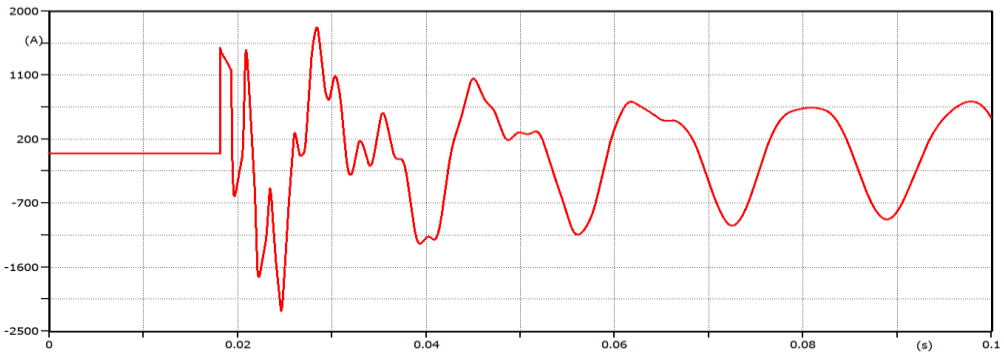

Figure 7.51(b) Fault Current at fault location A on PV hybrid system: when line length is 180 km

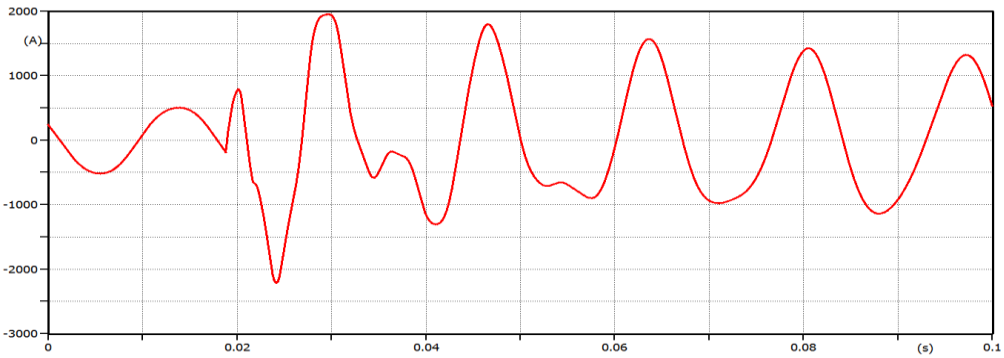

Figure 7.52(a) Fault Current at location C on PV hybrid system: when line length is 200 km

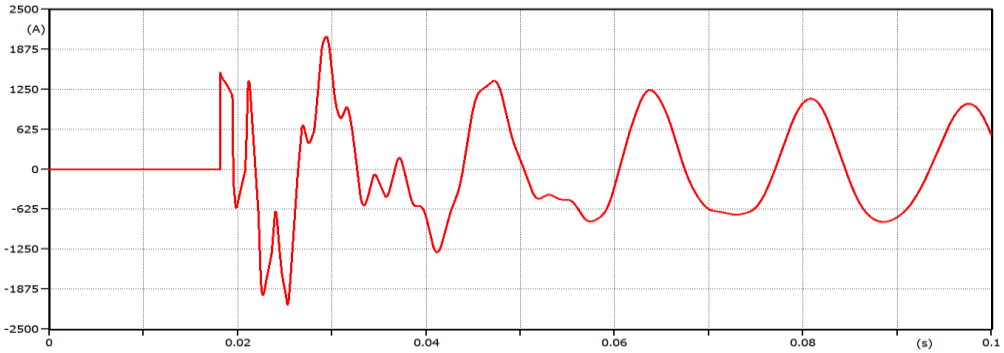

Figure 7.52(b) Fault Current at fault location A on PV hybrid system: when line length is 200 km

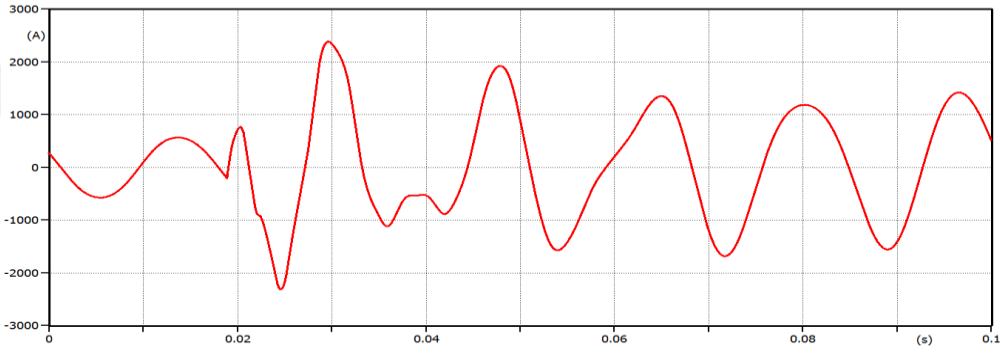

Figure 7.53(a) Fault Current at location C on PV hybrid system: when line length is 220 km

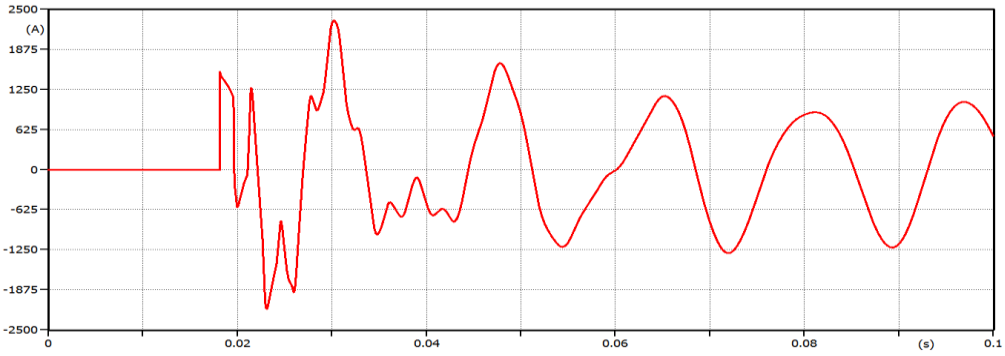

Figure 7.53(b) Fault Current at fault location A, on PV hybrid system: when line length is 220 km

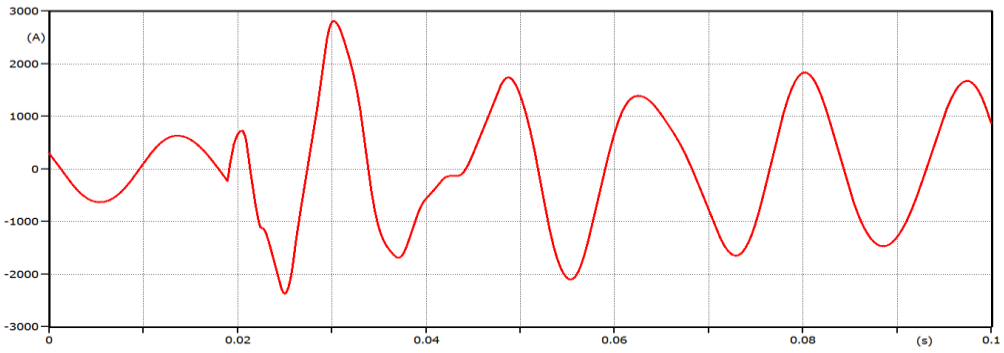

Figure 7.54(a) Fault Current at location C on PV hybrid system: when line length is 240 km

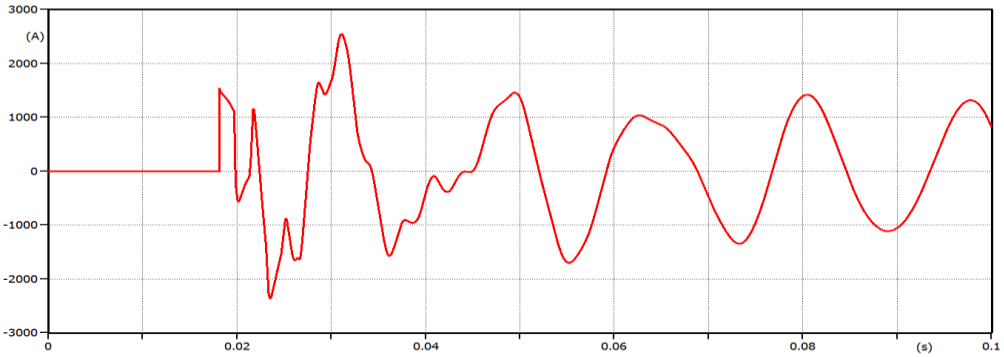

Figure 7.54(b) Fault Current at fault location A, on PV hybrid system: when line length is 240 km

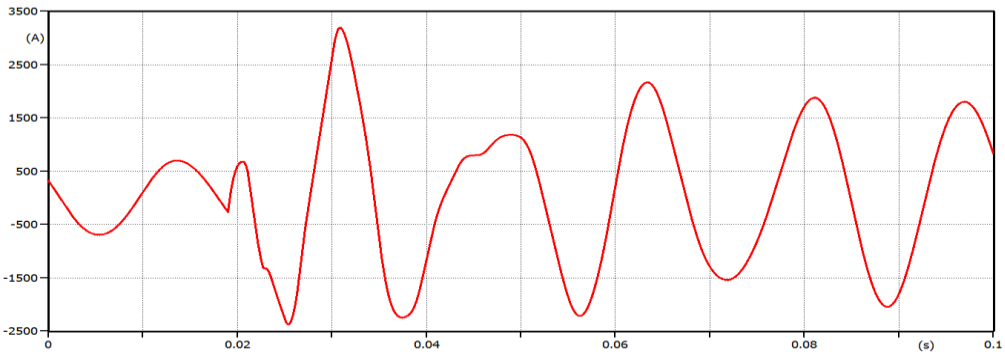

Figure 7.55(a) Fault Current at location C on PV hybrid system: when line length is 260 km

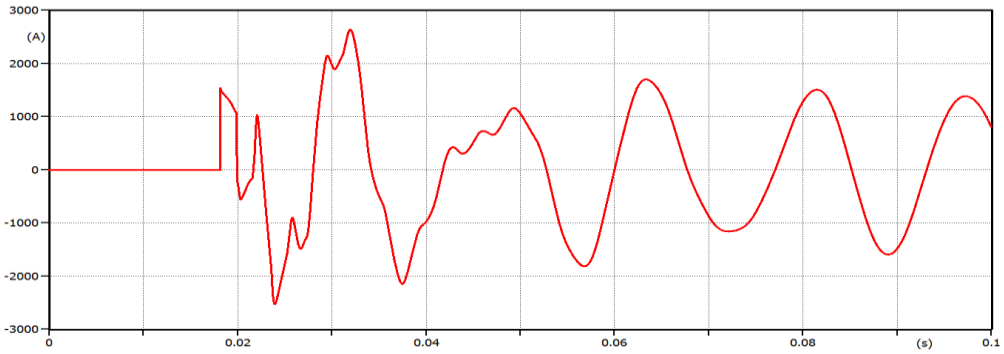

Figure 7.55(b) Fault Current at fault location A, on PV hybrid system: when line length is 260 km

7.4 Wind Hybrid Power System

The integrated wind generator and the transformer T_3 specifications are given in Tables 7.16 and 7.17 respectively. The integrated wind generator is connected with conventional power system. 100 MW wind generator is connected at mid-point of 200 km transmission line at a voltage of 400 kV as given in Figure 7.56. The wind speed is maintained constant at 12 m/s. In modern wind energy system, the most popular wind power generator used is Double Fed Induction Generator (DFIG) because of its

capability to operate at different variable speed ranges. It is observed from Figure 7.56 that voltages at bas-bar C is greater than voltages at bas-bar A due to the effect of capacitance of transmission line i.e. Ferranti effect at no-load.

Table 7.16 Data for Wind Generator

Wind Generator (IM56A)	
L-L Voltage(kV)	34.5
Power (MW)	100
Rated Frequency	60 Hz
Poles	2
Initial Slip	-0.3889
R_S (pu)	0.037
L_S (pu)	0.07
R_R (pu)	0.018
L_R (pu)	0.03

Table 7.17 Data of Hybrid Transformers T_3

Hybrid Transformer T_3	
L-L Voltage(kV)	34.5/400 (Δ-Y)
Power (MVA)	100
Test Frequency	60 Hz
Type of Core	3 leg stacked
Number of Windings	2
C_{P-G}	27.877nF
C_{S-G}	6.223 nF
C_m	2.666 nF

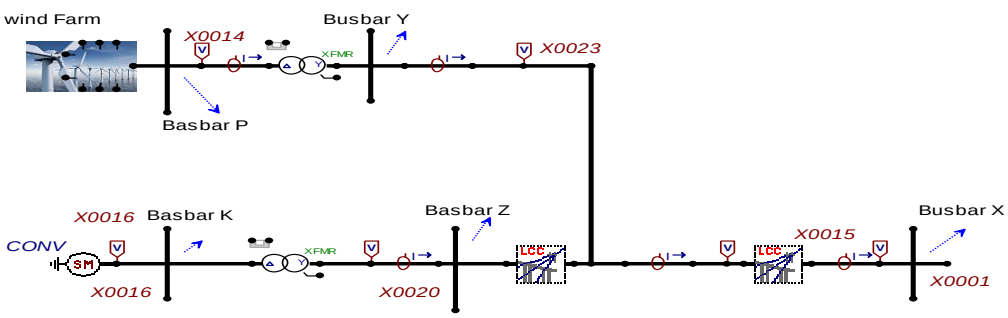

Figure 7.56 Wind hybrid power system at no-load

7.4.1 Effect of 3-phase SCF at different location on wind hybrid system

This section analysed the effect of 3-phase SCF at different location on Wind hybrid system. 3-phase SCF occurs at different location on Wind hybrid power system i.e. at bus X, Y and Z respectively. Configuration of studied Wind hybrid system is

shown in Figure 7.57. Waveforms of currents for 3-phase SCF at bus X, Y and Z are shown in Figures 7.58 to 7.60 respectively.

It is observed from the results that as fault come closer to source point (bus Z) from end point (bus X), magnitude of 3-phase SCF currents increases, so 3-phase SCF is most severe near to source i.e. bus Z and it's least severe at end point near to load i.e. bus X. Wave attenuation is higher when fault occurs at bus Y due to wind generator is interconnected at bus Y and its least at bus Z. Magnitude of 3-phase SCF currents increases from 6.08 kA to 11.03 kA as shown in Table 7.18.

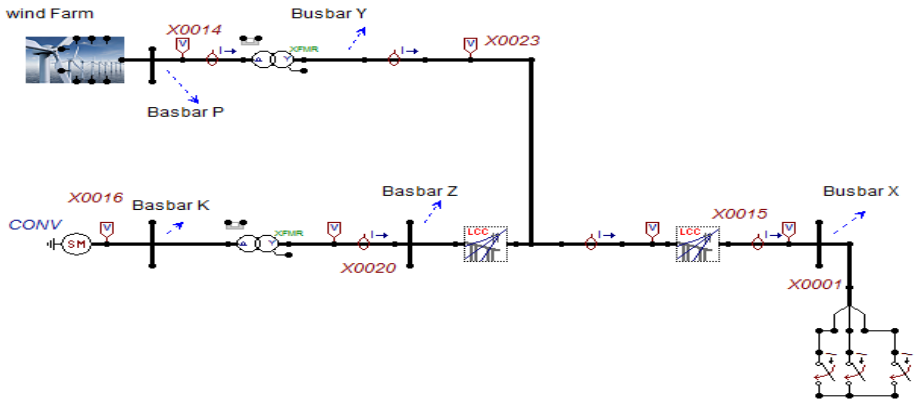

Figure 7.57 Configuration of Wind hybrid systems when 3-phase SCF occurs at bus X

Table 7.18 Maximum magnitude of 3-Phase SCF currents when fault occurs at different location on Wind hybrid power system

Fault Location	**Maximum Magnitude of 3-Phase SCF Currents at Fault Location (A)**		
	Phase A	Phase B	Phase C
3-phase SCF occur at bus X	6008	6060	5252
3-phase SCF occur at bus Y	8070	8255	7439
3-phase SCF occur at bus Z	11030	9840	8371

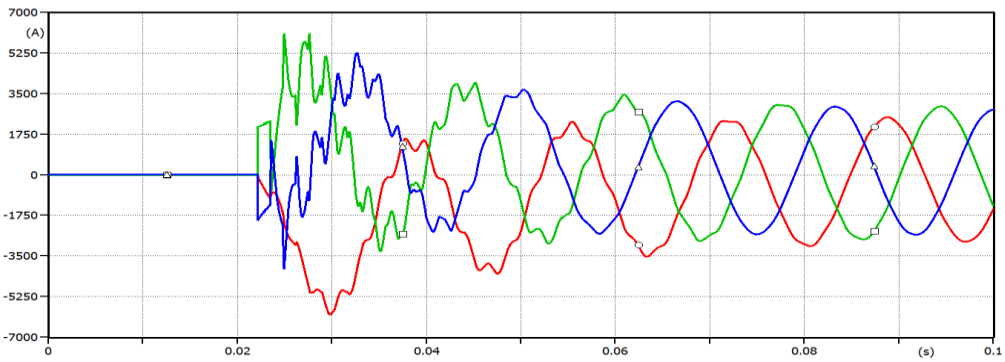

Figure 7.58 Fault current at fault location, when 3-phase SCF occur at bus X on Wind hybrid system

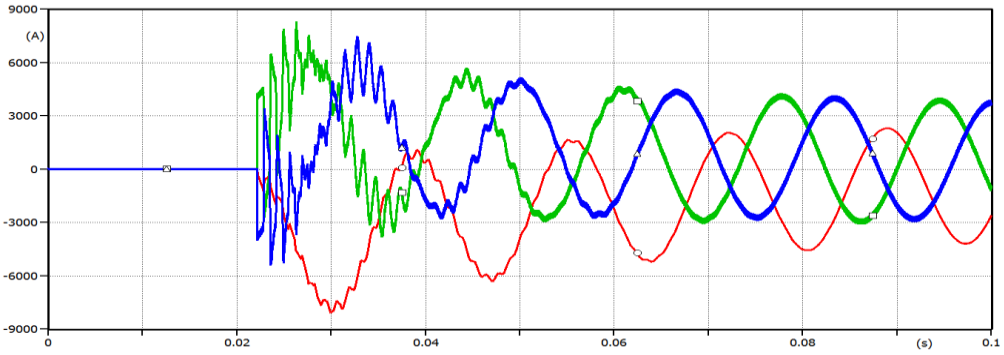

Figure 7.59 Fault current at fault location, when 3-phase SCF occur at bus Y on Wind hybrid system

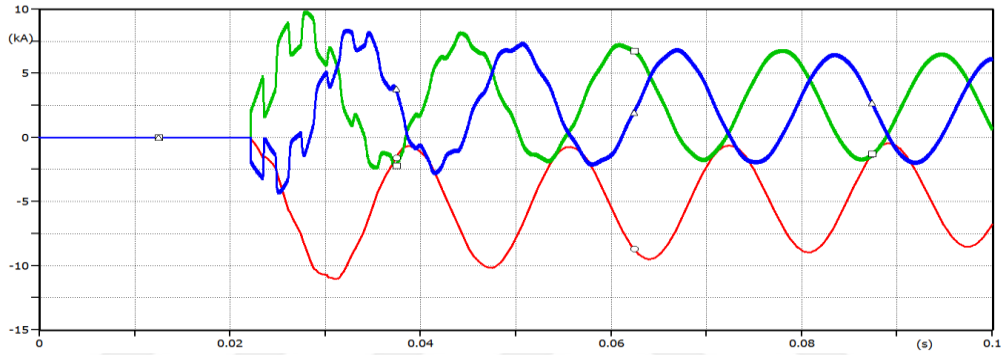

Figure 7.60 Fault current at fault location, when 3-phase SCF occur at bus Z on Wind hybrid system

7.4.2 Effect of 3-phase SCF on current at wind generator side (bus P)

3-phase SCF occurs at different location on wind hybrid power system, it also causes an effect on currents flowing through Wind generator i.e. at bus P. It is analysed from the results that effect of 3-phase SCF is high at interconnection point i.e. bus-bar Y, where wind generator is connected to 400 kV transmission line at conventional power system as shown on Table 7.19. It is also observed from waveforms that wave attenuation is higher when 3-phase SCF takes place at bus X i.e. near to end point and least at bus Y as shown in Figures from 7.61 to 7.63 respectively.

Table 7.19 shows the effect of 3-phase SCF at bus P and maximum magnitude of fault currents flow through Wind generator i.e. bus P. Fault current increases from 8.371 kA to 11.85 kA, when 3-phase SCF occur at different locations X to location Z.

Table 7.19 Effect of 3-phase SCF at bus P on wind hybrid power system

Fault Location	**Maximum Magnitude of 3-Phase SCF Currents at Bus P (kA)**		
	Phase A	Phase B	Phase C
3-phase SCF occur at bus A	8.371	4.204	7.797
3-phase SCF occur at bus B	11.85	5.407	11.24
3-phase SCF occur at bus C	11.24	5.760	10.59

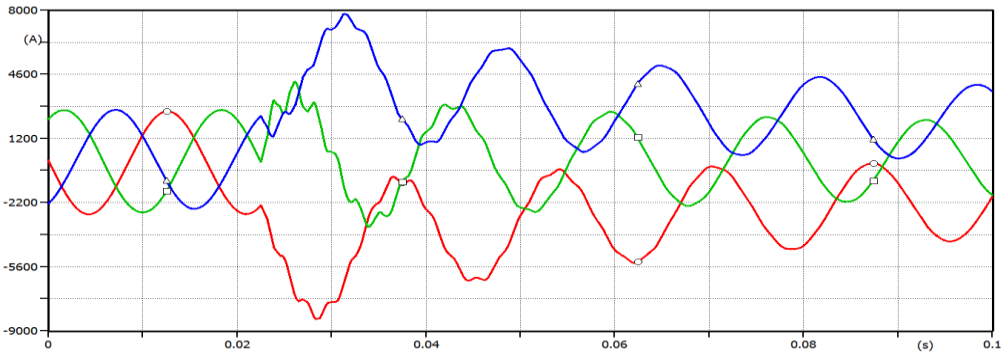

Figure 7.61 Effect of 3-phase SCF at bus P on wind generator terminal 34.5 kV side when fault occurs at bus X

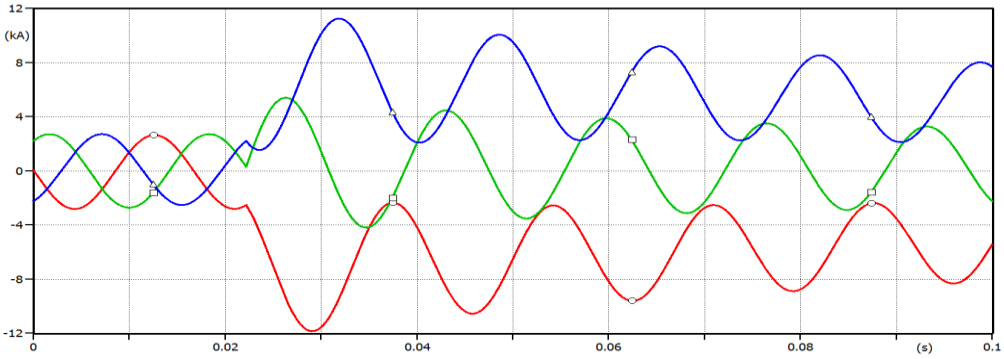

Figure 7.62 Effect of 3-phase SCF at bus P on wind generator terminal 34.5 kV side when fault occurs at bus Y

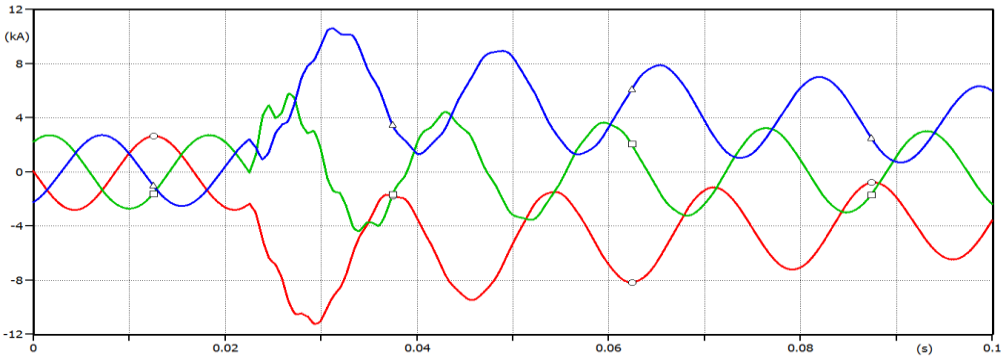

Figure 7.63 Effect of 3-phase SCF at bus P on wind generator terminal 34.5 kV side when fault occurs at bus Z

Effect of 3-phase SCF on voltages at bus K and P are also observed. It is analysed that voltages of 3-phases is reduced to low value due to SCF. At bus K voltage is reduced from 21.86 kV to 10.29 kV as shown on Table 7.20. It is observed that effect of SCF on voltages at bus K is least when fault occurs at bus X i.e. far away from generation point and highest near the generation point. It is also observed that wave attenuation is highest at when fault occurs at bus X and least at bus Z as shown in Figures 7.64 to 7.66 respectively. Wave attenuation in voltage wave forms is higher due to 3-phase SCF.

Table 7.20 Effect of 3-phase SCF at bus K on conventional generator side and maximum magnitude of Voltages at bus K

Fault Location	**Maximum Magnitude of Voltages at Bus K (kV)**		
	Phase A	Phase B	Phase C
3-phase SCF occur at bus X	21.86	30.69	19.18
3-phase SCF occur at bus Y	19.62	28.48	16.21
3-phase SCF occur at bus Z	10.29	5.931	6.139

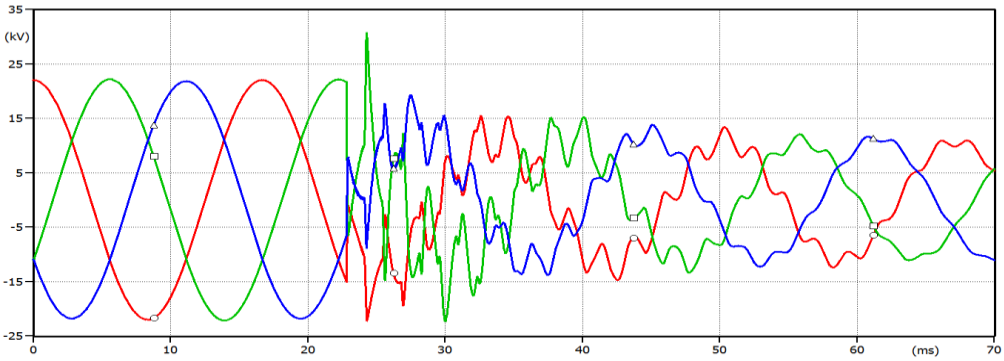

Figure 7.64 Voltages at bus at K: when fault occurs at bus X on Wind hybrid system

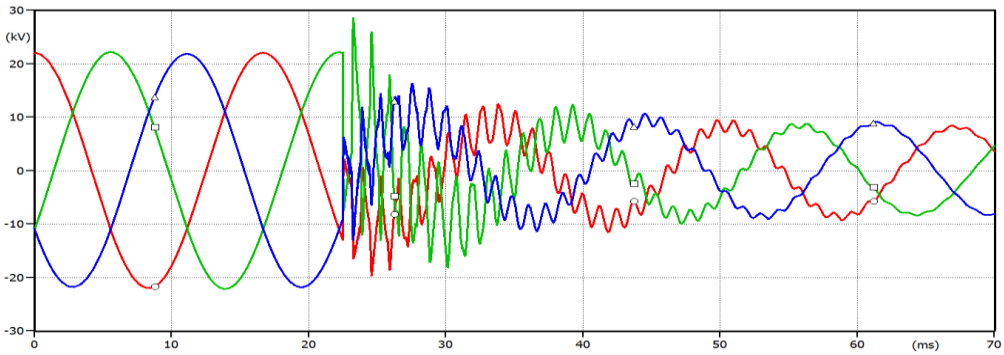

Figure 7.65 Voltage at bus at K when fault occur at bus Y on Wind hybrid system

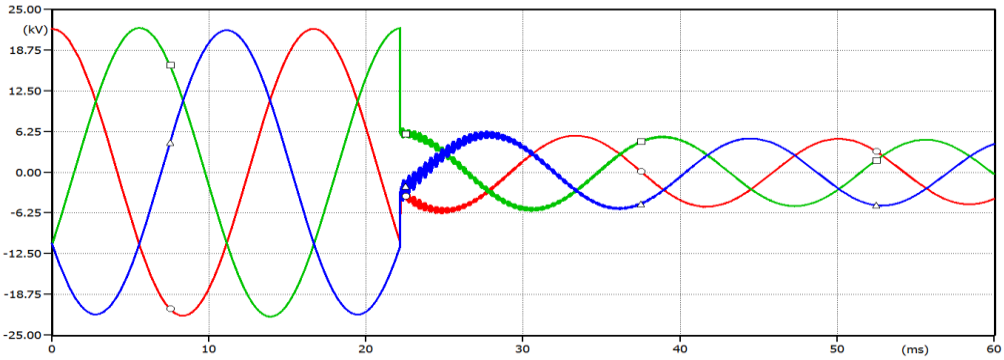

Figure 7.66 Voltage at bus at K when fault occur at bus Z on Wind hybrid system

Effect of 3-phase SCF on voltages at bus P is also observed. It is analysed that voltages of 3-phases is reduced to low value due to SCF. At bus P Voltage is reduced from 32.78 kV to 8.85 kV as shown on Table 7.21. It is observed that effect of SCF on voltages at bus P is least when fault occurs at bus Z i.e. near to conventional generation point and highest near the wind generator interconnection point i.e. bus Y. It is also observed that wave attenuation is highest at when fault occurs at bus Y due to interconnection point and least at bus Z as shown in Figures 7.67 to 7.68 respectively. Wave attenuation in voltage wave forms is higher due to 3-phase SCF.

Table 7.21 Effect of 3-Phase SCF on Voltages at Bus P

Fault Location	**Maximum Magnitude of Voltages at Bus P (kV)**		
	Phase A	Phase B	Phase C
3-phase SCF occur at bus X	24.65	32.78	19.82
3-phase SCF occur at bus Y	4.802	8.85	21.1
3-phase SCF occur at bus Z	18.57	28.5	17.27

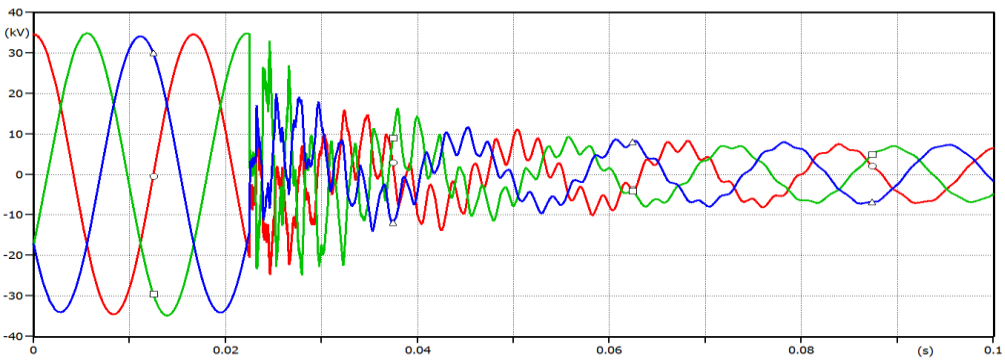

Figure 7.67 Voltages at bus P: when SCF occurs at bus X on Wind hybrid system

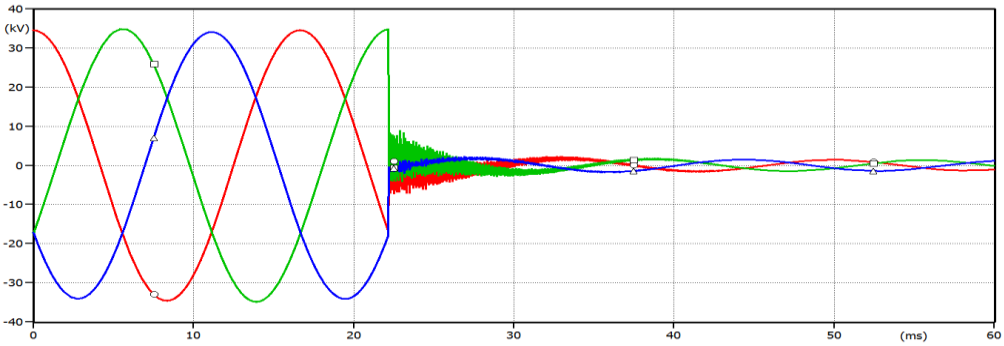

Figure 7.68 Voltages at bus P: when SCF occurs at bus Y on Wind hybrid system

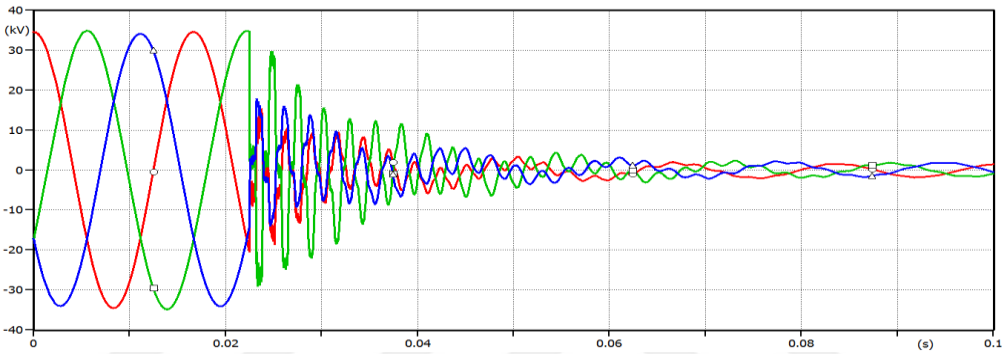

Figure 7.69 Voltages at bus P: when SCF occurs at bus Z on Wind hybrid system

7.4.3 Effect of fault resistance on wind hybrid system

A LG fault is considered to take place on phase A at bus X on the line as given in Figure 7.70. LG fault take place when voltage of phase A is at peak value i.e. at 22.15 msec. The waveforms of the fault current at bus Z and bus X are given in Figures 7.71 to 7.77. For various values of fault resistance, maximum magnitude of fault currents at bus Z and at the fault location X is given on Table 7.22.

The maximum magnitude of fault currents at bus Z and at fault location X decreases as the fault resistance increase. Fault current at bus Z on Wind hybrid system is decreases from 1.842 kA at 1Ω fault resistance to 1.248 kA at 100 Ω fault resistances. Fault current at fault location A is decreases from 2.108 kA at 1Ω fault resistance to 1.275 kA at 100 Ω fault resistances. Comparison between conventional and Wind hybrid system is shown on Table 7.22, it is observed that fault currents on conventional system is less as compare to hybrid system. It means wind farm has considerable effects on conventional system, when effect of fault resistance is studied. Transients in the fault

current waveform are higher at lower value of the fault resistance as compared to that of higher value.

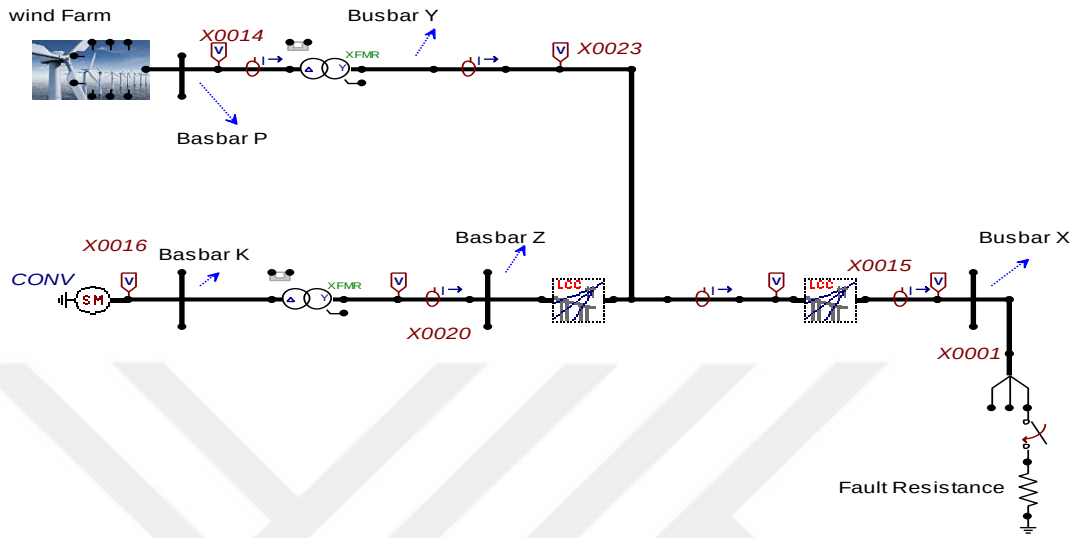

Figure 7.70 Configuration of studied Wind hybrid power system: when fault resistance varies from 1Ω to 100Ω with SLG fault occurs on phase A at bus X

Table 7.22 Effect of fault resistance on fault current at bus Z and X on Wind hybrid power system

Fault Resistance (Ω)	**Maximum Magnitude of Fault Current at Bus Z (A)**		**Maximum Magnitude of Fault Current at Fault Location X (A)**	
	Conventional Power System Alone	Wind Hybrid System	Conventional Power System Alone	Wind Hybrid System
1	2136	1842	1742	2108
5	2098	1806	1699	2024
10	2051	1764	1649	1926
20	1966	1686	1561	1756
30	1889	1617	1486	1612
50	1753	1499	1365	1415
100	1499	1280	1159	1275

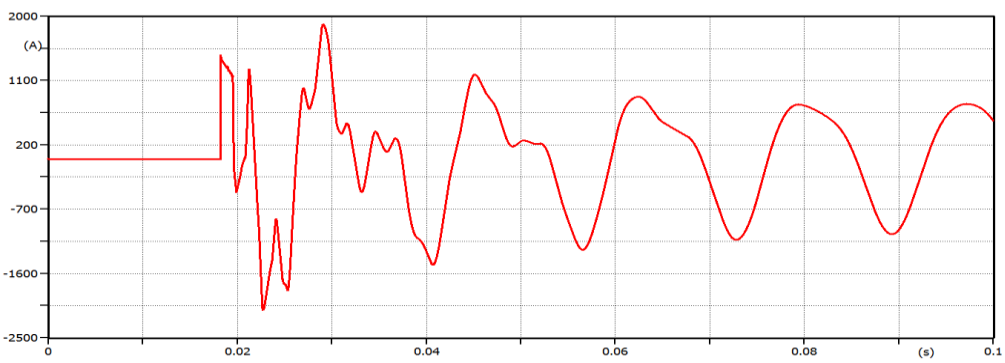

Figure 7.71(a) Fault Current at fault location X when fault resistance is 1Ω on Wind hybrid system

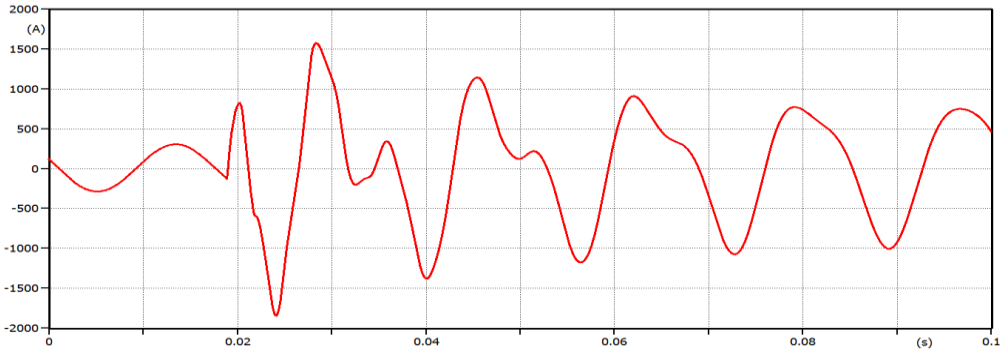

Figure 7.71(b) Fault Current at bus Z when fault resistance 1Ω on Wind hybrid system

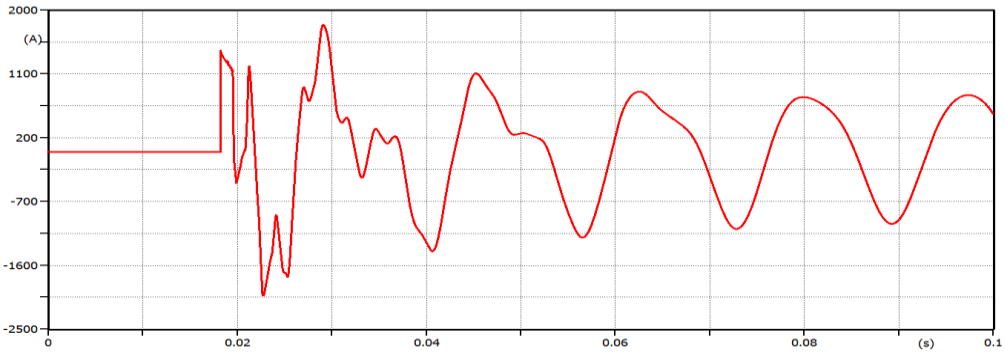

Figure 7.72(a) Fault Current at fault location X when fault resistance is 5Ω on Wind hybrid system

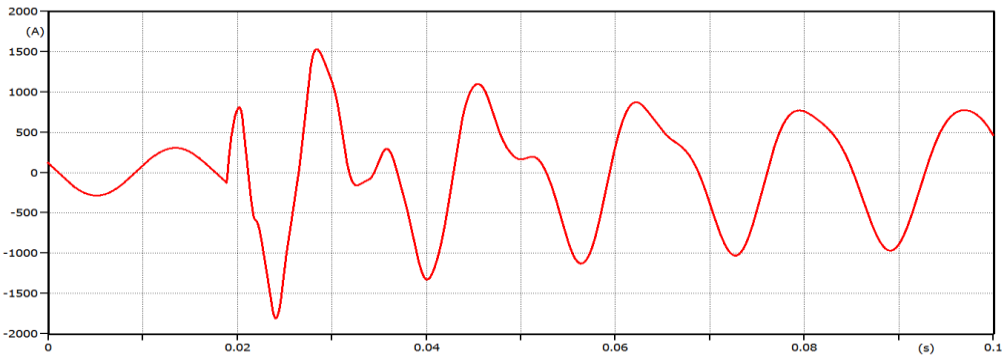

Figure 7.72(b) Fault Current at bus Z when fault resistance 5Ω on Wind hybrid system

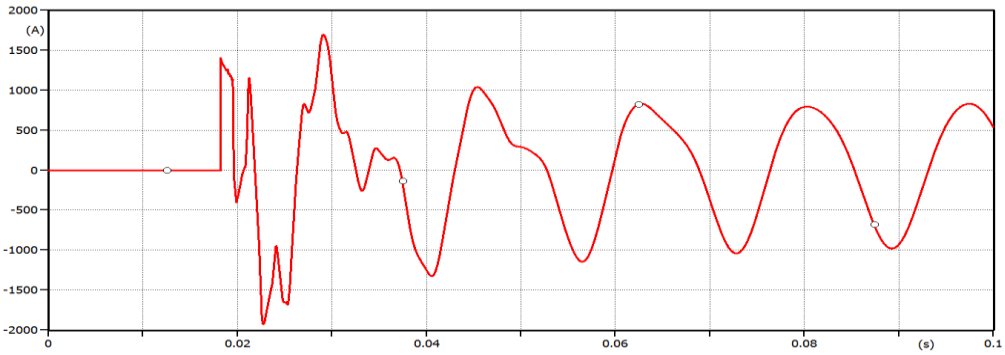

Figure 7.73(a) Fault Current at fault location X when fault resistance is 10Ω on Wind hybrid system

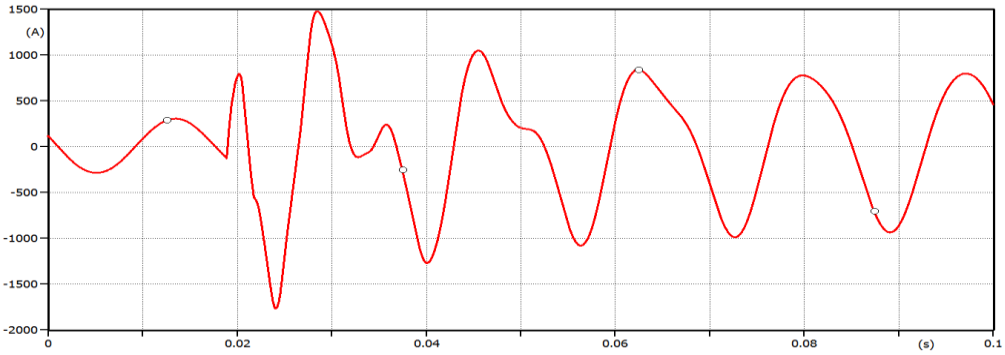

Figure 7.73(b) Fault Current at bus Z when fault resistance 10Ω on Wind hybrid system

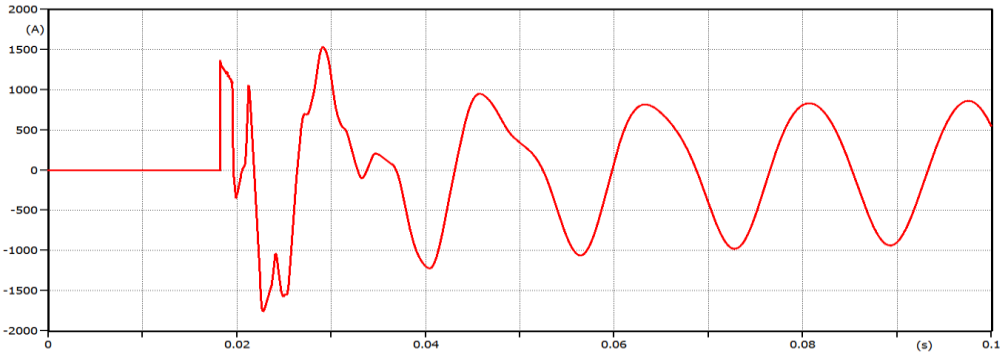

Figure 7.74(a) Fault Current at fault location X when fault resistance is 20Ω on Wind hybrid system

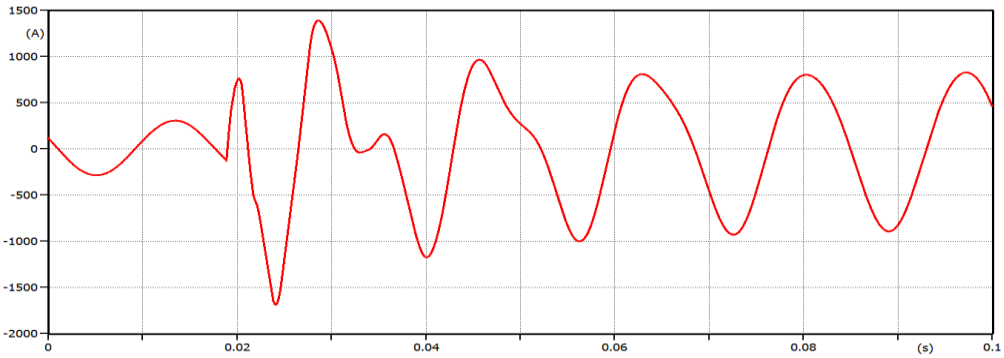

Figure 7.74(b) Fault Current at bus Z when fault resistance 20Ω on Wind hybrid system

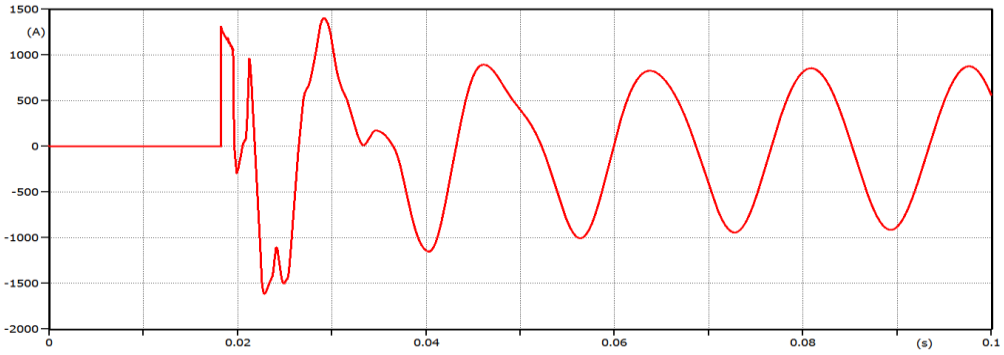

Figure 7.75(a) Fault Current at fault location X when fault resistance is 30Ω on Wind hybrid system

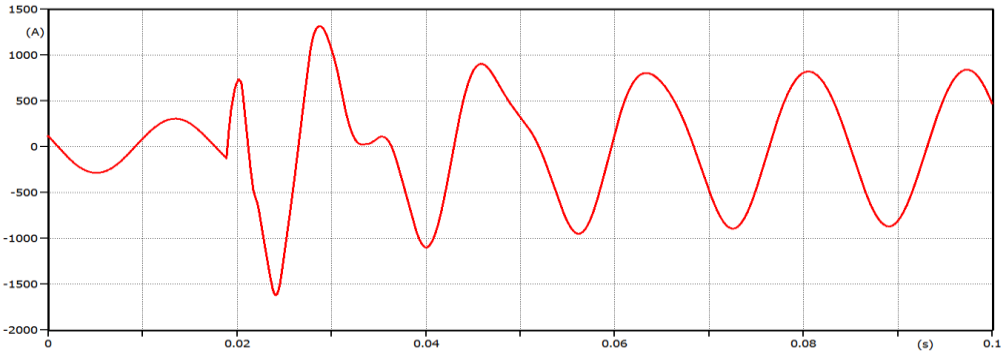

Figure 7.75(b) Fault Current at bus Z when fault resistance 30Ω on Wind hybrid system

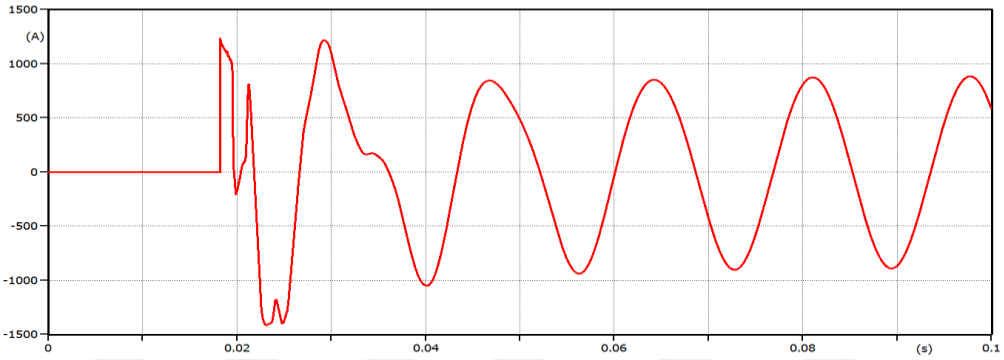

Figure 7.76(a) Fault Current at fault location X when fault resistance is 50Ω on Wind hybrid system

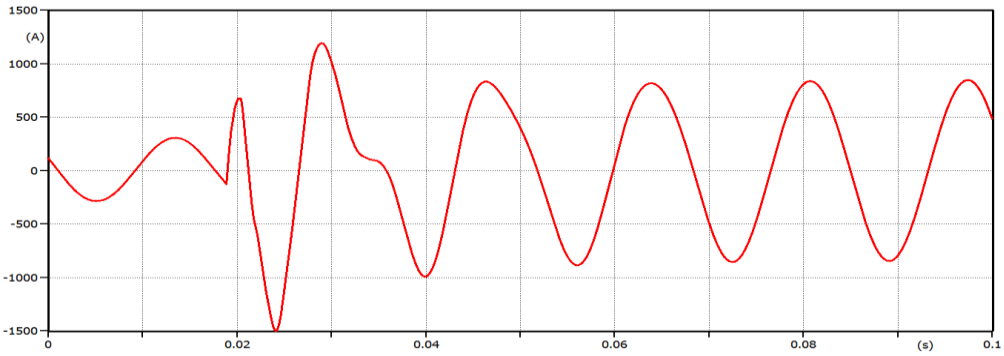

Figure 7.76(b) Fault Current at bus Z when fault resistance 50Ω on Wind hybrid system

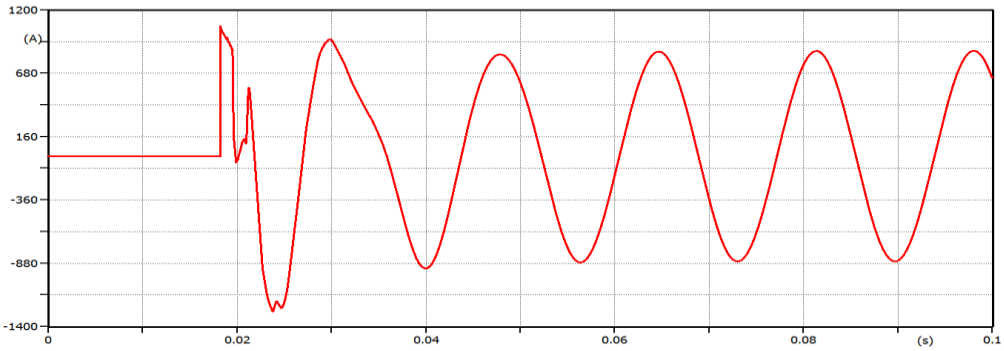

Figure 7.77(a) Fault Current at fault location X when fault resistance is 100Ω on Wind hybrid system

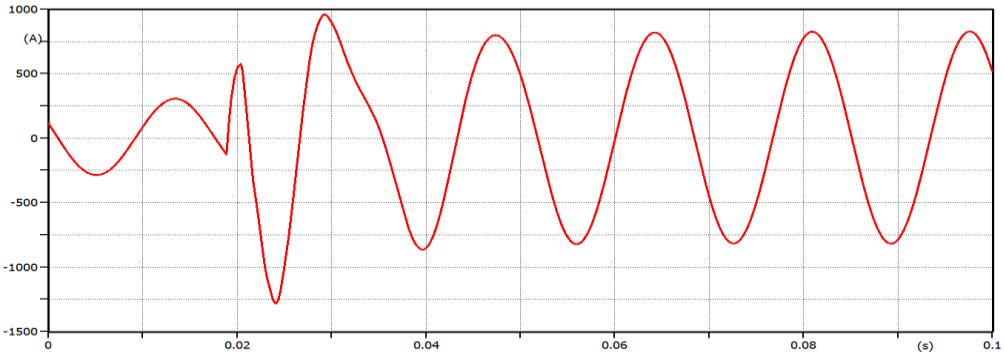

Figure 7.77(b) Fault Current at bus Z when fault resistance 100Ω on Wind hybrid system

When SLG fault occurs on phase A at bus X, than voltage of faulted phase drop to zero and have no wave attenuation because fault occurs at same location and phase, while voltage of un-faulted phases becomes higher than rated voltage. While voltage of faulted phase at bus Z is not exactly drop to zero but it has small value of voltage and wave attenuation because fault occurs far from bus Z as shown in Figures from 7.78 to 7.81. Voltage of un-faulted phases measured at fault resistances 1 Ω, 10 Ω, 50 Ω and 100 Ω as given in Table 7.23. It is observed that as fault resistance increases voltages of un-faulted phases decreased & wave attenuation is also decreased. Voltages of un-faulted voltage at bus-bar decreases from 1.215 MV to 0.9551 MV and at fault location decreases from 1.132 MV to 0.938 MV while, rated voltage at this transmission line is 400 kV.

Table 7.23 Maximum magnitude of voltage of un-faulted phases at bus Z and fault location X: when SLG fault occurs with fault resistance varies from 1 Ω to 100 Ω

Fault Resistance (Ω)	**Wind Hybrid Power System**			
	Maximum Magnitude of Voltage of Un-faulted phases at Bus Z (MV)		Maximum Magnitude of Voltage of Un-faulted Phases at Fault Location X (MV)	
	Phase B	Phase C	Phase B	Phase C
1	1.215	1.115	1.09	1.132
10	1.17	1.076	1.061	1.106
50	1.018	1.007	0.9678	1.014
100	0.8897	0.9551	0.8668	0.938

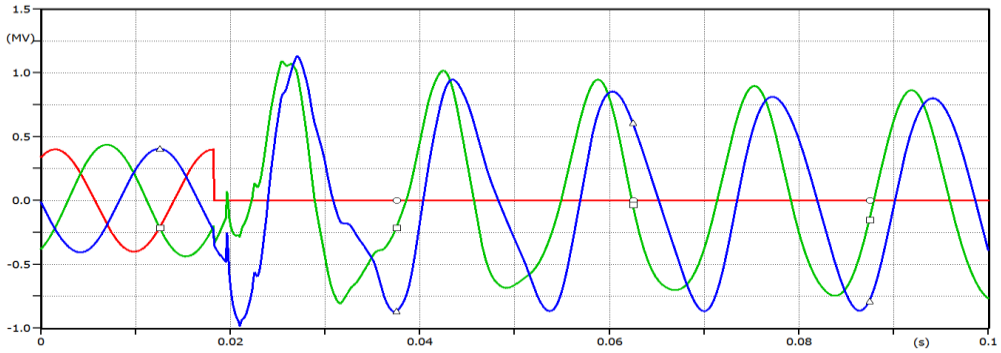

Figure 7.78(a) 3-phase voltages at fault location X: when SLG fault occurs on phase A with fault resistance 1 Ω on Wind hybrid system

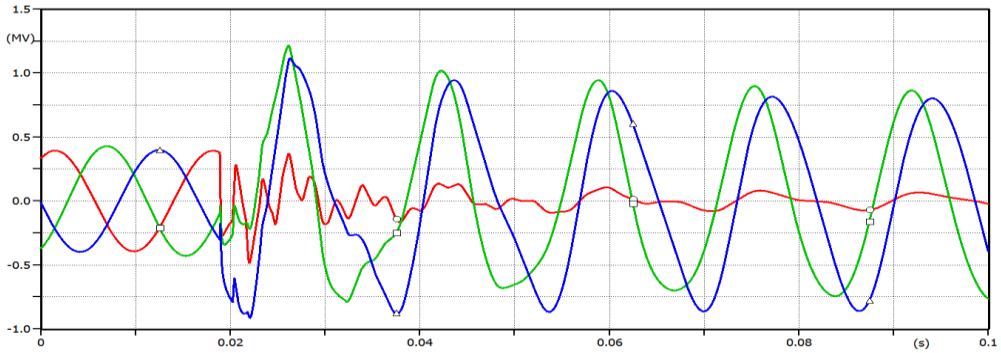

Figure 7.78(b) 3-phase voltages at bus Z: when SLG fault occurs on phase A with fault resistance 1 Ω on Wind hybrid system

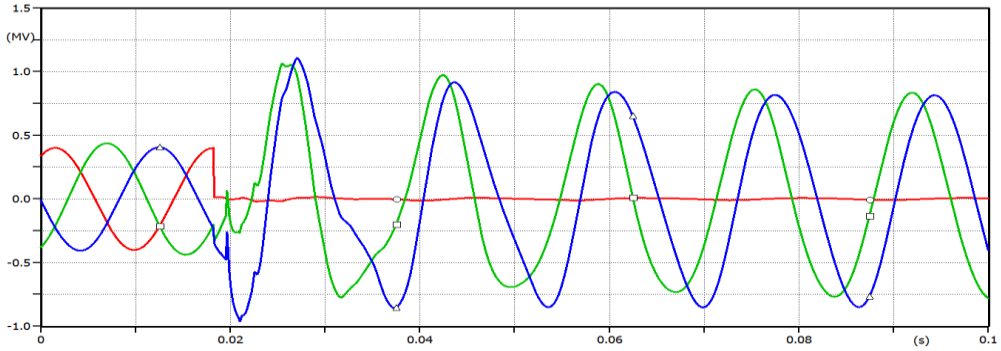

Figure 7.79(a) 3-phase voltages at fault location X: when SLG fault occurs on phase A with fault resistance 10 Ω on Wind hybrid system

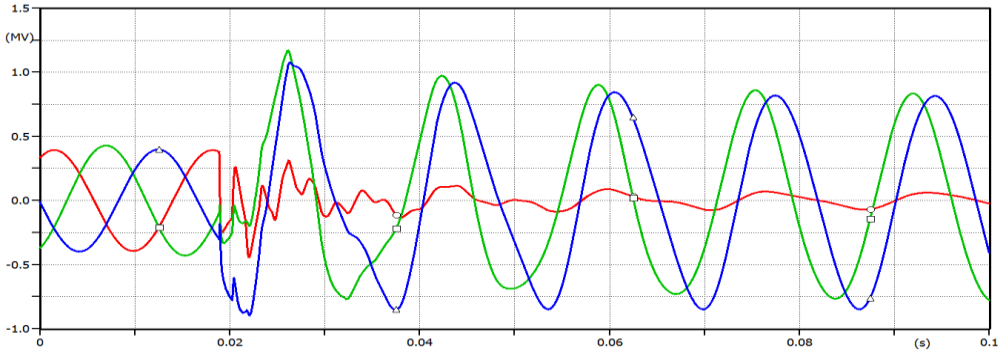

Figure 7.79(b) 3-phase voltages at bus Z: when SLG fault occurs on phase A with fault resistance 10 Ω on Wind hybrid system

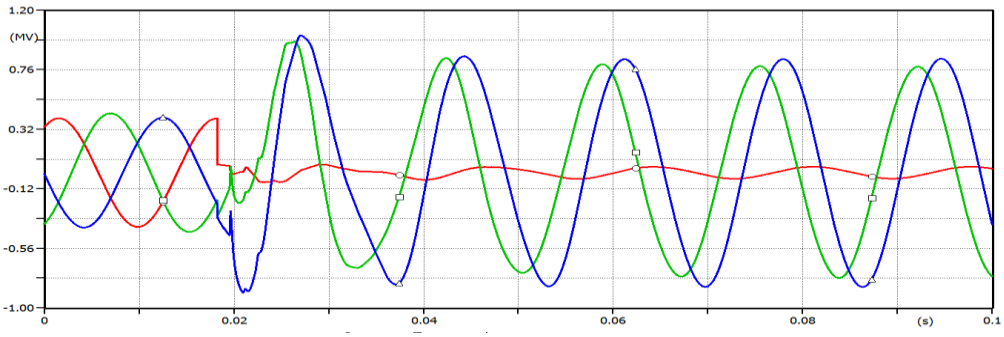

Figure 7.80(a) 3-phase voltages at fault location X: when SLG fault occurs on phase A with fault resistance 50 Ω on Wind hybrid system

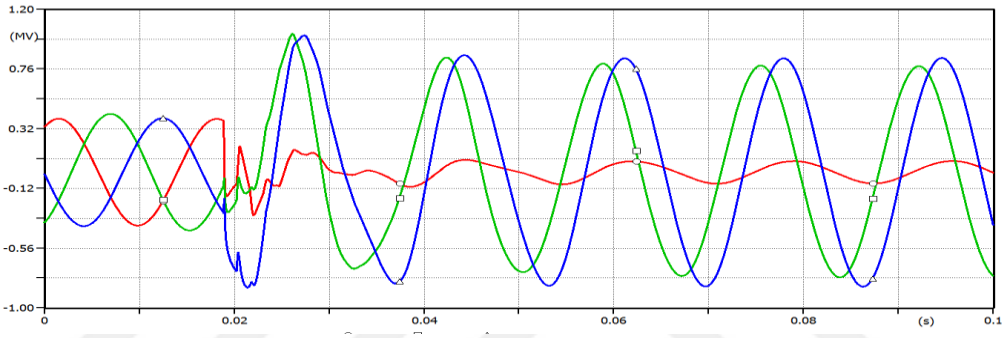

Figure 7.80(b) 3-phase voltages at bus Z: when SLG fault occurs on phase A with fault resistance 50 Ω on Wind hybrid system

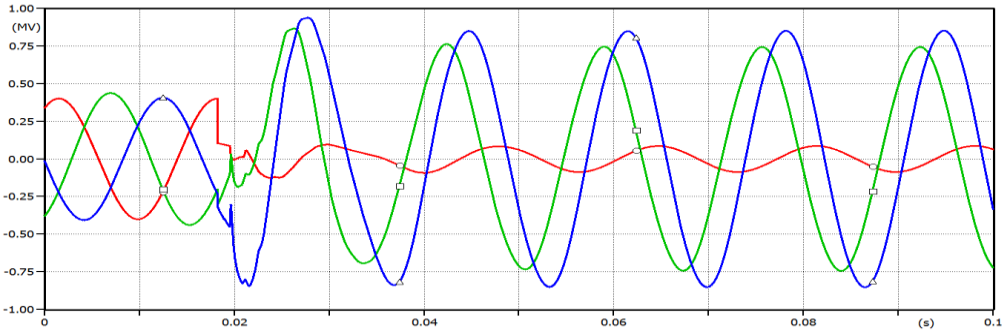

Figure 7.81(a) 3-phase voltages at fault location X: when SLG fault occurs on phase A with fault resistance 100 Ω on Wind hybrid system

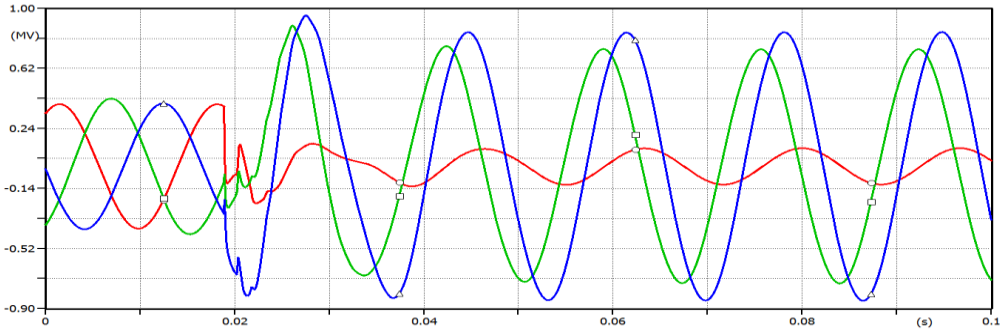

Figure 7.81(b) 3-phase voltages at bus Z: when SLG fault occurs on phase A with fault resistance 100 Ω on Wind hybrid system

7.4.3.1 Effect of fault resistance due to 3-phase SCF

3-phase SCF is considered to take place at bus X on the line as given in Figure 7.82. The waveforms of the fault current at fault location X are given in Figures 7.83 to 7.89. For various values of fault resistance, maximum magnitude of fault currents at the location X is given in Tables 7.23.

The maximum magnitude of fault currents at fault location X decreases as the fault resistance increase. Fault current at fault location X is decreases from 6.193 kA at 1Ω fault resistance to 2.580 kA at 100 Ω fault resistances. Comparison between fault currents due to LG fault and SCF at fault location X is shown in Tables 7.23, it is observed that fault currents due to LG fault is less as compare to SCF on Wind hybrid system. It means short circuit fault has severe effects as compare to LG on Wind hybrid system, when effect of fault resistance is studied. It's also observed that SCF current is reduced as fault resistance is increased. Transients in the fault current waveform are higher at lower value of the fault resistance as compared to that of higher value. It is also analysed that that wave attenuation is also higher due to short circuit fault as compare to single line to earth fault.

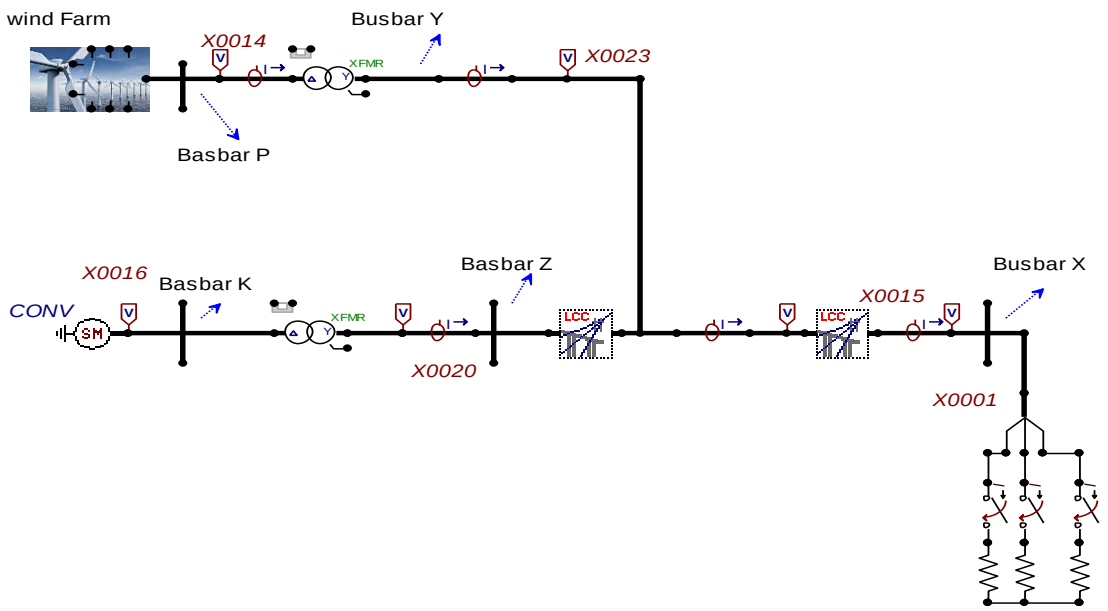

Figure 7.82 Configuration of studied Wind hybrid power system: when fault resistance varies from 1Ω to 100Ω with 3-phase SCF occurs at bus X

Table 7.24 Maximum magnitudes of faulted phase currents at fault location X on Wind hybrid system due to LG fault and 3-phase SCF for different fault resistances

Fault Resistance R_f (Ω)	**Maximum magnitude of fault current (A)**			
	SLG Fault	3-Phase SCF		
	Phase A	**Phase A**	**Phase B**	**Phase C**
1	1742	4995	6193	5787
5	1699	4756	5831	5420
10	1649	4481	5436	5005
20	1561	3998	4797	4556
30	1486	3590	4297	4150
50	1365	2989	3570	3535
100	1159	2373	2580	2532

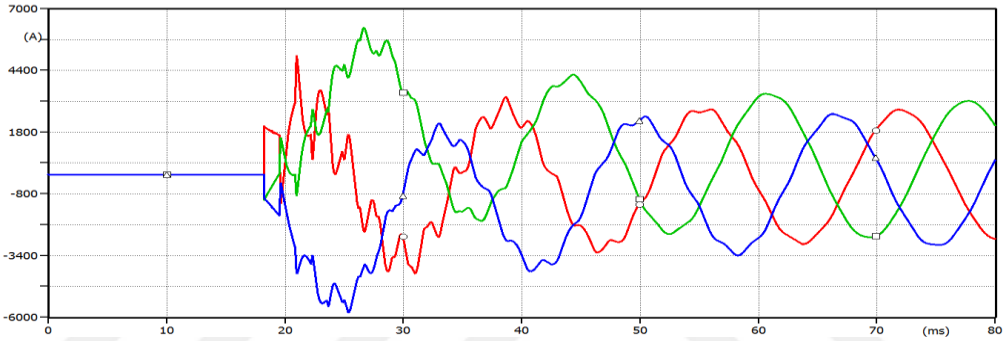

Figure 7.83 3-phase voltages at fault location X: when SCF occurs at fault location X with fault resistance 1 Ω on Wind hybrid system

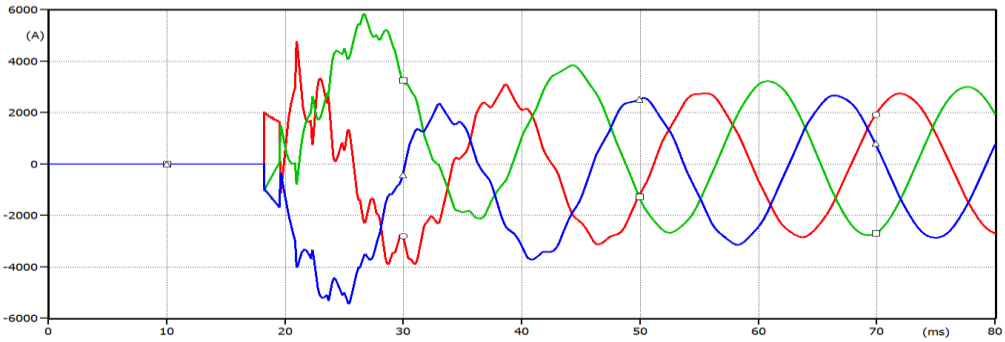

Figure 7.84 3-phase voltages at fault location X: when SCF occurs at fault location X with fault resistance 5 Ω on Wind hybrid system

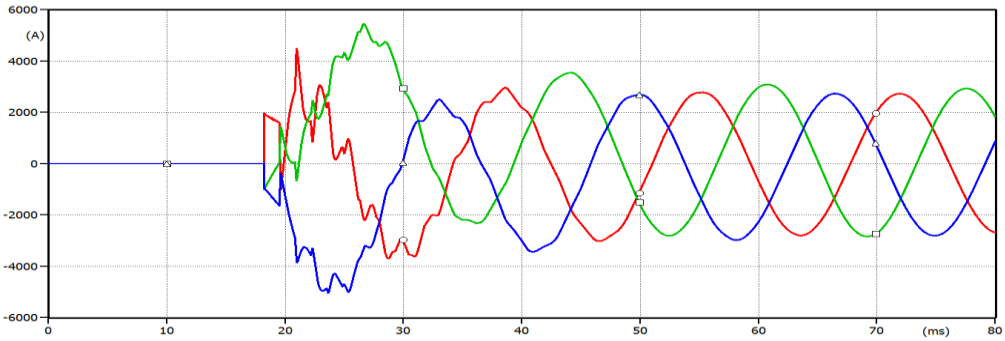

Figure 7.85 3-phase voltages at fault location X: when SCF occurs at fault location X with fault resistance 10 Ω on Wind hybrid system

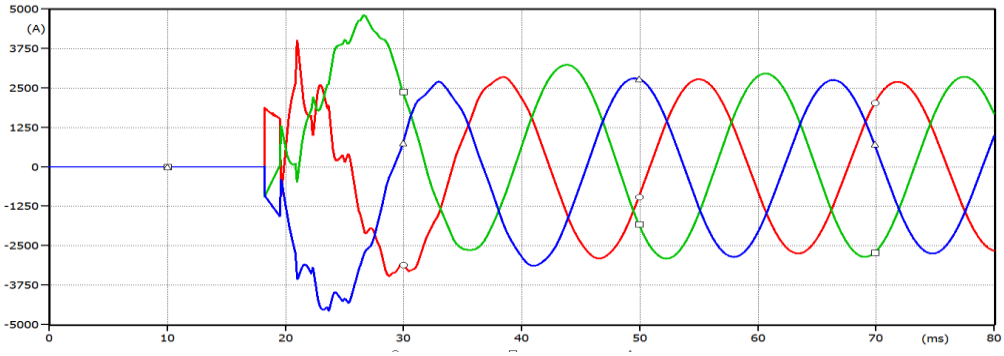

Figure 7.86 3-phase voltages at fault location X: when SCF occurs at fault location X with fault resistance 20 Ω on Wind hybrid system

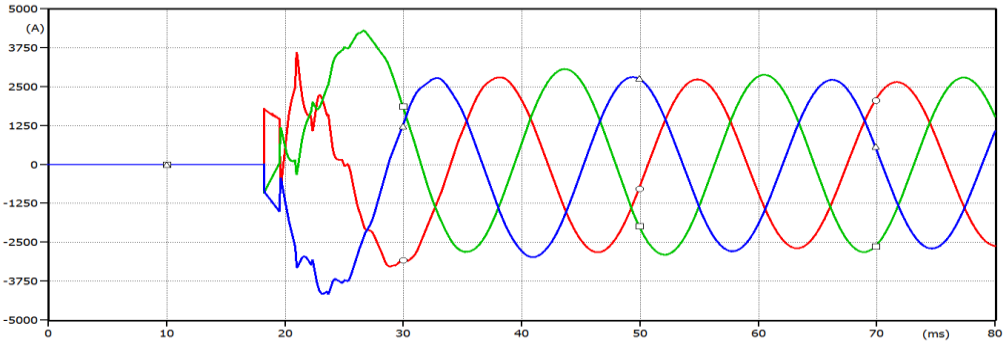

Figure 7.87 3-phase voltages at fault location X: when SCF occurs at fault location X with fault resistance 30 Ω on Wind hybrid system

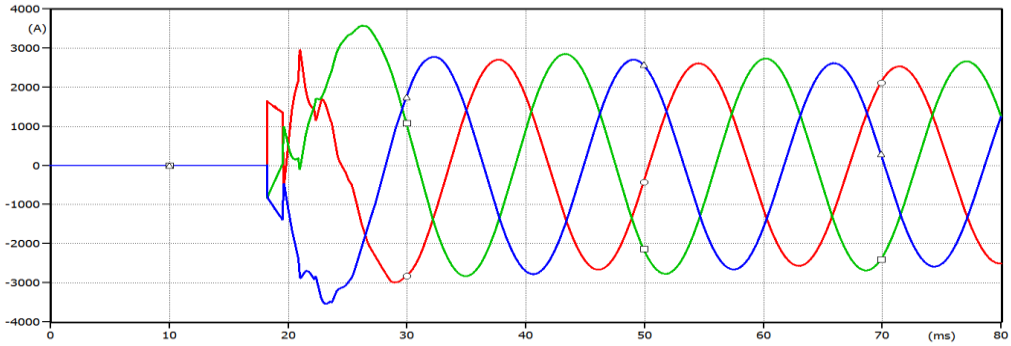

Figure 7.88 3-phase voltages at fault location X: when SCF occurs at fault location X with fault resistance 50 Ω on Wind hybrid system

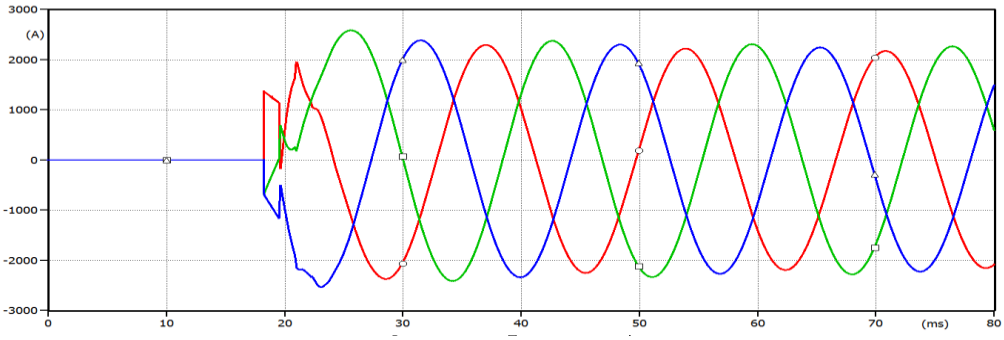

Figure 7.89 3-phase voltages at fault location X: when SCF occurs at fault location X with fault resistance 100 Ω on Wind hybrid system

7.4.4 Effect of wind farm and line length on fault current on wind hybrid system

LG fault takes place on phase A at the end of line. The faulted phase currents at bus Z & X, during fault are computed for various line lengths from 100 km to 260 km and plotted to obtain faulted phase current waveforms at fault location X are shown in Figures 7.90 to 7.94 on Wind hybrid power system. The Maximum values of the faulted phase current at fault location X for different line lengths are shown on Table 7.25.

The simulation result shows that the maximum magnitude of the currents at fault point increases as the line length increases due to capacitance of transmission line, also ripples along the line attenuate as the line length increases. Fault current at fault location X increases from 1.814 kA to 2.643 kA as shown on Table 7.25 so, effect of wind farm on fault currents at fault location X is much more as compare to conventional system alone. It is also observed that as line length increases travel time of fault current at bus Z is increasing and harmonics frequency is decreasing.

Voltages of un-faulted phases are shown in Figures 7.95 to 7.98. Voltage of faulted phase is reduced to minimum value at bus Z and voltages of un-faulted phases are increased. It is also observed that wave attenuation is also decreased as line length increases.

Table 7.25 Maximum magnitude of faulted phase current against line length at bus Z and fault location X and effects of Wind on it

Line Length (km)	**Maximum Magnitude of Fault Current at Fault Location X (A)**	
	Conventional System Alone	Hybrid System (With Wind Farm)
100	1483	1814
200	1754	2122
220	1814	2312
240	2005	2588
260	2205	2643

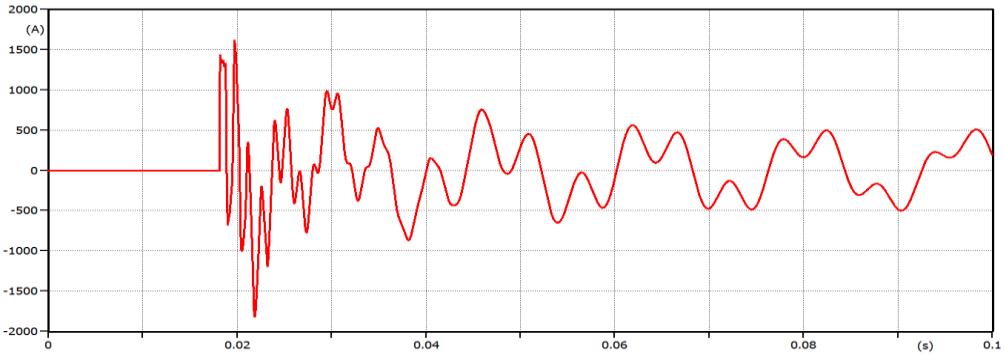

Figure 7.90 Fault Current at fault location X on Wind hybrid system: when line length is 100 km

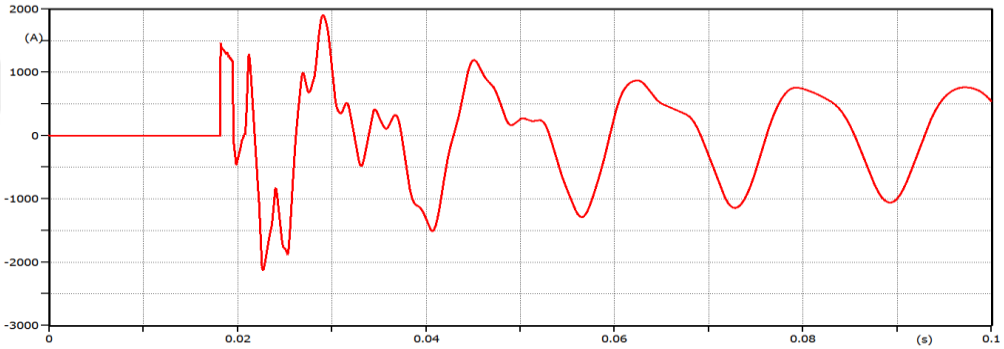

Figure 7.91 Fault Current at fault location X on Wind hybrid system: when line length is 200 km

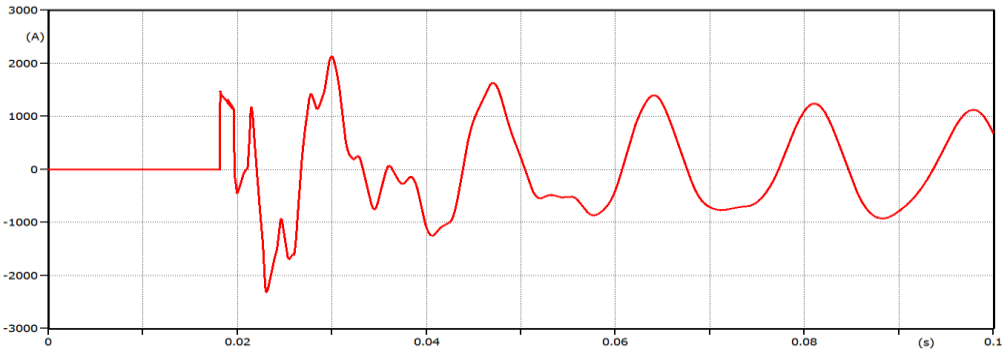

Figure 7.92 Fault Current at fault location X, on Wind hybrid system when line length is 220 km

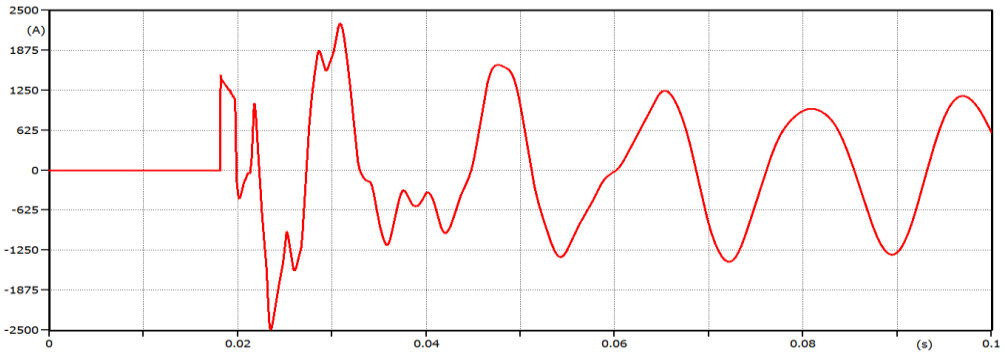

Figure 7.93 Fault Current at fault location X on Wind hybrid system when line length is 240 km

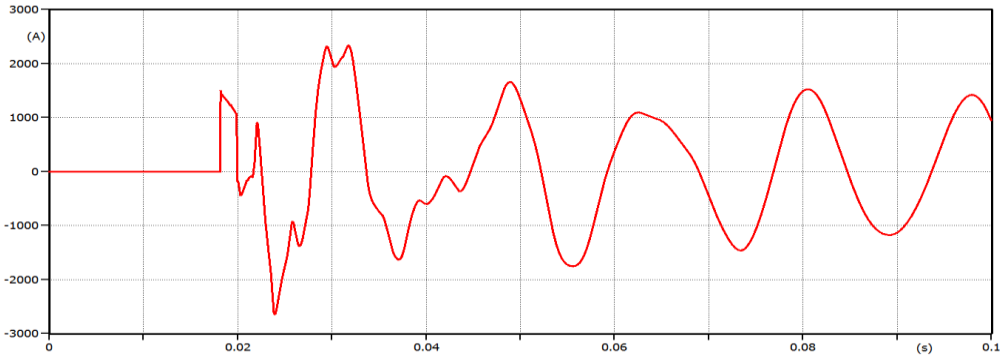

Figure 7.94 Fault Current at fault location X on Wind hybrid system: when line length is 260 km

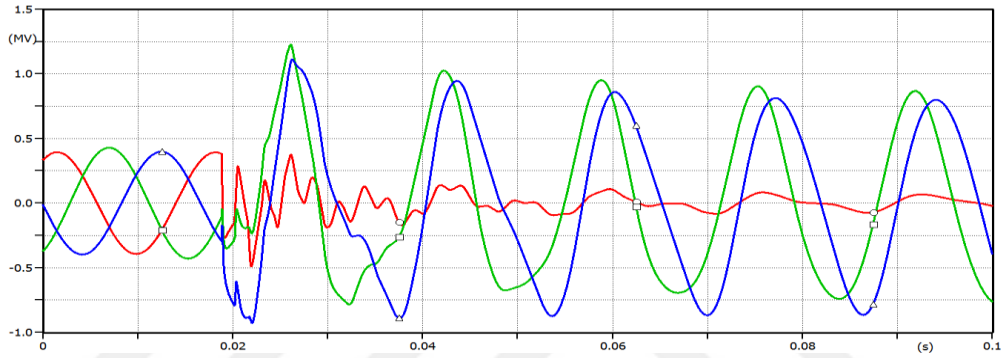

Figure 7.95 Voltages of un-faulted phases at bus Z on Wind hybrid system: when line length is 200 km

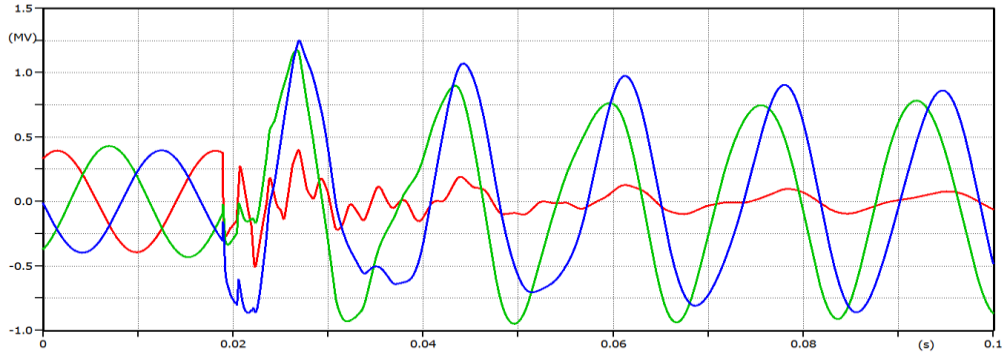

Figure 7.96 Voltages of un-faulted phases at bus Z on Wind hybrid system when line length is 220 km

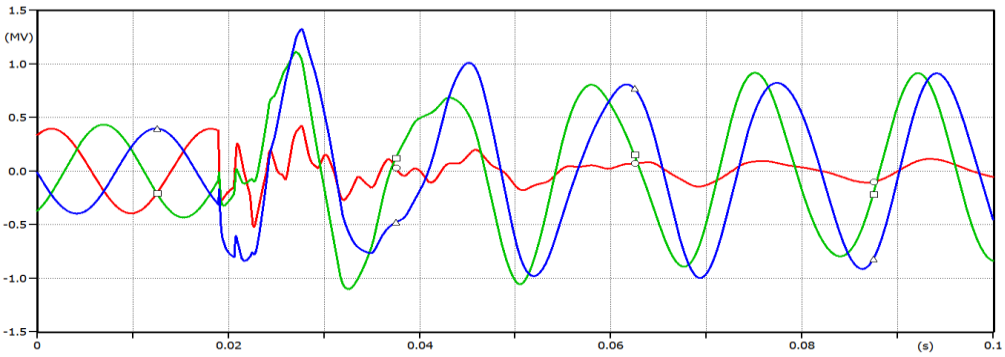

Figure 7.97 Voltages of un-faulted phases at bus Z on Wind hybrid system: when line length is 240 km

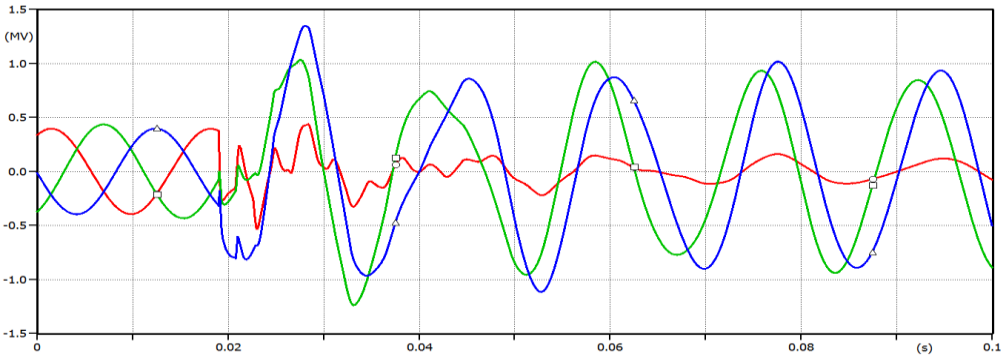

Figure 7.98 Voltages of un-faulted phases at bus Z on Wind hybrid system: when line length is 260 km

7.5 Hybrid Power System Connected with Wind/PV Hybrid System

The integrated wind/PV generators are connected with conventional power system. 100 MW wind and PV generators are connected at mid-point of 200 km transmission line at a voltage of 400 kV as shown in Figure 7.99.

7.5.1 Effect of 3-phase SCF at different location on Wind/PV hybrid power system

This section analysed the effect of 3-phase SCF at different location on hybrid system with Wind/PV generator. 3-phase SCF occur at different location on hybrid power system i.e. at bus X, Y and Z respectively. Configuration of studied hybrid system (with Wind/PV generator) is shown in Figure 7.99. Waveforms of currents for 3-phase SCF at bus X, Y and Z are shown in Figures 7.100 to 7.102 respectively.

It is observed from the results that as fault come closer to source point (bus Z) from end point (bus X), magnitude of 3-phase SCF currents increases, so 3-phase SCF is most severe near to source i.e. bus Z and it's least severe at end point near to load i.e. bus X. Wave attenuation is higher when fault occurs at bus Y and its least at bus Z. Magnitude of 3-phase SCF currents increases from 6.176 kA to 10.86 kA as shown on Table 7.26.

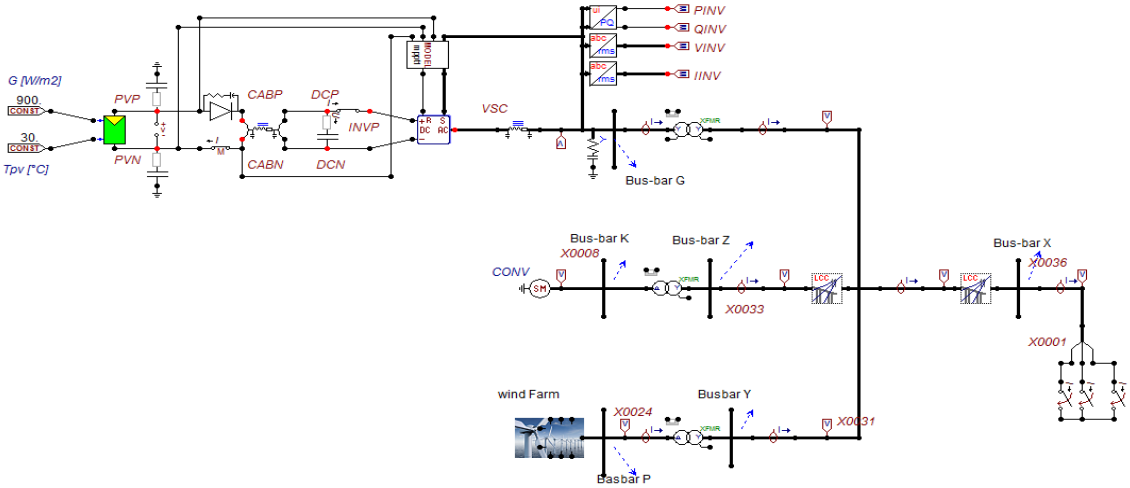

Figure 7.99 Configuration of Wind/PV hybrid system: when 3-phase SCF occur at bus X

Table 7.26 Maximum Magnitude of 3-Phase SCF currents at different locations on Wind/PV hybrid power system

Fault Location	**Maximum Magnitude of 3-Phase SCF Currents at Fault Location (A)**		
	Phase A	Phase B	Phase C
3-phase SCF occur at bus X	5011	6176	5832
3-phase SCF occur at bus Y	6362	8199	7956
3-phase SCF occur at bus Z	6535	10860	10830

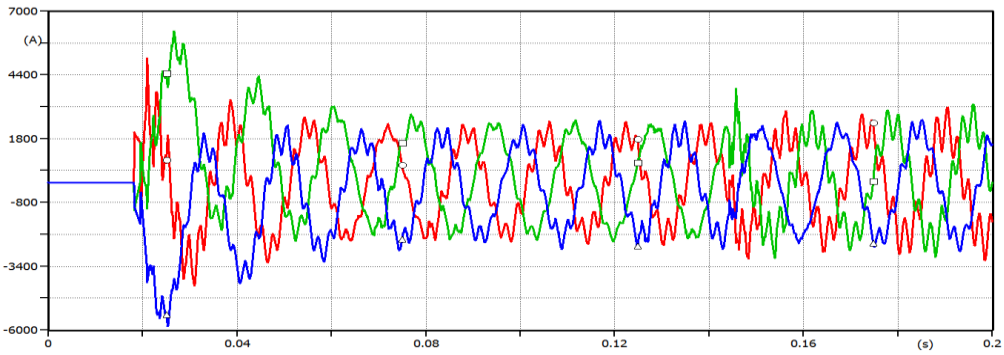

Figure 7.100 Fault current at fault location, when 3-phase SCF occurs at bus X on Wind/PV hybrid system

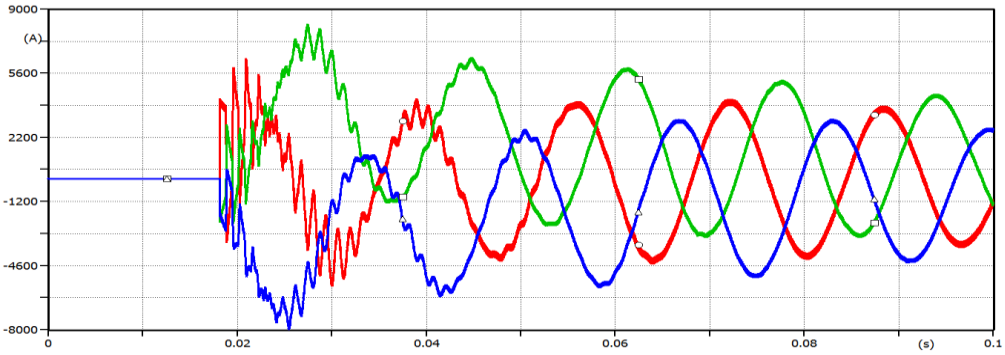

Figure 7.101 Fault current at fault location, when 3-phase SCF occurs at bus Y on Wind/PV hybrid system

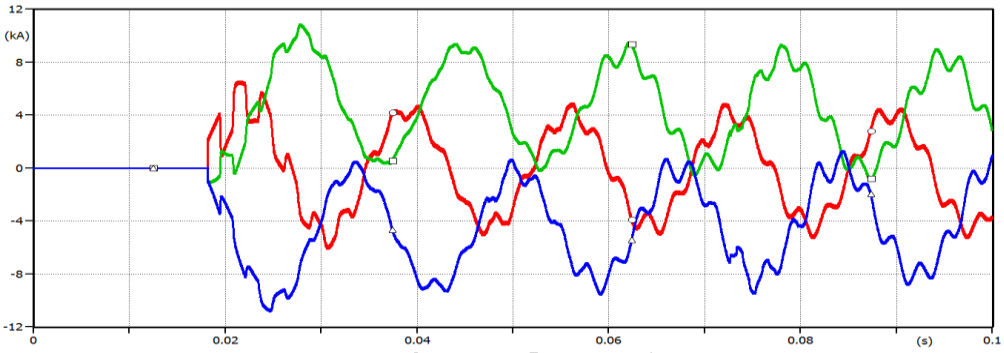

Figure 7.102 Fault current at fault location, when 3-phase SCF occurs at bus Z on Wind/PV hybrid system

7.5.2 Effect of 3-phase SCF current at Wind/PV generator side (bus P and bus G)

3-phase SCF occur at different location on Wind/PV hybrid power system, it also causes an effect on currents flowing through Wind and PV generators i.e. bus P and bus G respectively. It is analysed from the results that effect of 3-phase SCF is high at interconnection point i.e. bus Y, where wind and PV generators are connected to 400 kV transmission line at conventional power system as shown on Table 7.27. It is also observed from waveforms that wave attenuation is higher when 3-phase SCF occurs at bus X i.e. near to end point and least at bus Y as shown in Figures from 7.103 to 7.105 respectively.

Table 7.27 shows the effect of 3-phase SCF at bus P and maximum magnitude of fault currents flow through Wind generator i.e. at bus P. Fault current increases from 8.371 kA to 12.55 kA, when 3-phase SCF occur at different locations X to location Z.

Table 7.27 Effect of 3-phase SCF at bus P on wind generator side hybrid power system

Fault Location	**Maximum Magnitude of 3-Phase SCF Currents at Bus P (kA)**		
	Phase A	Phase B	Phase C
3-phase SCF occur at bus X	6.321	8.732	6.0
3-phase SCF occur at bus Y	8.703	12.55	8.642
3-phase SCF occur at bus Z	8.715	11.9	8.70

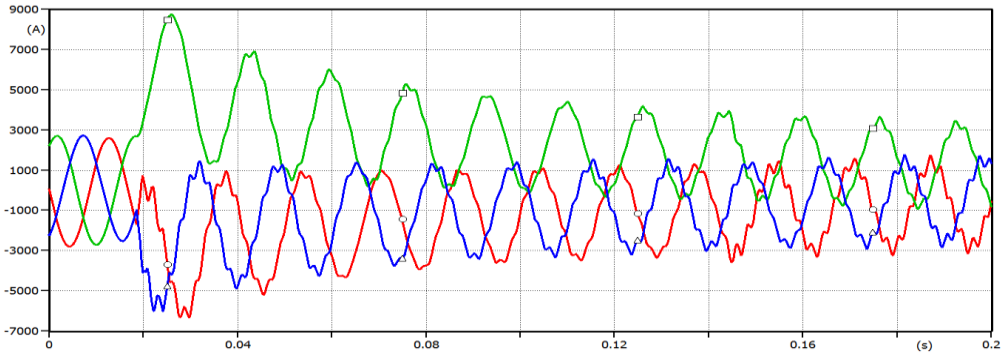

Figure 7.103 Effect of 3-phase SCF at bus P on wind generator terminal 34.5 kV side when fault occurs at Bus X

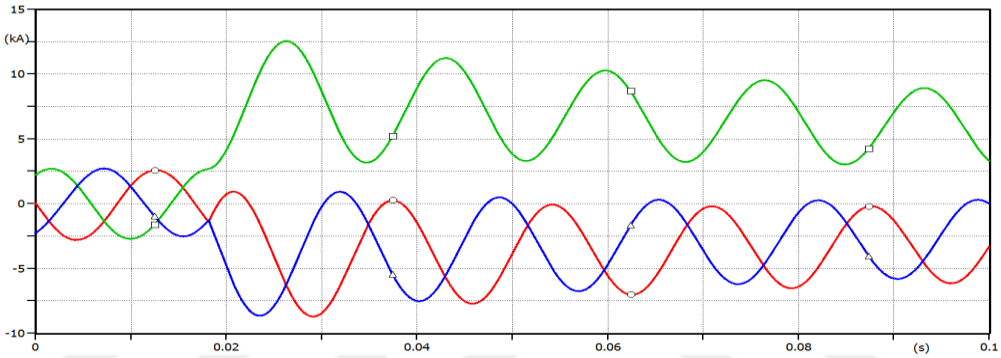

Figure 7.104 Effect of 3-phase SCF at bus P on wind generator terminal 34.5 kV side when fault occurs at bus Y

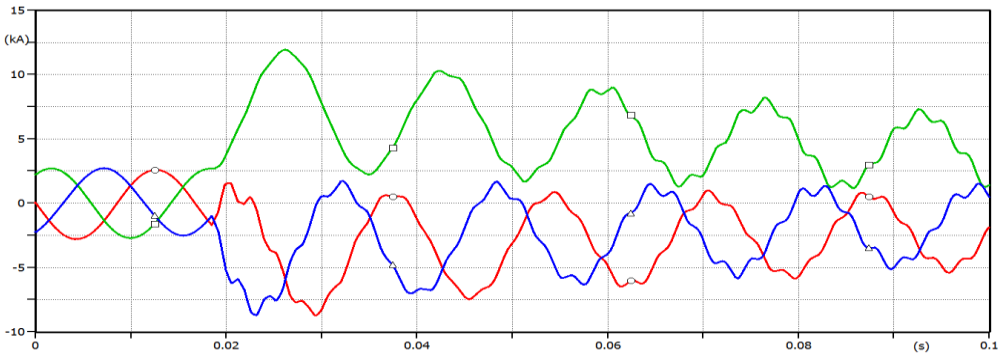

Figure 7.105 Effect of 3-phase SCF at bus P on wind generator terminal 34.5 kV side when fault occurs at bus Z

When 3-phase SCF occur at different location on Wind/PV hybrid power system, it also causes an effect on currents flowing through PV farm i.e. bus G. It is analysed from the results that effect of 3-phase SCF on PV side is highest at bus X, It's also analysed that wave attenuation is highest when 3-phase SCF occurs at bus X i.e. near to end point and least at bus Y i.e. interconnection point as shown in Figures from 7.106 to 7.108 respectively. Table 7.28 shows the effect of 3-phase SCF at bus G and maximum magnitude of fault currents flow through PV generator. Fault current

decreases from 1.954 MA to 0.909 MA, when 3-phase SCF occur at different locations X to location Z.

Table 7.28 Effect of 3-phase SCF at bus G on PV generator side hybrid power system

Fault Location	**Maximum Magnitude of 3-Phase SCF Currents at Bus G (kA)**		
	Phase A	Phase B	Phase C
3-phase SCF occur at bus X	1077	1954	959.8
3-phase SCF occur at bus Y	693.5	705.2	719.4
3-phase SCF occur at bus Z	843	752.6	909.9

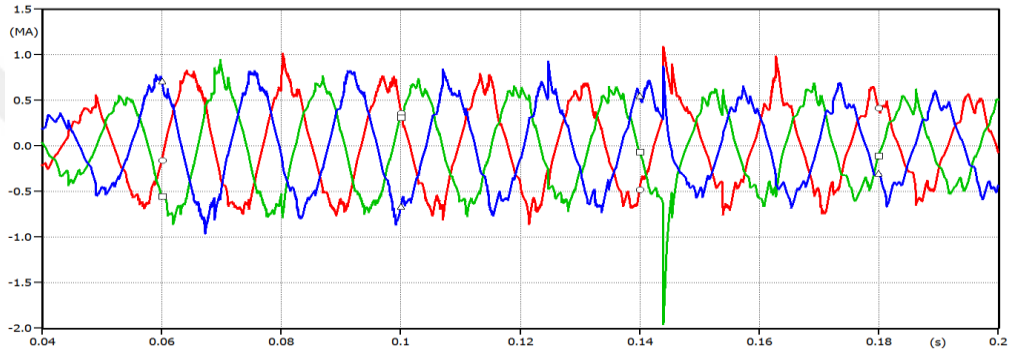

Figure 7.106 Effect of 3-phase SCF at bus P on wind generator terminal 34.5 kV side when fault occurs at bus X

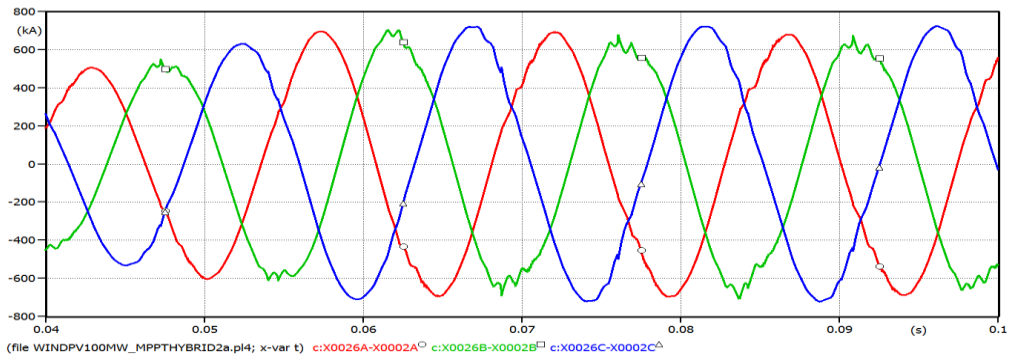

Figure 7.107 Effect of 3-phase SCF at bus P on wind generator terminal 34.5 kV side when fault occurs at bus Y

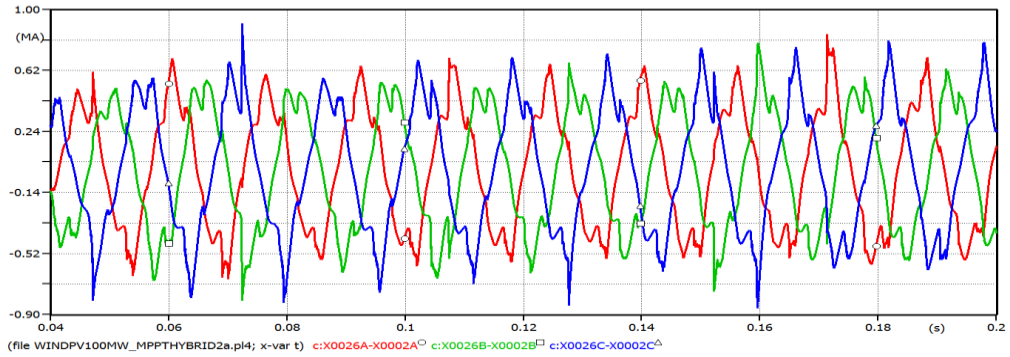

Figure 7.108 Effect of 3-phase SCF at bus P on wind generator terminal 34.5 kV side when fault occurs at bus Z

Effect of 3-phase SCF on voltages at bus-bars K and P are also examined. It is analysed that voltages of 3-phases is reduced to low value due to SCF. At bus K voltage is reduced from 14.68 kV to 4.875 kV as shown in Table 7.29. It is examined that effect of SCF on voltages at bus K is least when fault occurs at bus X i.e. far away from generation point and highest near the generation point. It is also observed that wave attenuation is highest at when fault occurs at bus X and least at bus Z because of fault location as shown in Figures 7.109 to 7.111 respectively. Wave attenuation in voltage wave forms is higher due to 3-phase SCF.

Table 7.29 Effect of 3-phase SCF on at bus K on conventional generator side and maximum magnitude of voltages at bus K

Fault Location	**Maximum Magnitude of Voltages at Bus K (kV)**		
	Phase A	Phase B	Phase C
3-phase SCF occur at bus X	22.1	14.68	30.4
3-phase SCF occur at bus Y	8.0	8.93	8.705
3-phase SCF occur at bus Z	5.077	4.875	5.177

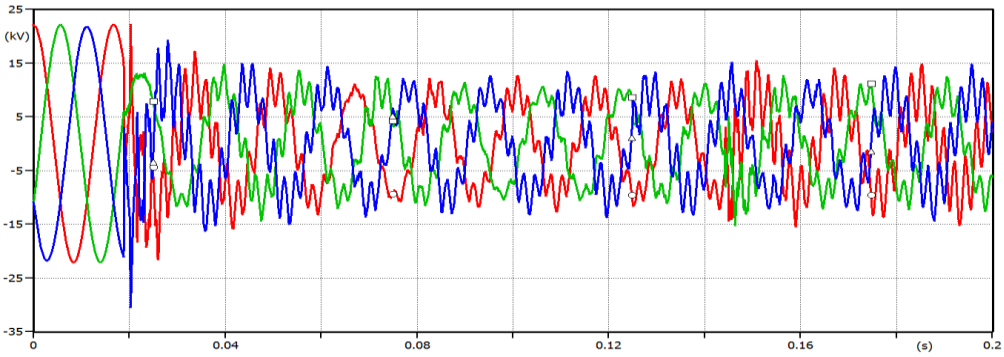

Figure 7.109 Voltages at bus at K: when SCF occurs at bus X on Wind/PV hybrid power system

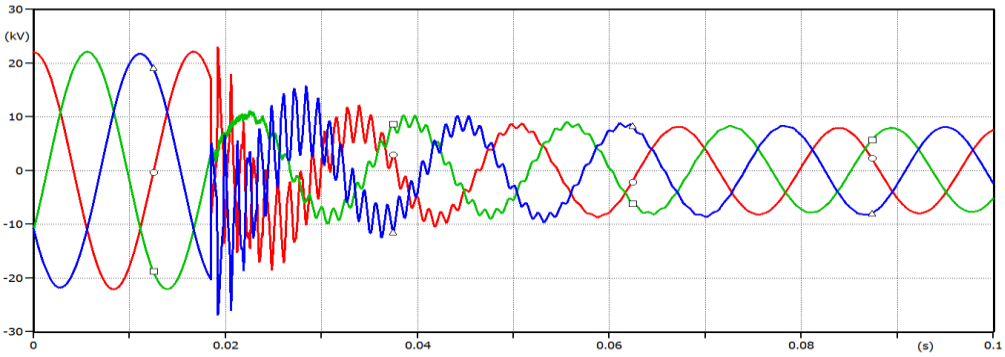

Figure 7.110 Voltage at bus at K when SCF occurs at bus Y on Wind/PV hybrid power system

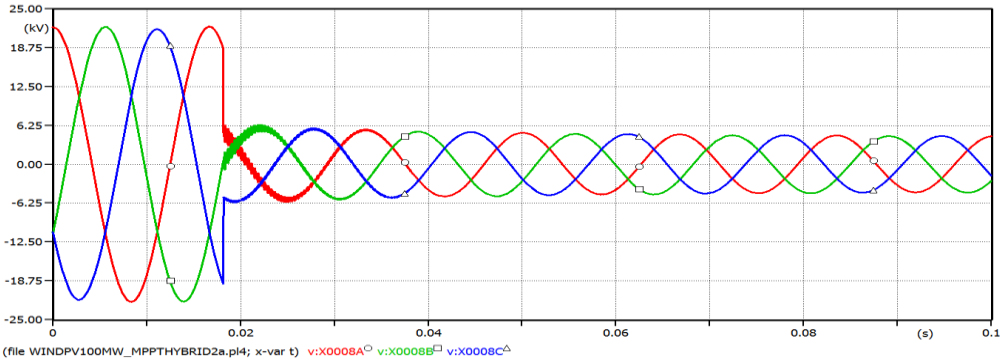

Figure 7.111 Voltage at bus at K when SCF occurs at bus Z on Wind/PV hybrid power system

Effect of 3-phase SCF on voltages at bus-bar P is also observed. It is analysed that voltages of 3-phases is reduced to low value due to SCF, At bus P Voltage is reduced from 11.9 kV to 1.165 kV as shown in Table 7.30. It is observed that short circuit voltage is reduced to least value at interconnection point i.e. bus Y and wave attenuation is also highest at when fault occurs at bus Y due to interconnection point and least at bus Z as shown in Figures 7.112 to 7.114 respectively. It is also analysed from Figures 7.115 to 7.117, that its effect on PV side is also examine and noticed that effect of SCF at PV side is very high more than at wind side. Wave attenuation is also very at PV terminal voltage as compare to wind terminal due to dc-ac converter.

Table 7.30 Effect of 3-Phase SCF on voltages at bus P at wind generator and maximum magnitude of voltages at bus K

Fault Location	**Maximum Magnitude of Voltages at Bus P (kV)**		
	Phase A	Phase B	Phase C
3-phase SCF occur at bus X	22	11.9	31
3-phase SCF occur at bus Y	1.637	1.165	1.288
3-phase SCF occur at bus Z	10.7	7.378	18.05

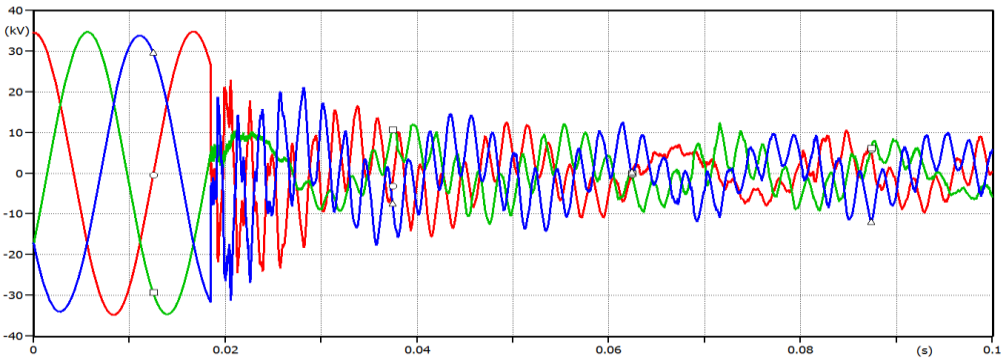

Figure 7.112 Voltages at bus P: when SCF occurs at bus X on Wind/PV hybrid power system

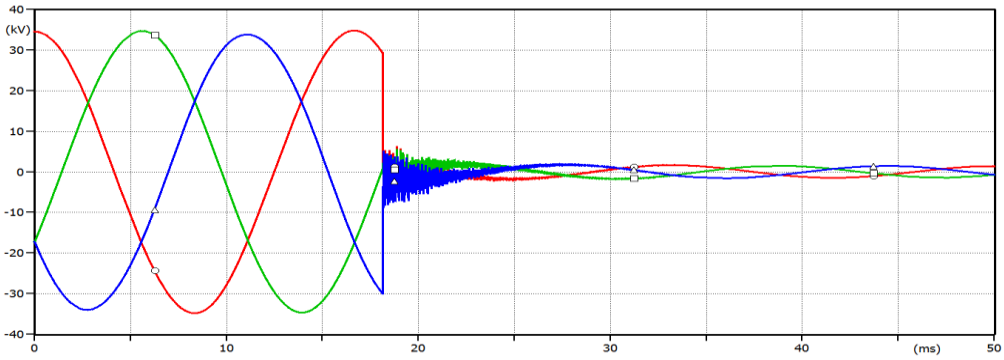

Figure 7.113 Voltages at bus P: when SCF occurs at bus Y on Wind/PV hybrid power system

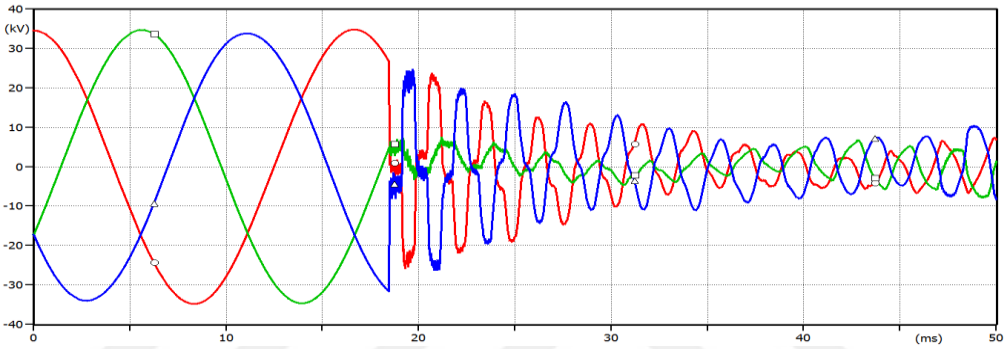

Figure 7.114 Voltages at bus P: when SCF occurs at bus Z on Wind/PV hybrid power system

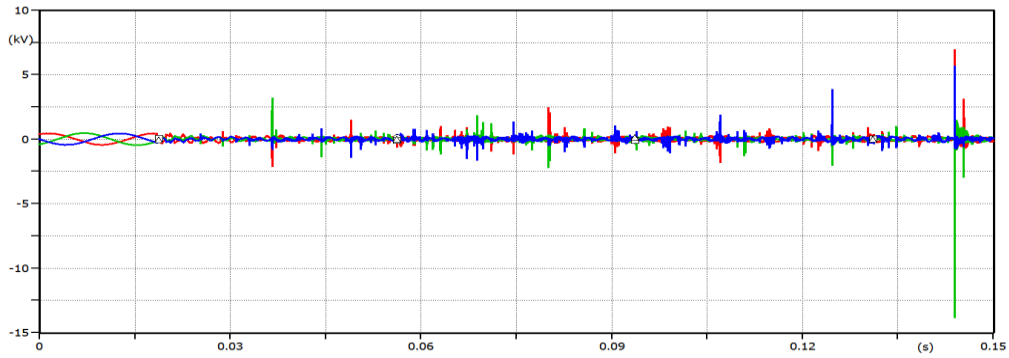

Figure 7.115 Voltages at bus G: when SCF occurs at bus X on Wind/PV hybrid system

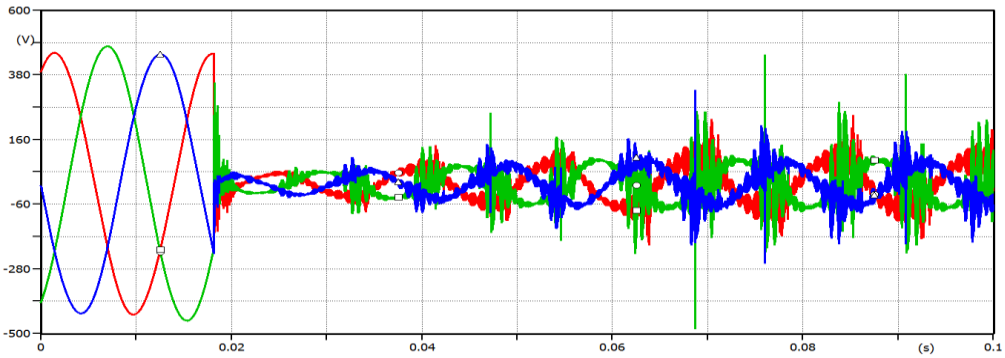

Figure 7.116 Voltages at bus G: when SCF occurs at bus Y on Wind/PV hybrid system

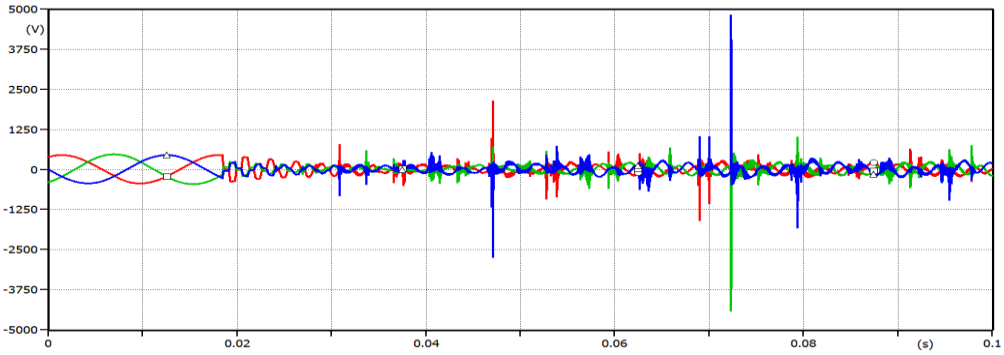

Figure 7.117 Voltages at bus P: when SCF occurs at bus Z on Wind/PV hybrid power system

7.5.3 Effect of fault resistance on Wind/PV hybrid system

A LG fault is considered to take place on phase A at bus X on the line as shown in Figure 7.118. SLG fault take place when voltage of phase A is at peak value i.e. at 22.15 msec. The waveforms of the fault current at location Z and X are given in Figures 7.119 to 7.125. For different values of fault resistance from 1Ω to 100Ω, maximum magnitude of fault currents at bus Z and at the fault location X is given on Table 7.31.

The maximum magnitude of fault currents at the bus Z and at fault location X decreases as the fault resistance increase. Fault current at bus Z on Wind/PV hybrid system is decreases from 1.833 kA at 1Ω fault resistance to 1.273 kA at 200 Ω fault resistances. Fault current at fault location X is decreases from 2.074 kA at 1Ω fault resistance to 1.266 kA at 200 Ω fault resistances. Comparison between conventional and Wind/PV hybrid system is shown in Table 7.31, it is observed that fault currents on conventional system is less as compare to Wind/PV hybrid system. It means Wind/PV farm has considerable effects on conventional system, when effect of fault resistance is studied. Transients in the fault current waveform are higher at lower value of the fault resistance as compared to that of higher value. Fault current at fault location is very high as compare to conventional system because at that point Wind/PV farms are also feeding currents.

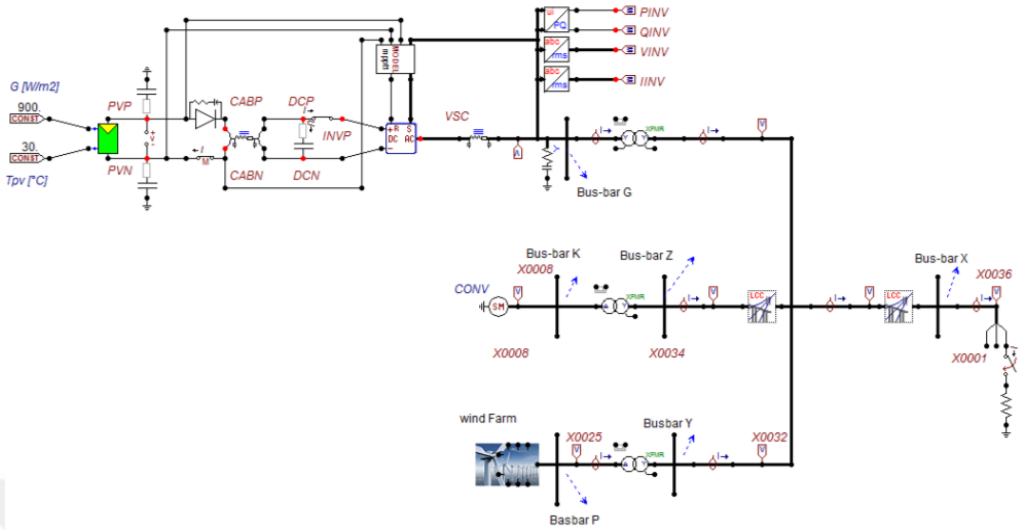

Figure 7.118 Configuration of studied Wind/PV hybrid system: when fault resistance varies from 1Ω to 100Ω with LG fault occurs on phase A at bus X

Table 7.31 Effect of fault resistance on fault current at bus Z and fault location X on Wind/PV hybrid power system & its comparison with conventional system alone

Fault Resistance (Ω)	**Maximum Magnitude of Fault Current at Bus Z (A)**		**Maximum Magnitude of Fault Current at Fault Location X (A)**	
	Conventional Power System (Without Wind/PV Farm)	Wind/PV Hybrid Power System	Conventional Power System (Without Wind/PV Farm)	Wind/PV Hybrid Power System
1	2136	1833	1742	2074
5	2098	1798	1699	1991
10	2051	1756	1649	1893
20	1966	1679	1561	1724
30	1889	1610	1486	1583
50	1753	1492	1365	1420
100	1499	1273	1159	1266

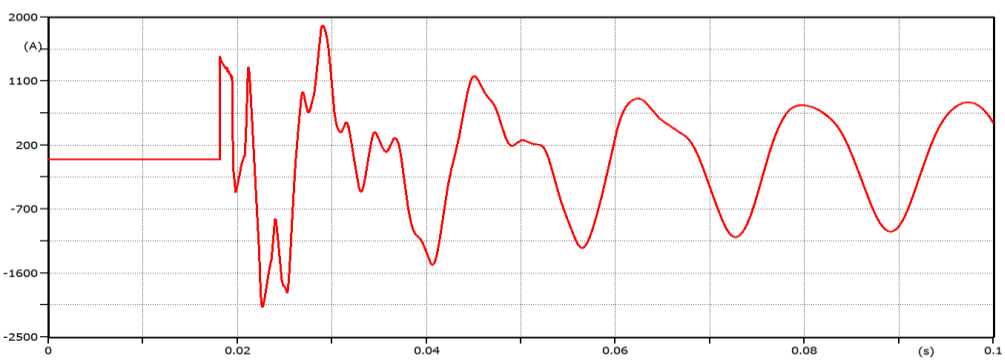

Figure 7.119(a) Fault Current at fault location X when fault resistance is 1Ω on PV/Wind hybrid system

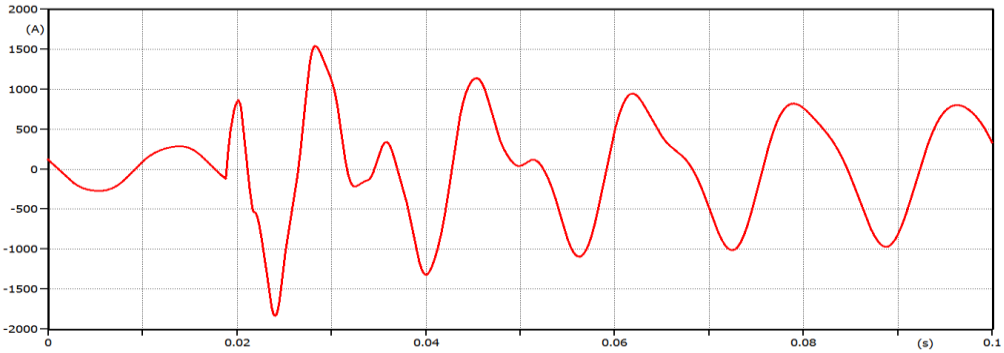

Figure 7.119(b) Fault Current at bus Z when fault resistance 1Ω on PV/Wind hybrid system

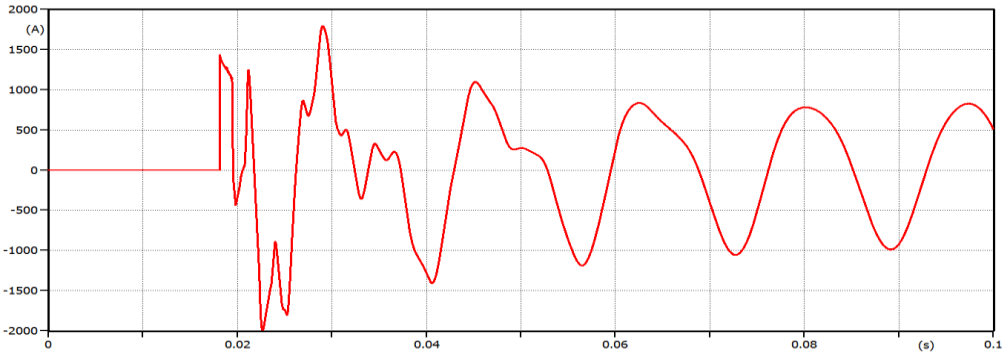

Figure 7.120(a) Fault Current at fault location X when fault resistance is 5Ω on PV/Wind hybrid system

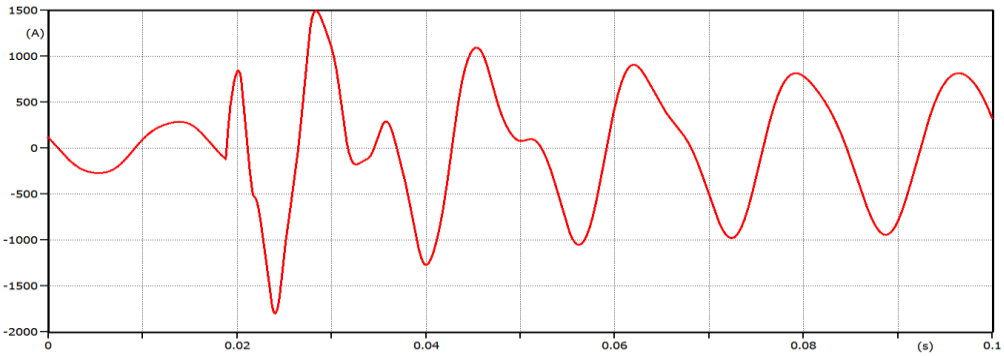

Figure 7.120(b) Fault Current at bus Z when fault resistance is 5Ω on PV/Wind hybrid system

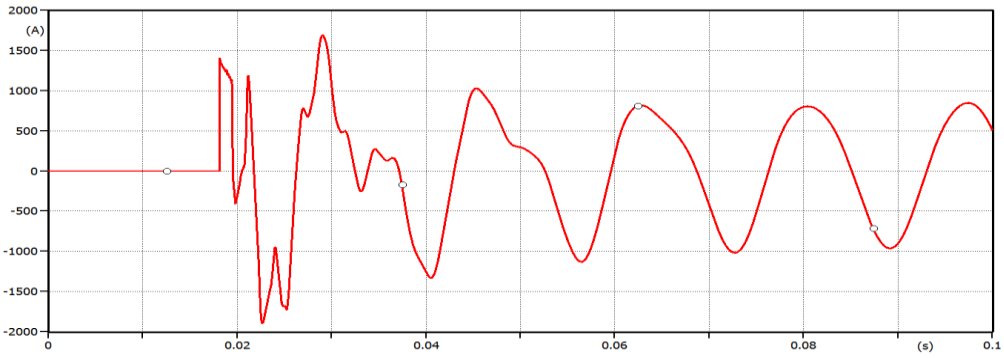

Figure 7.121(a) Fault Current at fault location X when fault resistance is 10Ω on PV/Wind hybrid system

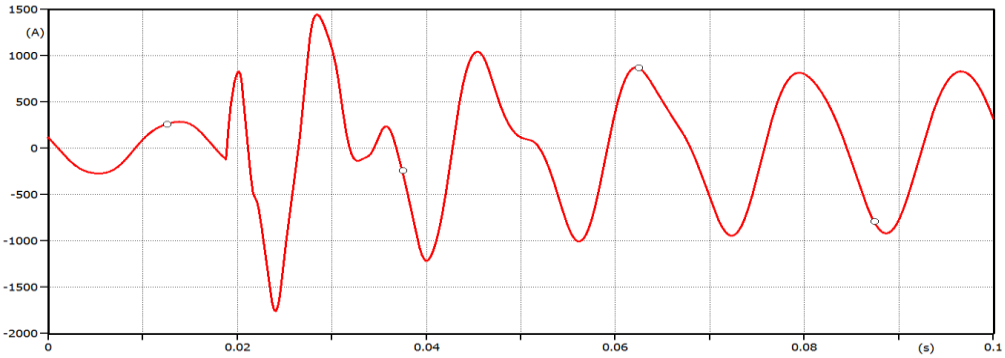

Figure 7.121(b) Fault Current at bus Z when fault resistance is 10Ω on PV/Wind hybrid system

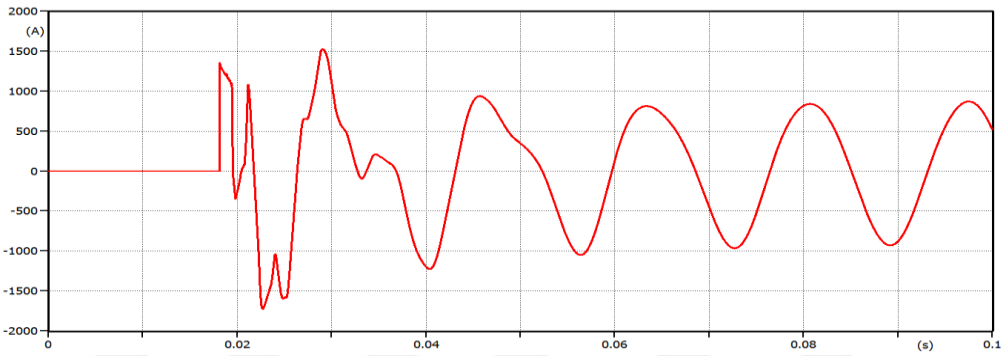

Figure 7.122(a) Fault Current at fault location X when fault resistance is 20Ω on PV/Wind hybrid system

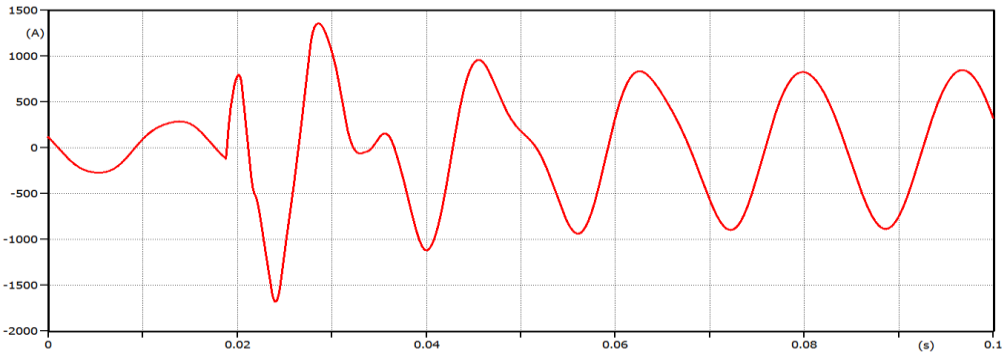

Figure 7.122(b) Fault Current at bus Z when fault resistance is 20Ω on PV/Wind hybrid system

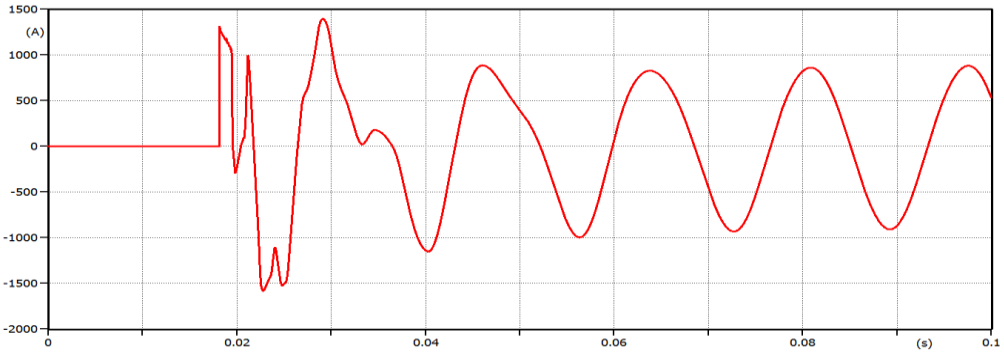

Figure 7.123(a) Fault Current at fault location X when fault resistance is 30Ω on PV/Wind hybrid system

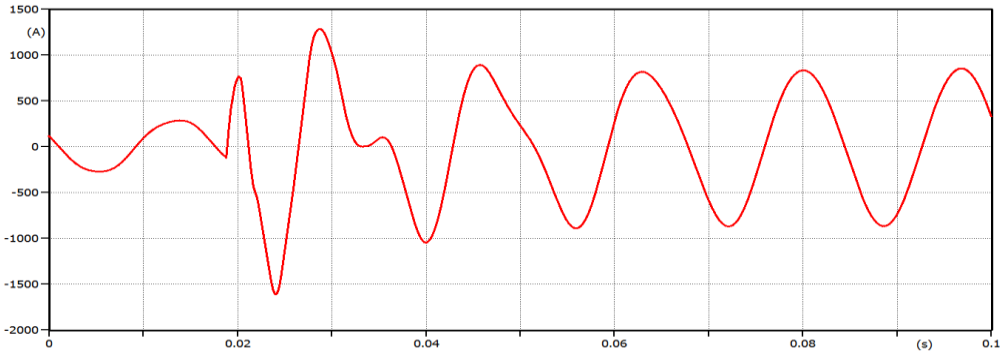

Figure 7.123(b) Fault Current at bus Z when fault resistance is 30Ω on PV/Wind hybrid system

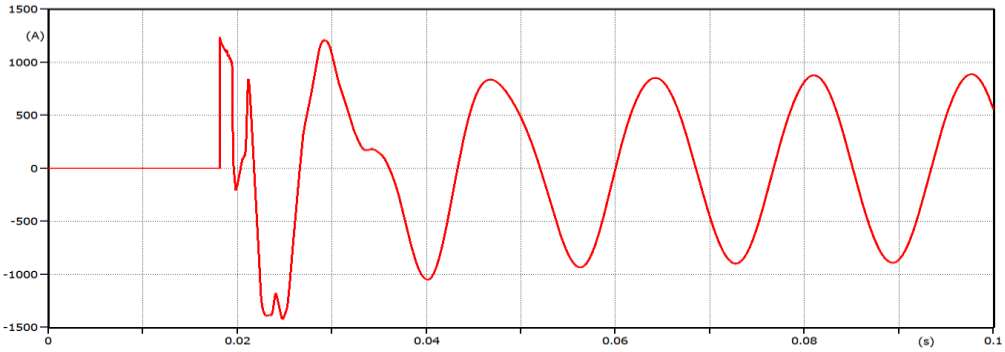

Figure 7.124(a) Fault Current at fault location X when fault resistance is 50Ω on PV/Wind hybrid system

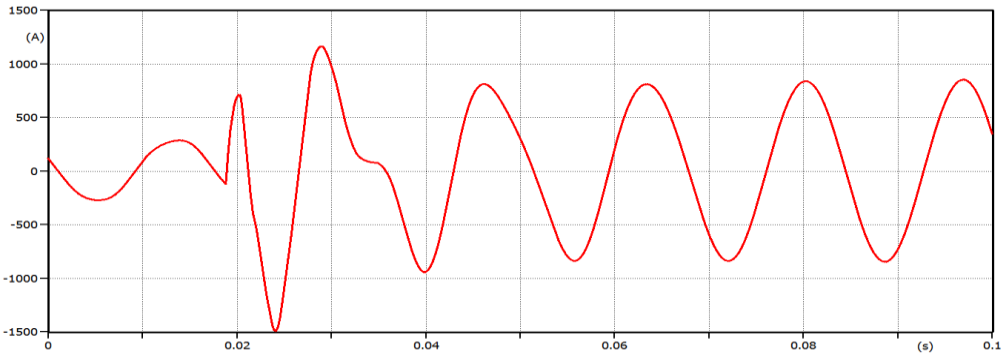

Figure 7.124(b) Fault Current at bus Z when fault resistance is 50Ω on PV/Wind hybrid system

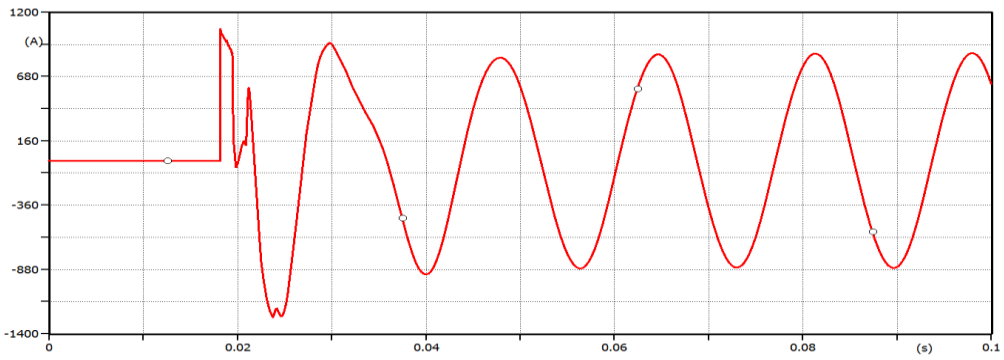

Figure 7.125(a) Fault Current at fault location X when fault resistance is 100Ω on PV/Wind hybrid system

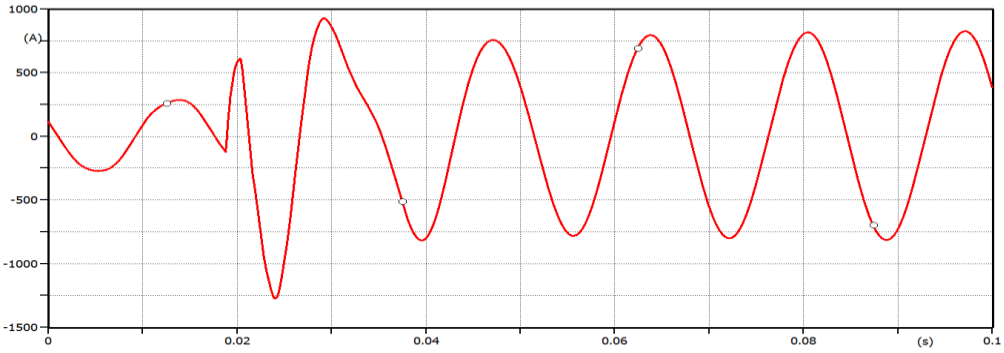

Figure 7.125(b) Fault Current at bus Z when fault resistance is 100Ω on PV/Wind hybrid system

When SLG fault occurs on phase A at fault location X, than voltage of faulted phase A, drop to zero and have no wave attenuation because fault occurs at same location, while voltage of un-faulted phases becomes higher than rated voltage. While voltage of faulted phase at bus Z is not exactly drop to zero but it has small value of voltage and wave attenuation because fault occurs far from bus Z as shown in Figures from 7.126 to 7.129. Voltage of un-faulted phases measured at fault resistances 1 Ω, 10 Ω, 50 Ω & 100 Ω. It is observed that as fault resistance increases voltages of un-faulted phases decreased & wave attenuation is also decreased. Voltages of un-faulted voltage at bus decreases from 1.098 MV to 0.950 MV and at fault location decreases from 1.128 MV to 0.935 as given in Table 7.32 while, rated voltage at this transmission line is 0.40 MV.

Table 7.32 Maximum magnitude of voltage of un-faulted phases at bus Z and fault location X: when SLG fault occur with fault resistance varies from 1 Ω to 100 Ω

Fault Resistance (Ω)	**Wind/PV Hybrid Power System**			
	Maximum Magnitude of Voltage of Un-faulted phases at Bus Z (MV)		Maximum Magnitude of Voltage of Un-faulted Phases at Bus X (MV)	
	Phase B	Phase C	Phase B	Phase C
1	1.216	1.098	1.082	1.128
10	1.171	1.059	1.057	1.101
50	1.018	1.003	9.696	1.006
100	0.889	0.950	0.867	0.935

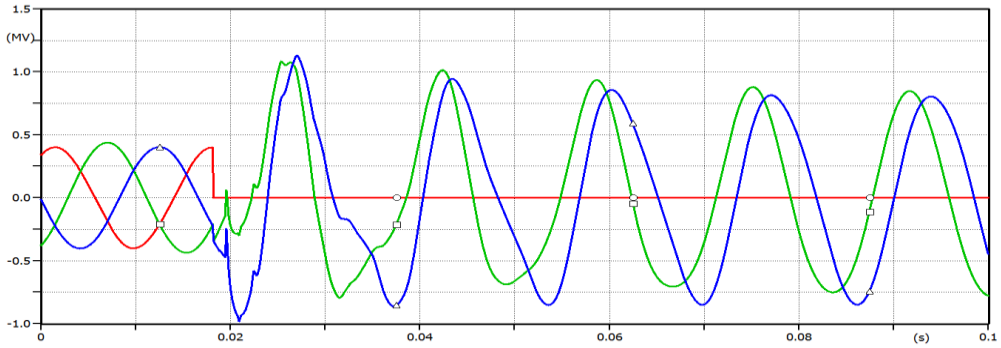

Figure 7.126(a) 3-phase voltages at fault location X: when SLG fault occurs on phase A with fault resistance 1 Ω on Wind/PV hybrid power system

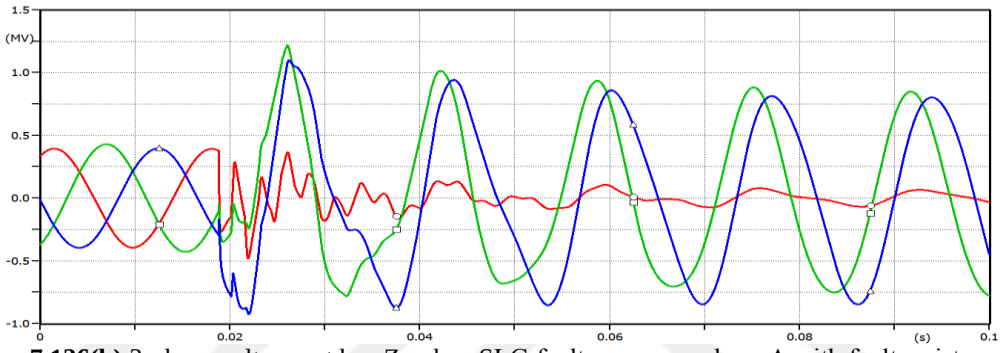

Figure 7.126(b) 3-phase voltages at bus Z: when SLG fault occurs on phase A with fault resistance 1 Ω on Wind/PV hybrid power system

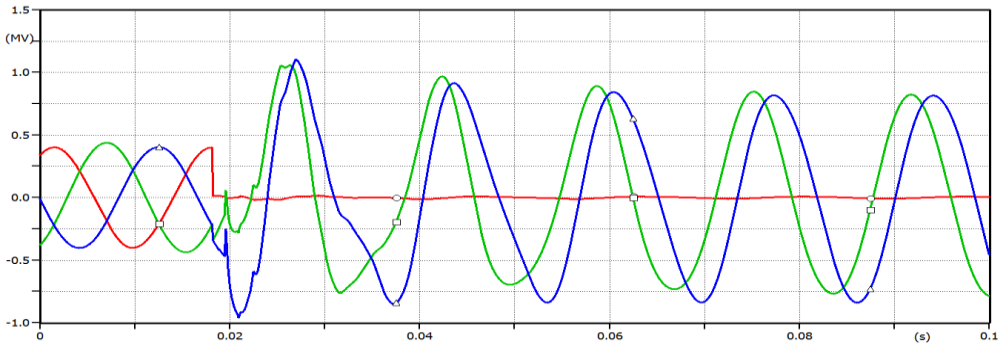

Figure 7.127(a) 3-phase voltages at fault location X: when SLG fault occurs on phase A with fault resistance 10 Ω on Wind/PV hybrid power system

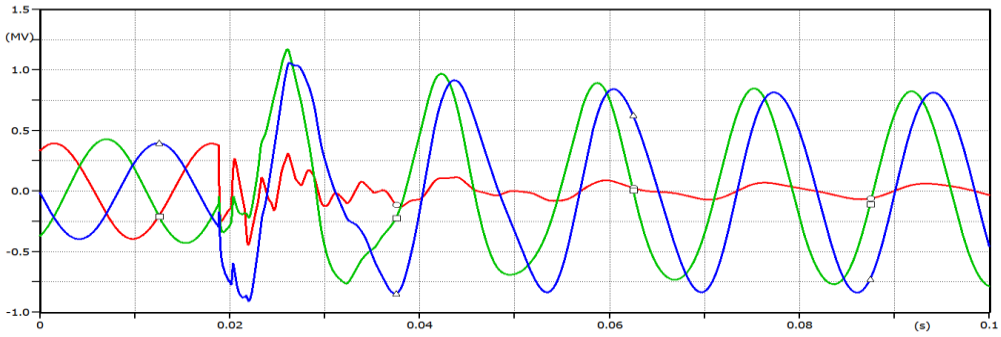

Figure 7.127(b) 3-phase voltages at bus Z: when SLG fault occurs on phase A with fault resistance 10 Ω on Wind/PV hybrid power system

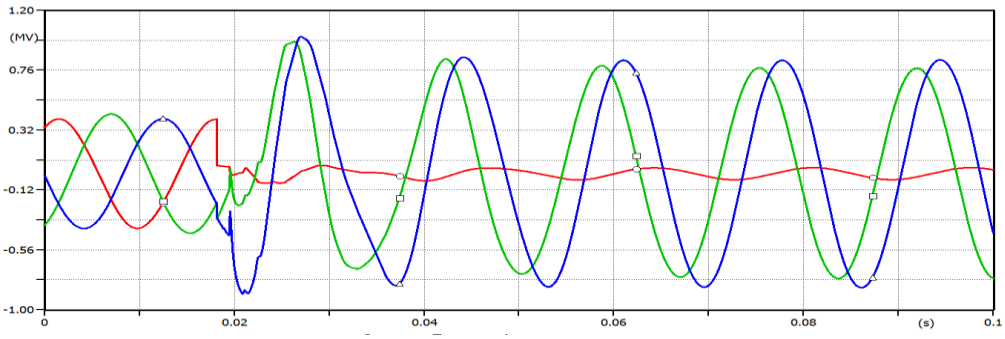

Figure 7.128(a) 3-phase voltages at fault location X: when SLG fault occurs on phase A with fault resistance 50 Ω on Wind/PV hybrid power system

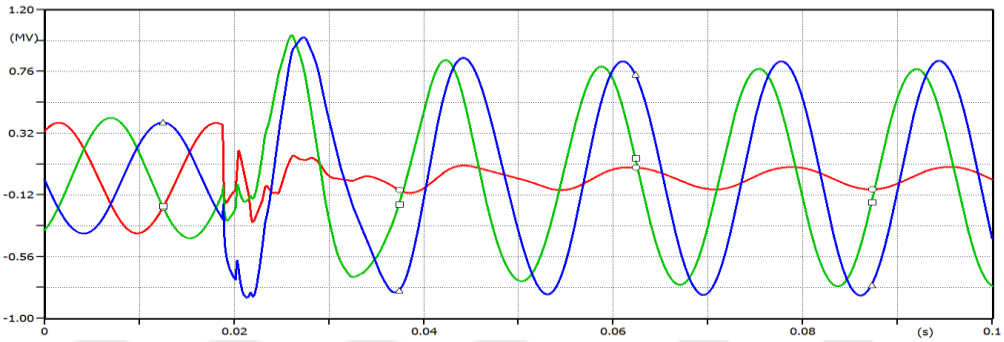

Figure 7.128(b) 3-phase voltages at bus Z: when SLG fault occurs on phase A with fault resistance 50 Ω on Wind/PV hybrid power system

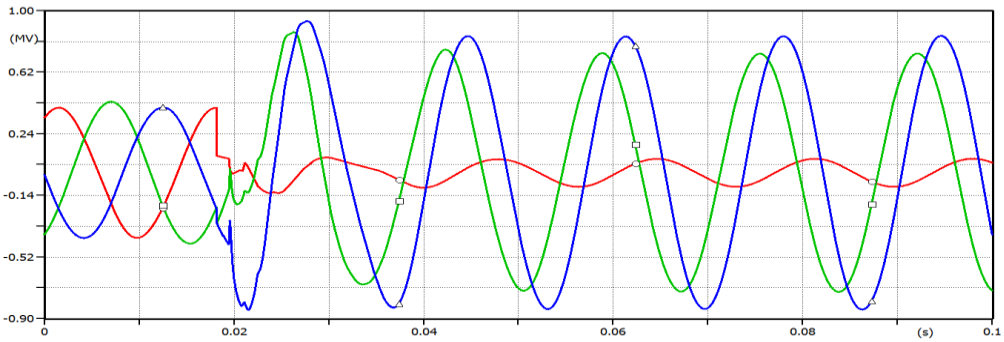

Figure 7.129(a) 3-phase voltages at fault location X: when SLG fault occurs on phase A with fault resistance 100 Ω on Wind/PV hybrid power system

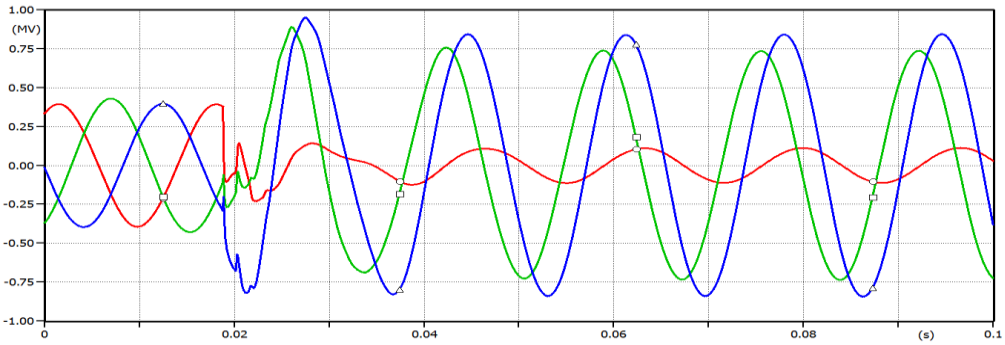

Figure 7.129(b) 3-phase voltages at bus Z: when SLG fault occurs on phase A with fault resistance 100 Ω on Wind/PV hybrid power system

7.5.3.1 Effect of fault resistance with 3-phase SCF

3-phase SCF is take place at bus X on the line as shown in Figure 7.130. SCF occurs when voltage of phase A is at peak value i.e. at 22.15 msec. The waveforms of the fault current at bus Z and fault location X are given in Figures 7.131 to 47. For various values of fault resistance, maximum magnitudes of fault currents at the fault location X and at bus Z are given on Tables 7.33.

The maximum magnitude of fault currents at fault location X decreases as the fault resistance increase. Fault current at fault location X is decreases from 5.976 kA at 1Ω fault resistance to 2.555 kA at 100 Ω fault resistances. Comparison between fault currents due to LG fault and SCF at fault location X and bus Z are shown in Tables 7.33, it is observed that fault currents due to LG fault is less as compare to SCF on Wind/PV hybrid system. It means SCF has severe effects as compare to LG fault on Wind/PV hybrid system, when effect of fault resistance is studied. It's also observed that SCF current is reduced as fault resistance is increased. Transients in the fault current waveform are higher at lower value of the fault resistance as compared to that of higher value. It is also analysed that that wave attenuation is also higher due to SCF as compare to LG fault.

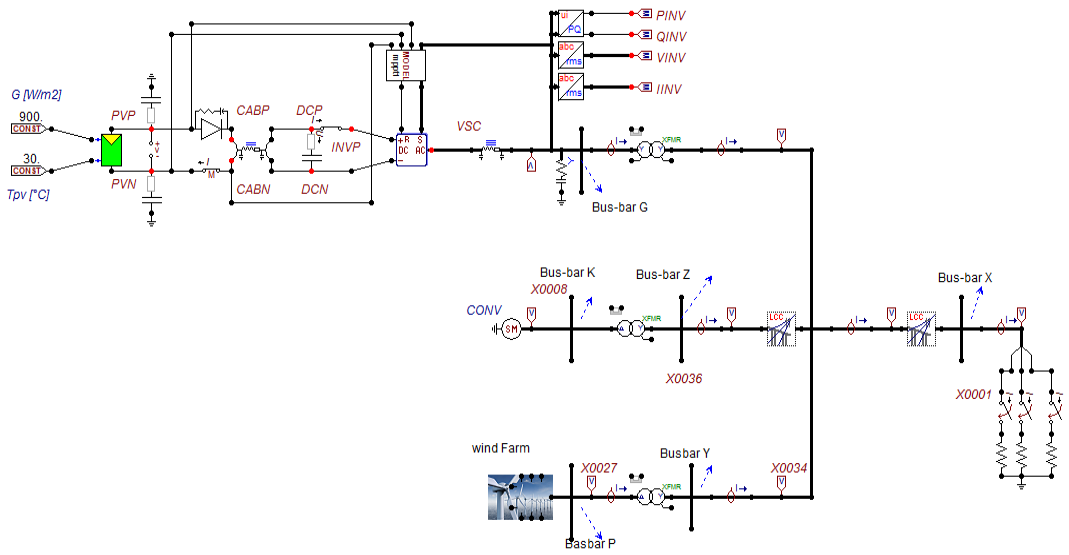

Figure 7.130 Configuration of studied Wind/PV hybrid power system: when fault resistance varies from 1Ω to 100Ω with SCF occurs at bus-bar X

Table 7.33 Maximum magnitudes of faulted phase currents at fault location X on Wind/PV hybrid system due to LG fault and SCF for different fault resistances

Fault Resistance R_f (Ω)	**Maximum magnitude of fault current (A)**			
	LG Fault	3-Phase SCF		
	Phase A	Phase A	Phase B	Phase C
1	1742	5263	5976	5767
5	1699	5006	5709	5411
10	1649	4709	5336	5009
20	1561	4190	4716	4534
30	1486	3753	4232	4135
50	1365	3065	3525	3481
100	1159	2347	2555	2508

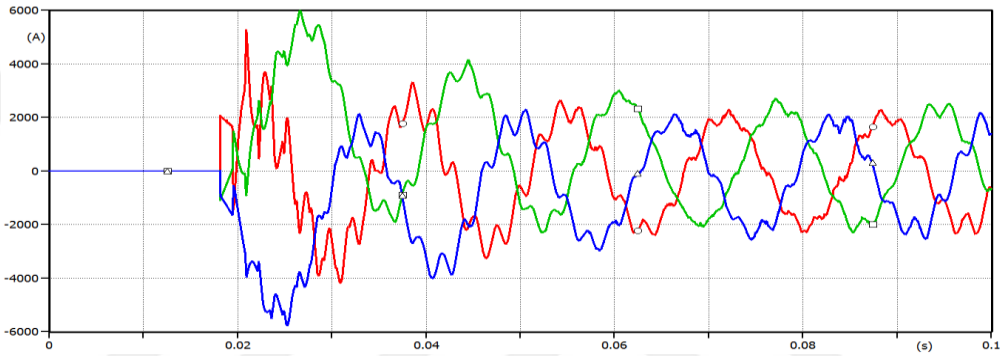

Figure 7.131 Short circuit current at fault location X: when SCF occurs at fault location X with fault resistance 1 Ω on Wind/PV hybrid power system

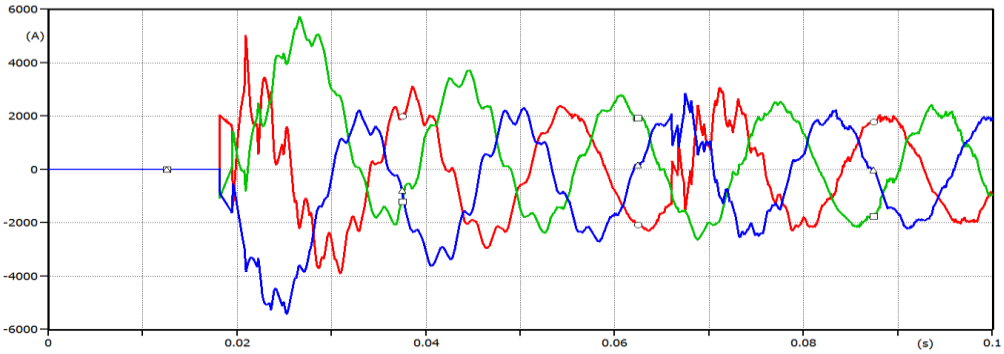

Figure 7.132 Short circuit current at fault location X: when SCF occurs at fault location X with fault resistance 5 Ω on Wind/PV hybrid power system

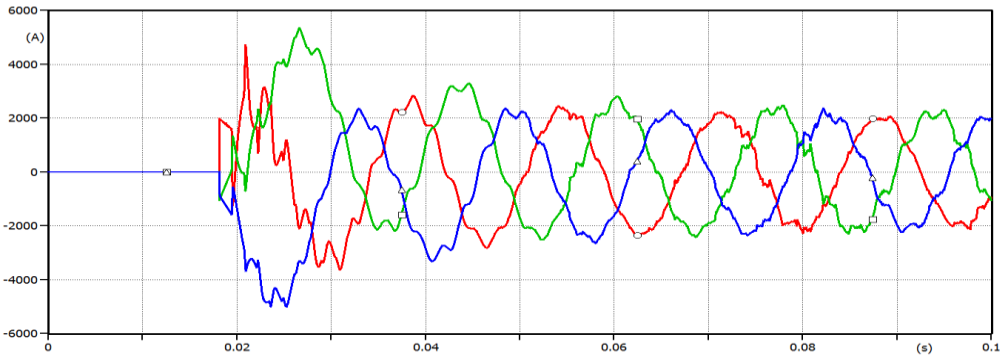

Figure 7.133 Short circuit current at fault location X: when SCF occurs at fault location X with fault resistance 10 Ω on Wind/PV hybrid power system

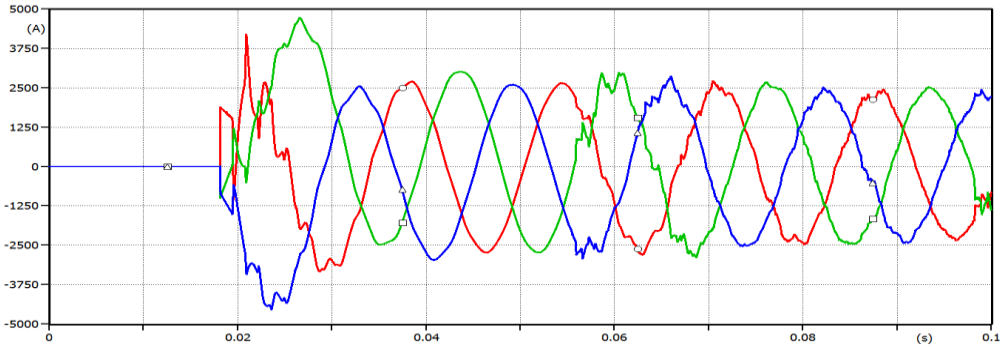

Figure 7.134 Short circuit current at fault location X: when SCF occurs at fault location X with fault resistance 20 Ω on Wind/PV hybrid power system

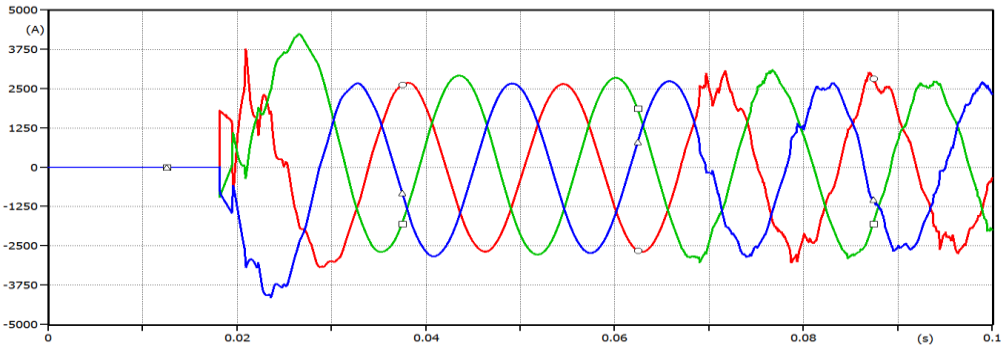

Figure 7.135 Short circuit current at fault location X: when SCF occurs at fault location X with fault resistance 30 Ω on Wind/PV hybrid power system

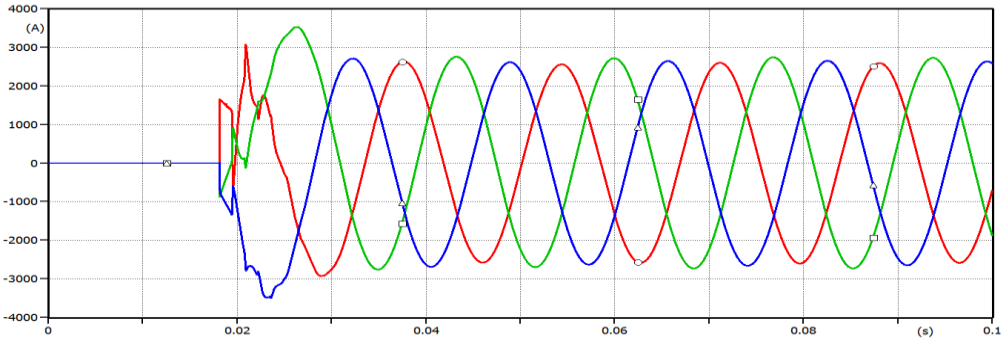

Figure 7.136 Short circuit current at fault location X: when SCF occurs at fault location X with fault resistance 50 Ω on Wind/PV hybrid power system

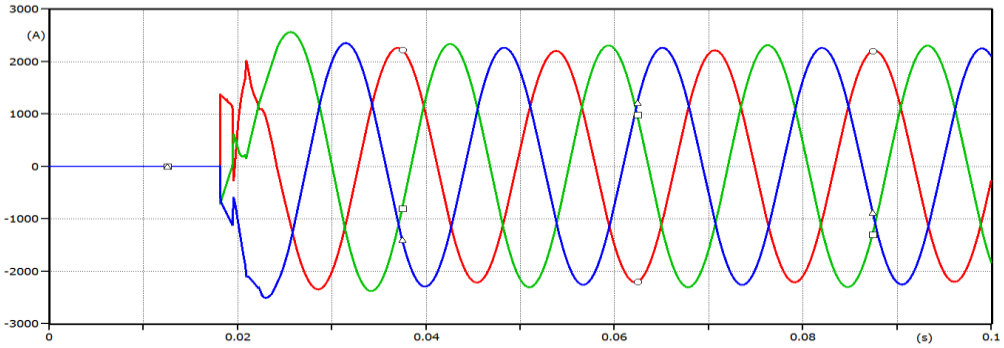

Figure 7.137 Short circuit current at fault location X: when SCF occurs at fault location X with fault resistance 100 Ω on Wind/PV hybrid power system

7.5.4 Effect of line length on PV/Wind hybrid system

The studied Wind/PV Hybrid power system is as given in Figure 7.138. SLG fault takes place on phase A at the end of line. Fault occurs on phase A, when the phase voltage is at the peak value i.e. 18.15 msec at fault point but at sending end it takes some travel time. The faulted phase currents at bus Z and bus X, during fault are computed for various line lengths from 20 km to 260 km and plotted to obtain faulted phase current waveforms at bus X and bus Z are shown in Figures 7.139 to 7.150 respectively on PV/Wind hybrid system. The Maximum values of faulted phase current at fault location X and bus Z for different line lengths are given in Table 7.34 and Table 7.35 respectively.

Simulation result shows that the maximum magnitude of the currents at fault point increases as the line length increases due to capacitance of transmission line, also ripples along the line attenuate as the line length increases. Fault current at fault location X increases from 1.427 kA to 2.642 kA as shown in Table 7.34 so, effect of wind/PV farm on fault currents at fault location X is much more as compare to conventional system alone. It is also observed that as line length increases travel time of fault current at bus Z is increasing and harmonics frequency is decreasing.

Voltages of un-faulted phases are shown in Figures 7.151 to 7.156. Voltage of faulted phase is reduced to minimum value at bus Z and voltages of un-faulted phases are increased. It is also observed that wave attenuation is also decreased as line length increases.

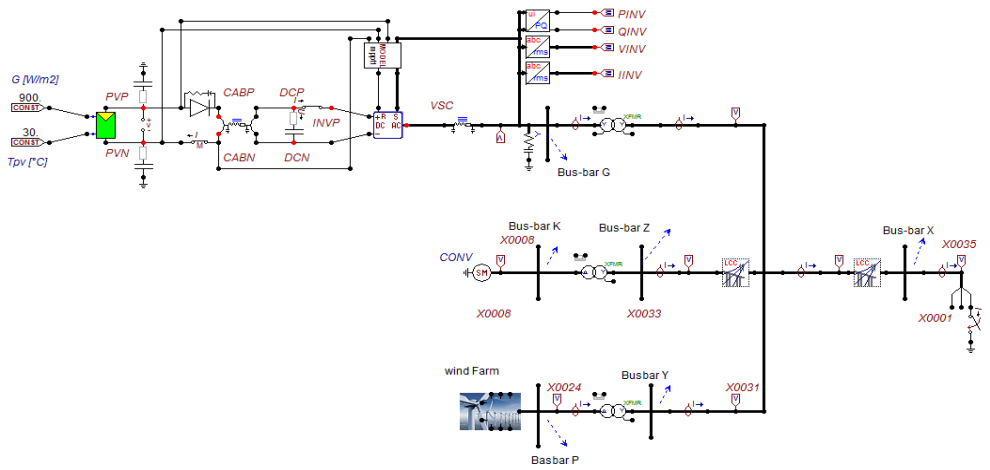

Figure 7.138 Configuration of studied Wind/PV hybrid system: when line length varies from 20 km to 260 km

Table 7.34 Maximum magnitude of faulted phase current against line length at location fault location X on Wind/PV hybrid power system

Line Length (km)	**Maximum Magnitude of Fault Current at Fault Location X (A)**	
	Conventional System Alone	Wind/PV Hybrid System
20	1159	1427
100	1483	1798
200	1754	2096
220	1814	2300
240	2005	2487
260	2205	2642

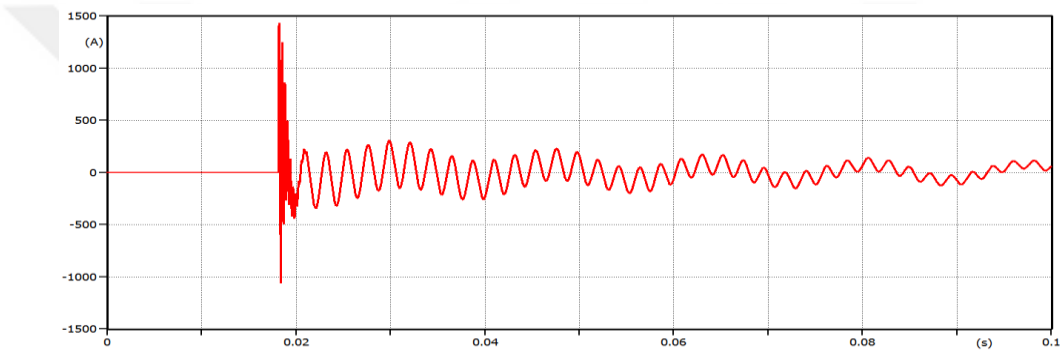

Figure 7.139 Fault Current at fault location X on Wind/PV hybrid system: when line length is 20 km

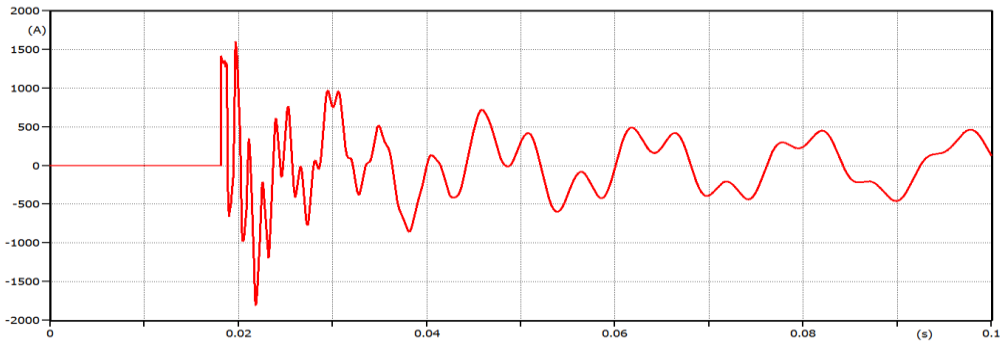

Figure 7.140 Fault Current at fault location X on Wind/PV hybrid system: when line length is 100 km

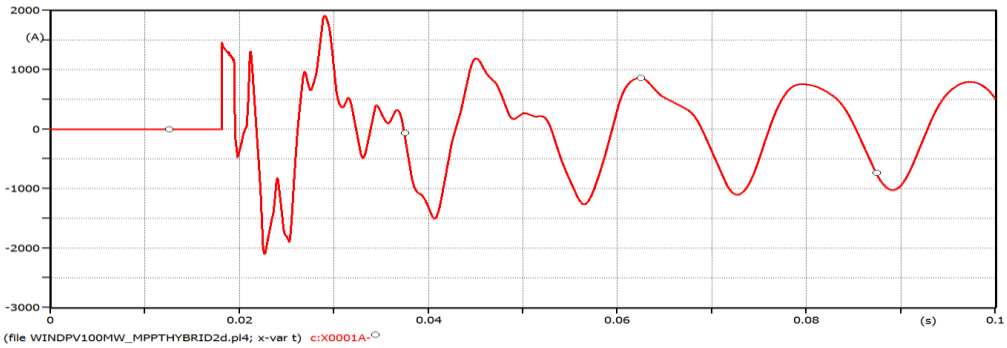

Figure 7.141 Fault Current at fault location X on Wind/PV hybrid system: when line length is 200 km

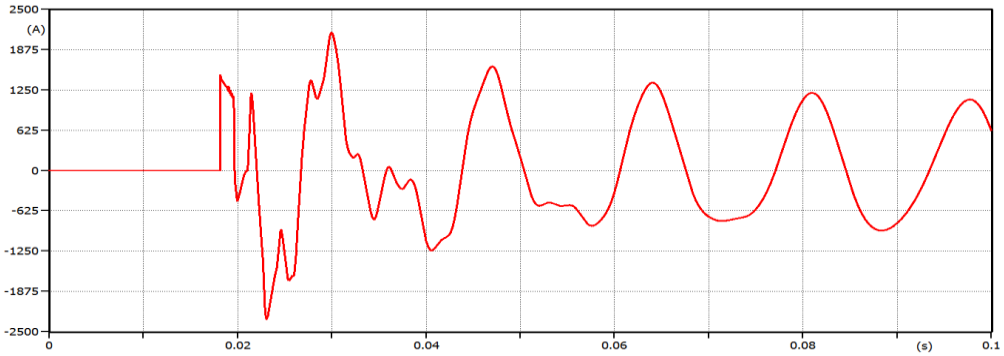

Figure 7.142 Fault Current at fault location X, on Wind/PV hybrid system: when line length is 220 km

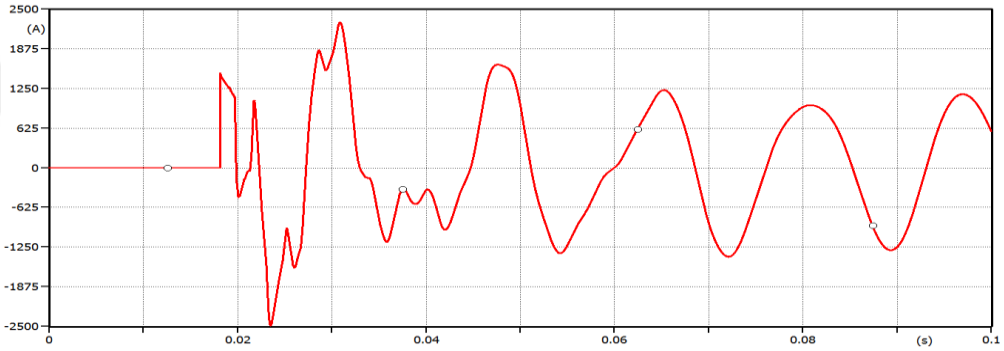

Figure 7.143 Fault Current at fault location X on Wind/PV hybrid system: when line length is 240 km

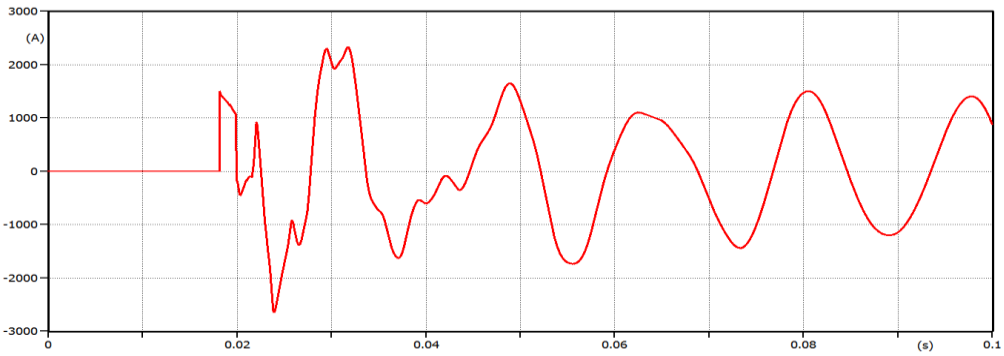

Figure 7.144 Fault Current at fault location X on Wind/PV hybrid system: when line length is 260 km

Table 7.35 Maximum magnitude of faulted phase current against line length at bus Z and effects of Wind/PV system on it

Line Length (km)	**Maximum Magnitude of Fault Current at Bus Z (A)**	
	Conventional System Alone	Hybrid System (With Wind/PV System)
20	371.9	381.1
100	1014	1097
200	2146	1842
220	2307	1907
240	2439	2197
260	2541	2453

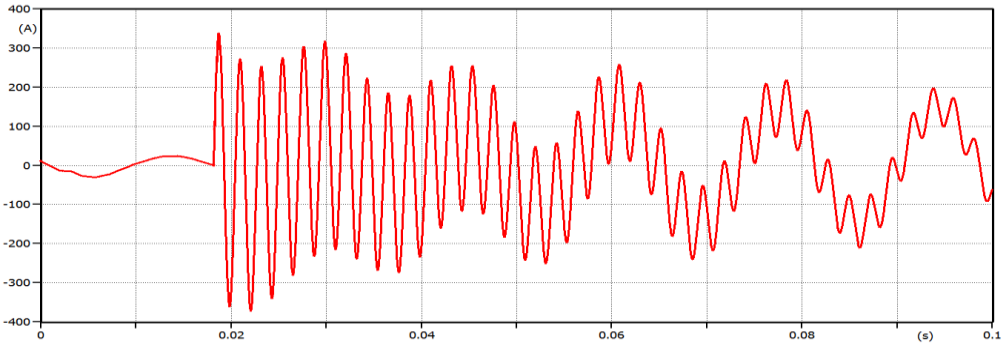

Figure 7.145 Fault Current at bus Z on Wind/PV hybrid system: when line length is 20 km

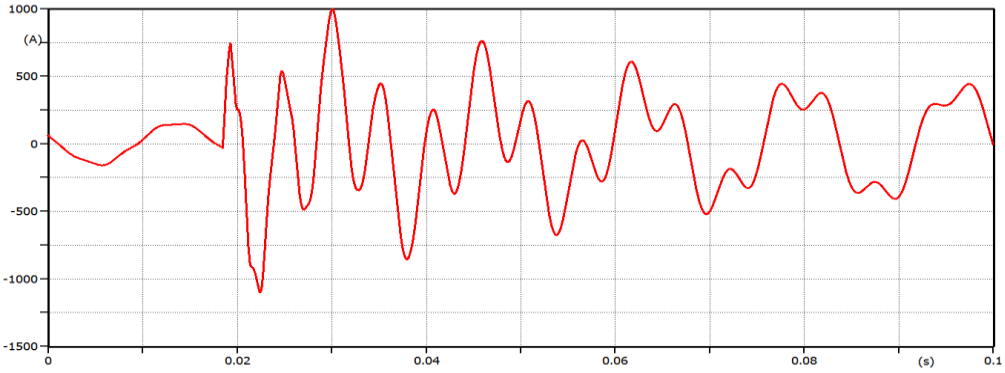

Figure 7.146 Fault Current at bus Z on Wind/PV hybrid system: when line length is 100 km

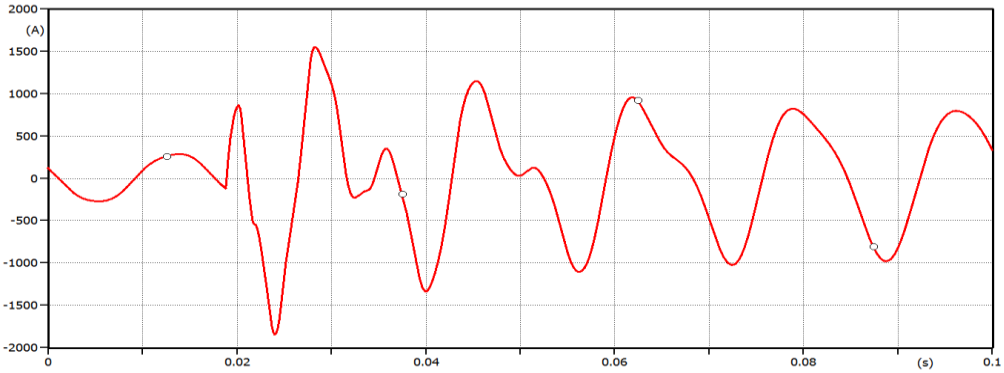

Figure 7.147 Fault Current at bus Z on Wind/PV hybrid system: when line length is 200 km

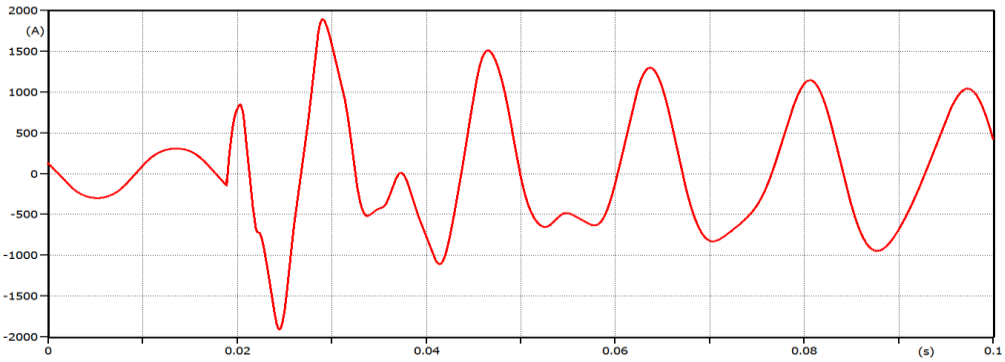

Figure 7.148 Fault Current at bus Z on Wind/PV hybrid system: when line length is 220 km

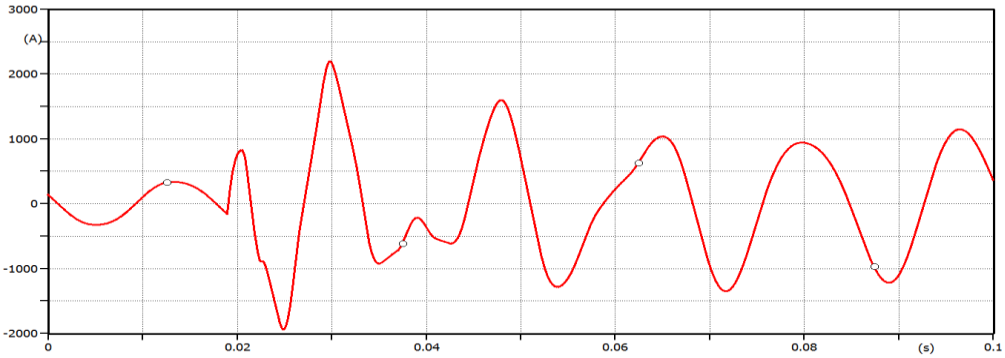

Figure 7.149 Fault Current at bus Z on Wind/PV hybrid system: when line length is 240 km

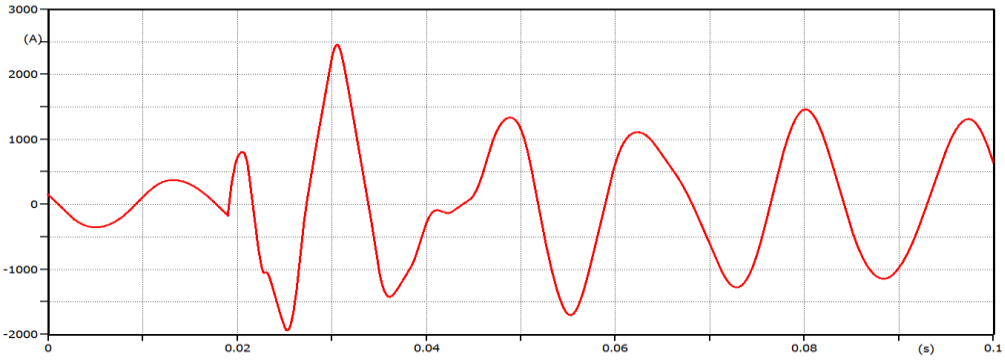

Figure 7.150 Fault Current at bus Z on Wind/PV hybrid system: when line length is 260 km

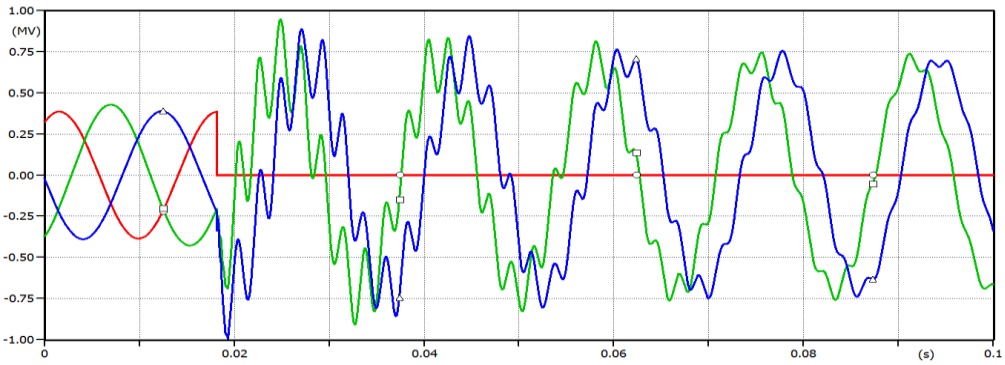

Figure 7.151(a) Voltages of un-faulted phases at bus X on Wind/PV hybrid system: when line length is 20 km

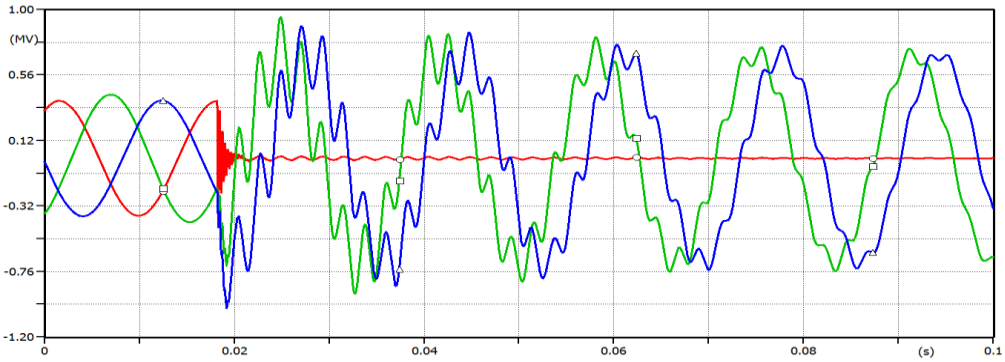

Figure 7.151(b) Voltages of un-faulted phases at bus Z on hybrid system: when line length is 20 km

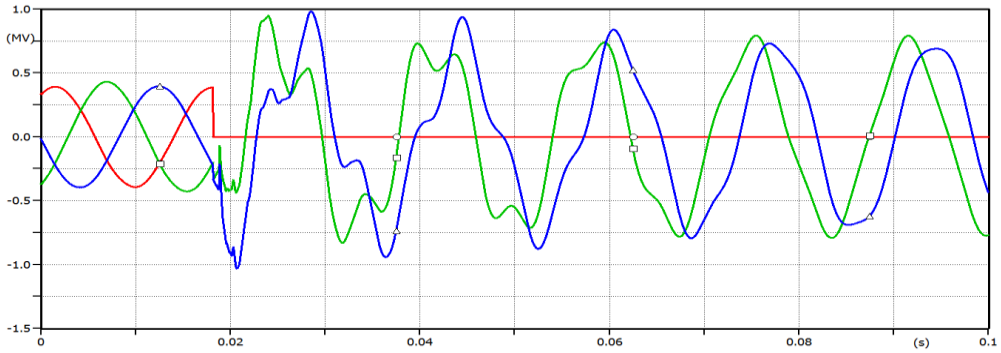

Figure 7.152(a) Voltages of un-faulted phases at bus X on Wind/PV hybrid system: when line length is 100 km

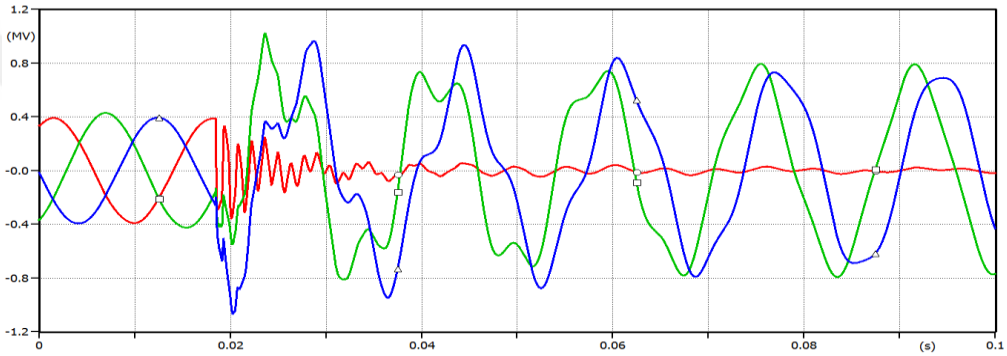

Figure 7.152(b) Voltages of un-faulted phases at bus Z on Wind/PV hybrid system: when line length is 100 km

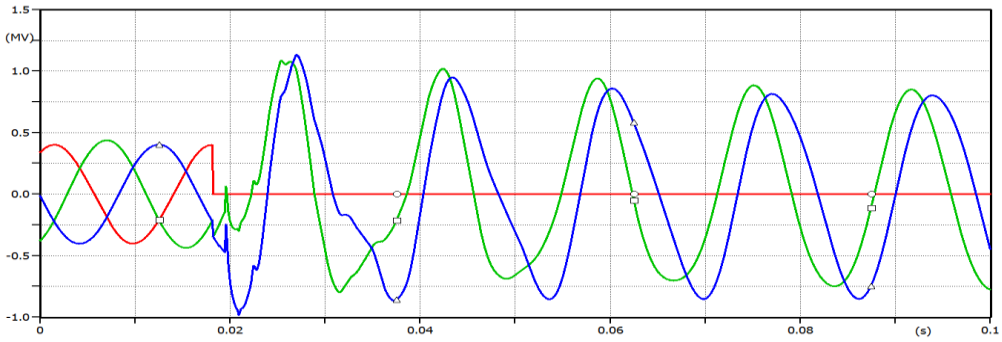

Figure 7.153(a) Voltages of un-faulted phases at bus X on Wind/PV hybrid system: when line length is 200 km

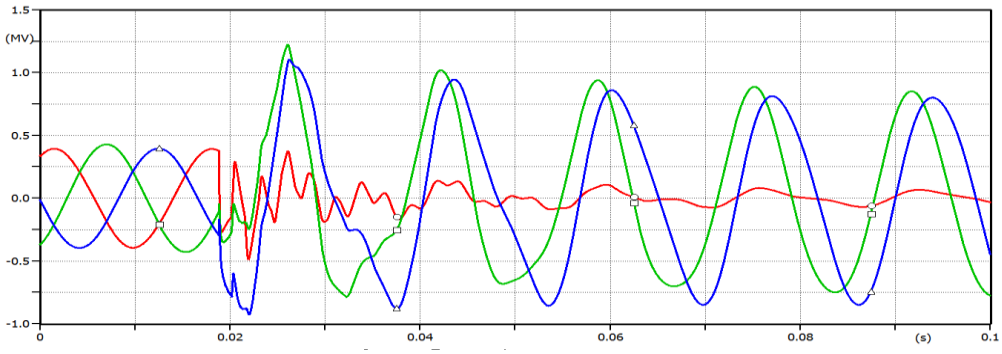

Figure 7.153(b) Voltages of un-faulted phases at bus Z on Wind/PV hybrid system: when line length is 200 km

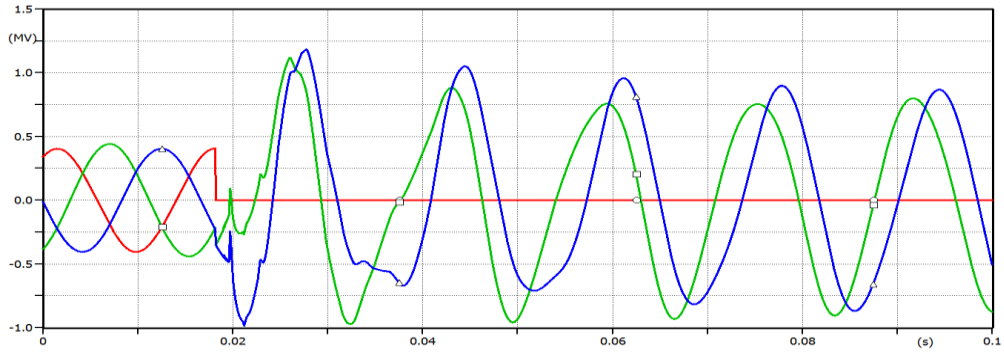

Figure 7.154(a) Voltages of un-faulted phases at bus X on Wind/PV hybrid system: when line length is 220 km

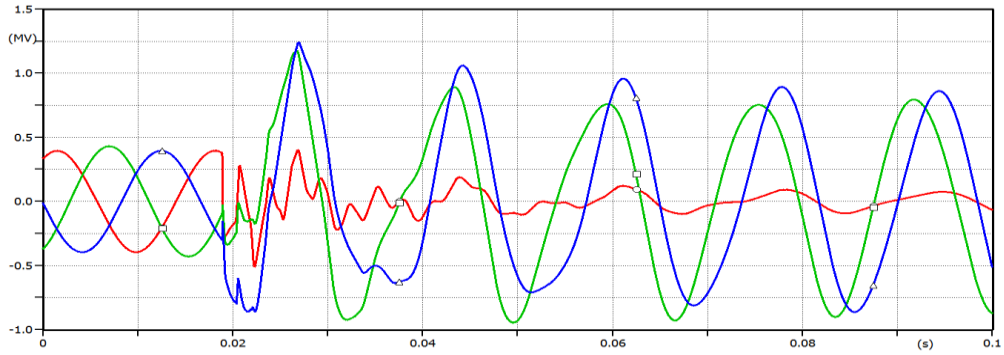

Figure 7.154(b) Voltages of un-faulted phases at bus Z on Wind/PV hybrid system: when line length is 220 km

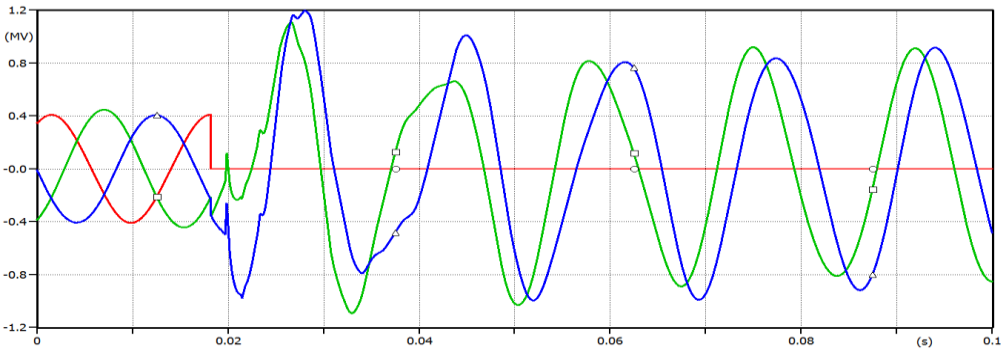

Figure 7.155(a) Voltages of un-faulted phases at bus X on Wind/PV hybrid system: when line length is 240 km

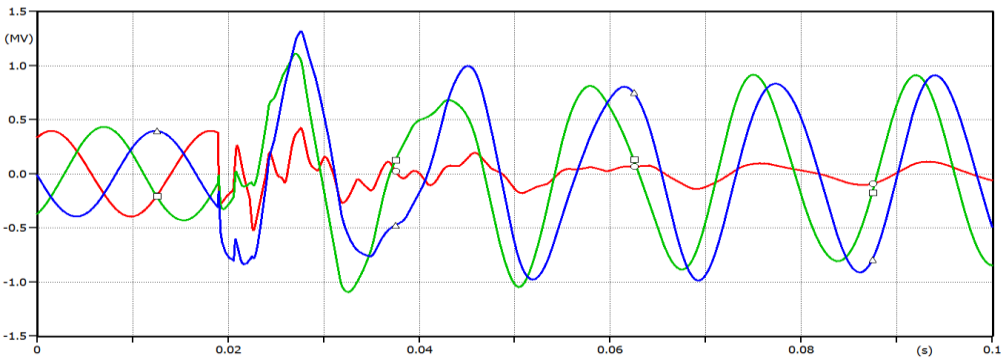

Figure 7.155(b) Voltages of un-faulted phases at bus Z on Wind/PV hybrid system: when line length is 240 km

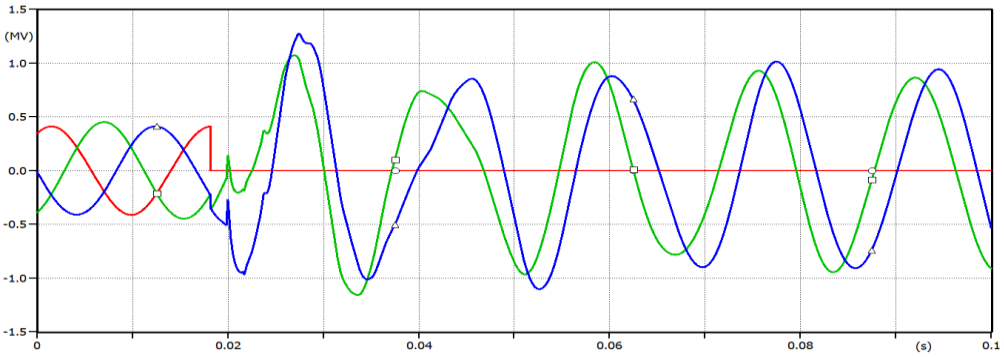

Figure 7.156(a) Voltages of un-faulted phases at bus X on Wind/PV hybrid system: when line length is 260 km

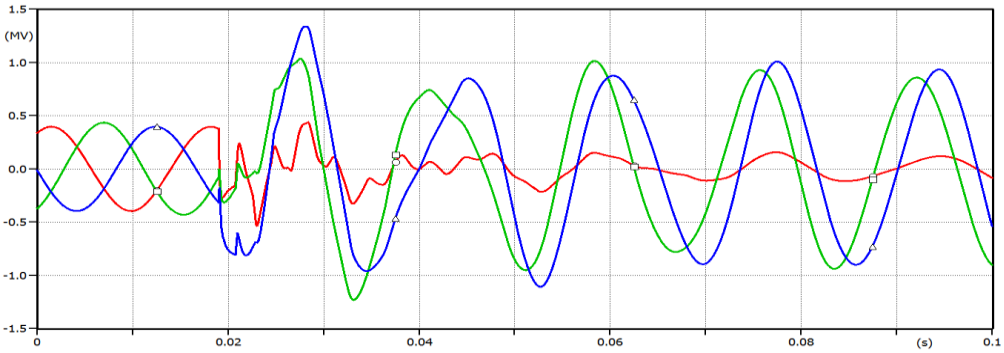

Figure 7.156(b) Voltages of un-faulted phases at bus Z on Wind/PV hybrid system: when line length is 260 km

7.5.5 Comparison between conventional and Wind/PV hybrid power system due to various faults

On this Wind/PV GCS different types of faults are considered such as SLG fault, DLG and SCF. The LG fault occurs on phase A at the end of transmission line i.e. 400 kV. In case of DLG fault, fault occurs at the receiving end of the line on phases A and B. The maximum magnitude of faulted and un-faulted currents at bus Z and fault location X is given in Table 7.36. Similarly, in the case of SCF simulation and currents computed were also taken at the fault location X and bus Z respectively as given in Table 7.36.

For different types of fault, waveforms of faulted and un-faulted phase currents at the both locations X and Z are given in Figures 7.157 to 7.159 respectively. It has been observed that maximum wave distortion occurs on the voltage waveform as compared to the current waveform. The dynamic behaviour of SCF is most severe fault than other type of faults. Hence, highest magnitude of fault current occurs at SCF.

Wind/PV contributes 10.88 % for SCF, 19.49 % for SLG fault and 19.6 % for DLG fault as compare to conventional system alone.

Table 7.36 Maximum magnitude of faulted phase current at fault location X on Wind/PV GCS

Fault Type	**Maximum Magnitude of Fault Current at Fault Location X (A)**						**Increment (%)**
	Conventional System Alone			**Wind/PV GCS**			
	Phase A	Phase B	Phase C	Phase A	Phase B	Phase C	
SCF	3716	5570	5220	5011	6176	5832	10.88
SLG	1754	-	-	2096	-	-	19.49
DLG	4279	4003	-	5119	4782	-	19.6

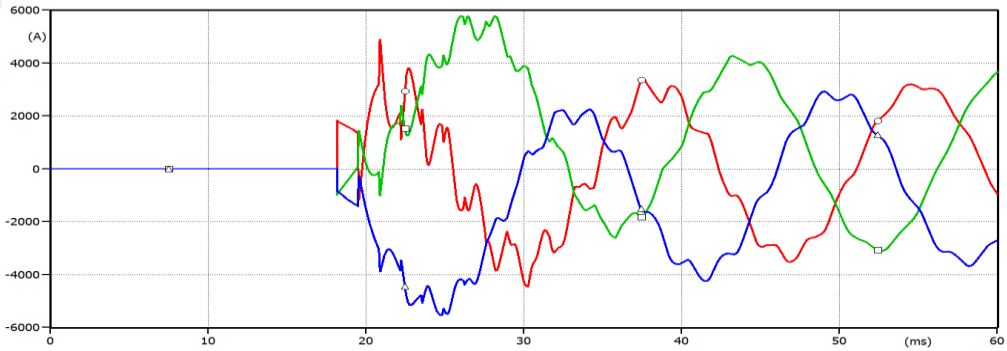

Figure 7.157(a) Three phase currents at fault location X when 3-phase SCF occur on conventional system alone

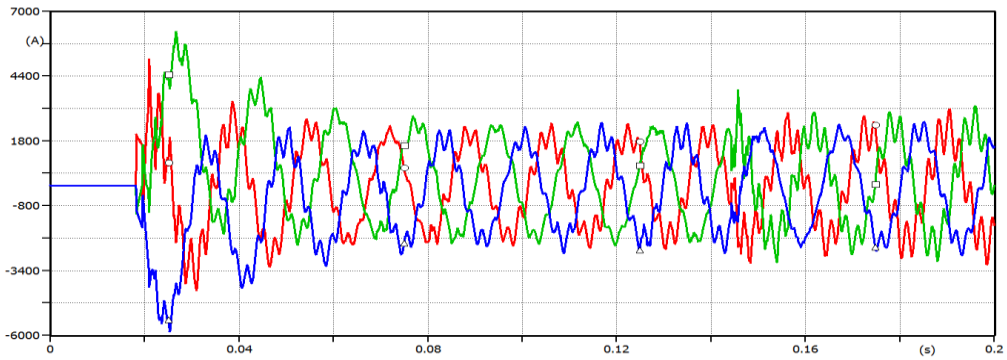

Figure 7.157(b) Fault current at fault location, when 3-phase SCF occur at location X on Wind/PV hybrid system

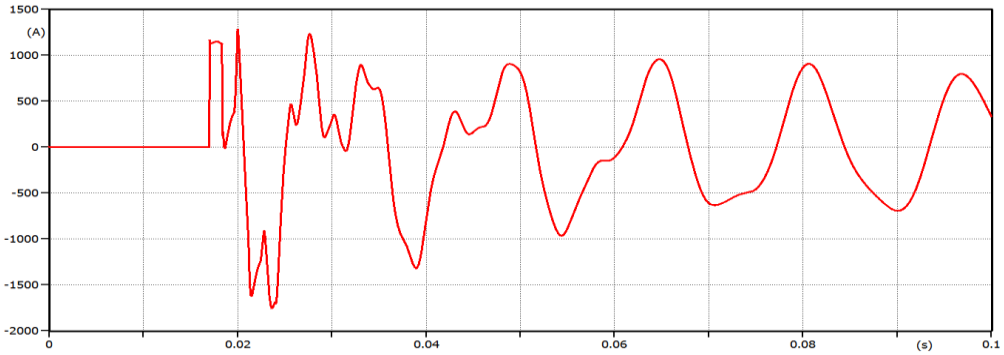

Figure 7.158(a) Faulted phase current at fault location X with SLG fault on conventional system

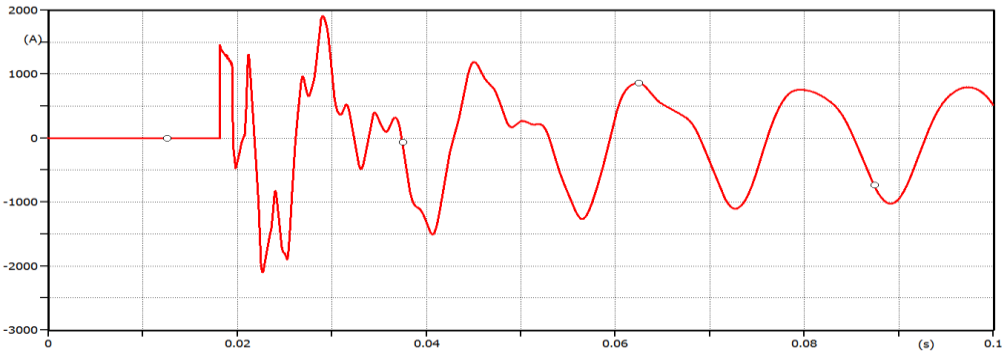

Figure 7.158(b) Faulted phase current at fault location X with SLG fault on system Wind/PV GCS

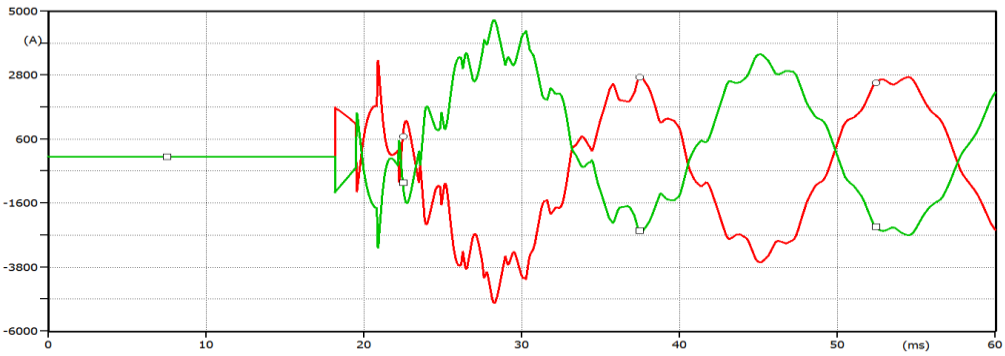

Figure 7.159(a) Current of faulted phases A and B at fault location X when DLG fault occurs on conventional system

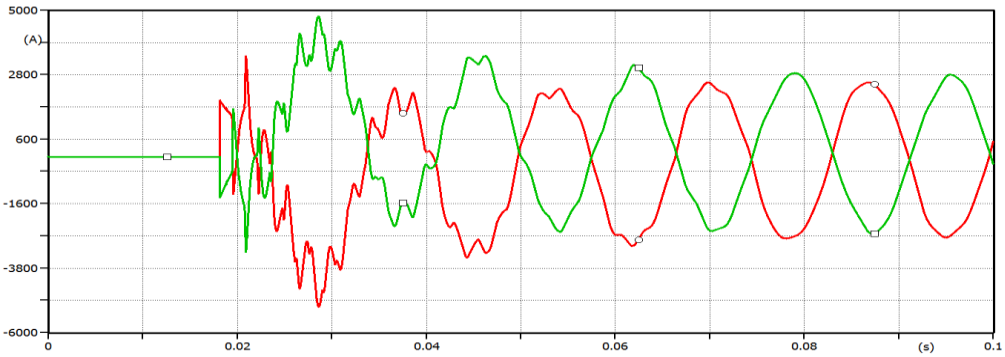

Figure 7.159(b) Current of faulted phases A and B at fault location X when DLG fault occurs on Wind/PV GCS

7.5.6 Effect of Peterson coil with SCF

SCF is considered to take place at bus-bar X with $R_f = 0$ as shown in Figure 7.160. Short circuit fault occurs when voltage of phase A is at peak value i.e. at 22.15 msec. As can be seen, the current resulting from the fault is small with resonant grounding due to the compensating effect of the Petersen coil. The system discharging and charging in SCF depends on the capacitances of the feeders with ground, and on the location of the fault. For resonant grounding (compensated) networks this process is changed, the current through Petersen coil compensates and reduces the capacitive current through the fault location. When a SLG fault occurs the faulty phase starts discharging to the ground through the fault. Healthy feeders, plus the other two healthy phases starts charging to the ground. These charging currents can be determined as zero sequence currents (Al-Zyoud and etc., 2015). Resonant coil condition is obtained when:

$$3\omega\, C_0 - \frac{1}{\omega\, L} = 0 \tag{7.1}$$

In case of complete compensation,

$$3\, L\, C\, \omega^2 = 1 \tag{7.2}$$

Table 15 gives the results in case of Petersen coil with solid earth fault. Fault current has a small value because of high percentage of compensation. This small value of fault current enables the system to continue in feeding the consumers under fault for a long time. To compensate for the capacitive earth fault current of the feeder (with 200 km), the zero sequence capacitance is approximately$0.0079\ {}^{\mu F}/_{km}$.

The waveforms of the fault current at fault location X are given in Figures 7.161 to 7.165. For different values of fault inductance, maximum magnitude of fault currents at the fault location X is given in Table 15. The maximum magnitude of fault currents at fault location X decreases as the fault inductance increases. Fault current at fault location X is decreases from 0.36 % at 1H fault inductance to 51.78 % at 65 H fault inductance. Transients in the fault current waveform are higher at lower value of the fault inductance as compared to that of higher value. It is also analysed that that wave attenuation is also higher due to SCF.

Voltage of faulted phases increased from zero at 1H 65H inductances because it also acts as voltage source. Wave attenuation is also increased as inductance increased as shown in Figures 7.166 to 7.170. It is observed that fault currents due to SLG fault is less as compare to SCF on Wind/PV GCS. It means SCF has severe effects as compare to SLG fault on Wind/PV hybrid system, when effect of fault inductance is studied. It is also analysed that that wave attenuation is also higher due to SCF as compare to SLG fault.

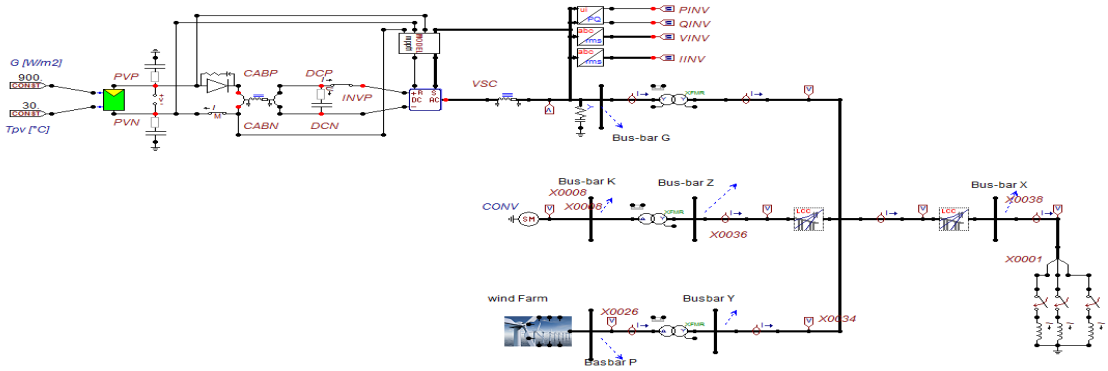

Figure 7.160 Configuration of studied Wind/PV GCS when Peterson coil varies from 1H to 65H with SCF occurs at bus X

Table 7.37 Minimization of fault currents at bus X on Wind/PV GCS due to SCF for different values of Peterson coil

Fault Inductance L_f (H)	**Maximum magnitude of fault current with SCF (A)**			**Current Minimizing (%)**
	Phase A	Phase B	Phase C	
1	5318	6154	5810	-0.36
10	4349	5733	5420	-7.73
30	3457	5111	4883	-20.84
58.6	2698	4251	3985	-45.28
65	2482	4069	3799	-51.78

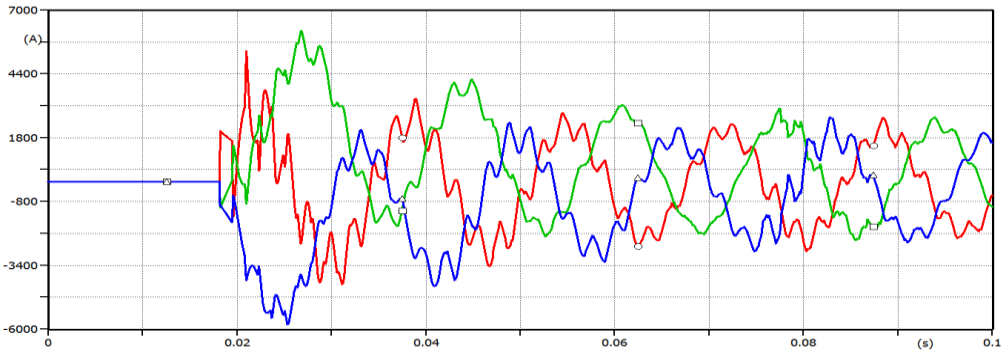

Figure 7.161 SC current at fault location X: when SCF occurs at bus X with fault inductance 1 H on Wind/PV GCS

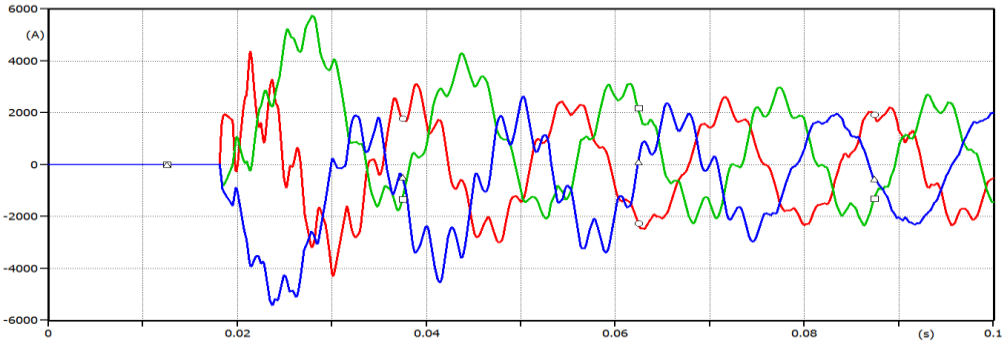

Figure 7.162 SC current at fault location X: when SCF occurs at bus X with fault inductance 10 H on Wind/PV GCS

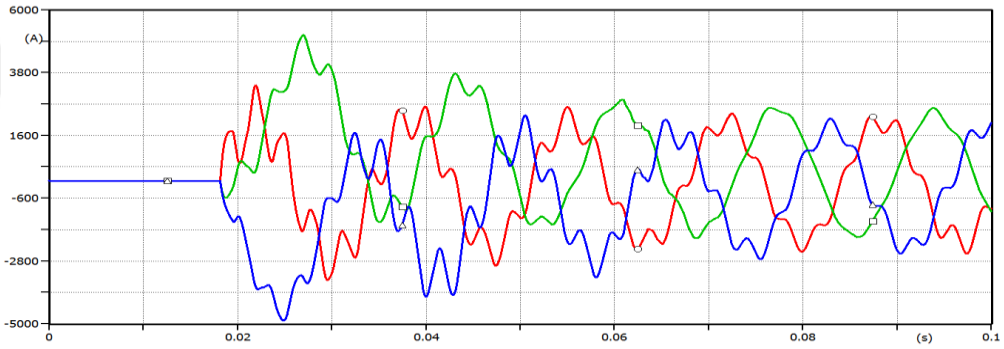

Figure 7.163 SC current at fault location X: when SCF occurs at bus X with fault inductance 30 H on Wind/PV GCS

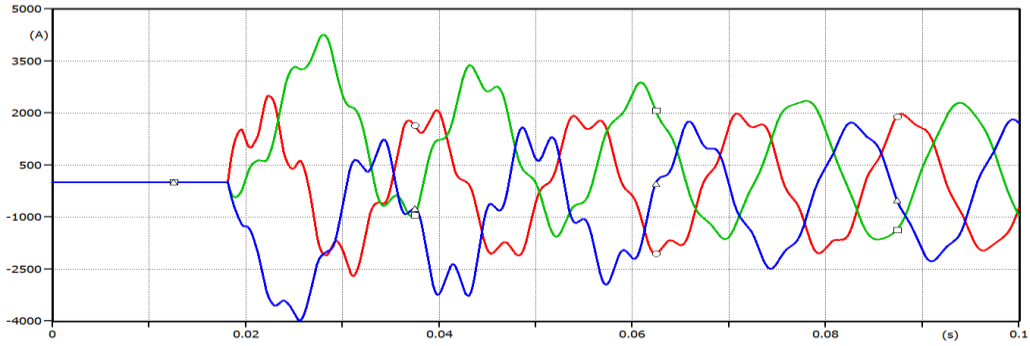

Figure 7.164 SC current at fault location X: when SCF occurs at bus X with fault inductance 58.6 H on Wind/PV GCS

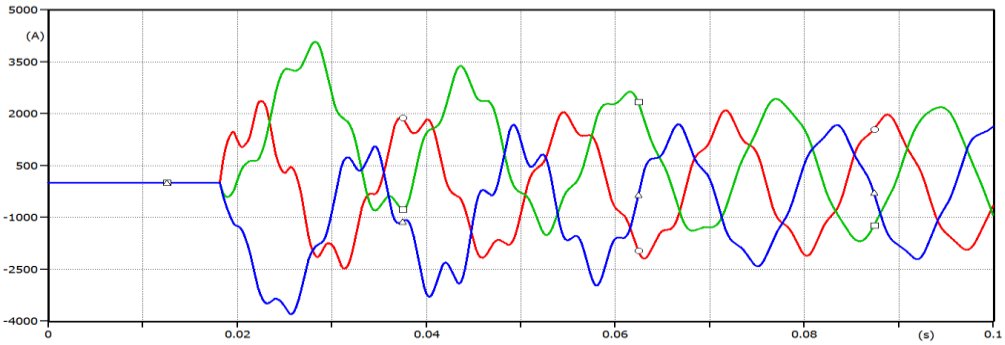

Figure 7.165 SC current at fault location X: when SCF occurs at bus X with fault inductance 65 H on Wind/PV GCS

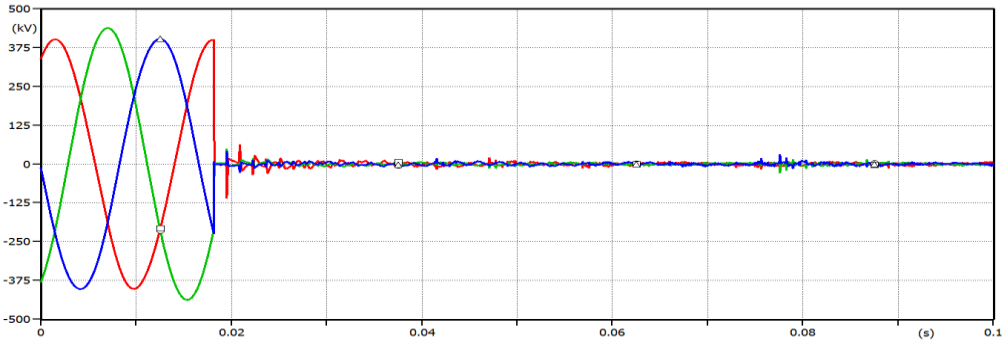

Figure 7.166 SC voltage at fault location X: when SCF occurs at bus X with fault inductance 1 H on Wind/PV GCS

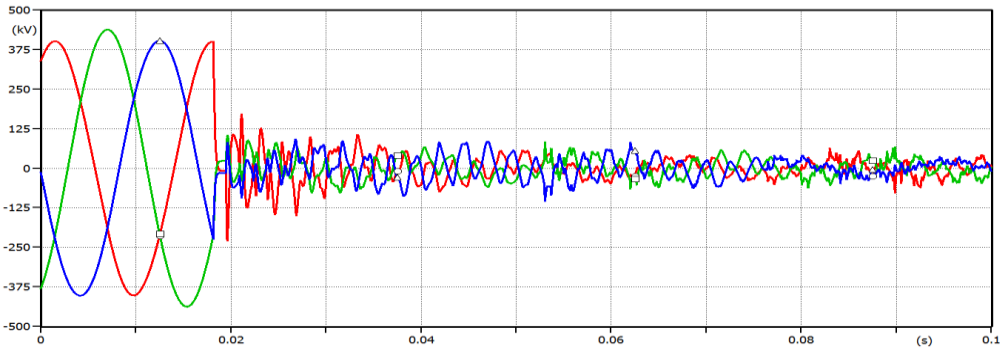

Figure 7.167 SC voltage at fault location X: when SCF occurs at bus X with fault inductance 10 H on Wind/PV GCS

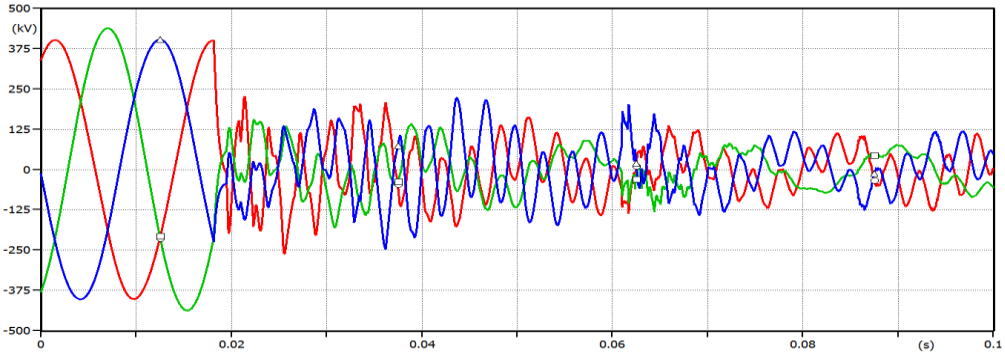

Figure 7.168 SC voltage at fault location X: when SCF occurs at bus X with fault inductance 30 H on Wind/PV GCS

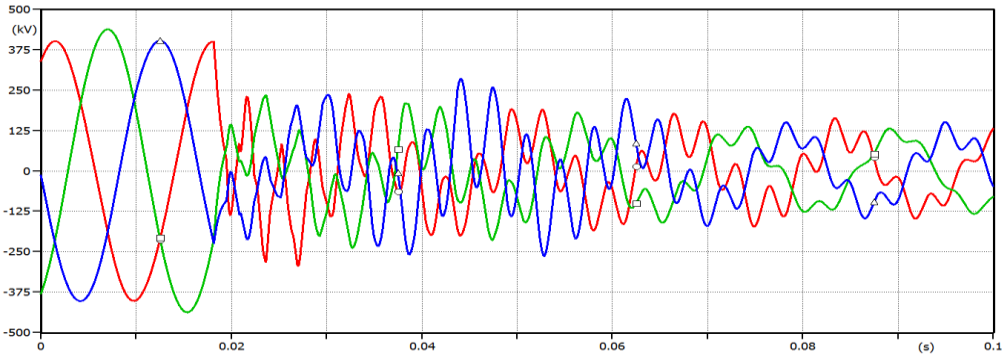

Figure 7.169 SC voltage at fault location X: when SCF occurs at bus X with fault inductance 58.6 H on Wind/PV GCS

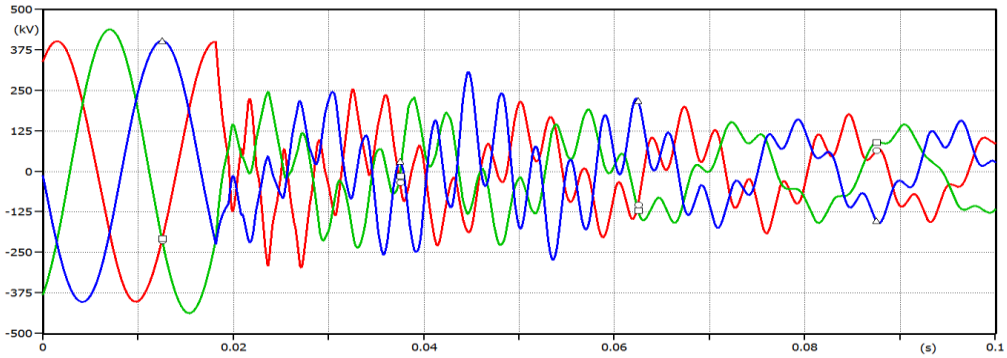

Figure 7.170 SC voltage at fault location X: when SCF occurs at bus X with fault inductance 65 H on Wind/PV GCS

7.5.7 Comparison between Wind/PV GCS with solidly grounding and with Peterson coil under various faults

On this Wind/PV GCS different types of faults are considered such as SLG fault, DLG and SCF. The SLG fault occurs on phase A at the end OHL i.e. 400 kV. In case of DLG fault, fault occurs at the receiving end of the line on phases A and B. Comparison between solidly grounding and Peterson coil grounding of 58.6 H inductance on Wind/PV GCS under various fault condition is given in Table 7.38.

Table 7.38 shows that SCF currents with solidly grounding and with Peterson coil of 58.6 H inductance. SCF current is reduced to 45.28 % and wave distortion is also reduced by using Peterson coil and it's very high when system is solidly grounding as shown in Figure 7.171 and Figure 7.172.

Table 7.38 shows that SLG currents with solidly grounding and with Peterson coil of 58.6 H inductance. SLG current is increased to 19.88 % and wave distortion is also reduced by using Peterson coil and it's very high when system is solidly grounding as shown in Figure 7.173 & Figure 7.174. It is also examined Peterson coil is unsuitable under SLG fault for 400 kV OHL.

Table 7.38 shows that DLG currents with solidly grounding and with Peterson coil of 58.6 H inductance. DLG current is reduced to 43.26 % and wave distortion is also reduced by using Peterson coil and it's very high when system is solidly grounding as shown in Figure 7.175 and Figure 7.176. It has been analysed that Peterson coil is most suitable for SCF and DLG.

Table 7.38 Comparison between solidly grounding and Peterson coil grounding of 58.6 H inductance on Wind/PV GCS under various fault condition

Fault Type	**Maximum Magnitude of Fault Current at Fault Location X (A)**						**Current Minimizing (%)**
	Wind/PV GCS with solidly grounding			Wind/PV GCS with Peterson Coil grounding			
	Phase A	Phase B	Phase C	Phase A	Phase B	Phase C	
SCF	5011	6176	5832	2698	4251	3985	-45.28
SLG	2096	-	-	2616	-	-	19.88
DLG	5119	4782	-	3208	3338	-	-43.26

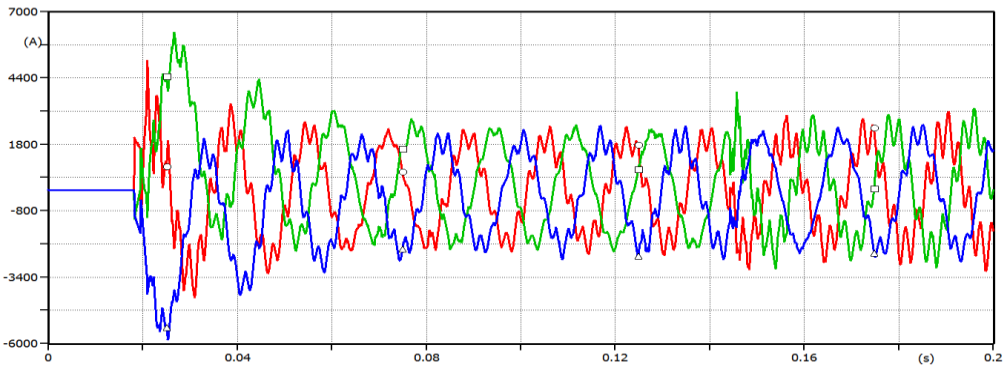

Figure 7.171SCF currents without Peterson coil at fault location X when SCF occur on Wind/PV GCS

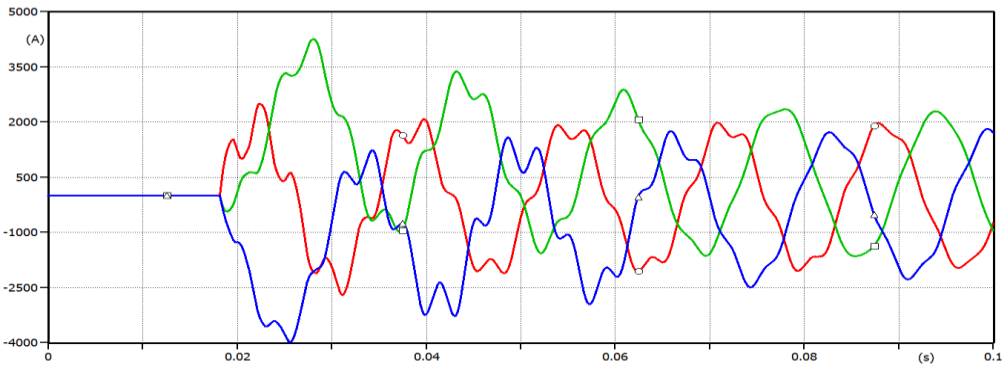

Figure 7.172 SCF currents with Peterson coil of 58.6H at fault location X when SCF occur on Wind/PV GCS

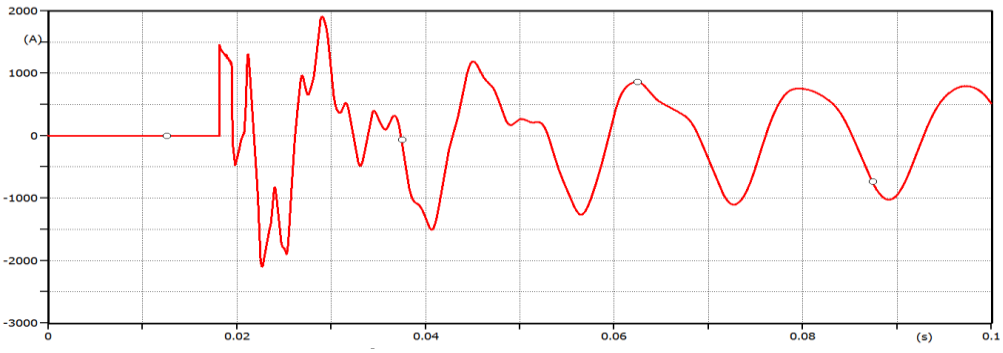

Figure 7.173 Faulted phase current without Peterson coil at fault location X with SLG fault on Wind/PV GCS

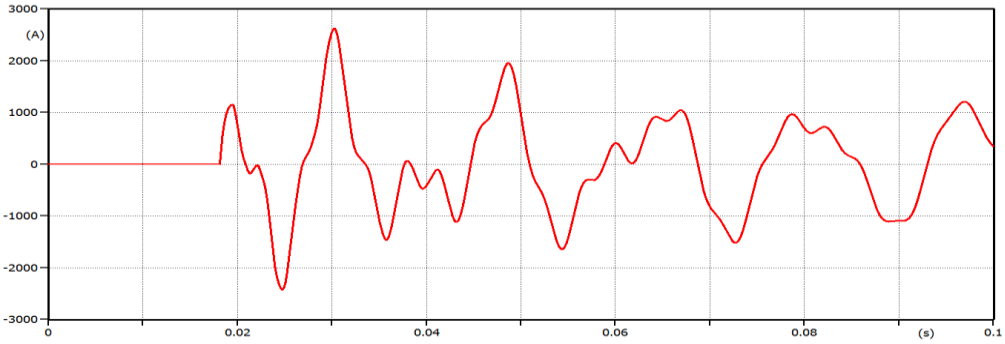

Figure 7.174 Faulted phase current with Peterson coil of 58.6 Hat fault location X with SLG fault on Wind/PV GCS

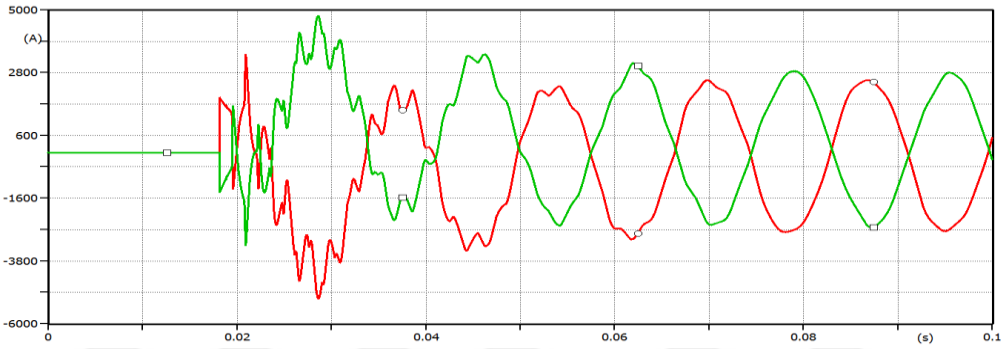

Figure 7.175 Current of faulted phases A and B without Peterson coil at fault location X when DLG fault occurs on Wind/PV GCS

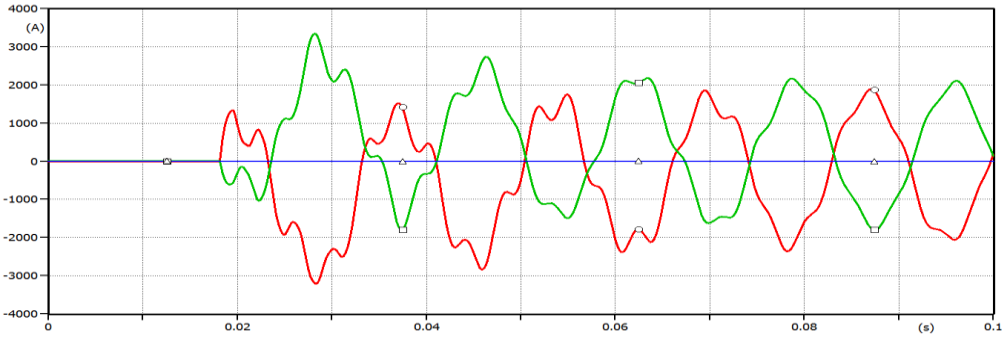

Figure 7.176 Current of faulted phases A and B with Peterson coil of 58.6 H at fault location X when DLG fault occurs on Wind/PV GCS

8. CONCLUSION AND FUTURE WORK

8.1 Conclusion

This thesis is significant for designing, planning and operation of hybrid power systems. These studies are important as they have a direct bearing on the insulation requirements, cost and reliability of the designed network. ATP/EMTP software is used to carry out this study. The data of transient fault currents computed for different type of faults are of importance in the design of protective strategies. In this thesis, contributions of SC current to Wind and PV generator due to faults at the terminal of the generators are examined.

For Wind/PV hybrid system, the largest short circuit current is expected due to 3-phase SCF. The period of the fault is the shortest due to the air gap flux collapses without the aid of enough line voltages. Planners and designers use SCF to compute the CBs duty and other switch gear devices and SLG fault is most frequently take place in power system. Planners should use SCF to calculate the minimum fault current value for protection.

It has been proved from the results that severity of transient over-currents due to SCF on PV/Wind hybrid system changes depending on the fault type, fault resistance, Peterson coil, line length and fault location. These factors have considerable effects on the magnitudes and shapes of the current and voltage waveforms.

From the waveforms obtained, as the line length or fault resistance increase the distortions in the current waveforms decrease. Higher amplitude and frequency oscillations are detected on the voltage waveforms as compared to those in the current waveforms. It is also observed from the waveforms that as fault resistance increases, the magnitudes of maximum fault currents are decreased. It is also seen from the results that when Wind/PV farm is interconnected to the conventional power system, maximum magnitude of the fault current and attenuation in the current waveforms become considerable compared to those obtained in the case of conventional power system alone. The maximum magnitude of fault currents obtained due to three-phase SCF is much more as compared to other type of faults on Wind/PV hybrid power system. The

maximum magnitudes of transient fault currents are observed to be considerably higher at interconnection point of Wind/PV farm and conventional system fault point along the transmission line. Voltage waveforms of faulted phases are decreased to smaller value than rated voltage on Wind/PV hybrid power system. Also wave attenuation increases as it come closer to source location.

Minimization of fault currents at fault location X on Wind/PV hybrid power system due to SCF for different values of Peterson coil at fault location X is also examined. The maximum magnitude of fault currents at fault location X decreases as the fault inductance increases. Fault current at fault location X is decreases from 0.36 % at 1H fault inductance to 51.78 % at 65 H fault inductance. Transients in the fault current waveform are higher at lower value of the fault inductance as compared to that of higher value. It is also analysed that that wave attenuation is also higher due to SCF.

Fault currents with solidly grounding and with Peterson coil of 58.6 H inductance under various fault is also observed. SCF current is reduced to 45.28 % and wave distortion is also reduced by using Peterson coil and it's very high when system is solidly grounding. DLG current is reduced to 43.26 % and wave distortion is also reduced by using Peterson coil and it's very high when system is solidly grounding. It has been analysed that Peterson coil is most suitable for SCF and DLG.

8.2 Future Work

In future, the effect of short circuit can be studied on a larger capacity of distributed generation installed in a distribution system. Transient behaviour due to variable speed Wind generator, variable irradiance & temperature on Wind/PV hybrid system can also be examined. Also the effect of balanced and unbalanced DGs can be studied. The effect of a high load condition, various types of wind generator & consequences of control algorithms of converters on SC current can also be examined. Optimised location for the integration of Wind/PV generators can also be examined.

REFERENCES

Edward Muljadi and Abraham Ellis, March 2010, A CIEE Report WECC Wind Generator Development, National Renewable Energy Laboratory (NREL), University of California.

Alternative Transient Program Rule Book, 9871.

Abdallah R. Al-Zyoud, A. Alwadie, A. Elmitwally, and Abdallah Basheer, Effect of Neutral Grounding Methods on the Earth Fault Characteristics, PIERS Proceedings, Prague, Czech Republic, PP 1144-1151, and July 6-9, 2015

Bogdan S. Borowy and Ziyad M. Salameh, 1996, Methodology for Optimally Sizing the Combination of a Battery Bank and PV Array in a Wind/PV Hybrid System, IEEE Transactions on Energy Conversion, Vol. 11, No. 2.

Binayak Bhandari, Kyung-Tae Lee, Gil-Yong Lee and Young-Man Cho, and Sung-Hoon Ahn, 2015, Optimization of Hybrid Renewable Energy Power Systems, International Journal of Precision Engineering and Manufacturing-Green Technology Vol. 2, No. 1, pp. 99-112.

B. A. Mork, F. Gonzalez, and D. Ishchenko, 2004, Parameter estimation and advancements in transformer models for EMTP simulations, Task MTU-7: Model performance and sensitivity analysis, Bonneville Power Administration, Portland, OR.

B.A. Mork, F. Gonzalez, D. Ishchenko, D. L. Stuehm, J. Mitra, 2007, Hybrid Transformer Model for Transient Simulation-Part II: Laboratory Measurements and Benchmarking, IEEE Trans. Power Delivery, Vol.22, pp. 256-262.

C.L. Wadhwa, 2006, Electrical Power Systems, pp 306, New Age International

D. Tziouvaras, 2008 Analysis of Complex Power System Faults and Operating Conditions, Schweitzer Engineering Laboratories, Inc., TP6327-01.

Dommel H.W, 1971, Nonlinear and time-varying elements in digital simulation of electromagnetic transients, IEEE Transactions on Power Apparatus and Systems, Vol. PAS-90, pp 2561–2567

E. M. Natsheh, A. Albarbar, and J. Yazdani, 2011, Modelling and Control for Smart Grid Integration of Solar/Wind Energy Conversion System, 2nd IEEE PES International Conference and Exhibition on Innovative Smart Grid Technologies (ISGT Europe), E-ISBN 978-1-4577-1420-7, Print ISBN 978-1-4577-1422-1

E. Muljadi, N. Samaan, V. Gevorgian,; J. Li; S. Pasupulati, 2010, Short Circuit Current Contribution for Different Wind Turbine generator Types, Power and Energy Society General Meeting, 2010 IEEE, pp 1-8.

Erdem ZB, 2010, the contribution of renewable resources Meeting in Turkey's energy-related challenges, Renew Sustainable Energy Rev, Time-14:27, pp 10–22.

E. Ercelebi, 1992, Analysis of Lightning Over-voltages in power system, MSc. Thesis, University of Gaziantep, Turkey, September.

F. Bonanno, A. Consoli, A. Raciti, B. Morgana and U. Nocera, 1999, Transient Analysis of Integrated Diesel-Wind-Photovoltaic Generation Systems, IEEE Transactions on Energy Conversion, Vol. 14, No. 2.

G. L. Wilson and K.A. Schmidt, 1974, Transmission Line Models for Switching Studies: Design Criteria II. Selection of Section Length, Model Design and Tests, IEEE Transactions on Power Apparatus and Systems, Vol. PAS-98, pp 389-395. 67.

Global Market Outlook for Solar Power 2015-2019, 2015, Solar Power Europe (SPE) or EPIA – European Photovoltaic Industry Association, Available from www.solarpowereurope.org

Gilbert M.Masters, 2004, Renewable & Efficient Electric Power Systems, John Wiley & Sons INC. Publication, Stanford University, ISBN 0-471-28060-7 (book)

G. Krzysztof, R. Kowalik, D. Rasolomampionona and S. Anwar, 2011, Traveling Wave Fault Location in Power Transmission Systems: An Overview, J. Electrical.

H. W. Dommel, 1969, Digital Computer Solution of Electromagnetic Transients in Single and Multiphase Networks, IEEE Trans. on Power Apparatus and Systems, Vol. PAS-88, No.4, pp 388-399.

Hadi Saadat, 1999, Power System Analysis (Book), ISBN: 0-07-561534-3 WBC/McGraw-Hill.

H. K. Høidalen, B. A. Mork, F. Gonzalez, D. Ishchenko, N. Chiesa, 2007, Implementation and verification of the Hybrid Transformer model in ATP Draw, IPST'07 Lyon, France on 4-7

International Energy Agency Photovoltaic Power Systems Program, 2015, Available from http://www.iea-pvps.org/index.php?id=32.

International Energy Outlook 2016, Energy Information Administration (EIA), Available from http://www.eia.doe.gov/iea

Juan A Martinez-Velasco, 2014, Transient Analysis of Power Systems Solution Techniques, Tools and Applications, IEEE Press Wiley, ISBN 978-1-118-35234-2

Jafar Zangina Sulaiman, 2014, Transient Analysis of Short Circuit Faults in a Hybrid Power System, M.S Thesis, Mevlana University, Turkey.

Jin Yang, John E. Fletcher, and John O Reilly, 2012, Short-Circuit and Ground Fault Analyses and Location in VSC-Based DC Network Cables, IEEE Transactions on Industrial Electronics, Vol. 59, NO. 10.

J. A. Ventre et al, 2004, Photovoltaic systems engineering, CRC press.

J.G. Slootweg, 2003, Wind power: modeling and impact on power system dynamics, PhD dissertation, Dept. Elect. Eng., Delft University of Technology, Delft, Netherlands

Juan A. Martinez-Velasco, 2015, Transient Analysis of Power Systems: Solution Techniques, Tools and Applications, ISBN: 978-1-118-35234-2, Wiley-IEEE Press.

J. A. Martinez, A. I. Ramirez, M. Dávila, 2010, Power System Transients Parameter Determination (Book) ISBN: 978-1-4200-6529-9, Taylor and Francis Group, LLC.

J. Izykowski, 2008, Fault location on power transmission lines, Publisher of Wrocław University of Technology, Wrocław

Jun Zhu, 2004, Analysis of Transmission System Faults the Phase Domain, Texas A&M University, Master Thesis.

J.R. Marti, 1982, Accurate Modelling of Frequency-dependent Transmission Lines in Electromagnetic Transient Simulations, IEEE Trans. Power Apparatus and Systems, vol. PAS-101, No 1, pp. 147–157.

J. A. Martinez and B. A. Mork, 2005, Transformer modelling for low- and mid-frequency transients – a review, *IEEE Trans. Power Delivery*, Vol. 20, No. 2, pp. 1625-1632.

J. A. Martinez, A. I. Ramirez, M. Dávila, 2010, Power System Transients Parameter Determination (Book) ISBN: 978-1-4200-6529-9, Taylor and Francis Group, LLC.

Lin Ye, Hai Bo Sun, Xu Ri Song and Li Cheng Li, 2012, Dynamic Modelling of a Hybrid Wind/Solar/Hydro Micro-grid in EMTP/ATP, Renewable Energy 39, pp 96-106.

L.V. Bewley, 1951, Travelling Waves on Transmission Systems, 2nd Edition, John Wiley & Sons, Inc. N.Y.

L. O. Chua, P. M. Lin, 1975, Computer-Aided Analysis of Electronic Circuits: Algorithms and Computational Techniques, (Book) ISBN 13: 9780131654150 Prentice-Hall, Inc. Englewood Cliffs, New Jersey.

Mukund R. Patel, 2000, Wind and Solar Power Systems, ISBN 0-8493-1605-7, CRC Press.

Lou van der Sluis, 2001, Transients in Power Systems", John Wiley & Sons LTD, ISBN 0-471-48639-6.

M. Uğur Ünver, 1995, Short-circuit fault analysis of transmission lines: double end fed system (in Turkish), Elektrik Müh. 6. Ulusal Kongresi.

Miroslav D. Markovic, 2009, Fault Analysis in Power Systems by Using the Fortescue Method, TESLA Institute

Medium-Term Renewable Energy Market Report 2014, 2014, IEA, Page 13.

Neville Watson and Jos Arrillaga , 2003, Power Systems Electromagnetic Transients Simulation, IET Power & Energy Series 39, ISBN 978-085296-106-3 (Book).

Nasser Tleis, 2007, Power Systems modelling and Fault Analysis, 1st Edition, eBook ISBN: 9780080554273.

Om Prakash Mahela & Sheesh Ram Ola, 2013, Modeling and Control of Grid Connected Photovoltaic System: A Review, International Journal of Electrical and Electronics Engineering Research (IJEEER), ISSN 2250-155X Vol. 3, Issue 1, pp 123-134.

P.L.Alrett, R.M. Shelley, 1996, The teaching travelling wave techniques using an improved graphical method I, International Journal of Electrical Engineering Education, Vol-4, pp 210-230.

R. Valarmathi, S. Palaniswami and N. Devarajan, 2012, Simulation and Analysis of Wind Energy and Photo Voltaic Hybrid System, International Journal of Soft Computing and Engineering (IJSCE), ISSN: 2231-2307, Volume-2, Issue-2.

R. Phukan, R. K. Gupter, S. Dadga, A. Rathinam, 2013, Fault Diagnosis of a High Voltage Transmission Line Using Waveform Matching Approach, IJSC Vol.4, No.4.

R. Mahmutcehajic, S. Babic, R. Garcanovic, S. Carsimamovic, 1993, Digital simulation of electromagnetic wave propagation in a multiconductor transmission system using the superposition principle and Hartley transform, IEEE Transactions on Power Delivery, Vol-8, No.3, pp 1377–1385.

Rajiv K. Varma, Shah Arifur Rahman, and Tim Vanderheide, 2015, New Control of PV Solar Farm as STATCOM (PV-STATCOM) for Increasing Grid Power Transmission Limits During Night and Day, IEEE Transactions on Power Delivery, Vol. 30, NO. 2.

S. Leva, 2009, Power Network Asymmetrical Faults Analysis Using Instantaneous Symmetrical Components, JEAA, 1: 205-213.

Seul-Ki Kim, Jin-Hong Jeon, Chang-Hee Cho, Eung-Sang Kim, Jong-Bo Ahn, 2009, Modelling and simulation of a grid-connected PV generation system for electromagnetic transient analysis, Solar Energy Conference, pp 664–678

Seul-Ki Kim, Eung-Sang Kim and Jong-Bo Ahn, 2006, Modelling and Control of a Grid-connected Wind/PV Hybrid Generation System, IEEE.

Sweeka Meshram, Ganga Agnihotri, and Sushma Gupta, 2013, Performance Analysis of Grid Integrated Hydro and Solar Based Hybrid Systems, Hindawi Publishing Corporation Advances in Power Electronics Volume.

Shahirinia AH, Tafreshi SMM, Hajizadeh A, Moghaddamjoo AR., 2005, Optimal sizing of hybrid power system using genetic algorithm, International conference of future power systems, Netherland.

Sriyananda et Al, 1986, Power System Studies, Published by Open University of Sri Lanka.

Saad Khalifa Omar Dau, 2008, Modelling of Lightning Over-voltages for the Protection of Transmission Lines by Means of Shielding Wires and Surge Arresters, Cracow- Poland, Ph.D. Thesis

S. Chimklai, J. R. Marti, 1995, Simplified Three-Phase Transformer Model for Electromagnetic Transient Studies, IEEE Trans. Power Delivery, Vol. 10, and pp. 1316-1325.

Thomas Ackermann a, Goran Andersson, Lennart Soder, 2001, Distributed generation: a definition, Electric Power Systems Research, pp 195–204.

Tushar K. Ghosh, Mark A. Prelas, 2011, Energy Resources and Systems, Volume 2, ISBN 978-94-007-1401-4 e-ISBN 978-94-007-1402-1, Springer

Turan Gonen, 2015, Electric Power Transmission System Engineering, Analysis and Design, Crc Press Taylor and Francis Group

Volker Quaschning, 2005, Understanding Renewable Energy Systems, ISBN: 1-84407-128-6 paperback 1-84407-136-7 hardback.

Wikipedia, 2015, Growth of photovoltaics, Available from https://en.wikipedia.org.

Y. Kang and J.D. Lavers, 1996, Transient Analysis of Electric Power Systems: Reformulation and Theoretical Basis, IEEE Transactions on Power Systems, Vol. 11. No.2.

APPENDIX

A.1 State Variable Equation

Consider the second order circuit in Figure (A.1)

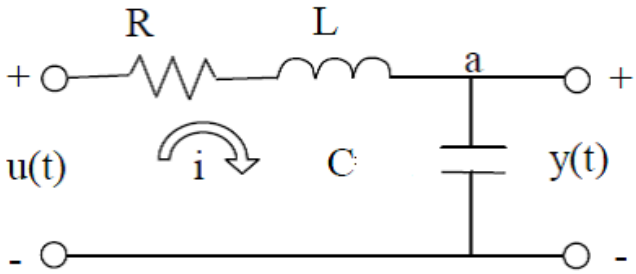

Figure A1.1 Simple RLC circuit

Consider a simplified mathematical model of the hybrid network below in which the input vector is related with the variable output vector.

NOTE: we will use u (t) to denote the input and use x (t) to denote the state.

$i_c = C\,\frac{dv_c}{dt}$ & $v_L = L\,\frac{di_L}{dt}$

We define state variables to be the capacitor voltage and inductor current

$x_1 = v_c\,(t)$

$x_2 = i_L\,(t)$

Note that there is one state variable for each memory storage element. Derive the "State" and "Output" equations express the derivatives of the states and the output in terms of the current state and the input only.

KCL at node a: $\frac{dx_1}{dt} = \frac{1}{C}\,x_2$ (A1.1)

KVL $\frac{dx_2}{dt} = -\frac{1}{L}\,x_1 - \frac{R}{L}\,x_2 + \frac{1}{L}\,u$ (A1.2)

Equation A1.1 & A1.2 can be more compactly written in matrix form:

$$\begin{bmatrix} \dot{x}_1 \\ \dot{x}_2 \end{bmatrix} = \begin{bmatrix} 0 & 1/C \\ -1/L & -R/L \end{bmatrix} \begin{bmatrix} x_1 \\ x_2 \end{bmatrix} + \begin{bmatrix} 0 \\ 1/L \end{bmatrix} u \quad \text{(A1.3)}$$

The above matrix equation is called the State Equation because it relates the change (1st-order derivative) of the state to the current state and input.

We can also relate the output to the state variables as follows:

Output equation: $y(t) = \begin{bmatrix} 1 & 0 \end{bmatrix} \begin{bmatrix} x_1 \\ x_2 \end{bmatrix}$ (A1.4)

Using this approach, we can write the state-variable representation for any circuit. For solving Equation A.4, the initial conditions of the inductor current and of the capacitor voltage have to be known. The solution of the equation can be determined from the method mentioned in Section 4.1.6 Among the solution methods is Euler's (first-order) method which can be used to calculate the state trajectory and capacitor voltage versus the time of the circuit.

A. 2 Overhead Transmission Line

The basic parameters of an overhead line are determined by series impedance matrix Z and shunt admittance matrix Y per unit length of the line. These are evaluated taking into account the effects of conductor internal impedance, conductor geometry and earth-return path, as described below.

A.2.1 Series Impedance Matrix

Series impedance matrix Z of a multi-conductor line is composed of three main components, Z_g, Z_c, and Z_e. The total series impedance is express as;

$$Z = Z_g + Z_c + Z_e \quad \text{(A2.1)}$$

The impedance Z and its component matrices are of the order of 3p + q.

Where,

Zg, Zc, and Ze are the impedance matrix due to physical geometry of the conductor, self-impedance of the conductors and earth-return path, respectively. P is the number of circuits and q is the number of earth wires.

A.2.2 Shunt Admittance Matrix

Shunt matrix Y has no real parts, because the conductance of the air path is negligible. The matrix Y is only a function of the line geometry, having an order of 3p + q where, p is the number of circuits and q is the number of earth wires. Consider Figure 2, the ground plane is a horizontal reference axis, the shunt admittance matrix due to the capacitors and earth are given by

$$Y = j\,\omega^2\,\varepsilon\,H^{-1} \quad \text{(A2.2)}$$

Where,ε is the electric permittivity of the medium and H is the geometry matrix, whose $(i,j)^{th}$ and $(i,i)^{th}$ element are expressed by

$$H_{ii} = \log_e\left[\frac{2h_i}{r_i}\right] \quad \text{(A2.3)}$$

$$H_{ij} = \log_e\left[\frac{D_{ij}}{d_{ij}}\right] \quad \text{(A2.4)}$$

Where;

D_{ij}: Distance between the ith conductor and the image of the jth conductor.

d_{ij}: Distance between i^{th} conductor and j^{th} conductor or radius of ith conductor for $i = j$

h_i: The mean height of the ith conductor

r_i: Equivalent radius of the ith conductor

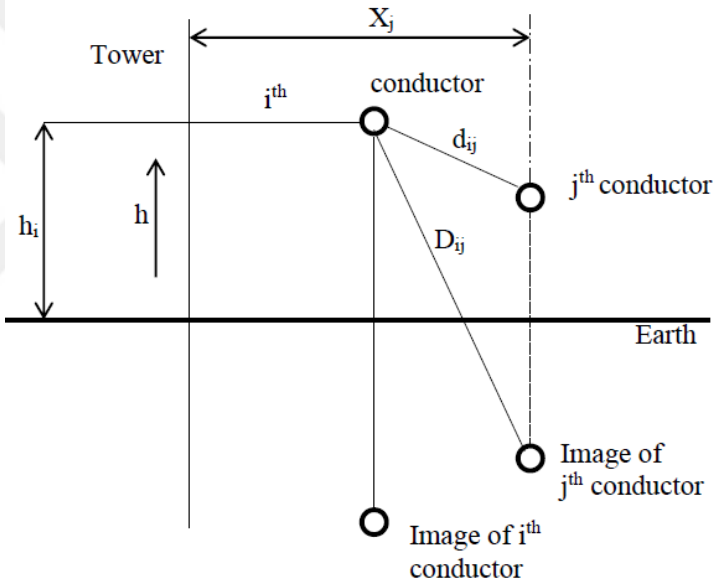

Figure A2.1 Physical positions of the line conductors

A.2.2 Self-Impedance Matrix

The self-impedance matrix Zc is a diagonal matrix, the elements of which corresponds to the self-impedance of the phase conductors and earth wire, such that self-impedance of the earth wire is position being the last diagonal elements of matrix Zc.

Self-impedance of the conductors are influenced by several factors, such as stranding of the conductor, presence of steel core, conductor characteristics and range of frequencies considered. At high frequencies, the resistance of the conductor increase due to skin effect, as such; self-impedance is expressed by two equations which take care of the frequency range.

For low range of frequencies, conductor self-impedance is expressed as;

$$Z_C = R_{dc} + \frac{j\omega\mu_0}{2\pi} \log_e \left[\frac{r}{r_{gm}}\right] \quad \text{(A2.5)}$$

Where,

r: overall conductor radius, r_{gm} conductor geometric mean radius, R_{dc}: d.c resistance in per unit length.

Direct current resistance is given by

$$R_{dc} = \frac{1}{\pi\, r_C^2\, \sigma_C} \quad \text{(A2.6)}$$

Where r_C & σ_C are radius and conductivity of the conductor respectively. At high frequencies, due to predominant skin effect, current density is not uniform within the conductor and is considerable only in the outer parts of the outermost layers. The self-impedance is expressed as;

$$Z_C = R_C + jX_C \quad \text{(A2.7)}$$

$$R_C = X_C = \frac{k\, m\, \rho_C}{[2\, r_C\, (2 + n_0)\, \pi]^{1/2}} \quad \text{(A2.8)}$$

$$m = \left[\frac{j\, \omega\, \mu_0\, \mu_r}{\rho_C}\right]^{1/2} \quad \text{(A2.9)}$$

k: Factor due to conductor strand; ρ_C : Conductor resistivity; r_C: Radius of conductor

n_0: Number of strand in outer layer ω: Angular frequency.

CURRICULUM VITAE

PERSONAL INFORMATION

Name Surname	:	Farhana UMER
Nationality	:	Pakistan
Birth Place and Date	:	Hyderabad Pakistan, 20-07-1986
Telephone	:	+905393483681 and +923423186559 (Pak)
Fax	:	-
e-mail	:	farhana.umer@iub.edu.pk farhanaumer@yahoo.com

EDUCATION

DEGREE		Name, Province, Country	Year of Passing
High School	:	Govt Nazareth girls college Hyderabad, Pakistan	2004
Bachelors	:	Mehran UET Jamshoro, Sindh, Pakistan	2009
Master	:	Mehran UET Jamshoro, Sindh, Pakistan	2013
Doctorate	:	Selçuk University, Konya, Turkey	2017

WORK EXPERIENCES

Year	Institution	Post
2009-2016	UCE&T, The Islamia University of Bahawalpur, Pakistan	Lecturer
2016-Till Now	UCE&T, The Islamia University of Bahawalpur, Pakistan	Assist. Professor

UZMANLIK ALANI
Electrical Engineer

YABANCI DİLLER
English, Urdu, Hindi

OTHERS
Awarded Ph.D. scholarship from the university

PUBLICATIONS
1. Farhana Umer, Noor Khan Afridi, Anwar Ali Sahito and Agha Zafarullah Pathan, Critical Analysis of Capacitors as a Potential Solution to Achieve Optimum Level Voltage Regulation in HESCO Network, IEEE Conference

TAEECE held at Mevlana University Turkey, May 2013, Print ISBN: 978-1-4673-5612-1

2. Farhana Umer, Syed Usman Sabir, Noor Khan, Muhammad Ali Mughal, Hassan Gauhar, Aftab Ahmed Almani and Ghulam Fizza Shah, De-Coupled Power System Analysis Using Parameter Injection Method, Universal Journal of Electrical and Electronic Engineering, USA. Published date: 30-Sep-2014 Print ISSN: 2332-3280, Online ISSN: 2332-3299
3. Farhana Umer and Nurettin Cetinkaya, Transient Analysis Due To Short Circuit Faults in Wind Hybrid Systems, ECBA Conference, 7-8 April 2017 (Made from Ph.D. thesis).
4. Farhana Umer, Nurettin Cetinkaya and Gaddafi Sani Shehu, Transient Analysis of Short Circuit Faults in PV Hybrid Systems, EEETEM Conference 2017, 26-18 April 2017, ISBN: 978-1-5090-0717-2 ©2017 IEEE (Made from Ph.D. thesis).
5. Nurettin Cetinkaya, Farhana Umer, Effect of Neutral Grounding Protection Methods for Compensated Wind/PV Grid Connected Hybrid Power Systems, in Review in International Journal of Photoenergy (Made from Ph.D. thesis).